2018

The Search for N* Resonances: Measurement of Differential Cross Sections and Polarization Observables for #p # p# and #p # K0#+ Using Circularly-Polarized Photons at CLAS, Jefferson Lab

Zulkaida Akbar

FLORIDA STATE UNIVERSITY

COLLEGE OF ARTS AND SCIENCES

THE SEARCH FOR N* RESONANCES: MEASUREMENT OF DIFFERENTIAL CROSS SECTIONS AND POLARIZATION OBSERVABLES FOR $\gamma p \rightarrow p\omega$ AND $\gamma p \rightarrow K^0\Sigma^+$ USING CIRCULARLY-POLARIZED PHOTONS AT CLAS, JEFFERSON LAB

By

ZULKAIDA AKBAR

A Dissertation submitted to the
Department of Physics
in partial fulfillment of the
requirements for the degree of
Doctor of Philosophy

2018

Zulkaida Akbar defended this dissertation on July 10, 2018.
The members of the supervisory committee were:

Volker Crede
Professor Directing Dissertation

Anke Meyer-Baese
University Representative

Jorge Piekarewicz
Committee Member

Paul Eugenio
Committee Member

Todd Adams
Committee Member

The Graduate School has verified and approved the above-named committee members, and certifies that the dissertation has been approved in accordance with university requirements.

“Indeed, in the creation of the heavens and the earth and the alternation of the night and the day are signs for Ulul Albab.”

-Quran, 3:190

ACKNOWLEDGMENTS

Tuesday afternoon, July 10th 2018, after my defense:

Volker Crede: "How is your feeling?"

Me: "I am feeling normal. To be honest, It's harder to think that I am gonna leave Tallahassee soon."

Volker Crede: "That is good. It means that you have a really good time here. And I am so happy about that."

Me: "Indeed."

Tallahassee and Florida State University indeed have been very nice to me. A lot of beautiful memories in the past 5 years, and Volker Crede, my major professor was one of the main reasons why choosing FSU and joining hadronic physics groups were one of the best decisions in my life. His guidence and dedication to his students were beyond words. I remember one day during 2014 spring, before my first summer in FSU, when he wanted to send me to a three-weeks summer school in JLab:

Volker Crede: "You should attend this summer school (HUGS), this is really good for you!"

Me: "But what if I should teach?" (It was still my first year when all PhD students normally still have to be a TA)

Volker Crede: "Don't worry. If needed, I will teach the class for you."

I felt that I and Volker Crede has worked as a great team. There is only one way I could thank him. Someday in the future, when I become a professor, I promise that I will be a good and dedicated mentor, just like him. I will certainly miss our almost daily conversation about physics and non-physics, also the wonderful and long trip to JLab.

Many thanks to the hadronic physics group at FSU for their helps. I would like to thank Priyashree Roy for teaching me ROOT and basic technical skills required in this field. Also for the many discussions which kept my enthusiasm up every day, and not to mention enjoying the coffee hour or the Student Life cinema with Raditya Utama. I would also like to thank Paul Eugenio for involving me in the construction of the light guide for the Central Neutron Detector, also for serving as my commiittee. This was my first hardware experience, and I was really glad to see our *gold* and *garnet* light guide will be installed to CLAS12 detector.

I was thankful to Alexander Ostrotridov for always taking care of our supercomputer. Many thanks to Ashley Ernst for the physics and coding discussions, and helping me by compiling new PDG data before my defense. I hope that my future office mate will be as generous as her, always provide a big bowl of chocolatte and candy on her desk. Thanks to Christopher Zeoli for generating the Monte Carlo at JLab and the political discussion. Thanks to Kyle Romines for the buffet adventure. I hope he will get better buffet in DC. Thanks to Brad Cannon, Angelica Goncalves, Sebastian Barriga and Jason barlow for the nice and memorable surprise after my defense.

I would also like to thank Jorge Piekarewicz, Todd Adams and Anke Meyer-Baese for serving as my committee. Jorge Piekarewicz was one of the first professors I met when I came to FSU. I knew him before I came as everybody said that Jorge was one of the best professors. I heard about his patience and dedication to his students even when I was still in Indonesia. And indeed, what I heard was true. Thanks to Jorge for the physics discussion and motivation, also for the recommendation letter for my Postdoctoral position.

A very important component of my life during the PhD journey was meeting many good friends in Physics department. Many Thanks to Hiram Menendez who taught me driving and never give up until I got my lisence after the fourth driving test. I will surely miss our night work in All Saint Cafe. Thanks to David Clarke, Yavuz Oz, Niraj Aryal, Arash Yuneshi, Jom Narbey and Valery for arranging the "goodbye" dinner. David, do not forget our adventure in DC during the APS meeting. Thanks to Jom for your sincerely-offering help of my moving. Thanks to Quintin Mabanta, I remember when suddenly you sent me burger at midnight in the office.

Thanks to Haykel, Laksmi and Raditya for the wonderful journey to Smoky Mountain and for sure the beautiful friendship. I spent most of my time in Tallahassee with my roommates and my Indonesian friends. Many thanks to them for everything since I came to FSU. Thanks to Marzul Hidayat, Andy Wally, Muhandis Shiddiq, Raditya Utama, Henry Pranoto, Julien Freire, Yohannes Hamman, Tunggul. So many things and memorable trips that I could not mention here. Thanks to Raditya Utama and Julien Freire for the nice and relaxing chat after work.

Many thanks to Sukatno, my high school physics teacher for everything you taught me about physics and life as well. I will always remember your advises forever.

Thanks to Bobby Eka Gunara, my undergraduate adviser, for introducing me to the beautiful world of particle physics.

Thanks to Yohannes Surya and Eddy Yusuf for introducing and sending me to FSU. Thanks to Eugene Pasyuk for the valuable physics discussion and the recommendation letter. Thanks to Lei Guo and others $g12$ members for helping me in shaping this analysis.

Most importantly, I would like to thank my family for being my pillars of support. To Siti Humaesoh, my loving wife, I was smitten the first day I met you and I have been smitten with you everyday afterward. You are a great source of my happiness. There is no word I can muster properly to convey what I would like to write about your supports and everything you gave me. A few underrated words would be lucky, patience, kindness etc. I love you and thanks for everything. This PhD is dedicated to you. To my son and daughter, Arya and Yuka, Bapak love you and will always be here for you.

And many thanks to my mother and my father. I always believe that behind this work, there were countless of prayers my parent did every day, even in the middle of the silence night. The only way I could do to thank you is by continuing my hardwork and proving that I will be a successful physicist in the future. Thanks for your *dua*, love and immense supports.

TABLE OF CONTENTS

LIST OF TABLES

LIST OF FIGURES

ABSTRACT

The study of baryon resonances offers a deeper understanding of the strong interaction, since the dynamics and relevant degrees of freedom hidden within them are reflected by the properties of these states. The baryon resonances have been fairly accurately predicted in the low-energy region by constituent quark models and lattice quantum chromodynamics. However, most of the predicted higher-lying excited resonances (center-of-mass energies above 1.7 GeV/c^2) and experimental findings do not match up. The model calculations predict more baryon resonances than have been experimentally observed. Quark model calculations have suggested that some of the unobserved resonances couple strongly to γp reactions.

The higher-lying excited states are also generally predicted to have strong couplings to final states involving a heavier meson, e. g. one of the vector mesons, ρ, ω, ϕ. The excited states of the nucleon are usually found as broadly overlapping resonances, which may decay into a multitude of final states involving mesons and baryons. Polarization observables make it possible to isolate single resonance contributions from other interference terms. This works presents measurements of the helicity asymmetry, E, for the reaction $\gamma p \to p\omega$ in the energy range 1.1 GeV $< E_\gamma <$ 2.3 GeV, differential cross sections, $\frac{d\sigma}{d\cos\theta^{\omega}_{c.m.}}$, and spin density matrix elements, $\rho^0_{MM'}$, also for the reaction $\gamma p \to p\omega$ in the energy range 1.5 GeV $< E_\gamma <$ 5.4 GeV.

Photoproduction of nucleon resonances in their decay to strange particles also offers attractive possibilities because the strange quark generates another degree of freedom and gives additional information not available from the nucleon-nucleon scattering. Thus, we have also extracted the helicity asymmetry, E, for the reaction $\gamma p \to K^0\Sigma^+$ in the energy range 1.1 GeV $< E_\gamma <$ 2.1 GeV, differential cross sections, $\frac{d\sigma}{d\cos\theta^{K}_{c.m.}}$, and recoil hyperon polarization, P, also for the reaction $\gamma p \to K^0\Sigma^+$ in the energy range 1.15 GeV $< E_\gamma <$ 3.0 GeV.

The data were collected at Jefferson Lab, using the CLAS detector, as part of the $g9a$ and $g12$ experiments. Both experiments, as part of the N^* spectroscopy program at Jefferson Laboratory, accumulated photoproduction data using circularly-polarized photons incident on a longitudinally-polarized butanol target in the $g9a$ experiment and un-polarized liquid hydrogen target for the $g12$ experiment.

A partial-wave analysis to the E data for the reaction $\gamma p \to p\omega$ within the Bonn-Gatchina framework found dominant contributions from the $3/2^+$ near threshold, which is identified with the sub-treshold $N(1720)3/2^+$ resonance. Some additional resonances, including 2 new resonances and the t-channel π and pomeron exchange are needed to describe the data.

CHAPTER 1

INTRODUCTION AND OVERVIEW

1.1 Quantum Chromodynamics

1.1.1 Standard Model of Particle Physics

Since the era of the Greek philosophers, humans have been fascinated with understanding the fundamental building blocks of the universe. This curiosity, as well as 2000 years of continuous efforts, have fructified an existing model, namely the standard model of particle physics that explains how the universe works in term of its fundamental building blocks and their interactions. According to this model, the universe contains two families of matter particles, quarks and leptons, and one family of gauge bosons that carries the interactions among particles.

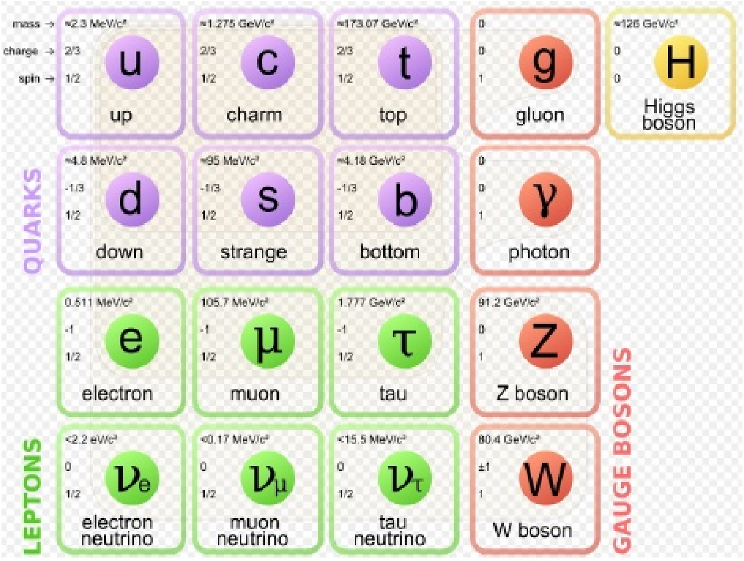

Figure 1.1: The standard model of particle physics, consists of *quarks, leptons* and *gauge bosons*, along with the *Higgs boson*, that is responsible for generating masses. Image source: Wikipedia.

Quarks that consist of six different flavors as shown in Figure 1.1, interact strongly, mediated by gluons. The theory that describes the strong interactions of quarks and gluons is called Quantum Chromodynamics (QCD). Unfortunately, QCD can not be solved analytically in the low energy regime. Furthermore, a free and isolated quark never exists in nature. Quarks (and gluons) always form a composite object called a hadron. This "confinement" feature and the analytically un-solvable nature of QCD, has remained the biggest obstacle to understanding the strong interaction since the discovery of QCD in the early 1970s. Therefore, physicists developed approximate phenomenological models or QCD inspired models, such as the Constituent Quark Model (CQM), and used the models to predict the spectrum of hadrons.

The principle goal behind this work is to understand how quark and gluon dynamics gives rise to the spectrum of hadrons. There are two classes of hadrons, classified based on their spin: mesons and baryons. Baryons have half integer spin and obey Fermi-Dirac statistics, while mesons have integer spin and obey Bose-Einstein statistics. Normal baryons, such as nucleons (protons and neutrons), consist of three valence quarks. Nowadays, the study of hadron structure and spectrum are the main tools, utilized by physicists to get insight into the nature of strong interactions. Baryon spectroscopy is the prime motivation of this analysis.

Baryon Spectroscopy is the study of excited nucleons. One way to excite nucleons is by using a high-energy photon beam. When a high-energy photon strikes the nucleon, an excited nucleon is formed in a very short time before decaying to a ground state nucleons while producing other particles. These types of events, namely photoproduction reaction, are the focus of this work. In this thesis, we present the differential cross section and the polarization observables from vector meson photoproduction and hyperon photoproduction channels. Those channels are very important for some reasons and will be discussed in section 1.4 and 1.5.

1.1.2 Nature of Quantum Chromodynamics

As manifest in its name, the strong interaction is the strongest force among other fundamental interactions, namely gravitational, weak, and electromagnetic interaction.

The electromagnetic interaction as described by a theory called Quantum Electrodynamics (QED) is the most understood interaction. QED dictates the behavior of most atomic and molecular phenomena that we see on the daily basis. In the language of group theory, QED is an U(1) gauge theory, represented by spin-$\frac{1}{2}$ dirac fermion fields coupled to a spin-1 photon field. In simple words, QED describes the interaction of charged spin-$\frac{1}{2}$ particles (quarks and charged leptons), mediated by photons. As the most established fundamental theory, QED can be understood precisely in all regions of energy.

QCD is an SU(3) gauge theory that governs the interaction among *color* particles, *i.e.*, quarks and gluons. There are three different *colors*: red, blue and green. Unlike QED, QCD has some features that make it challenging to understand the strong interaction. In QED, charged particles interact by photons exchange, but the photons do not self interact since a photon is a neutral-charged particle. On the other hand, gluons in QCD are not only mediating the interaction among quarks but also interacting with each other since they are not *color*-neutral.

The strength of an interaction is determined by a quantity called coupling constant. The coupling constant that appears in the interaction term of the Lagrangian dictates the interaction strength among the field of particles. As an example, the QED Lagrangian

$$L_{int} = e\overline{\psi}\gamma^{\mu}\psi A_{\mu} \tag{1.1}$$

describes the charged particle interaction that is mediated by a photon field, denoted by A_μ with the coupling constant e. Usually, it is more convenient to write the coupling in terms of a dimensionless fine-structure constant:

$$\alpha_{QED} = \frac{e^2}{4\pi} \approx \frac{1}{137}. \tag{1.2}$$

The electromagnetic-interaction coupling-constant is much less than one. Thus, the QED calculation can be performed perturbatively. Quite the contrary, the strong coupling constant, α_{QCD} is energy-dependent. Figure 1.2 shows the value of α_{QCD} as a function of four-momentum transfer.

In the high energy regime, α_{QCD} is small; hence a perturbative calculation can be performed. Unfortunately, α_{QCD} is exponentially growing as we go to the low-energy regime. This non-perturbative regime is the region where the physics is less understood. The situation has led to a worldwide effort to build particle accelerators that operate in the non-perturbative regime of energy. One of the leading player is the Thomas Jefferson National Laboratory (JLab).

One of the prominent features in QCD is quark confinement. Quarks are never seen as isolated particles; instead, quarks (and antiquarks) always form composite objects, which are called hadrons. The large value of α_{QCD} at low energy makes it impossible to break a hadron and isolate its constituent quarks since this requires an infinite amount of energy. The origin of confinement is still mysterious but qualitatively it can be explained by the *antiscreening* effect of gluons.

The coupling constant for both QED and QCD actually depends on the momentum transfer. This dependence of the running coupling constant is due to the *vacuum* polarization effect. In QED,

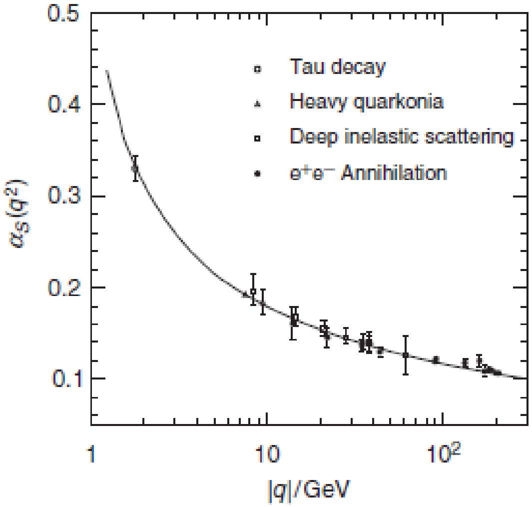

Figure 1.2: Measurements of α_{QCD} at different four-momentum transfer scales from various experiments. The results show evidence for the asymptotic freedom at large momentum transfer or short distances. Image source: [1].

we have the following Feynman diagram where the photon propagator creates an electron-positron pair.

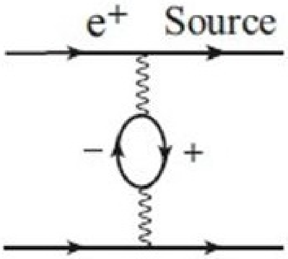

Figure 1.3: The pair production of electron-positron from the photon propagator. Image source [2].

The creation of the electron and positron pairs provide a *screening* effect, a phenomenon that also happens in dialectric medium, which reduces the effective charge. The running coupling constant will increase with an increasing momentum transfer (probing shorter distances),

$$\alpha_{QED} = \alpha(0)\left\{1 + \frac{\alpha(0)}{3\pi}\ln\left(\frac{|q^2|}{(mc)^2}\right)\right\}, \tag{1.3}$$

where $\alpha(0) = \frac{1}{137}$. The correction is usually in the order of $\approx 10^{-6}$. Thus, $\alpha_{QED} = \frac{1}{137}$ is still a good approximation to be used in a calculation.

QCD also exhibits *vacuum* polarization, where the gluon line produces quark-antiquark pairs as shown in Figure 1.3. However, since a qluon may interact with other gluons, the diagram shown in Figure 1.4 also exists. This diagram produces an *antiscreening* effect opposite to QED. The running coupling constant for QCD is

$$\alpha_{QCD} = \frac{\alpha_{QCD}(\mu^2)}{1 + (\frac{\alpha_{QCD}(\mu^2)}{12\pi})(11n - 2f)\ln\left(\frac{|q^2|}{\mu^2}\right)}, \tag{1.4}$$

Where, n is the number of colors (3, in the standard model) and f is the number of flavors (6, in the standard model). Therefore, QCD behaves in the opposite way of QED. The running coupling constant will decrease with an increasing momentum transfer $|q^2|$. At short distances, the "strong" force becomes relatively weak. This is the basis of what we call $asymptotic freedom$, where we can treat quarks as essentially free particles. David Gross, Frank Wilcek and David Politzer won the Nobel Prize in 2004 for their work on *asymptotic freedom.*

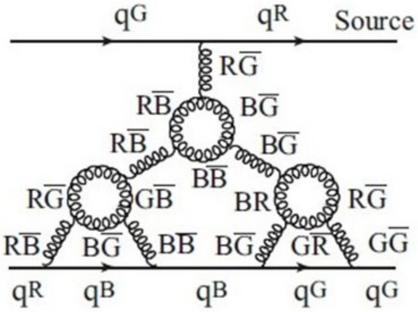

Figure 1.4: The *antiscreening* effect due to the self-interaction among gluons. This effect explains qualitatively the origin of the running coupling constant of QCD, α_{QCD}. Image source [2].

1.1.3 Hadron Properties and Nomenclature

There are two groups of hadrons, classified based on their spin: namely, baryons and mesons. Baryons have half integer spin and obey Fermi-Dirac statistics, while mesons have integer spin and obey Bose-Einstein statistics. Hadrons are named based on the mass and a set of quantum number; for instance, isospin (I), parity (P), spin (S), orbital angular momentum (L), total angular momentum (J), charge conjugation (C) and flavor content. There are some naming schemes based on the practical purposes:

1. In the early era of hadron spectroscopy, the newly discovered hadrons are named based on the atomic spectroscopy notation, *i.e* ${}^{2s+1}L_J$., For examples, the spectroscopy notations for π and ω are ${}^1S_0$ and ${}^3S_1$.
2. Charge conjugation C is a good quantum number only for neutral mesons. Thus, mass (MeV/c^2), isospin I, and J^{PC} are sufficient to identify a meson. For example, π's are denoted as $J^{PC} = 0^{-+}$ mesons with mass≈140 Mev/c^2.
3. Nucleon (N) and Delta (Δ) are baryons with quark content u and d. N states have $I = \frac{1}{2}$ while Δ states have $I = \frac{3}{2}$. All the N and Δ states are denoted by $N(\text{mass})J^P$ and $\Delta(\text{mass})J^P$. For examples, a nucleon can be denoted as $N(938)\frac{1}{2}^+$ and the ground state of Δ can be denoted as $\Delta(1232)\frac{3}{2}^+$

1.2 Hadron Spectroscopy and Structure

There are some main tools, utilized by physicists to study the composite objects of strongly interacting particles: hadron spectroscopy, the study of hadron structures and the hadronic jets finding and reconstruction. Spectroscopy is the study of excited states, where, in this case, a ground-state nucleon is excited by means of a high energy particle (photon, electron, pion, or proton) beam. Mapping out the whole spectrum of excited states is the main goal of spectroscopy research. Based on the properties of the observed excited states, physicists create models to explain the underlying mechanism behind the emerged pattern.

1.2.1 Pre-QCD Strong Interaction Models: Regge Theory

In the early 1960s, before the discovery of quarks and QCD, physicists utilized quantum scattering theory to understand high-energy scattering data. Regge-pole theory was introduced in particle physics and, up to present time, is still widely used for descriptions of the high-energy interactions of hadrons and nuclei. Named after Tulio Regge, the Regge approach establishes an important connection between high-energy scattering and the spectrum of particles and resonances.

The transition of a closed system of particles from an initial state $|i\rangle$ to a final state $|f\rangle$ is described in quantum theory by the S matrix:

$$|f\rangle = S\,|i\rangle\,, \tag{1.5}$$

where the matrix element of the S matrix:

$$S_{fi} = \langle f|\, S\, |i\rangle \tag{1.6}$$

can be represented in the form

$$S_{fi} = \delta_{fi} + i(2\pi)^4 \delta^4(P_i - P_f) T_{fi}. \tag{1.7}$$

T_{fi} is called the transition (scattering) amplitude from state $|i\rangle$ to state $|f\rangle$. For a spinless particle, T_{fi} is a function of the invariant Mandelstam variables:

$$s = (P_1 + P_2)^2 = (P_3 + P_4)^2, \tag{1.8a}$$

$$t = (P_1 - P_3)^2 = (P_2 - P_4)^2, \tag{1.8b}$$

$$u = (P_1 - P_4)^2 = (P_2 - P_3)^2. \tag{1.8c}$$

Here, for a case of binary reaction, T_{fi} is a function of two variables: $T_{fi}(s,t)$ or equivalently $T_{fi}(s, \cos\theta)$. According to the partial wave analysis technique, the transition amplitude can be expanded to the form

$$T_{fi} \propto \sum_{l=0}^{\infty} (2l + 1) f_l(s) P_l(\cos\theta). \tag{1.9}$$

The crossing symmetry principle also allow us to write the partial wave as a function of t, $f_l(t)$. Suppose the $f_l(t)$ in t-channel reaction has a singularity in the form

$$f_l(t) = \frac{r(t)}{l - \alpha(t)}, \tag{1.10}$$

and $\alpha(t)$ is Taylor expanded around $t = t_R \equiv M_R^2$, then

$$\alpha(t) \approx Re\, \alpha(t_R) + i\, Im\, \alpha(t_R) + \alpha'(t_R)(t - t_R). \tag{1.11}$$

If we assume that $Re\, \alpha(t_R) = l_R$, then

$$f_{l_R}(t) \approx \frac{r(t)}{l_R - [l_R + i\, Im\, \alpha(t_R) + \alpha'(t_R)(t - t_R)]}. \tag{1.12}$$

According to the optical theorem that was derived from the unitarity principle, the amplitude of a partial wave is proportional to its imaginary part

$$|f_l(t)|^2 = f_l^*(t) f_l(t) \propto Im\, f_l(t) = \frac{1}{2i}(f_l(t) - f_l(t)^*). \tag{1.13}$$

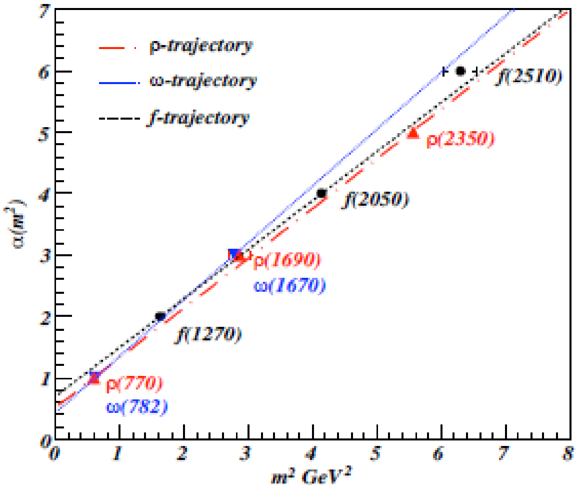

Figure 1.5: Some of the meson trajectories. The trajectories are almost linear, connecting the mass and spin of the particles. High-energy particles scattering is described by the t-channel exchange of particles within trajectories. Image source [3]

Therefore,

$$\frac{r}{l-\alpha(t)} - \frac{r^*}{l-\alpha(t)^*} \propto 2i\frac{rr^*}{(l-\alpha(t))(l-\alpha(t)^*)}. \tag{1.14}$$

Thus, this proportionality is valid if

$$r = r^*, \tag{1.15}$$

and

$$Im\,\alpha(t) \propto r(t). \tag{1.16}$$

Therefore,

$$f_{l_R}(t) \approx \frac{Im\,\alpha(t)}{\alpha'(t_R)(t-t_R) + i\,Im\,\alpha(t_R)}. \tag{1.17}$$

Or we can write this as

$$f_{l_R}(t) \approx \frac{1}{M_R^2 + t + i\,M_R\Gamma}, \tag{1.18}$$

where $M_R\Gamma \equiv \frac{Im\,\alpha(t_R)}{\alpha'(t_R)}$. In conclusion, Regge poles in the physical region of the t-channel correspond to a Breit-Wigner resonance with $Re\,\alpha(t) = l_R$ (spin of exchange particles). Thus, all strongly interacting particles fall into groups of linear trajectories that relate the mass of the particles and their spin.

1.2.2 Baryon Spectroscopy

A baryon is a type of hadron with half-integer spin that obeys Fermi-Dirac statistics. A normal baryon consists of three quarks with three different colors, which establishes a colorless object. Spectroscopy of baryons, which means mapping out the spectrum of the excited states (resonances) of the baryons, is an essential tool for studying the underlying dynamics behind the confinement. To describe the spectrum, physicists start with the assumption that the constituents of baryons (partons) obey SU(N) group symmetry, where N is the number of quark flavors. Some models differ in the origin and dynamics of the excitation. For example, in the Constituent Quark Model (CQM), the origin of the excitation is the orbital angular momentum and the harmonic oscillator potential. CQM, as well as Lattice QCD, are two approaches (or methods) that explain the underlying dynamics of hadrons and their resulting resonance spectrum.

Constituent Quark Model. In this model, a baryon is considered a system of three constituent quarks, which constitutes the effective degrees of freedom of the system. Those quarks obey the SU(N) flavor symmetry, where $N = 3$, if we only consider the three lightest quarks (u, d, s).

The full wave function of a baryon is given by

$$\psi = \psi_{color}\, \psi_{flavor}\, \psi_{spin}\, \psi_{space}. \tag{1.19}$$

The overall wave function should be antisymmetric since baryons obey Fermi-Dirac statistics. The color wave function, ψ_{color} is antisymmetric; hence, the remaining wave function, $\psi_{flavor}\, \psi_{spin}\, \psi_{space}$ should be symmetric.

The spatial part of the wave function for the three-body system (baryon) is described in terms of two harmonic oscillators, ρ and λ, as shown in Figure 1.6. The quantum excitations consist of angular excitations, which we denote as l_ρ and l_λ, and radial excitations, denoted as n_ρ and n_λ. The total quantum numbers of an excited baryon can then be written as

$$N = 2(n_\rho + n_\lambda) + l_\rho + l_\lambda. \tag{1.20}$$

The SU(3)$_{flavor}$ group can be combined with the SU(2)$_{spin}$ group into SU(6)$_{flavor\times spin}$. The multiplets formed by qqq combinations containing the u, d and s quarks are

$$\mathbf{6} \otimes \mathbf{6} \otimes \mathbf{6} = \mathbf{56}_S \oplus \mathbf{70}_M \oplus \mathbf{70}_M \oplus \mathbf{20}_A, \tag{1.21}$$

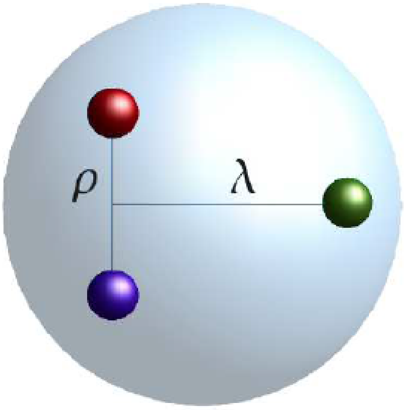

Figure 1.6: Model of a baryon used in a Constituent Quark Model. According to this model, a baryon is an object with two independent oscillators, ρ and λ, which describe the spatial part of the wave function. Image source [7].

where S, M and A represents symmetric, mixed, and antisymmetric wave functions. These SU(6) multiplets decompose into flavor SU(3) multiplets as follows:

$$\mathbf{56} = {}^{4}\mathbf{10} \oplus {}^{2}\mathbf{8} \tag{1.22a}$$

$$\mathbf{70} = {}^{2}\mathbf{10} \oplus {}^{4}\mathbf{8} \oplus {}^{2}\mathbf{8} \oplus {}^{2}\mathbf{1} \tag{1.22b}$$

$$\mathbf{20} = {}^{2}\mathbf{8} \oplus {}^{4}\mathbf{1}. \tag{1.22c}$$

The superscript $(2S+1)$ gives the net spin of the quarks for each particle in an SU(3) multiplet. The resonances can then be classified into different excitation bands based on the quanta of excitations. The supermultiplets can be specified by $(\mathbf{D}, L_N^P)$, where D is the dimensionality (**56**, **70** or **20**), N is the quanta of excitation, L is the total angular momentum, and P is the parity. The ground state baryons, $N = 0$, contain one supermutiplet $(\mathbf{56}, 0_0^+)$ since only the **56**plet has a symmetric wave function. These ground state baryons decompose into a spin-$\frac{1}{2}$ octet $({}^{2}\mathbf{8})$ and a spin-$\frac{3}{2}$ decuplet $({}^{4}\mathbf{10})$. The members of the baryon octet and decuplet are shown in Figure 1.7.

Nucleons (protons and neutrons) and Δ's are baryons with the quark content u and d. The nucleon is a member of octet (**8**) and has $I = \frac{1}{2}$ while the Δ baryon is a member of decuplet (**10**) and has $I = \frac{3}{2}$. The spectrum of nucleon resonances (N^*) and Δ resonances (Δ^*) are built based on the symmetric/antisymmetric properties of the spatial and the SU(6) multiplets wave function.

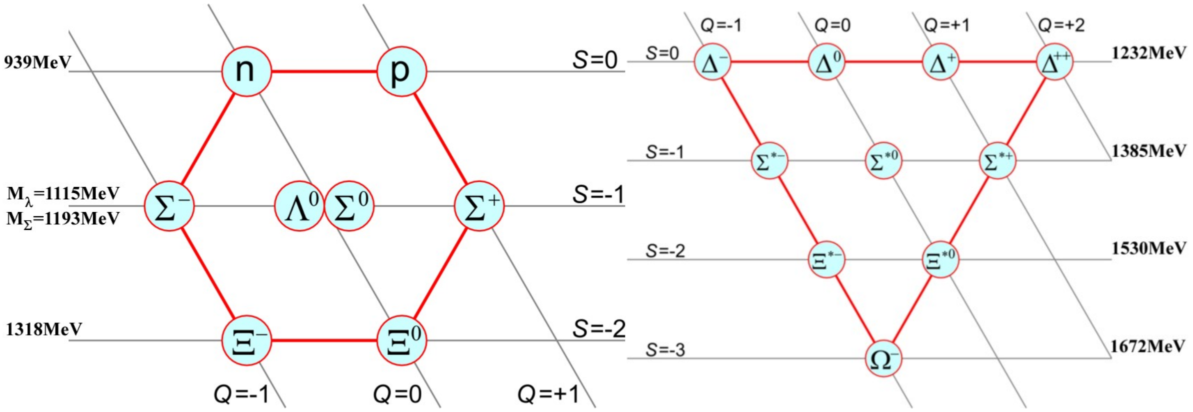

Figure 1.7: The members of ground state baryons: baryon octet (left) and baryon decuplet (right). The symbol Q denotes the electric charge and the symbol S denotes the strangeness. Image source: Wikipedia.

1. **Excitation band 1:** The 1^{st} excitation, $N = 1$, has one quantum of angular excitation, which is carried by the ρ or λ oscillator ($n_\rho = 1$ or $n_\lambda = 1$). The first angular excitation has a mixed symmetry wave function; therefore, the combined wave function of flavors and spin should also have a mixed symmetry in order to create an overall symmetric wave function, which is the **70** multiplet. The **70** multiplet contains one spin-$\frac{1}{2}$ decuplet, two octets ($S = \frac{1}{2}$ and $S = \frac{3}{2}$), and one spin-$\frac{1}{2}$ singlet. The 1^{st} excitation band has $L = 1$ and $P = -1$.

   Since the nucleon is an octet member, the N^* resonances are formed with the possible values of $J = \frac{1}{2}, \frac{3}{2}$ for $L = 1$ and $S = \frac{1}{2}$ and $J = \frac{1}{2}, \frac{3}{2}, \frac{5}{2}$ from the coupling of $L = 1$ and $S = \frac{3}{2}$. The Δ is a decuplet member, thus the Δ^* resonances are formed with the possible values of $J = \frac{1}{2}, \frac{3}{2}$ from the coupling of $L = 1$ and $S = \frac{1}{2}$.

   Therefore, the first excitation band contains five N^* resonances and two Δ^* resonances.

2. **Excitation band 2:** The 2^{nd} excitation band can be formed from three different excitation modes according to equation 1.20:

   - This band can have one quantum number of radial excitation and zero quantum number of angular excitation ($L = 0$ and $P = +1$). The spatial wave function is symmetric; hence, the combined wave function of flavors and spin should also be symmetric, which is the **56** multiplet. This multiplet contains one spin-$\frac{3}{2}$ decuplet and one spin-$\frac{1}{2}$ octet. Due to the coupling with $L = 0$, this excitation mode results in one N^* ($J = \frac{1}{2}$) and one Δ^* ($J = \frac{3}{2}$).
   - The band can also be formed when one of the oscillator carries two units of angular excitation ($L = 2$ and $P = +1$). The spatial wave function of this mode is symmetric,

hence it also requires to be coupled with **56** multiplet. The coupling with $L = 2$ result in two N^* ($J = \frac{3}{2}, \frac{5}{2}$) and four Δ^* ($J = \frac{1}{2}, \frac{3}{2}, \frac{5}{2}, \frac{7}{2}$).

- It is also possible that both the ρ and λ oscillators carry one quantum of angular excitation each. This gives $L = 0, 1, 2$. The spatial wave functions are mixed and antisymmetric. The resulting N^* and Δ^* resonances are listed in the first five rows of Table 1.1.

Table 1.1: N and Δ states in the N=0,1,2 harmonic oscillator bands. L^P denotes angular momentum and parity. A, S and M denote the symmetry of the spatial wave function. This chart was compiled in [9].

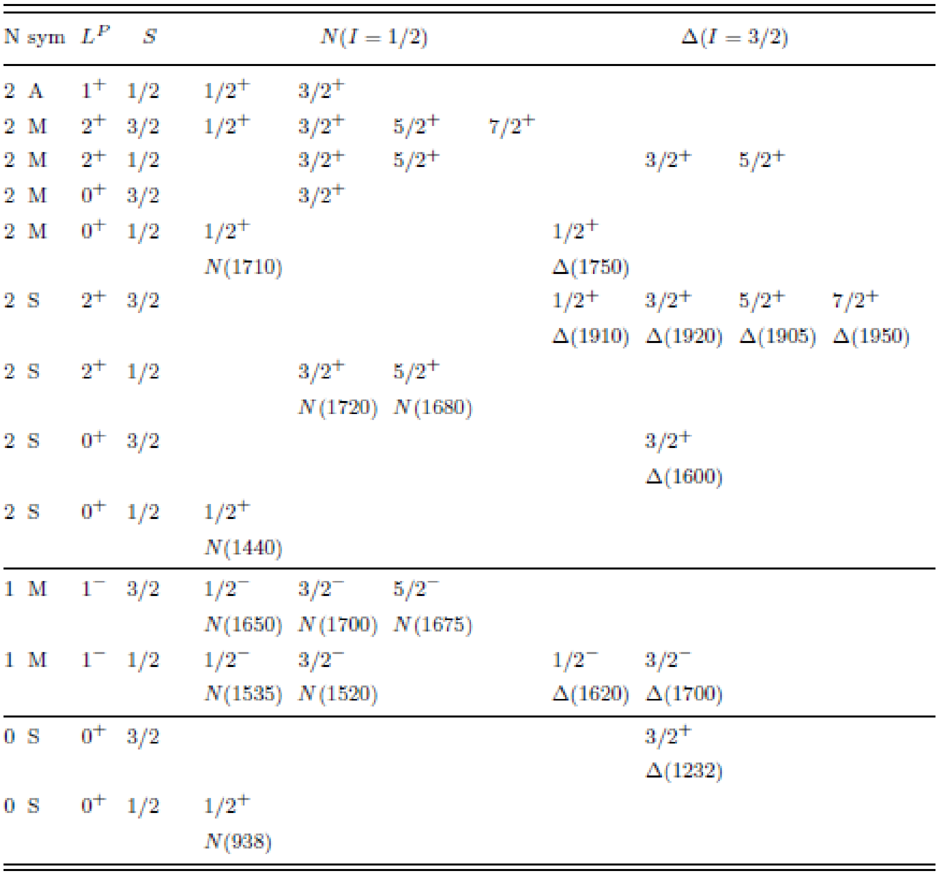

N	sym	L^P	S	$N(I = 1/2)$				$\Delta(I = 3/2)$			
2	A	1^+	1/2	$1/2^+$	$3/2^+$						
2	M	2^+	3/2	$1/2^+$	$3/2^+$	$5/2^+$	$7/2^+$				
2	M	2^+	1/2		$3/2^+$	$5/2^+$			$3/2^+$	$5/2^+$	
2	M	0^+	3/2		$3/2^+$						
2	M	0^+	1/2	$1/2^+$ $N(1710)$				$1/2^+$ $\Delta(1750)$			
2	S	2^+	3/2					$1/2^+$ $\Delta(1910)$	$3/2^+$ $\Delta(1920)$	$5/2^+$ $\Delta(1905)$	$7/2^+$ $\Delta(1950)$
2	S	2^+	1/2		$3/2^+$ $N(1720)$	$5/2^+$ $N(1680)$					
2	S	0^+	3/2						$3/2^+$ $\Delta(1600)$		
2	S	0^+	1/2	$1/2^+$ $N(1440)$							
1	M	1^-	3/2	$1/2^-$ $N(1650)$	$3/2^-$ $N(1700)$	$5/2^-$ $N(1675)$					
1	M	1^-	1/2	$1/2^-$ $N(1535)$	$3/2^-$ $N(1520)$			$1/2^-$ $\Delta(1620)$	$3/2^-$ $\Delta(1700)$		
0	S	0^+	3/2						$3/2^+$ $\Delta(1232)$		
0	S	0^+	1/2	$1/2^+$ $N(938)$							

Lattice QCD. In the Lattice QCD (LQCD) framework, the non-perturbative QCD is solved numerically on a discretized space-time ”lattice” with periodic boundary conditions. The quark fields are defined at the lattice site, and the gluon fields are introduced on the links as a 3×3 special unitary matrix to preserve gauge invariance. The Minkowski metric is converted to a 4-

dimensional Eucledian metric by Wick rotations, which allows analytic continuation of the time variable t to imaginary time it. The behavior of the continuum limit can be recovered by decreasing the lattice spacing. The finite spacing and box-size naturally introduce ultraviolet and infrared cut-offs, which regularizes the theory. Although these numerical calculations are very computationally expensive, with recent technological advances in computation, LQCD has seen tremendous progress in the prediction of the baryon spectrum, which is consistent with CQM in terms of the number of predicted states.

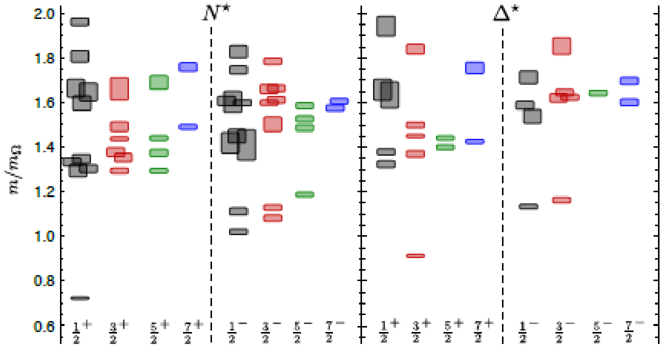

Figure 1.8: The spectrum of nucleons and deltas from the Lattice QCD calculation obtained with the latice spacing of 0.123 fm and the box-size of 2 fm [10].

1.2.3 Baryon Structure

The structure of the proton has been under investigation in hadronic physics since the early 20th century in order to understand the fundamental internal structure of matter. Thus, the study of hadron structures is complementary to spectroscopy study. We need to understand, for example, the internal structure of a nucleon as well as its excited states to obtain a coherent picture and a complete knowledge of a nucleon. In fact, the study of proton structures led to the discovery of quarks. If a proton were a point-like object, the cross section of the scattered relativistic electron off the proton could be calculated by Mott, and would be expected to follow

$$(\frac{d\sigma}{d\Omega})_{Mott} = \frac{\alpha^2}{4E^2 \sin^4 \frac{\theta}{2}} \cos^2(\frac{\theta}{2}), \tag{1.23}$$

where E and E' are the energies of the incident and scattered electron, θ is the scattering angle in the lab frame, and α is the fine structure constant. However, this calculation failed to agree with the experimental data at large scattering angles, as shown in Figure 1.9. As a result, Hofstadter introduced the idea that the proton was not a point-like particle but had an internal structure. In 1950, Rosenbluth then introduced the concept of an electric form factor, G_E and magnetic form factor G_M to describe the electric and magnetic distribution inside the proton.

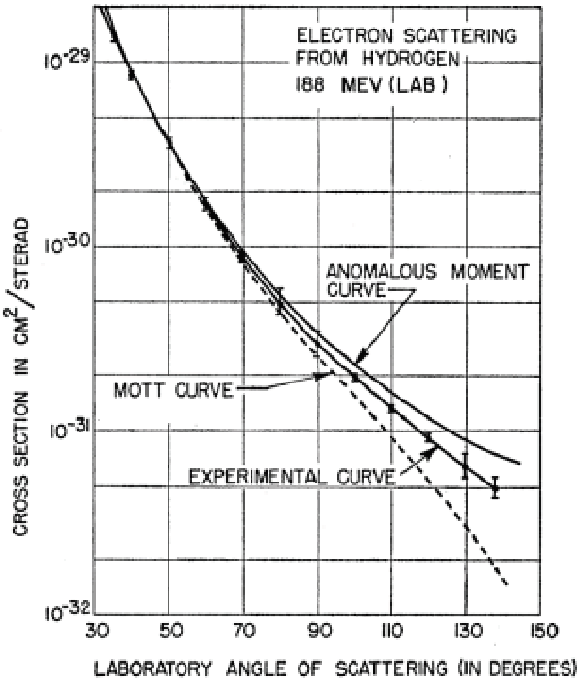

Figure 1.9: Elastic electron-proton scattering measurement at Stanford University [11]. The experimental results show deviations from the Mott calculation based on the proton as a point-like particle.

Because of the finite size of the proton, the cross section for electron-proton elastic scattering decreases rapidly with energy. Consequently, high-energy e^-p interactions are dominated by inelastic scattering processes where the proton breaks up,

$$e^-p \to e^-X. \tag{1.24}$$

As shown in Figure 1.10, the hadronic final states resulting from the break-up of the proton usually consist of many particles. Whereas $e^-p \to e^-p$ elastic scattering was described in terms of the electron scattering angle alone (see equation 1.23), two kinematic variables are needed to describe inelastic scattering. The form factors in elastic scattering were then replaced by two

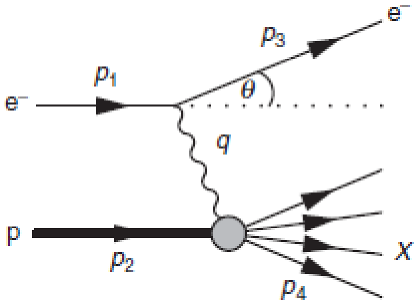

Figure 1.10: Inelastic electron-proton scattering where the proton break-up into multiple hadrons in the final states. Image source [1].

structure functions, which are a function of two kinematic variables, $F_1(x, Q^2)$ and $F_2(x, Q^2)$, where Q^2 is the negative of the four-momentum transfer and x, or the *Bjorken* variable, is defined as

$$x \equiv \frac{Q^2}{2p_2 q}. \tag{1.25}$$

It expresses the "elasticity" of the scattering process. x is always in the range of $0 < x < 1$ and the extreme case of $x = 1$ corresponds to elastic scattering. The first studies of structure functions in inelastic $e^- p$ scattering were obtained in a series of experiments at SLAC. The differential cross sections, measured over a range of incident electron energies, were used to determine the structure functions. The experimental data, shown in Figure 1.11 reveal two surprising phenomena. The first observation, known as *Bjorken* scaling, was that $F_1(x, Q^2)$ and $F_2(x, Q^2)$ are almost independent of Q^2. The lack of Q^2 dependence of the structure functions is strongly suggestive of scattering from point-like constituents within the proton. The second observation was that in the deep inelastic scattering regime, the structure functions $F_1(x)$ and $F_2(x)$ satisfy the $Callan - Gross$ relation

$$F_2(x) = 2xF_1(x). \tag{1.26}$$

This relation can be explained by assuming that the underlying process in $e^- p$ inelastic scattering is the *elastic* scattering of electrons from point-like spin-half constituent particles within the proton, namely quarks. Therefore, the study of proton structure using deep inelastic scattering experiments has led to the discovery of quarks.

One of the major goals in the recent study of nucleon structure is to understand the *Spin Crisis* phenomenon. Protons are classified as fermions, or half integer spin particles, with quarks

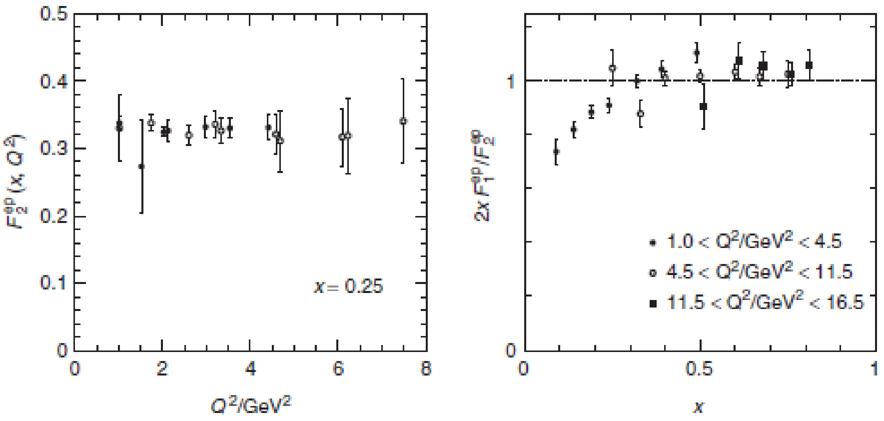

Figure 1.11: Structure function measurements from inelastic electron-proton scattering at SLAC [12] and [14]. The experiment results show Bjorken scaling (left) and the Callan-Gross relation (right). Image source [1].

also being fermions. This led to the assumption that the proton's spin of $\frac{1}{2}$ was the result of the addition of the spins from the two up quarks and the down quark. But the EMC experiment at CERN in 1987 concluded that the valence quarks only contribute about 30% to the total spin [15].

The total contribution to the nucleon spin can be written using spin sum rule

$$S_N = \frac{1}{2} = \frac{1}{2}\Delta\Sigma + \Delta G + L_g + \sum_q L_q, \tag{1.27}$$

where $\Delta\Sigma$ is the contribution from the quarks spin, ΔG is from the gluons spin, and L_g and L_q are from the gluons and quarks angular momentum, respectively. The contribution from the gluon spin has been measured in PHENIX, STAR, and COMPASS but, currently, is in agreement with zero. This result suggests that the orbital angular momentum of the quarks is the most likely candidate. In order to study the quark orbital angular momentum, it is necessary to understand and probe quarks inside the proton in three dimensions.

1.3 Experimental Status and Challenges in Baryon Spectroscopy

Baryon spectroscopy is a very difficult field to study. Unlike the atom, which can be excited using domestic electricity, exciting a nucleon requires a large particle accelerator and a complex detector system. Baryon resonances are also more unstable than atomic resonances, with their typical lifetime of the order of 10^{-24} s for strongly decaying resonances. According to the *Heisenberg*

Figure 1.12: An example of the hydrogen spectrum. The discrete peaks are visible and easily identified. Image source [54].

Uncertainty Principle, the energy of any unstable quantum state is spread over the range

$$\Delta E \approx \frac{\hbar}{\tau}, \tag{1.28}$$

where τ is the mean lifetime of the state. Therefore, the energy width turns out to be in the order of 100 MeV, which is larger than the average separation between resonances, causing the states to overlap. Thus, the baryon resonances are difficult to identify. Figures 1.12 and 1.13 show the contrast between an atomic and baryonic spectra.

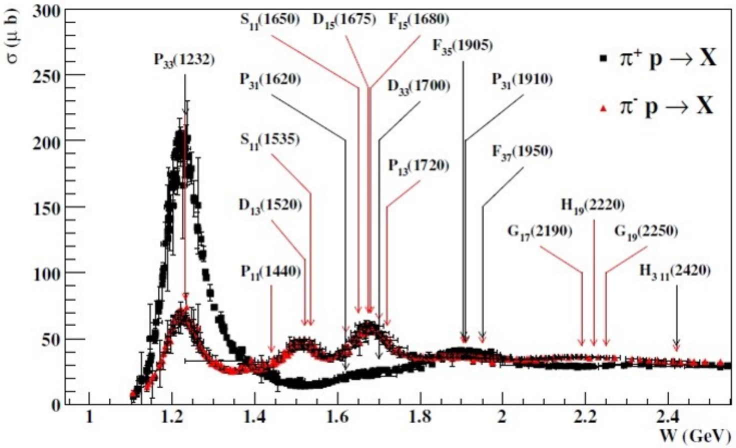

Figure 1.13: The cross sections of π^+ and π^- scattering off the proton and nucleon resonances that have obtained a 4-star rating from the PDG 2006 [16]. The resonances are labeled using notation $L_{2I2J}(M)$, where I is the isospin, J is the total spin, L is the orbital angular momentum of the $p\pi$ system, and M is the mass of the resonances. The picture shows that the resonances are highly overlap. Image source [54].

The severe overlap of the resonance states makes it impossible to simply go "peak-hunting" for their identification. However, the quantum numbers of each nucleon resonance determine the angular distribution of its decay products. Thus, by measuring these decay distributions, it is possible to identify nucleon resonance states. This technique to extract the nucleon resonances is known as Partial Wave Analysis (PWA) [6].

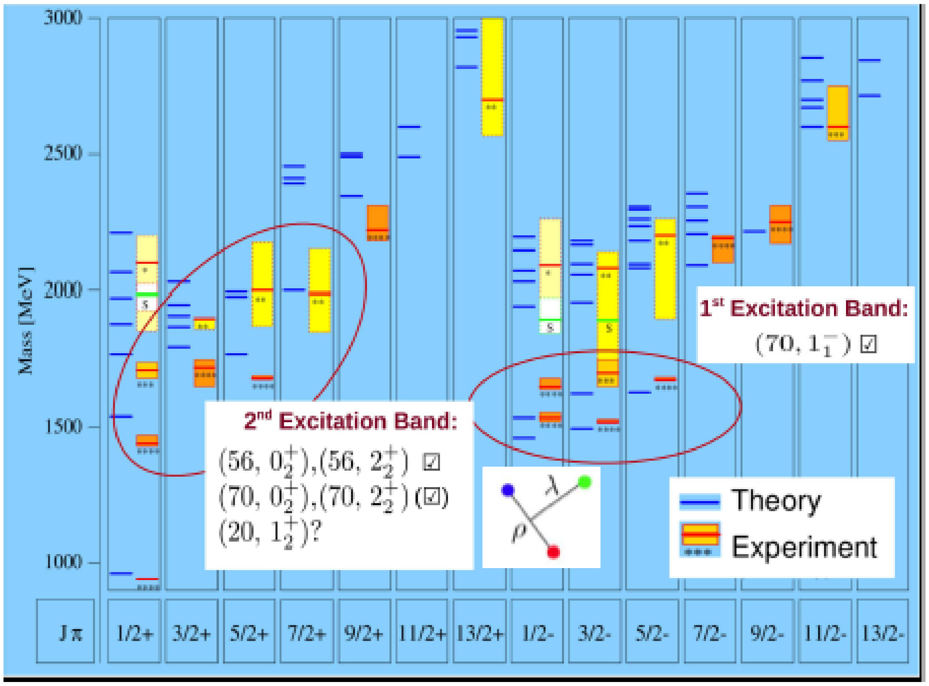

Figure 1.14: Predictions for the nucleon resonances spectrum from a constituent quark model and the experimentally observed states. The blue lines represent the predicted states from [4] and the red lines represent the experimentally observed states along with the star-rating as of PDG 2010 [17]. Many predicted states have not been experimentally observed. Image source [35].

Figure 1.14 shows the nucleon resonances expected from the CQM and the states that are observed experimentally. A glaring problem is that the number of states predicted is much higher than the number of excited states observed. This over-abundance of predicted states is called *the missing baryon resonances* problem. The missing states are most noticeably missing at higher energy, above 1.7 GeV, as shown in Figure 1.15.

The known excited states were observed up to 20 years ago mostly in the πN scattering experiment. This leads to the question: have we not seen the ”missing” states because they couple to the non-πN sector? A paper by Capstick and Roberts [5], indeed, predicted that some of the unseen resonances have strong couplings to non-πN chanels. These predictions have instigated an extensive worldwide program at several particle accelerator facilities to hunt for the missing states, including at the Thomas Jefferson National Laboratory (JLab).

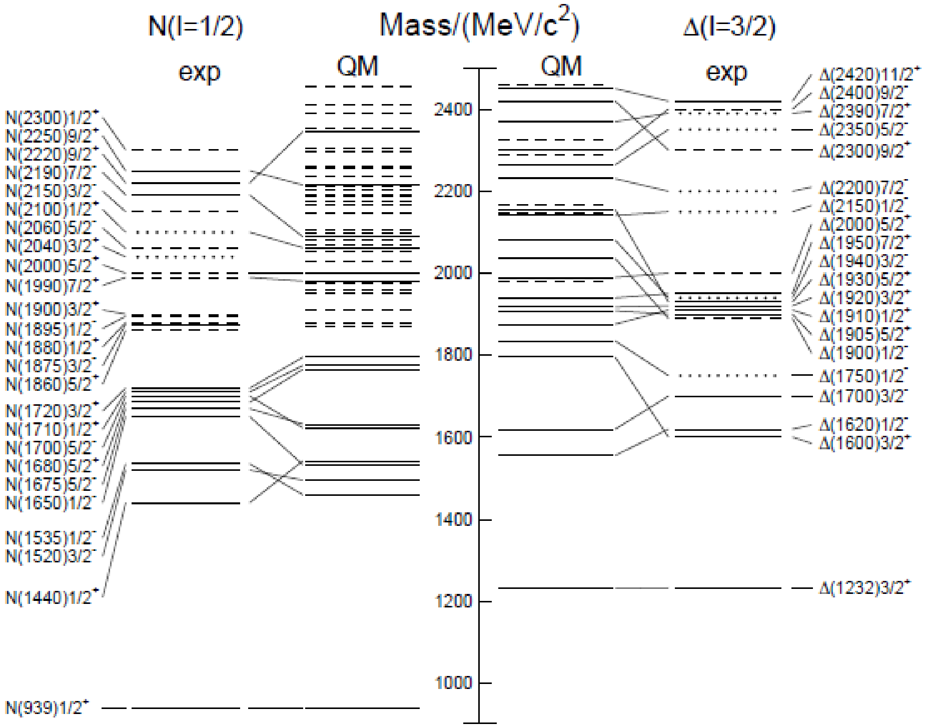

Figure 1.15: The predicted $N^\star$ states in a relativized quark model and the states identified in experiments along with the star-rating indicated by full lines (three- and four-star rating), dashed lines (two-star) and dotted lines (one-star) according to PDG 2016 [52]. Many predicted states at above 1.7 GeV/c^2 have not been experimentally observed.

Table 1.2 shows the known resonances observed in various decay channels. There are two features that can be concluded from this table:

1. Vector-meson photoproduction is under-explored; and
2. Kaon-Hyperon (KY) photoproduction channels are promising.

As spin-1 particles, vector mesons such as ω, ρ, ϕ are more difficult to analyze than pseudoscalar mesons due to the additional degrees of freedom from the spin projection. Vector mesons play an important role especially in photoproduction since they carry the same $J^{PC} = 1^{--}$ quantum numbers as the photon. According to Vector Meson Dominance (VMD) model [13], the photon is a superposition of the pure electromagnetic photon (which interacts only with electric charge) and the vector meson since they share the same quantum number.

Table 1.2: The status of nucleon resonances observed at various decay channels as of PDG 2016 [52].

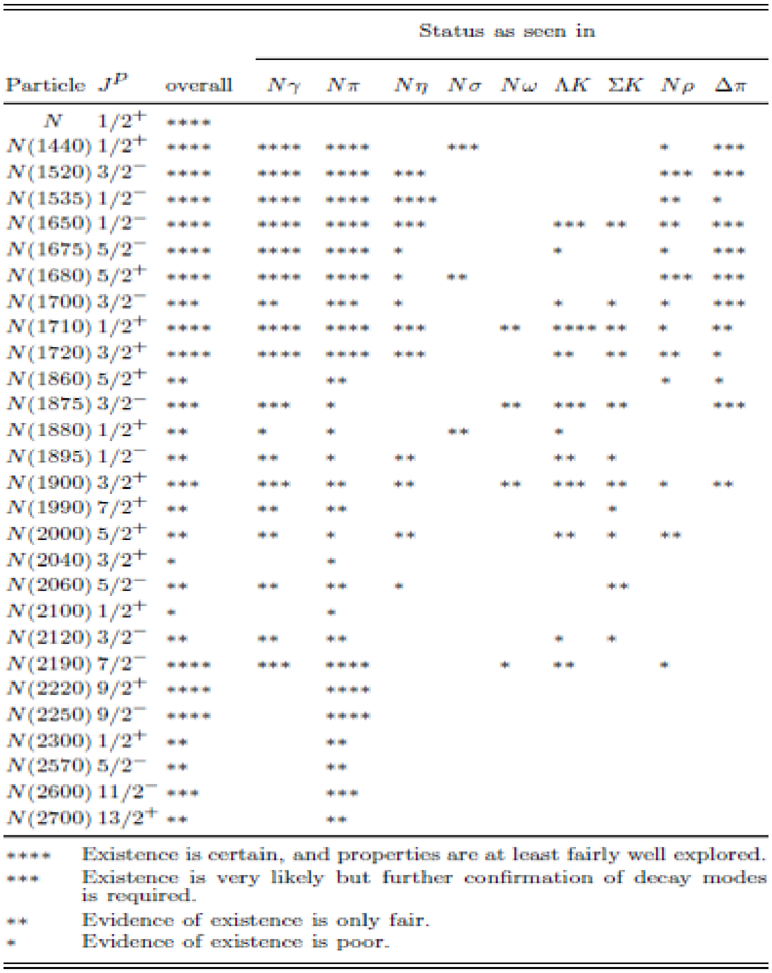

			Status as seen in								
Particle	J^P	overall	$N\gamma$	$N\pi$	$N\eta$	$N\sigma$	$N\omega$	ΛK	ΣK	$N\rho$	$\Delta\pi$
N	$1/2^+$	****									
$N(1440)$	$1/2^+$	****	****	****		***				*	***
$N(1520)$	$3/2^-$	****	****	****	***					***	***
$N(1535)$	$1/2^-$	****	****	****	****					**	*
$N(1650)$	$1/2^-$	****	****	****	***			***	**	**	***
$N(1675)$	$5/2^-$	****	****	****	*			*		*	***
$N(1680)$	$5/2^+$	****	****	****	*	**				***	***
$N(1700)$	$3/2^-$	***	**	***	*			*	*	*	***
$N(1710)$	$1/2^+$	****	****	****	***		**	****	**	*	**
$N(1720)$	$3/2^+$	****	****	****	***			**	**	**	*
$N(1860)$	$5/2^+$	**		**						*	*
$N(1875)$	$3/2^-$	***	***	*			**	***	**		***
$N(1880)$	$1/2^+$	**	*	*		**		*			
$N(1895)$	$1/2^-$	**	**	*	**			**	*		
$N(1900)$	$3/2^+$	***	***	**	**		**	***	**	*	**
$N(1990)$	$7/2^+$	**	**	**					*		
$N(2000)$	$5/2^+$	**	**	*	**			**	*	**	
$N(2040)$	$3/2^+$	*		*							
$N(2060)$	$5/2^-$	**	**	**	*				**		
$N(2100)$	$1/2^+$	*		*							
$N(2120)$	$3/2^-$	**	**	**				*	*		
$N(2190)$	$7/2^-$	****	***	****			*	**		*	
$N(2220)$	$9/2^+$	****		****							
$N(2250)$	$9/2^-$	****		****							
$N(2300)$	$1/2^+$	**		**							
$N(2570)$	$5/2^-$	**		**							
$N(2600)$	$11/2^-$	***		***							
$N(2700)$	$13/2^+$	**		**							

****	Existence is certain, and properties are at least fairly well explored.
***	Existence is very likely but further confirmation of decay modes is required.
**	Evidence of existence is only fair.
*	Evidence of existence is poor.

The hyperon is a baryon that contains at least one s quark. The Bonn-Gatchina PWA group has discovered a set of eight resonances from these channels. Since these channels are promising, the KY and vector meson photoproduction channels are the main topic of this dissertation and will be described in detail in the following section.

1.4 Vector Meson Photoproduction

1.4.1 Physical Observables in Vector Meson Photoproduction

A complete description of vector meson photoproduction requires 24 complex helicity amplitudes. Two helicities are for the beam, two for the target, three for the vector meson and two for the recoil proton, amounting to a total of $2 \times 2 \times 3 \times 2 = 24$ scattering amplitudes. However, parity invariance reduces the number of independent amplitudes to 12. This implies that we need to perform many different experiments to fully determine the 23 independent real numbers needed to completely describe the reaction $\gamma p \to pV$ (the overall phase is irrelevant). These scattering amplitudes are embedded in the cross section and the polarization observables.

For the reaction $\gamma p \to pV$, when only the beam and target polarization are measured, the differential cross section reduces to the form [18]:

$$\begin{aligned}\frac{d\sigma}{dx_i} =\sigma_0\Big(&1 - \delta_l \mathbf{\Sigma} \cos 2\beta + \Lambda_x(-\delta_l \mathbf{H} \sin 2\beta + \delta_\odot \mathbf{F}) - \Lambda_y(-\mathbf{T} + \delta_l \mathbf{P} \cos 2\beta) \\ &- \Lambda_z(-\delta_l \mathbf{G} \sin 2\beta + \delta_\odot \mathbf{E})\Big),\end{aligned} \tag{1.29}$$

where x_i are the kinematic variables and $\delta_l(\delta_\odot)$ denote the degree of linear (circular) polarization of the beam. Λ_x, Λ_y and Λ_z are the components of the target polarizations with respect to the reaction plane (which will be described in section 4.1.1). The angle β denotes the angle between the direction of the linearly-polarized photon beam and the reaction plane. σ_0 is the cross section, which is associated with the likelihood of scattering when both the target and beam are unpolarized. $(\Sigma, \mathbf{T})$, and $(\mathbf{H}, \mathbf{F}, \mathbf{P}, \mathbf{G}, \mathbf{E})$ are the single and double polarization observables.

There are also polarization observables associated with the decay distribution of the vector meson called the Spin Density Matrix Elements (SDMEs). A density matrix is a matrix that describes a quantum system in a mixed state, a statistical ensemble of several quantum states. If the density matrix for a particle is known, then all quantum mechanical observables can be calculated. The SDMEs of a vector meson then refer to the density of the vector meson's spin projections. For a particle with n states, in a given basis, each having wave function $|\psi\rangle$, the density matrix is

$$\rho = \sum_{ij}^{n} a_{ij} \left|\psi_j\right\rangle \left\langle\psi_i\right| . \tag{1.30}$$

Diagonal elements of the matrix, a_{ii}, represent the probability that the particle is in state ψ_i. Thus, the decay angular distribution of the vector meson in its rest frame can be constructed using the density matrix as

$$\frac{\mathrm{d}N}{\mathrm{d}\cos\theta \mathrm{d}\phi} = M\rho(V)M^\dagger, \tag{1.31}$$

where M is the decay amplitude and $\rho(V)$ is the spin density matrix of the vector meson. The exact form of the SDME were derived by K. Schilling *et al.* [68] and will be described in detail in section 4.3.

1.4.2 Photoproduction of ω Mesons

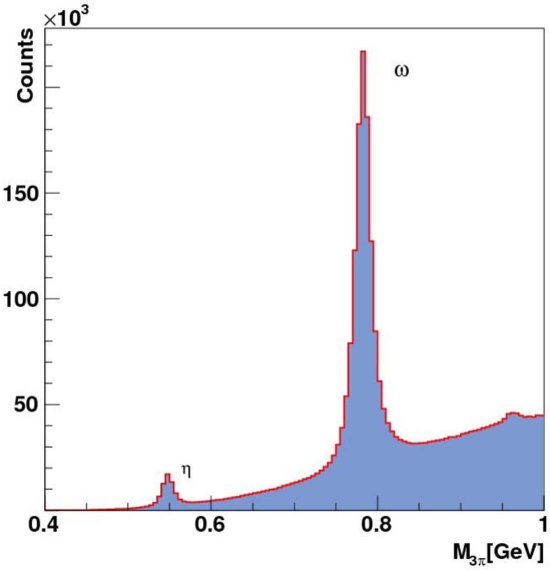

Figure 1.16: The invariant mass of $M_{3\pi}$ shows clear omega signals over a smooth background.

The ω meson is our vector meson of interest and the primary focus of this dissertation. The ω has an observed mass of 782.59±0.11 MeV/c^2, is a neutral particle and has isospin I=0, which means that $p\omega$ can only couple to states with $I = \frac{1}{2}$, i.e. N^* states. Thus, it serves as an isospin filter. The ω has a width of ± 8.49 MeV, which is relatively narrow compared to ρ meson ($\Gamma \approx$ 125 MeV) and which enables a clean detection above background.

Another advantage of studying this reaction is that ω photoproduction has a threshold energy that lies in the higher lying third resonance region where many resonances are notably missing. This reaction also has a large cross section and provides a lot of statistics.

The ω photoproduction has been experimentally studied for more than 40 years. In the 1970s and early 1980s, ω photoproduction experiments were performed at SLAC [20] and Daresbury [21]. The unpolarized differential cross sections and SDMEs were measured at $W \in$ [2.47, 2.9] GeV. Recent advances in accelerator and detector technologies have inspired more measurements all over the world and have greatly improved the quality of the world database of this reaction. Table 1.3 summaries the previous measurements of ω photoproduction in different experiments.

Table 1.3: Previous measurements of various observables of ω photoproduction from different experiments.

Year	Experiment	Observables	Energy Range	References
1970s	SLAC and Daresbury	$\frac{d\sigma}{d\cos\theta^{\omega}_{c.m.}}$, and ρ^0	$2.48 < E_\gamma < 2.96$ GeV	[20], [21]
2003	CLAS	$\frac{d\sigma}{d\cos\theta^{\omega}_{c.m.}}$	$2.624 < \sqrt{s} < 2.87$ GeV	[22]
2003	SAPHIR	$\frac{d\sigma}{d\cos\theta^{\omega}_{c.m.}}$, and ρ^0	$1.72 < \sqrt{s} < 2.4$ GeV	[23]
2008	CBELSA/TAPS	Σ	$1.1 < E_\gamma < 1.7$ GeV	[24]
2009	CLAS	$\frac{d\sigma}{d\cos\theta^{\omega}_{c.m.}}$, and ρ^0	$1.7 < \sqrt{s} < 2.8$ GeV	[25]
2015	A2	$\frac{d\sigma}{d\cos\theta^{\omega}_{c.m.}}$	$1.1 < E_\gamma < 1.4$ GeV	[26]
2015	CBELSA/TAPS	E and G	$1.16 < E_\gamma < 2.24$ GeV	[27]
2015	CBELSA/TAPS	$\frac{d\sigma}{d\cos\theta^{\omega}_{c.m.}}$, ρ^0, ρ^1, and ρ^2	$1.15 < E_\gamma < 2.5$ GeV	[28]

Several attempts to extract the underlying resonant contributions as well as the production mechanism from the published data have been made by various group. The ω meson can be photoproduced via an s-channel resonant process, where a proton is excited and forms a short life N^* state before it decays to $p\omega$. Others production mechanisms are non-resonant processes. An example of this process is the t-channel meson and the Pomeron exchange.

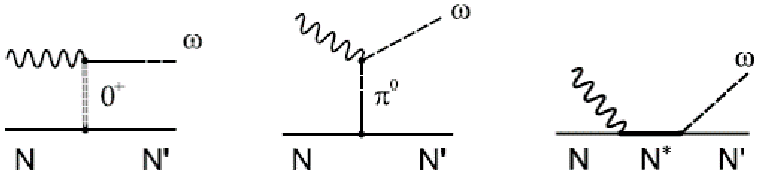

Figure 1.17: Feynman diagrams for (left) t-channel pomeron exchange, (middle) t-channel π^0 exchange and (right) s-channel, which is a resonant process. Image source [24]

All of the authors agree that at very high energies, $E_\gamma > 20$ GeV, ω photoproduction can be successfully described as a t-channel diffractive process [33]: the photon converts to a vector meson, which then scatters off the nucleon by the exchange of pomerons; these colorless objects carry no charge and share the $J^{PC} = 0^{++}$ quantum numbers of the vacuum. At medium energies $4 < E_\gamma < 20$ GeV, additional contributions from the t-channel exchange of Regge families is needed, and pion exchange is generally expected to dominate especially in the forward region. Close to the reaction threshold in the baryon resonance regiome, N^* states strongly contribute to ω photoproduction. The Bonn-Gatchina (BnGa) coupled channels partial-wave analysis determined the contributions of twelve N^* resonances, along with their $N^* \to p\omega$ branching ratios using data from the CBELSA/TAPS experiment. The dominant contribution near the threshold was found to be the $N(1720)3/2^+$ resonance. M. Williams *et al.* [29] published the results of a partial-wave analysis that described the high quality and statistics of differential cross section and unpolarized SDMEs from CLAS. They found strong contributions from $N(1680)3/2^+$ and $N(1700)3/2^-$ near the threshold, a higher mass resonance $N(2190)7/2^-$, and suggestive evidence for $N(2000)5/2^+$.

The scattering amplitudes from both the resonant and non-resonant processes are entangled with each other. Therefore, to disentangle the resonant contribution we need the phase information from the scattering amplitudes as well as their magnitudes. The unpolarized cross section alone is not enough to extract the resonant contributions without ambiguity since it only gives information on the magnitude of the amplitudes. Additional polarization observables are required since they provide information on the phase of the scattering amplitudes. Figure 1.18 shows an example of the importance of a polarization observable. Polarization observables are sensitive to the presence of a resonance. It shows the polarization observables C_x and C_z for the reaction $\gamma p \to K\Lambda$ along with the partial wave analysis solutions with and without the $N(1900)P_{13}$ resonance. The presence of the $N(1900)P_{13}$ state highly improves the fit solutions.

Unfortunately, the published data on the $\gamma p \to p\omega$ polarization observables in general lack statistics. For instance, the first measurement of the polarization observable **E** for ω photoproduction reaction, as shown in Figure 1.19, exhibits large statistical uncertainties [27]. Therefore, extracting the **E** observable for ω photoproduction using high quality data and better statistics is one of the main goals of this analysis.

Understanding both resonant and non-resonant production mechanisms is equally important to disentangle N^* resonances contributions. The high statistics data in the energy range beyond the resonances production regime ($E_\gamma > 4$ GeV) are required to study non-resonant production mechanisms. Thus, providing high-quality statistical data on the $\gamma p \to p\omega$ differential cross section and unpolarized SDMEs are also among the goals of this analysis.

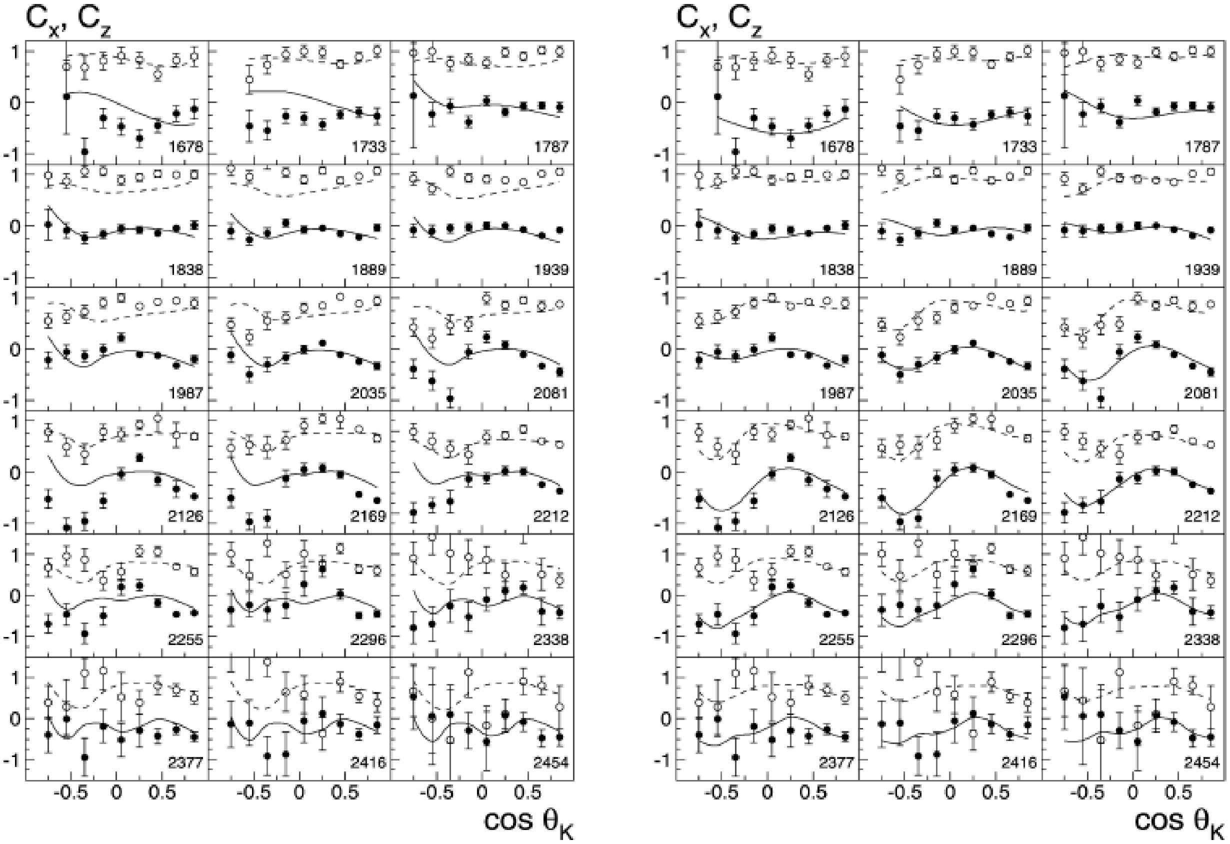

Figure 1.18: Double polarization observables C_x (black circle) and C_z (open circle) for $\gamma p \to K\Lambda$. The C_x (solid lines) and C_z (dashed lines) are the partial wave analysis results obtained (Left) without the $N(1900)P_{13}$ state and (Right) with the $N(1900)P_{13}$ included in the fit [19]. Notice that the solutions with the $N(1900)P_{13}$ are highly improved.

1.5 Σ Hyperon Photoproduction

Photoproduction of nucleon resonances in their decay to strange particles also offers attractive possibilities. The strange quark in the particle generates another degree of freedom and gives additional information not available from nucleon-nucleon scattering. For instance, due to the conservation of the strangeness, the photoproduction of kaons (strangeness = 1) is always accompanied by the creation of hyperons (strangeness = -1). The channels involved in the production of K mesons also give the opportunity to assess the validity of the SU(3) symmetry of the quark model in describing the decay of the resonances. Some of the missing resonances are predicted to couple strongly to $K\Sigma$ and $K\Lambda$, which give another advantage for studying hyperon photoproduction chan-

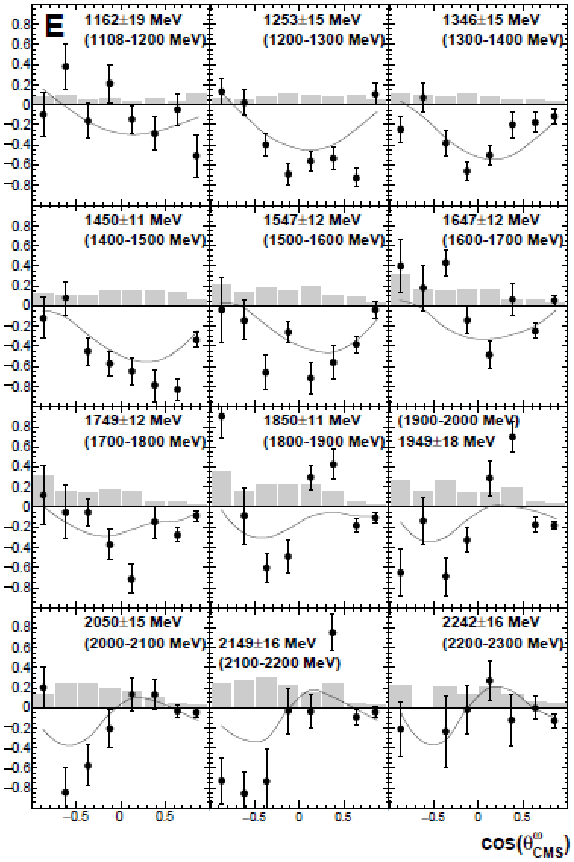

Figure 1.19: The first measurements of the double polarization observable **E** for the reaction $\gamma p \to p\omega$ from CBELSA/TAPS collaboration [27].

nels. Our hyperon channel of interest is Σ^+, which is photoproduced off the proton accompanied by the production of K^0.

1.5.1 Photoproduction of $K^0\Sigma^+$

By considering the spin states of the particles involved, the $\gamma p \to K^0\Sigma^+$ reaction is fully described by $2 \times 2 \times 2 = 8$ complex amplitudes. Parity invariance reduces this number to 4 independent amplitudes. The pseudoscalar nature of K^0 simplifies the study of this reaction. The complete characterization of these amplitudes depends upon the measurement of a limited number of observables, listed in table 1.4.

Previously available cross section data for the photoproduction of $K^0\Sigma^+$ were published by the ABBHHM collaboration in 1969 [30] and the SAPHIR collaboration in 2005 [31]. The CBELSA/TAPS

Table 1.4: The spin observables for the photoproduction of a single kaon. This table was compiled in [38]

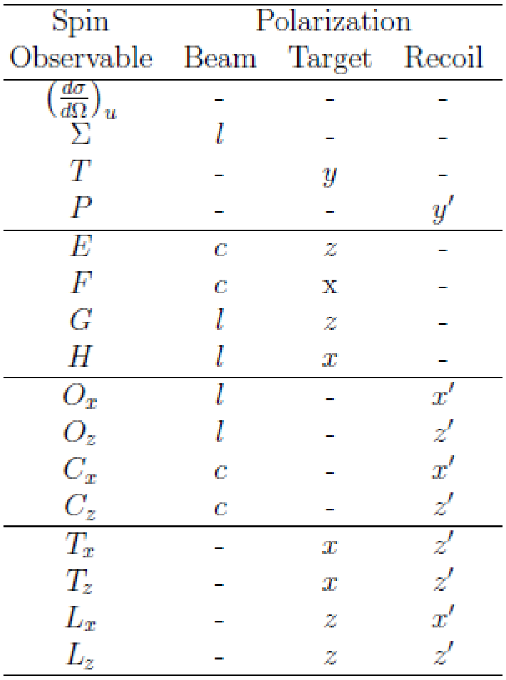

Spin	Polarization		
Observable	Beam	Target	Recoil
$\left(\frac{d\sigma}{d\Omega}\right)_u$	-	-	-
Σ	l	-	-
T	-	y	-
P	-	-	y'
E	c	z	-
F	c	x	-
G	l	z	-
H	l	x	-
O_x	l	-	x'
O_z	l	-	z'
C_x	c	-	x'
C_z	c	-	z'
T_x	-	x	z'
T_z	-	x	z'
L_x	-	z	x'
L_z	-	z	z'

collaboration [72], [73] and [74] then published the polarization observables and the unpolarized cross sections in 2008, 2012 and 2014. Recent data on the polarization observable of $K^0\Sigma^+$ were published by the CLAS collaboration [75] in 2013. All of the previous measurements are summarized in table 1.5.

Table 1.5: Previous measurements of various observables of $K^0\Sigma$ photoproduction from different experiments.

Year	Experiment	Observables	Energy Range	References
1969	ABBHHM	σ	$1.05 < E_\gamma < 5.9$ GeV	[30]
2005	SAPHIR	σ	$1.05 < E_\gamma < 2.6$ GeV	[31]
2008	CBELSA/TAPS	$\frac{d\sigma}{d\Omega}$, and P	$1.05 < E_\gamma < 2.25$ GeV	[72]
2012	CBELSA/TAPS	$\frac{d\sigma}{d\Omega}$	$1.05 < E_\gamma < 2.25$ GeV	[73]
2013	CLAS	P	$1.17 < E_\gamma < 3.5$ GeV	[75]
2014	CBELSA/TAPS	Σ, and P	$1.05 < E_\gamma < 2.25$ GeV	[74]

The available data of the $K^0\Sigma^+$ channel are of lower quality compared with other strange decay channels such as $K^+\Sigma^-$ and $K^+\Lambda$. Both data on $\gamma p \rightarrow K^0\Sigma^+$ and $\gamma p \rightarrow K^+\Sigma^0$ are strongly required to disentangle contributions from the the N^* and Δ^* resonances since these reactions are isospin-related channels. The strong coupling strength is linked via $SU(2)$ Clebsch-Gordan coefficients

$$g_{K^0\Sigma^+p} = \sqrt{2}\, g_{K^+\Sigma^0p}. \tag{1.32}$$

The lack of $K^0\Sigma^+$ photoproduction data is another prime motivation for this analysis. We will present measurements of differential cross sections and the recoil hyperon polarization for the reaction $\gamma p \rightarrow K^0\Sigma^+$. The data of this channel, as well as the $\gamma p \rightarrow p\omega$ channel, were collected at Jefferson Laboratory, using the CLAS detector.

CHAPTER 2

JEFFERSON LABORATORY, CEBAF AND THE CLAS DETECTOR

The data used in this analysis were taken as part of the $g9a$ and $g12$ run periods at the Thomas Jefferson National Accelerator Facility (TJNAF), also referred to as Jefferson Laboratory or JLab, in Newport News, Virginia. In "$g9a$" and "$g12$", the "g" refers to a photoproduction experiment, the "9a" implies that this was the first iteration of the ninth approved experiment, and the "12" indicate that this was the twelfth approved experiment.

The $g9a$ experiment, a subset of the Frozen Spin Target (FROST) experiment, utilized a linearly- or circulary-polarized photon beam in combination with a longitudinally-polarized target. The data for the $g9a$ experiment (FROST-g9a) were taken between November 2007 and February 2008. In this analysis, the data with a circularly-polarized photon beam were used.

The $g12$ experiment was a high-luminosity and high-energy photon run. The data were collected in 44 days of beam time from April to June 2008. The experiment was dedicated to several analyses ideas with the main goal to search for meson resonances in multi-particle final states by performing partial wave analysis.

There are currently four experimental halls at JLab, denoted as A, B, C and D, along with the CEBAF electron accelerator, a free-electron laser and a number of other research facilities. Both the $g9a$ and $g12$ run periods were conducted in Hall B. The detector used for the experiments was the CEBAF Large Acceptance Spectrometer (CLAS). CLAS was a nearly-4π spectrometer and optimized for the detection of multi-particle charged final states.

The accelerator has been recently upgraded to deliver continuous electron beams with energies up to 12 GeV and the CLAS spectrometer has been removed and replaced with the new CLAS12 detector. However, at the time of the FROST and $g12$ experiments, the accelerator was designed to deliver beam energies only up to 6 GeV. Therefore, we will describe the facility in the following section as it was when the experiments were conducted at CLAS using the 6 GeV electron accelerator.

Figure 2.1: An aerial view of Jefferson Lab. Hall B is seen at the bottom of the figure, in the middle of the three mounds. Image source [41].

2.1 CEBAF

The Continuous Electron Beam Accelerator Facility (CEBAF) at Jefferson Laboratory is an electron accelerator based on Superconducting-Radio-Frequency (SRF) technology dedicated to probing the atomic nucleus and to exploring QCD in the confinement regime. CEBAF has a racetrack geometry with a circumference of about 7/8 of a mile. Superconducting cavities are non-resistive, allowing CEBAF to obtain a 100% duty factor since the cooling time between beam spills is not required. CEBAF is capable of providing electron beams simultaneously to four different experimental halls.

The electrons were produced in the injector by illuminating a GaAs photocathode with pulsed lasers at a frequency of 499 MHz, so that each hall received electron bunches every 2 ns. After extraction from the photocathode, the beam was accelerated to 5 MeV by the first two of the SRF cavities. Finally, there are two accelerating modules, each containing 8 SRF cavities, that boost the energy of the electrons to a final energy, typically 23 to 68 MeV. An optical chopper was used to cleanly separate the two-ns bunches prior to sending the beam to CEBAF's recirculating linear accelerators (LINACs).

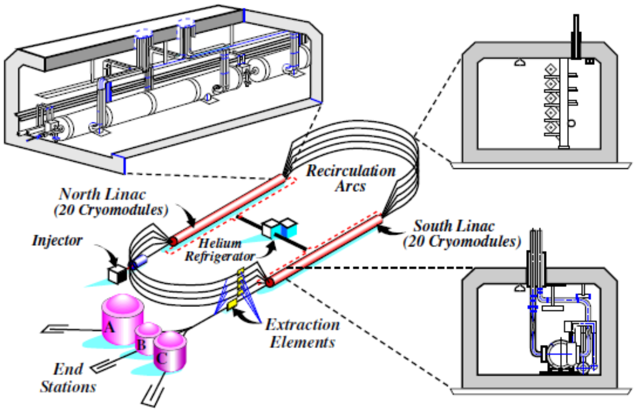

Figure 2.2: A schematic view of CEBAF and its major components, clockwise from the top, a module in the LINAC, a steering magnet, and a part of the RF separator. Image source [41].

The two LINACs were used to accelerate the electrons by 600 MeV per pass. The recirculation arcs on either end of the linacs allowed the electrons to make up to five passes through the LINACs, achieving the maximum energy of 6 GeV. The acceleration gradient for the electron beam was provided by inducing a standing radio-frequency electromagnetic wave inside the niobium cavities. The RF standing waves were kept in phase with the electron bunches, resulting in a continuous positive electric force on each bunch as it passed through the cavities. To maintain the superconductivity, each cavity was maintained in a 2K heat bath by immersing it in liquid helium. Each linac consisted of 21 cryomodules, where each module was comprised of 8 Niobium RF cavities. Thus, there were 168 cavities per LINAC.

After passing through one LINAC, the electron beam is bent in the recirculation arcs throughs a series of dipole magnets and directed to the other LINAC, which further accelerate the electrons. The beam was divided into five sub-beams by energy such that electrons of different energies can pass through a different recirculation arc before re-entering the LINACs. Once a beam of electrons

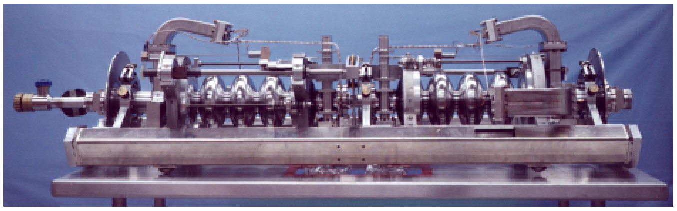

Figure 2.3: A pair of superconducting RF cavities with its support hardware and beam-pipe before transferred to the LINAC. Image source [41].

has passed the LINACs the desired number of times, it is directed to the designated hall using an RF separator. The electron beam current in the $g12$ experiment was set up to 65 nA while the FROST experiment was maintained at lower currents, within the range 5 - 14 nA, mainly to sustain the target polarization.

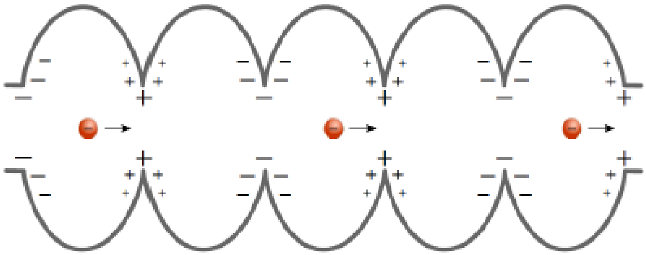

Figure 2.4: A diagram of an RF cavity with the charge gradient produced. As the electrons travel from one cell to the next cell, the RF-phase induces the appropriate charge distribution to maintain positive acceleration on the electron. Image source [41].

2.2 The Photon Tagger

As the electron beam entered Hall B through the RF separator, the conversion of an electron into a photon was handled by the Hall B tagging system, which is shown schematically in Figure 2.5. The electron beam produced a photon beam by means of bremsstrahlung radiation. When the electron beam interacted with a radiator, the electromagnetic field of the radiator's nuclei slowed the electrons down, which led to the emission of photons to conserve the total energy and momentum of the system. The choice of the radiator's material depended on the desired photon polarization, but typical radiators have high atomic numbers to reduce photon contamination from electron-electron scattering. The $g9a$ and $g12$ experiments used a gold (Au) foil of 10^{-4} radiation length.

After passing through the radiator, the beam was a mixture of recoil electrons, photons and non-interacting electrons.

The tagger magnetic spectrometer allowed for bending the non-interacting electrons away from the beam line into a beam dump. The tagger magnetic spectrometer was a dipole producing a maximum magnetic field of 1.75 T, which was the field value required to transport the full-energy (non-interacting) electrons. Since the energy transferred to the nucleus was negligible, the bremsstrahlung reaction obeys the energy conservation relation:

$$E_\gamma = E_0 - E_e, \tag{2.1}$$

where E_0 is the incident energy of the electron, E_e is the energy of the recoil electron and E_γ is the energy of the emitted bremsstrahlung photon. Since E_0 can be measured from the accelerator, a measurement of the recoil electron energy in the tagger spectrometer provides a determination of the photon's energy and time.

The tagger spectrometer consisted of two hodoscope planes, each made of overlapping arrays of scintillators. The first scintillator plane, referred to as the E-counter, was used to determine the momentum of the recoiling electrons since the radius of the electron's curvature due to a magnetic field is proportional to the electron's momentum. Thus, by knowing the exact position on a plane, the momentum and energy of the electron can be determined. The E-counter was made of 384 plastic scintillators that are 20-cm long and 4-mm thick, with widths varying from 6 to 18 mm. The paddles were arranged in an overlapping fashion, creating 769 separate channels to determine the electron's position and, hence, its momentum and energy. The energy resolution of the E-counter was 0.1 % of the incident electron energy.

The second plane of scintillators, referred to as the T-counter, were used to make accurate timing measurements of the recoiling electrons, and hence the associated photon time. The T-counter was positioned in parallel and 20 cm behind the E-counter. This counter was comprised of 61 scintillators, 2-cm thick, which varied in length from 9 cm to 20 cm, resulting in 121 channels, allowing for a timing resolution of 110 ps. The spectrometer was able to tag photons ranging from 20 - 95 % of the incident electron beam energy. To trim the beam halo, the photon beam also passed through a pair of collimators before it reached the CLAS detector.

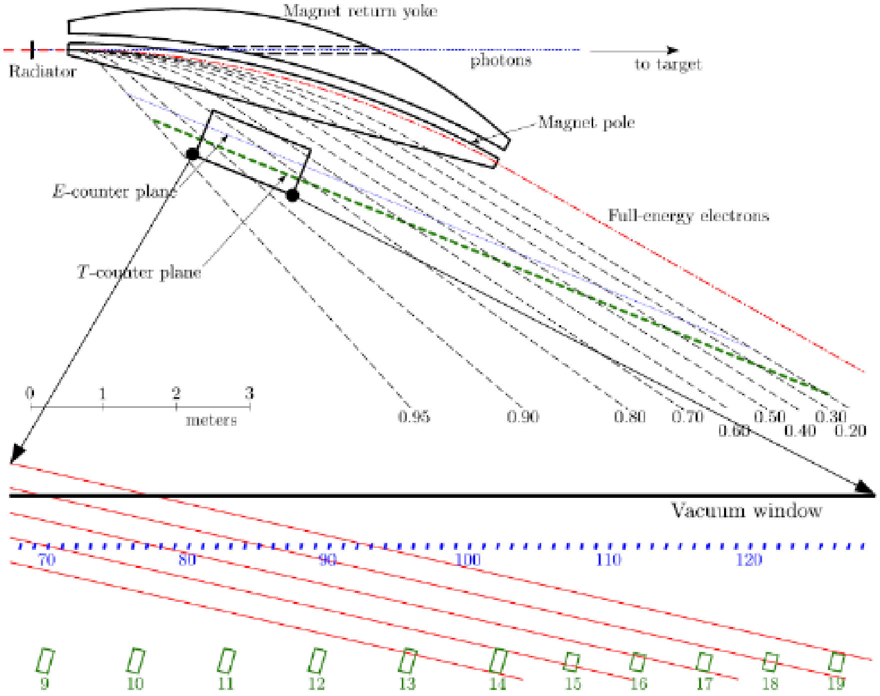

Figure 2.5: Schematic diagram of the tagger spectrometer. The blue dot-dashed lines are the E-counters and the green dashed lines are the T-counters. The dashed red lines are the electrons that have not lost any energy. The dashed red lines are the scattered electrons that radiated a bremsstrahlung photon and carry the fractional energy of the non-scattered electron. Image source [39]. Image was adapted from [42].

2.3 The Frozen Spin Target and the $g12$ Cryotarget

2.3.1 The Frozen Spin Target (FROST)

A polarized target is needed to align the spin of the target nuclei in a particular direction by some external means. The $g9a$ experiment used a frozen spin butanol ($C_4H_{10}OH$) target with longitudinally polarized protons. This Frozen Spin Target (FROST) also could be transversely polarized (for the $g9b$ experiment) and had a nearly-4π angular coverage for the scattering angle. This angular coverage was achieved since only a small holding magnetic field was required to maintain the polarization for a long period. The FROST target also could reach degrees of polarization over 80 %.

A technique called Dynamic Nuclear Polarization (DNP) was used to polarize the protons within the FROST material. The polarization of the target in the $g9a$ experiment began with the free electrons being polarized according to the Boltzman distribution:

$$P = \tanh\left(\frac{\vec{\mu}\cdot\vec{B}}{kT}\right). \tag{2.2}$$

Therefore, a high magnetic field and low temperatures were required to achieve a high degree of polarization. This process was performed at temperature of approximately 0.3 mK using a 5 T polarizing magnet. Then the spin polarization of the electrons was transfered to the nuclei using microwaves.

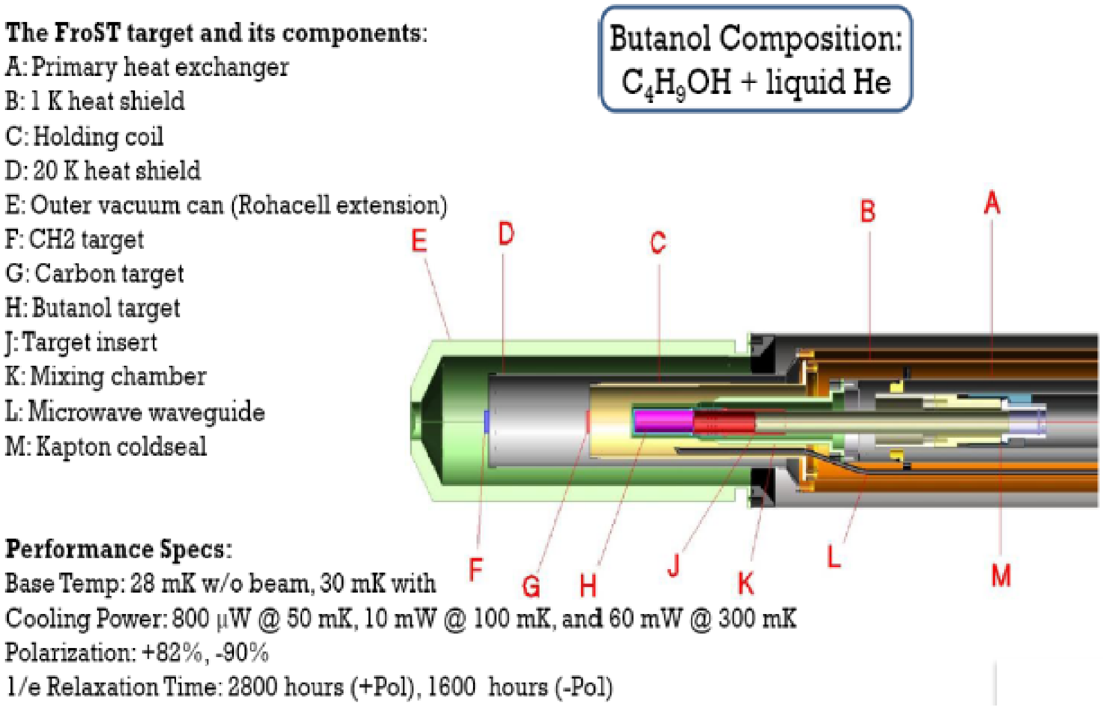

Figure 2.6: A cross section of the target area of FROST and its main components. Image source [38].

The DNP phenomenon was theoretically predicted by Albert Overhauser in 1953. It was first realized using the concept of *the Overhauser effect*, which is the perturbation of nuclear spin level population when electron spin transitions are saturated by the microwave irradiation. Thus, DNP consist of transferring high-spin polarization from the electrons of paramegnetic impurities to the host nuclei by means of microwave irradiation close to the Electron Paramegnetic Resonance (EPR) frequency.

Figure 2.7: The FROST magnets clockwise from the top: the longitudinal holding magnet, the transverse holding magnet, and the polarizing magnet. Image source [43].

Once the polarization was complete, the microwave generator was switched off. In order for the spin polarization of the butanol target to be frozen, the target needed to be cooled below 50 mK. The FROST used a ^{3}He/^{4}He dilution refrigerator to reach this temperature. After the target was in the "Frozen Spin Mode", a relatively small holding magnet of 0.5 T and these extremely low temperatures were applied to sustain the target polarization. The holding magnet produced a magnetic field, either parallel or anti-parallel to the beamline. Since the beam had a heating effect on the target and raised the temperature of the target, the target polarization decreased exponentially the target and was required to be regularly re-polarized every 4 to 5 days after the polarization decayed to about 50 % of its initial value.

The $g9a$ experiment utilized butanol (C_4H_9OH) as the main target materials. The protons in the hydrogen atoms were polarized, but the protons bound within the nuclei of carbon and oxygen atoms were not polarized. Thus, events from these bound nucleons were considered background events. A graphite (carbon) target, and a polyethylene (CH_2) were also placed downstream of the butanol target to determine the contribution from bound nucleons and for various systematics checks.

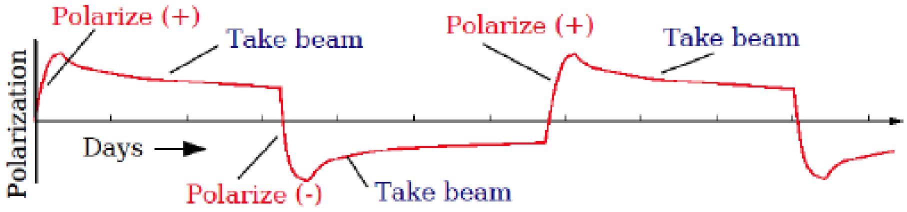

Figure 2.8: The polarization schedule for the FROST. Image source [43].

2.3.2 The $g12$ Cryotarget

CLAS was designed such that the ”Target Cell” could be moved, removed and replaced according to an experimental advantage. Target cells with various shapes and sizes have been employed by experiments using the CLAS detector. The $g12$ experiment used a cylindrical cell made of kapton. The cell was 40-cm long with a radius of 2 cm. The target material used for the $g12$ experiment was liquid Hydrogen (LH_2). The $g12$ physics motivation required the experiment to increase the forward angular coverage of the detector. For this reason, the $g12$ target cell was moved upstream of the CLAS center to increase the forward geometric acceptance of the detector. The pressure and temperature of the target was measured hourly to calculate the density of the liquid Hydrogen. This density is an important quantity to measure the cross sections.

Figure 2.9: Target cell used during the $g12$ run period, placed 90 cm upstream of the CLAS center, and filled with liquid hydrogen. Image source [44].

2.4 The CLAS Detector

The CEBAF Large Acceptance Spectrometer (CLAS) was the main detector in Hall B. It was primarily used to detect charged and multi-particle final states produced by interactions of the photon beam with the target at the CLAS center. CLAS had an almost 4π coverage in solid angle, and was almost 10 m in diameter. The CLAS spectrometer was a multi-layered arrangement of different kinds of particle detectors arranged symmetrically around the beam axis. This arrangement of the detectors provided an angular coverage of 8° to 142° in the polar angle. The superconducting toroidal magnet was a vital piece of the CLAS detector. CLAS was azimuthally divided into six independent sectors. Each sector was composed of a start counter, drift chambers, and time-of-flight scintillators. CLAS also had Cerencov counters and electromagnetic calorimeters in the forward region, but these were not used in our analysis and, thus, will not be discussed here.

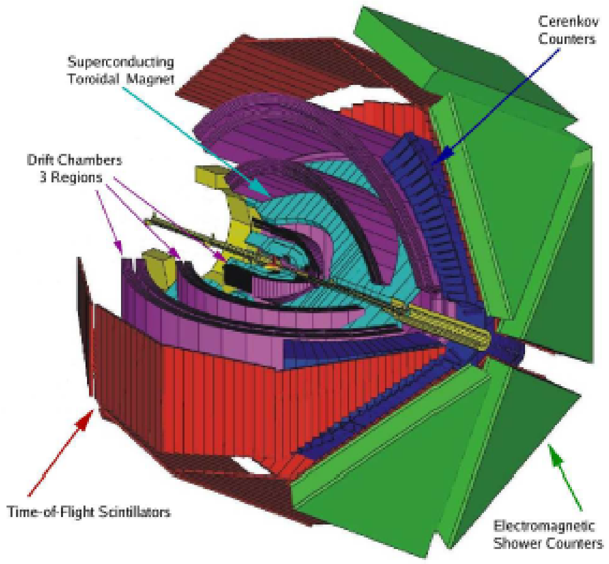

Figure 2.10: Schematic diagram of the CLAS spectrometer showing the major subsystems. This spectrometer, approximately 10 m in diameter, was housed in experimental hall B. Image source [45].

2.4.1 Start Counter (ST)

The start counter (ST) was the first detector to detect charged particles traveling from the target region. It was located close to the center of the CLAS spectrometer and directly surrounded the target. The start counter provided a precise start time for every trigger recorded and time of the hadronic interaction.

The start counter was divided into six sectors, matching the six-sector geometry of the CLAS. Each sector consisted of four scintillator paddles, each coupled to an acrylic light guide. A charged particle entering the paddle produced light inside the scintillator and the light then travelled into a light guide, which was attached to a Photo Multiplier Tube (PMT). At the PMT, the photo-signal was collected, converted and amplified for later use in the analysis. The start counter also served a crucial role in the trigger system.

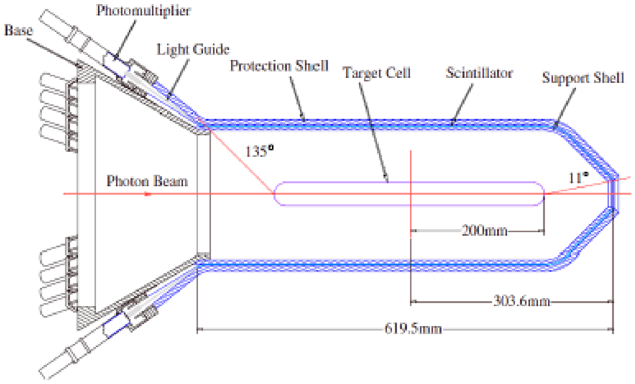

Figure 2.11: A cross section cut along the beamline of the start counter, depicting the labeled components and the angular coverage when placed at the center of CLAS. Image source [39].

2.4.2 Superconducting Toroidal Magnet

The superconducting toroidal magnet, or torus magnet, generated a magnetic field that caused charged particles to travel along a non-linear path through the drift chambers, a tracking detector discussed in the next section. The torus magnet bent the particles toward or away from the beamline without changing their azimuthal angles. The magnet was approximately 5 m in diameter and 5 m in length, and it utilized six kidney-shaped superconducting coils, each separated at 60° angles in the azimuthal direction.

Each of the six coils had four layers of 54 turns of aluminum-stabilized NbTi/Cu conductors. The map of the magnetic field produced by the torus is shown in Figure 2.13. The main field was in the ϕ direction with a deviation from a pure ϕ field close to the coils. The maximum designated

Figure 2.12: The CLAS torus coils in Hall B before installation of the rest of the detectors. Image source [41].

current in the torus coils was 3860 A. However, the current was limited to 1920 A during the $g9a$ experiment, and was limited to 1930 A during the $g12$ experiment. The magnet was cooled down to 4.4 K using liquid helium running through cooling tubes at the edge of the windings.

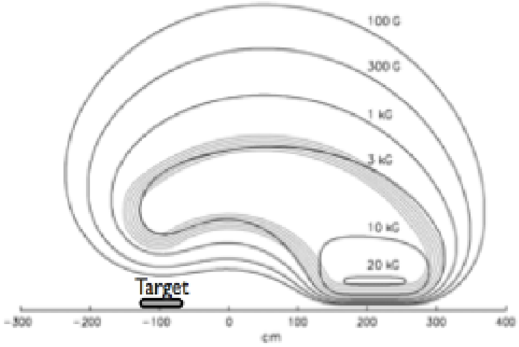

Figure 2.13: Strength contours of the CLAS magnetic field in the midplane between the two coils. The target position for the $g12$ experiment is also shown. Image source [47].

2.4.3 Drift Chambers (DC)

The special wire-chambers known as Drift Chambers (DC) were used for tracking the charged particles as they traveled through the field generated by the torus magnet. The chambers occupied most of the CLAS volume and were filled with a mixture of 90% Argon an 10 % CO_2. The charged particles interacted and ionized the gas mixture via collisions or electromagnetic interactions. The ionized particles were then quickly collected by wires maintained at a potential difference. This flow of current in those particular wires told us the position and trajectory of the particles. The momentum of the charged particles could then be determined from their trajectory:

$$p = qBR, \tag{2.3}$$

where B is the magnetic field, R is the radius of the trajectory and q is the charge of the particle. The charge was determined by observing whether the particle was bent towards or away from the beam line.

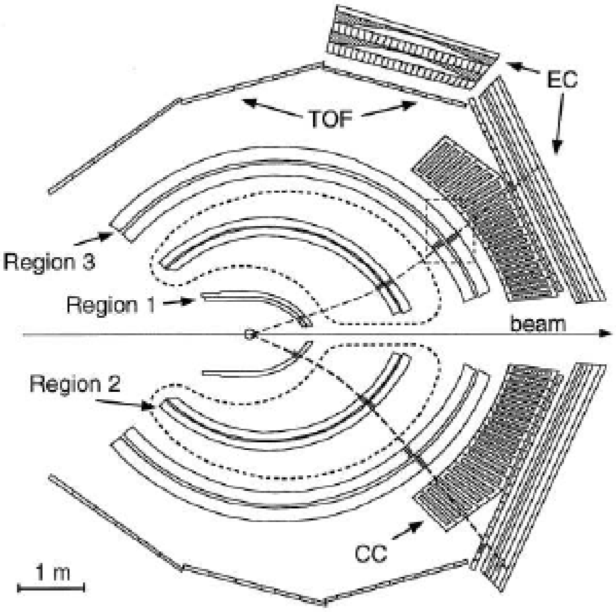

Figure 2.14: A cut away diagram of CLAS showing the arrangement of the drift chambers. The kidney-shaped dashed lines outline the location of the torus coils. Also shown are the trajectories of two charged particles travelling through DC in different sectors. Image source [48].

The drift chambers were divided into six sectors and each sector consisted of three regions, as shown in figure 2.14. Region 1 (R1) was located close to the target in a low magnetic area. Region 2 (R2) occupied the space where the magnetic field was the strongest. Region 3 (R3) was positioned outside the coil, in a region of zero magnetic field. Each DC region was divided into two separate superlayers, and each superlayer consisted of six layers of drift cells. In total, about

13,000 wires were strung to the cells of the Drift Chambers. The drift cells consisted of a 20 micron gold-plated tungsten sense wire in the center of a hexagonal arrangement of six 140 micron gold-plated aluminum alloy field wires. The sense wires were maintained at a positive potential and the field wires at a negative potential. A high voltage system was applied to all wires in the chambers.

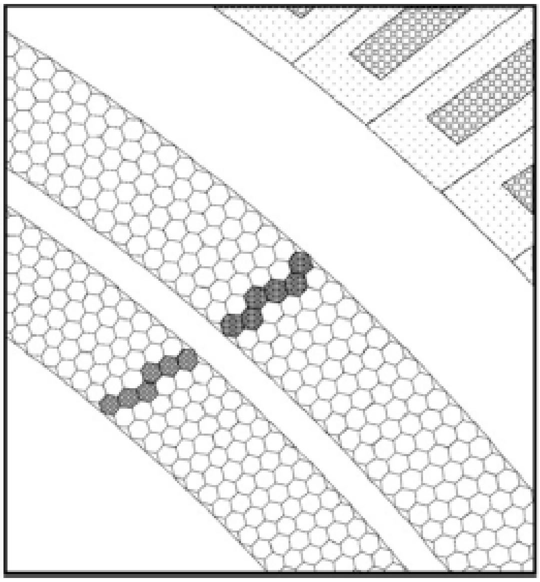

Figure 2.15: A schematic diagram showing the Region 3 superlayers of the drift chambers. Sense wires are at the center of each hexagon and the field wires are at the vertices. The lines connecting the vertices of the hexagons are not real. The shaded region shows a charged particle's trajectory as it has ionized the gas and is recorded by the hexagonal cells. Image source [48].

2.4.4 Time-of-Flight Scintillators

The time-of-flight (TOF) scintillator paddles measured the time information of charged particles crossing the drift chambers. The time information measured from the TOF paddles combined with the hadronic interaction time provided by the start counter gives us the "time-of-flight" of the particles. In addition to the track length that was calculated by using the information from the drift chambers, the velocity of the particles, β, was determined. Once we have β and p, the mass of the particle was calculated, and hence identified as pions, protons, kaons, etc.

The TOF paddles were located radially outside the tracking system and comprised of six panels, one for each sector, at a distance of about 4 meters from the center of the CLAS. Each panel contained 57 scintillator paddles of varying lengths and widths but of a uniform thickness of 2 inches.

Photons were created when a scintillator was hit by particles. The signals from the scintillators were then collected via PMTs mounted at each end of the tubes. The timing resolution of each scintillator is between 80 and 160 ps, depending on the length of the paddle.

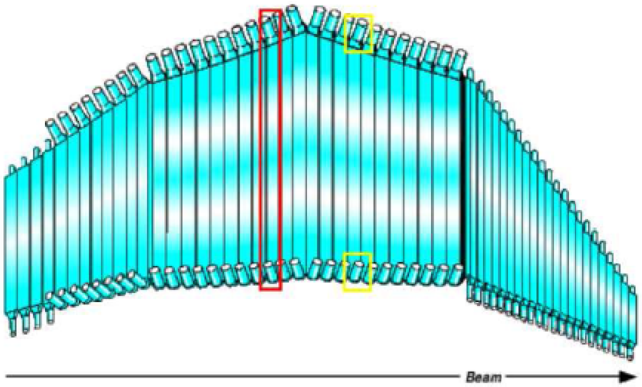

Figure 2.16: Diagram of the TOF scintillation counters for one CLAS sector, with PMTs boxed in yellow and a whole scintillator boxed in red. Image source [39]. Image was adapted from [49].

2.5 Beamline Devices

The quality of the beam was monitored using a number of beamline devices. These devices were included in the upstream and downstream beamlines. The upstream devices included Beam Position Monitors (BPMs), harps and a Mϕller Polarimeter. The Beam Position Monitors (BPMs) operated using current induced by the beam. The BPM current was used to calculate the x and y positions of the beam. The profile of the electron beam was measured using harp scanners made of tungsten and iron crossed wires. Electrons that were scattered by the wires were detected by PMT arrays arranged around the beam line upstream from CLAS. The polarization of the electron beam was measured by the *Mϕller* Polarimeter. Mϕller measurements were performed in special runs.

In the downstream beamline, a total absorption shower counter (TASC) was used to measure the photon flux. It consisted of four lead glass blocks, coupled to a PMT, with 100% photon detection efficiency. A low beam current, less than 100 pA, was required to measure the photon flux. Thus, special normalization runs were taken periodically during the experiment.

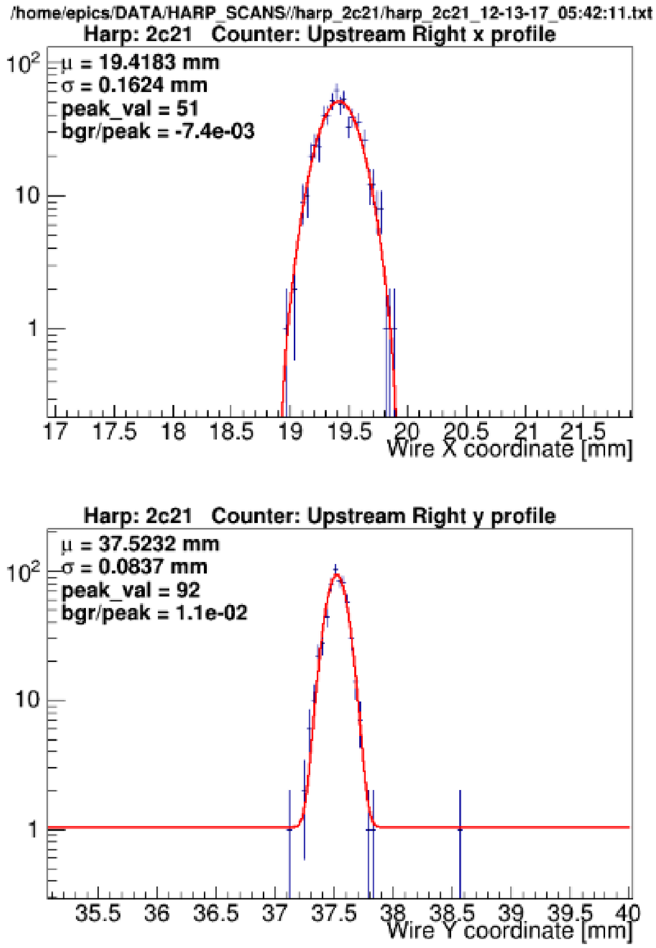

Figure 2.17: A typical harp scan to measure the electron beam profile. Shown are the x and y profiles of the electron beam just before hit the tagger. The orange lines is a Gaussian fit to the data. Image source [50].

2.6 Triggering and Data Acquisition

CLAS and its subsystems had their own electronic systems that constantly read out signals. These electronic signals were generated in the PMTs, which were connected to various scintillators, the current in the DC wires, and other instruments in the hall. The signals were then converted into digital numbers using Analog to Digital Converters (ADCs), Time to Digital Converters (TDCs) and other devices. All the analog signals from the CLAS detectors were digitized by FASTBUS and VME modules in the Read-Out Crates (ROCs). These ROCs were controlled by a central Data Acquisition System (DAQ), which was managed by the CEBAF Online Data Acquisition (CODA).

Due to the limitation of the data acquisition, "triggers" were employed in the experiments. A trigger system also used to maintain quality control since a signal in a single detector did not necessarily corresponded to a physics event of interest. A number of unwanted sources, such as cosmic radiation, electronic noise or a malfunctioning detector could produce signals. Therefore, the main job of the trigger was to decide which set of signals constituted an interesting physics event. Triggers required the detector hits to satisfy a predefined set of conditions for various CLAS systems within a short window of time. When the conditions of the trigger were satisfied by an event, the DAQ then recorded the event data to the tape.

The $g9a$ experiment used a trigger that required at least one charged particle that made a hit in both start counter and time-of-flight scintillators in the same sector. The $g12$ experiment was the first Hall-B experiment to implement a Field Programmable Gate Array (FPGA) processor to handle the trigger logic of the detectors. The FPGA system enabled the ability to modify the trigger quickly during the experiment. Thus, there were different trigger setups for different groups of runs in the $g12$ experiment. The main production trigger for the $g12$ data that we analyzed, which are the run periods of 56520 to 56646, required tracks in two distinct sectors of CLAS in conjunction with a hit in the tagger where at least one of the tagged photons had an energy $\geq$ 3.6 GeV.

A track was considered a true event when a hit was registered in the start counter and the time-of-flight scintillators (ST X TOF) of a CLAS sector within a short window of time ($\approx$ 150 ns). The trigger also required at least one photon with energy above 3.6 GeV, or the first 25 tagger paddles registered a hit if only two tracks in two different secctors ((ST X TOF) X 2) were recorded during the trigger window. The photon energy requirements were encoded in the tagger Master OR (MOR) Boolean condition. Bit 12 was added in addition to the main production trigger where there was no photon energy requirement if the event had three tracks in three different sectors ((ST X TOF) X 3).

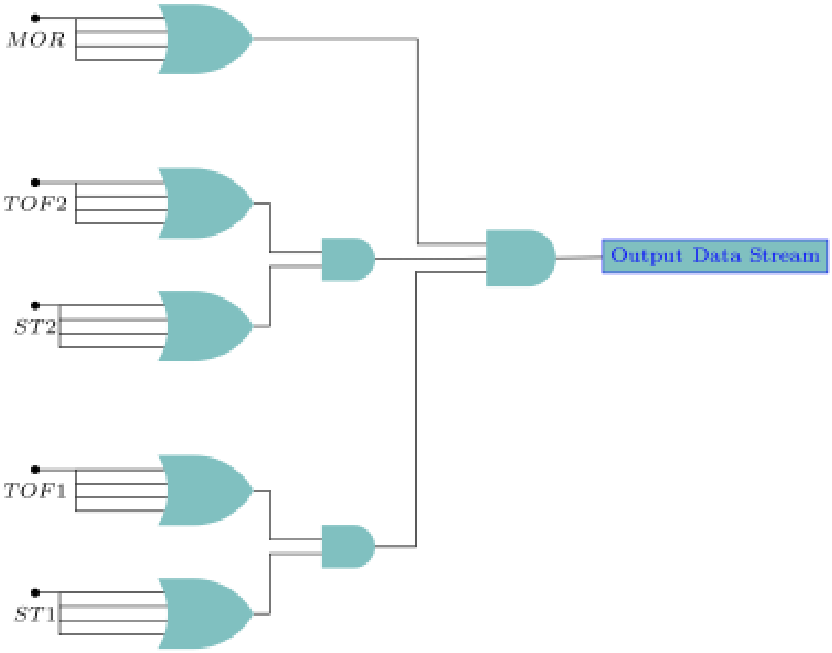

Figure 2.18: The main production trigger diagram, where ST X TOF hits are registered in two distinct CLAS sectors in conjunction with a hit in the first 19 tagger paddles. Image source [39].

Table 2.1: Trigger configuration for the $g12$ experiment from runs 56363 to 58594 and 56608 to 56647 [46]. (ST X TOF)$_i$ indicates a coincidence between a start counter and time-of-flight hit in the i^{th} sector. An added X2 or X3 indicates the multiple coincidences of the ST and TOF hits, which are in two or three different sectors. MORA and MORB represent coincidence with tagger hits within a certain energy range, as specified in table 2.2

	$g12$ runs 56363–56594, 56608–56647		
bit	definition	L2 multiplicity	prescale
1	MORA·(ST×TOF)$_1$·(ST×TOF)	–	1
2	MORA·(ST×TOF)$_2$·(ST×TOF)	–	1
3	MORA·(ST×TOF)$_3$·(ST×TOF)	–	1
4	MORA·(ST×TOF)$_4$·(ST×TOF)	–	1
5	MORA·(ST×TOF)$_5$·(ST×TOF)	–	1
6	MORA·(ST×TOF)$_6$·(ST×TOF)	–	1
7	ST×TOF	–	1
8	MORA·(ST×TOF)×2	–	1
11[a]	MORB·(ST×TOF)×2	–	1
12	(ST×TOF)×3	–	1

---

[a] bit 11 and MORB were included in the trigger starting with run 56519.

Table 2.2: Master-OR definition for $g12$ [46]. The TDC counters were used in the trigger. T-counter number 1 corresponds to the highest energy photon of approximately 5.4 GeV.

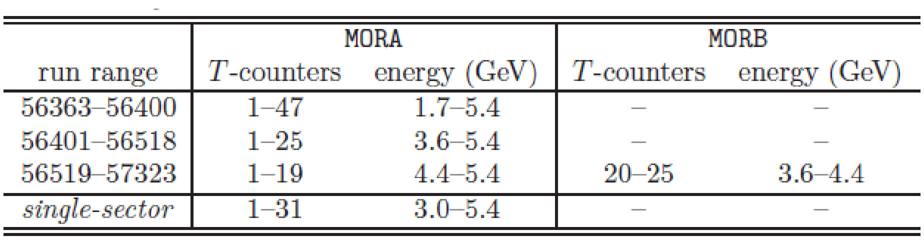

	`MORA`		`MORB`	
run range	T-counters	energy (GeV)	T-counters	energy (GeV)
56363–56400	1–47	1.7–5.4	–	–
56401–56518	1–25	3.6–5.4	–	–
56519–57323	1–19	4.4–5.4	20–25	3.6–4.4
single-sector	1–31	3.0–5.4	–	–

CHAPTER 3

EVENT SELECTION

3.1 The CLAS-g9a and CLAS-g12 Data Set

The information collected from the detectors and included in the raw data consisted of QDC (Charge to Digital Convertor) and TDC (Time to Digital Converter) channel IDs and values. In a first step, the data had to undergo reconstruction, or be *cooked.* This process converted the data into physical quantities like particle IDs, positions, angles, energies, and momenta. The data calibration was carried out independently for each detector component of CLAS. After the detectors had been calibrated and the particle tracks had been reconstructed, the data were made available for physics analysis. Each event had its information organized in CLAS data banks[1]. These data banks contained not only the properties of the particles involved in a reaction but also information about detector hits.

Here we list the most relevant data banks that we used in our analyses:

1. **PART** – This bank contained most of the details about the detected particles, such as the particle IDs, 4-vectors, vertex of each particle, and other information from various detectors.
2. **TAGR** – In this bank, information about all incident photons was stored, e.g. the energy of the photon(s), the time of the photon(s) after the reconstruction in the Tagger, the time of the photon(s) after the RF correction, the status of the photon(s) (used to identify those which were not reconstructed properly), and the E- and T-counter ID information of the corresponding scattered electron.
3. **TBER** – Time-based tracking error bank containing fit parameters and the covariance matrix.
4. **TBID** – Bank containing information on time-based particle ID (including β ($= \frac{v}{c}$) values).
5. **TGBI** – Trigger bank; it also stored polarization information, e.g. the helicity bit.

---

[1] http://clasweb.jlab.org/bos/browsebos.php?bank=gpid&build=64bit/STABL

3.1.1 The CLAS-g9a Data Set

The data for the *g*9*a* experiment were taken between November 3th, 2007 and February 12th, 2008. The circularly-polarized photon data set is categorized into two parts according to the electron beam energy: one is the data using $E_e = 1.645$ GeV and another is using $E_e = 2.478$ GeV. These data are broken up into seven different periods as shown in table 3.1

Table 3.1: The circularly-polarized photon dataset of the *g*9*a* experiment classified according to the electron beam energy and run numbers.

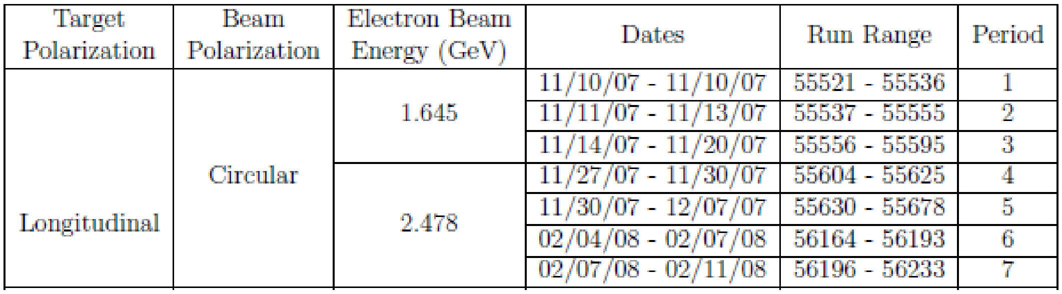

Target Polarization	Beam Polarization	Electron Beam Energy (GeV)	Dates	Run Range	Period
Longitudinal	Circular	1.645	11/10/07 - 11/10/07	55521 - 55536	1
			11/11/07 - 11/13/07	55537 - 55555	2
			11/14/07 - 11/20/07	55556 - 55595	3
		2.478	11/27/07 - 11/30/07	55604 - 55625	4
			11/30/07 - 12/07/07	55630 - 55678	5
			02/04/08 - 02/07/08	56164 - 56193	6
			02/07/08 - 02/11/08	56196 - 56233	7

3.1.2 The CLAS-g12 Data Set

The data for the *g*12 experiment were taken between April 1st and June 9th, 2008. The data set was further divided into ten different groups of runs according to different trigger configurations.

Table 3.2 shows the different g12 trigger configurations. We used only Period 2 (starting from run 56520) for our analyses at FSU. For these data, the trigger required either (at least) three charged tracks with no restrictions on the photon energy or only two tracks with the additional requirement of having at least one photon detected with an energy above 3.6 GeV. Since our primary motivation initially was to extract the ω (and $\pi^+\pi^-$) cross sections with high quality, we decided not to mix trigger configurations and thus, avoided the prescaled data and those using an Electromagnetic Calorimeter (EC)-based photon or lepton trigger (Period 3 - 8). Period 1 suffered from lower statistics and using it would not have significantly improved the statistical uncertainties of our results. Moreover, this period switched from a three-track requirement to a two-track requirement at a different energy and also used a different beam current.

Table 3.2: The different trigger configurations used in g12 (from the g12 wiki and Ref. [46]).

Period	Runs	Trigger Configuration
1	56519 and earlier	not prescaled, trigger change at 4.4 GeV
2	56520 - 56594, 56608 - 56646	not prescaled, trigger change at 3.6 GeV
3	56601 - 56604, 56648 - 56660	prescaled
4	56665 - 56667	prescaled
5	56605, 56607, 56647	prescaled
6	56668 - 56670	prescaled
7	56897 and later	prescaled
8	57094 and later	prescaled
9	56585, 56619, 56637	single-sector, not prescaled
10	56663 and later	single-sector, not prescaled

3.2 Reaction Channels and General Event Selection

The channel of interest in this analysis is $\gamma p \to p\,\pi^+\pi^-\ (\pi^0)$. The π^0 could be identified through the missing-mass technique. For this method, the Lorentz vectors of the incoming beam and the target were used. The four-momentum of a missing particle in the reaction was then determined from the measured three-momenta and the particle energies. The missing four-momentum was given by:

$$x^\mu \,=\, k^\mu \,+\, P^\mu \,-\, \sum_{i=1}^{2,3} p_i^\mu\,, \tag{3.1}$$

where k^μ and P^μ are the initial photon and target-proton four-momenta and p_i^μ are the four-momenta of the two or three detected final-state particles. The missing mass m_X was defined as:

$$m_X^2 \,=\, x^\mu x_\mu\,. \tag{3.2}$$

The missing-mass distribution was used for a data quality check after all corrections and cuts had been applied. The four-momentum vector x^μ in Equation 3.1 was used to complete the set of four-vectors for all particles.

Events were pre-selected based on the particles' identification number (PID), which was determined during the cooking process. Events that did not meet our requirement (exactly one proton, one π^+ and one π^- in the final states) were ignored and subsequently omitted from the analysis. The calculation of the detected particles' masses, which was necessary to determine the PIDs, used two independently-measured quantities, the momentum, p, and the velocity as a fraction of the speed of light, β. The magnitude of a particle's momentum was determined with an uncertainty of $< 1\,\%$ using information from the CLAS Drift Chambers (DC) [48]. The quantity β of a detected final-state particle was determined with an uncertainty of up to $5\,\%$ [49] using a combination of the Start Counter (SC), the Time-of-Flight (TOF) spectrometer, and the particle's trajectory through CLAS. The detected particle's mass could then be calculated by:

$$m^2_{\text{particle } X} \;=\; \frac{p^2\,(1\,-\,\beta^2)}{\beta^2}\,. \tag{3.3}$$

After the particle's mass had been calculated, it was compared to the masses of known particles (hadrons and leptons). If this calculated mass matched that of a known particle (within resolution), the PID associated with that mass was assigned to the final-state particle. This value could then be used to select certain final-states for analysis. In this analysis, the physical properties of the final-state particles (e.g. their 4-vectors, vertex information, etc.) were extracted from the PART data banks. Photon and final-state particle selection was further improved by applying cuts and corrections (see Section 3.3). We also used kinematic fitting (see Section 3.5) to fine-tune the initial- and final-state momenta by imposing energy- and momentum conservation. Finally, to separate signal events from the remaining background, we used an event-based Q-factor method which is discussed in more details in Section 3.12.

In a short summary, listed below are the cuts and corrections that were applied to the data:

1. Tagger-sag corrections (done in the cooking process).
2. ELoss corrections using the standard CLAS package [51].
3. Beam-energy corrections based on the CLAS-approved run-group approach [46].
4. Momentum corrections based on the CLAS-approved run-group approach [46].
5. Vertex cut: $-110.0 < z\text{-vertex} < -70.0$ cm.
6. Photon selection & accidentals
   (nGammaRF() = 1 & TAGR_ID equal for all tracks; information from TAGR bank)

7. Particle ID cut [2], $\Delta\beta = |\beta_\mathrm{c} - \beta_\mathrm{m}| \leq 3\sigma$, and timing cut, $|\Delta t_\mathrm{TBID}| < 1$ ns [3]. The theoretical β values for all particle types, β_c, were calculated from the measured momentum and the PDG mass m for the particle

$$\beta_c = \sqrt{\frac{p^2}{m^2 + p^2}}. \tag{3.4}$$

β_m is the measured β value that is obtained from the Drift Chambers (DC), Start Counter (SC), and the Time-of-Flight (TOF) spectrometer.

8. Confidence-level cut of CL > 0.001 for $\gamma p \to p\,\pi^+\pi^-\,(\pi^0)$.

9. Fiducial cuts: *nominal* scenario [46]. This nominal-fiducial cuts will be described in section 3.9

The order of these applied cuts and corrections was quite flexible with the exception of a few cases. Momentum corrections were applied after the energy-loss corrections. The following sections describe the applied cuts and corrections in more detail.

3.3 Photon and Particle Identification

3.3.1 Initial-Photon Selection

The electrons, which were used to produce the beam of polarized photons via bremsstrahlung radiation, were delivered from the accelerator into Hall B in the form of 2-ns bunches. Since each bunch contained many electrons, there were several potential photon candidates per recorded event that could have triggered the reaction inside the target. Random electron hits could also occur from various background sources (e.g. cosmic rays). These did not create bremsstrahlung photons but the hits were registered in the tagger scintillators. It was important to determine the correct photon in each event (out of about five candidates on average) because the corresponding photon energy was key to understanding the initial state of the event. The analysis steps taken in the photon selection were as follows:

1. The Start Counter time per track at the interaction point, t_track, was given by:

$$t_\mathrm{track} = t_\mathrm{ST} - \frac{d}{c\,\beta_\mathrm{calc}}\,, \tag{3.5}$$

where t_ST was the time when the particle was detected by the Start Counter, d was the length of the track from the interaction point to the Start Counter, and $c\,\beta_\mathrm{calc}$ was the calculated velocity of the particle. These (track) times could be averaged to give an event time, t_event.

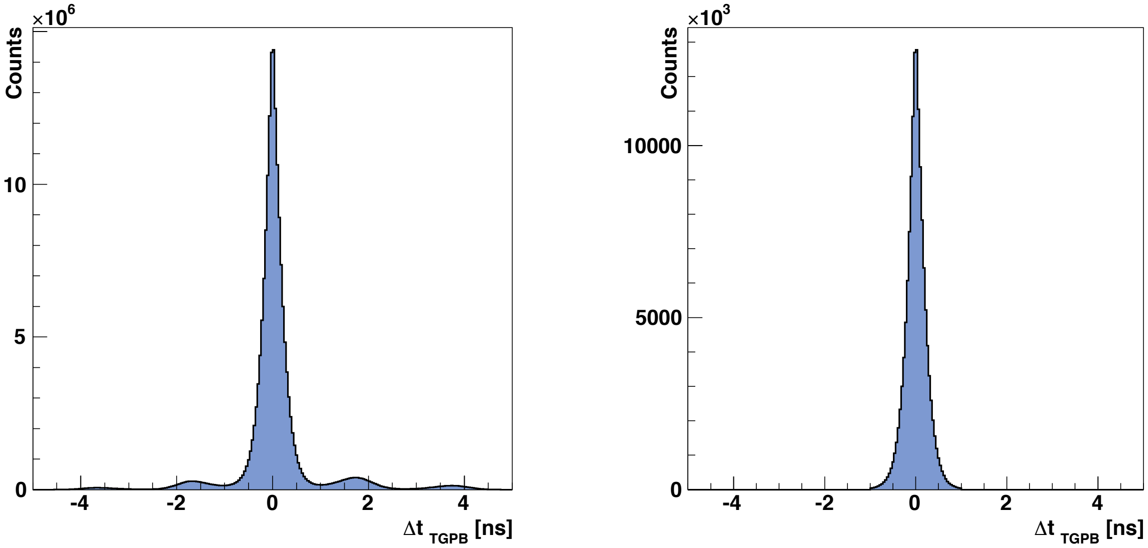

Figure 3.1: Left: Example of a coincidence-time distribution, Δt_{TGPB}, for the inclusive $p\,\pi^+\pi^-$ final-state topology. The 2-ns bunching of the photon beam is clearly visible in the histogram. Right: Distribution of $\Delta t_{\mathrm{TBID}} = t_{\mathrm{event}} - t_\gamma$ for the selected photon (one entry per event) after PID cuts. The event vertex time, t_{event}, was based on Equation 3.5. We only considered events which had exactly one candidate photon in the same RF bucket per track; each identified track had to be associated with the same photon.

The time at which a candidate photon arrived at the interaction point, t_γ, was given by:

$$t_\gamma \,=\, t_{\mathrm{center}} \,+\, \frac{d'}{c}\,, \tag{3.6}$$

where t_{center} was the time at which the photon arrived at the center of the target and d' was the distance between the center of the target and the event vertex along the beam-axis. We did not consider the x- and y-coordinates of the event vertex because they were comparable to the vertex resolution. In this analysis, the t_γ values were obtained from TAGR[ ].TPHO.

Both, t_γ as well as t_{event}, describe the time of the γp interaction – based on initial- and final-state particles, respectively. To find the correct initial photon, we looked at the corresponding time differences. The *coincidence time*, Δt_{TBID}, was thus defined per photon as the difference between the Tagger time and the Start Counter time at the interaction point, $t_{\mathrm{event}} - t_\gamma$. Since each event had several candidate photons, several Δt_{TBID} values were available, which could be obtained from information in the TBID bank. Figure 3.1 (left) shows an example distribution of the coincidence time, Δt_{TBID}. The figure clearly shows the 2-ns bunching

---

[2] In the final analysis, we applied the $\Delta\beta \leq 3\sigma$ cut on either the proton or the π^+ (no cut on the π^-).

[3] $\Delta t_{\mathrm{TBID}} = stVtime() - vtime()$ is the coincidence time between the vertex and the photon time.

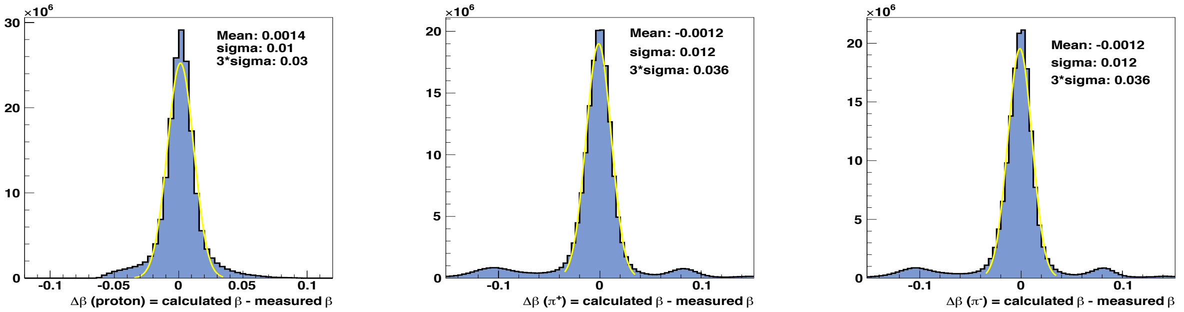

Figure 3.2: Distributions of $\Delta\beta = \beta_{\rm c} - \beta_{\rm m}$ for protons (left) as well as for the π^+ (middle) and for the π^- (right) from the g12 experiment (full statistics used in our FSU analyses, Period 2 (see Table 3.2)). The quantity $\beta_{\rm c}$ was calculated based on the particle's PDG mass [52]. Events in the center peak were selected after applying a $|\beta_{\rm c} - \beta_{\rm m}| \leq 3\sigma$ cut. See text for more details.

of the photons that arrived at the target. In each event, the information on energy and timing, t_γ, was written to the event's TAGR bank for all photons. The total number of photon candidates per event was also available. *The* photon selection itself was performed by the CLAS offline software in the cooking process. However, we applied a timing cut of $\Delta t_{\rm TBID} < 1$ ns in this analysis.

2. Occasionally, events could have more than one candidate photon with $|\Delta t_{\rm TBID}| < 1$ ns. In such cases, the photon selection could not be made based on their time information. The fraction of these events was about 13 % in the g12 experiment. To prevent any ambiguity, only events with exactly one photon candidate in the same RF bucket for all selected tracks (nGammaRF() = 1) were considered in this analysis. In addition, we also ensured that the selected photon was the same for all reconstructed tracks (TAGR_ID equal for all tracks). Figure 3.1 (right) shows an example of the coincidence-time distribution for the selected initial photon (one entry per event) after PID cuts.

3.3.2 Proton and Pion Selection

The photon energy for each event was selected according to the procedure outlined in Section 3.3.1. In the next step, the identification of the final-state particles, proton, π^+, and π^-, was needed. As mentioned in Section 3.2, we initially used particle ID information from the PART bank and selected those events which belonged to our channel of interest. For a more refined selection of the particles, we used the information on the measured and calculated β values of each particle. The TBID bank contained the CLAS-measured momentum of a particle; a theoretical value, $\beta_{\rm c}$, for that particle could then be calculated from this measured momentum and an assumed mass. The β_c values for all possible particle types were compared to the CLAS-measured empirical $\beta_{\rm m} = \frac{v}{c}$ value. Particle identification then proceeded by choosing the calculated $\beta_{\rm c}$ closest to the measured $\beta_{\rm m}$. Figure 3.2 shows the differences, $\Delta\beta = \beta_{\rm c} - \beta_{\rm m}$ for the different final-state particles based on the full g12 statistics that we used in our FSU analyses, (Period 2, see Table 3.2). Assuming a PDG mass m for the particle [52], $\Delta\beta$ was given by:

$$\Delta\beta = \beta_{\rm c} - \beta_{\rm m} = \sqrt{\frac{p^2}{m^2 + p^2}} - \beta_{\rm m}\,. \tag{3.7}$$

The prominent peaks around $\Delta\beta = 0$ shown in Figure 3.2 correspond to the particles of interest. It can be seen in the figures that the $\Delta\beta$ distributions for the pions are slightly broader than for the proton and long tails including a prominent enhancement on either side of the central peak are visible. When the PART bank was created during the track reconstruction, electrons were not separated from pions. The additional features in the $\Delta\beta$ distributions for the pions represent these electrons which need to be filtered out. To identify the protons and pions, loose cuts on $|\beta_{\rm c} - \beta_{\rm m}|$ were applied. The cut values were determined by fitting the main peak around $\Delta\beta = 0$ with a Gaussian. Figure 3.3 shows the measured momentum, p, versus the measured $\beta_{\rm m}$ for protons and pions before (left) and after (right) applying the $|\beta_{\rm c} - \beta_{\rm m}| < 3\sigma$ cut. The bands for the pions and protons (lower band) are clearly visible.

Although the $\Delta\beta$-PID cuts significantly help avoid misidentified tracks in the selected event sample, we applied only a loose $|\Delta\beta| < 3\sigma$ cut in our final event selection on either the proton or the π^+ (no cut on the π^-). This allowed us to retain as many signal events as possible. The remaining background caused by misidentified tracks did not cause structures under the signal in the relevant mass distributions and was taken care of by our background-subtraction technique (see Section 3.12). The loose cuts were also in line with an earlier CLAS analysis of the ω and η photoproduction cross sections [25, 53, 54].

3.4 Vertex Cut

The *g9a* experiment had three kinds of targets: a butanol, carbon, and a polyethylene target. The butanol target was 5 cm long and 3 cm in diameter with its center located at the center of the CLAS. Since we did not use the data from the carbon and polyethylene target, a vertex cut of

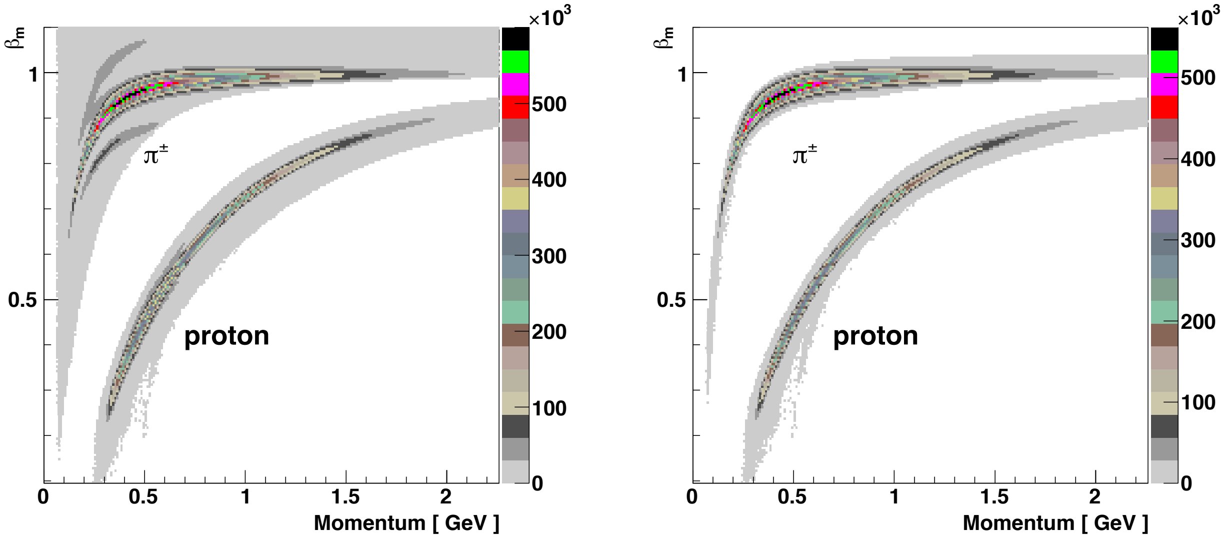

Figure 3.3: Left: The measured β_m versus momentum on a logarithmic color scale. Note a thin horizontal line close to one for electrons, and the broad stripes for pions (top) followed by protons (bottom). Right: The measured β_m versus momentum after applying the 3σ cut based on the difference $\Delta\beta = \beta_\mathrm{c} - \beta_\mathrm{m}$. Clean pion and proton bands are visible. These figures were made using the full statistics used in our FSU analyses, (Period 2, see Table 3.2).

$-3 < z$ vertex < 3 cm was applied to the data. Figure 3.4 shows the z-vertex distribution in the *g9a* experiment for the three different targets.

In the g12 experiment, the liquid hydrogen target was not located at the center of CLAS but moved 90 cm upstream to increase the angular resolution for heavier-meson photoproduction in the forward direction. The target itself was 40 cm long and 2 cm in diameter. Therefore, a z-vertex cut of $-110 < z$ vertex < -70 cm was applied; the full z-vertex distribution is shown in Fig. 3.5.

3.5 Introduction to Kinematic Fitting

The 4-vectors of the final-state particles were determined in the *cooking* or reconstruction phase. Kinematic fitting [55] slightly modified these *raw* 4-vectors by imposing energy-momentum conservation on the event as a physical constraint. In a brief summary, all measured components of the Lorentz 4-vectors (the magnitude of the momentum as well as the two angles used in the drift-chamber reconstruction – $p,\ \lambda,\ \phi$, respectively) in addition to the initial photon energy were modified within their given uncertainties until the event satisfied energy-momentum conservation

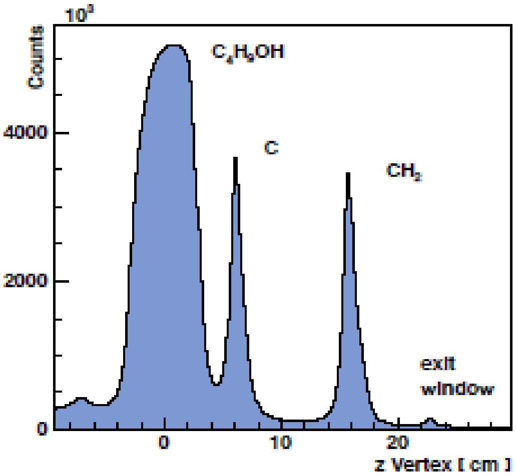

Figure 3.4: The z-vertex distribution in the $g9a$ experiment based on 30% of the total statistics for the full photon energy range [33]. The three peaks for the three different targets are clearly visible as well as a peak from the exit window of the vacum chamber.

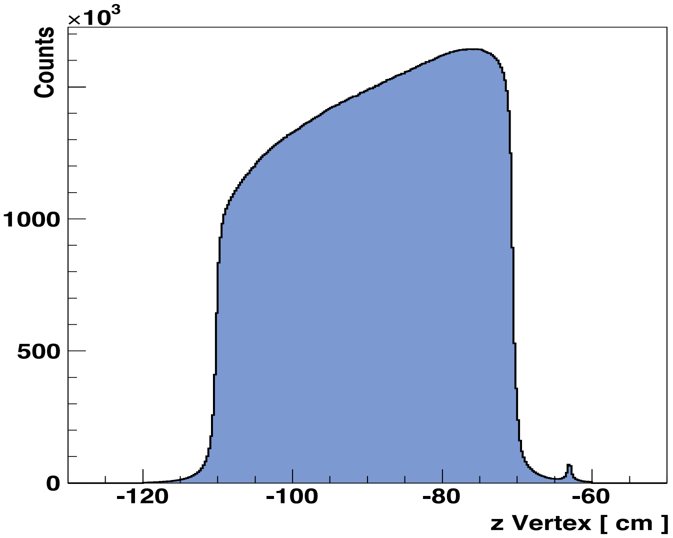

Figure 3.5: The z-vertex distribution (axis along the beam line) of all reconstructed particles we used in our FSU analyses. The shape of the liquid hydrogen target is clearly visible. The small enhancement at about $z = -63$ cm originates from the exit window of the vaccuum chamber.

exactly. The determination of the correct uncertainties (or covariance matrix) was important in this fitting procedure. The kinematically-fitted event had then several quantities which could be used to inspect the quality of the kinematic fitting: a pull value for each measured quantity and an overall χ^2 value. The latter could be converted to a confidence-level (CL) value to judge the goodness-of-fit. The pull distributions were used to evaluate the initial uncertainty estimation and to study systematics. It turned out that kinematic fitting provided an effective tool to verify kinematic corrections, e. g. momentum corrections.

3.5.1 Confidence Level

To check the *goodness-of-fit* or the agreement between the fit hypothesis and the data, the fit χ^2 value was used. The corresponding CL value was defined as:

$$CL = \int_{\chi^2}^{\infty} f(z;n)\,dz\,, \tag{3.8}$$

where $f(z;n)$ was the χ^2 probability density function with n degrees of freedom. It denoted the probability distribution for certain external constraints, e. g. energy-momentum conservation or also a missing-particle constraint. In the ideal case where all events satisfied the fit hypothesis and the measured quantities were all independent and had only statistical uncertainties, the confidence-level distribution would be flat from $(0,1]$. However, the real data had a confidence-level distribution which showed a peak near zero (Fig. 3.6, left side). This peak contained events which did not satisfy the imposed constraints. These events could be hadronic background events, poorly-reconstructed events with significant systematic uncertainties, or events with misidentified particles. A cut on small CL values eliminated the majority of these background events while only a relatively small amount of good data was lost.

3.5.2 Pulls

A *pull value* is a measure of how much and in what direction the kinematic fitter has to alter a measured parameter – or to *pull* at it – in order to make the event fulfill the imposed constraint. All three fit parameters for every detected final-state particle had pull distributions. The pull value for the $i^{\,\text{th}}$ fit parameter was given by:

$$z_i = \frac{\epsilon_i}{\sigma(\epsilon_i)}\,, \tag{3.9}$$

where $\epsilon_i = \eta_i - y_i$ was the difference between the fitted value, η_i, and the measured value, y_i. The quantity σ represents the standard deviation of the parameter ϵ_i. Therefore, the $i^{\,\text{th}}$ pull can be written as:

$$z_i = \frac{\eta_i - y_i}{\sqrt{\sigma^2(\eta_i) - \sigma^2(y_i)}}\,. \tag{3.10}$$

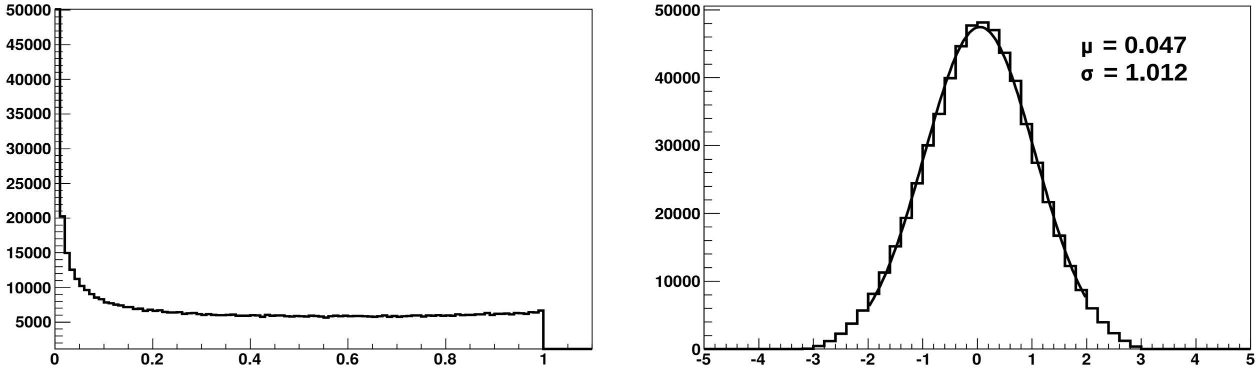

Figure 3.6: Example of results from kinematic fitting [7]. Energy and momentum conservation was imposed on Topology 4 in $\gamma p \rightarrow p\pi^+\pi^-$. Left: A confidence-level distribution. It peaks toward zero but flattens out toward one. Right: Pull distribution of the incoming photon energy. Ideally, such a distribution is Gaussian in shape, centered at the origin ($\mu = 0$) with a width of one ($\sigma = 1$).

Daniel Lersch from Juliech Research Center used the reaction $\gamma p \rightarrow p\pi^+\pi^-$ to fine tune the covariance matrix or the error of the measurements. Since the reconstruction of each particle was based on three parameters, this exclusive channel had ten pull distributions including a pull for the initial photon energy. In the ideal case that the error matrix of these parameters was correctly determined and all remaining systematic uncertainties were negligible, the pull distributions would be Gaussian in shape with a width of one ($\sigma = 1$) and centered at zero ($\mu = 0$); such an example is shown in Figure 3.6 (right side). A systematic problem with the data in the quantity η_i would be observed as an overall shift away from zero. Similarly, if the uncertainties of η_i were consistently (overestimated) underestimated, then the corresponding pull distribution would be too (narrow) broad, and the slope of the CL distribution toward $CL = 1$ would be (positive) negative. The uncertainties of the measured parameters could be corrected from the pull distributions in an iterative procedure.

In our analysis, kinematic fitting served as an effective tool to double-check the final-state corrections approved in Ref. [46]. We also used the reaction $\gamma p \rightarrow p\pi^+\pi^-$ for this purpose. The pull and confidence level distributions for the $g12$ and $g9a$ data are presented in Fig. 3.7, 3.8, and 3.9.

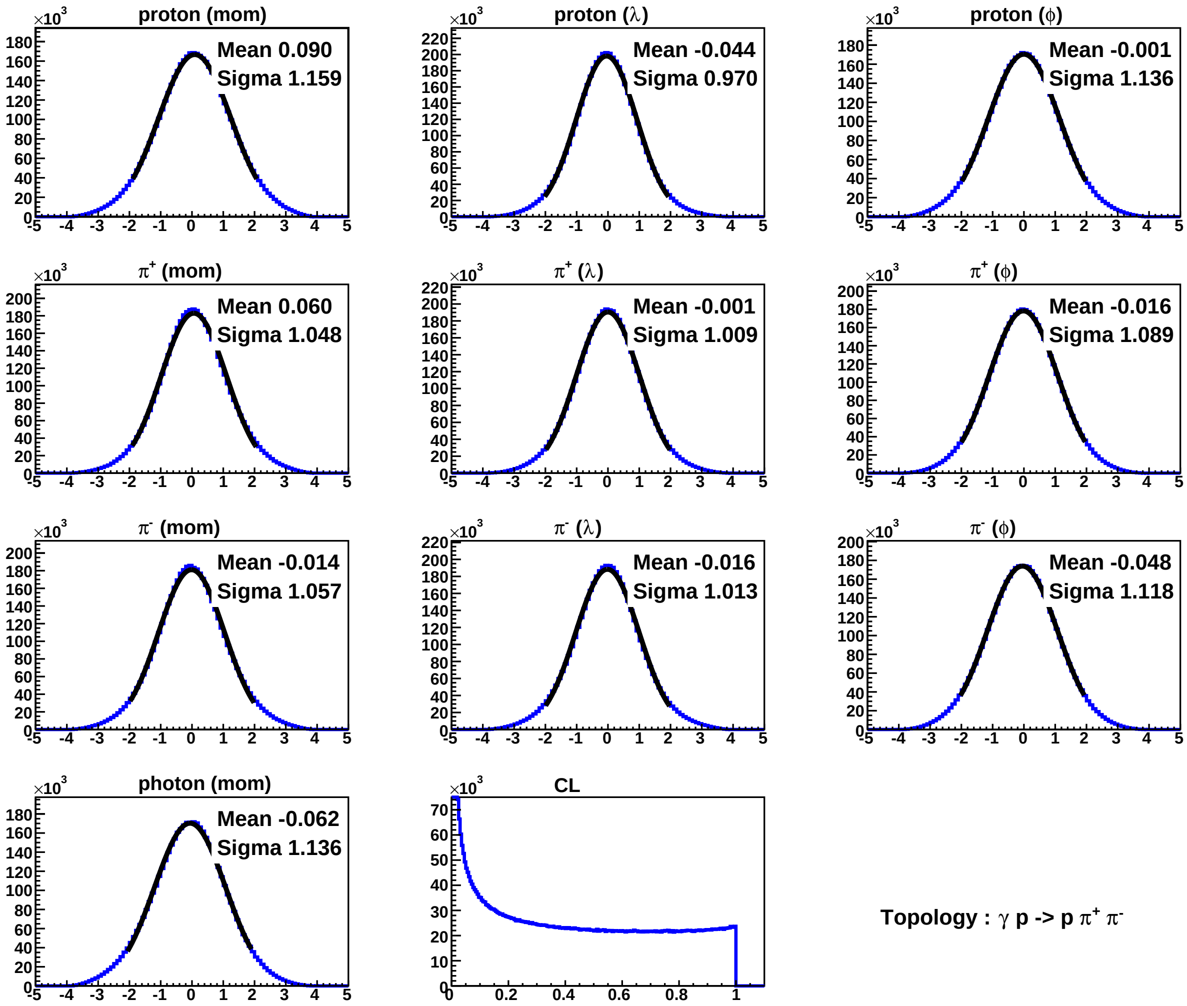

Figure 3.7: The g12 pull and CL distributions for the exclusive reaction $\gamma p \to p\,\pi^+\pi^-$ (full statistics of Period 2).

3.6 Kinematic Corrections

The following subsections briefly summarize some of the standard CLAS corrections. We only give a brief description here (in the order of application) without showing the actual effect on the data. The latter was discussed in Ref. [46] and was approved by the CLAS collaboration.

3.6.1 Tagger-Sag Correction

The energy of the incoming photons was determined by the Hall-B tagging system. It was observed in previous experiments that a physical sagging of the holding structure supporting the

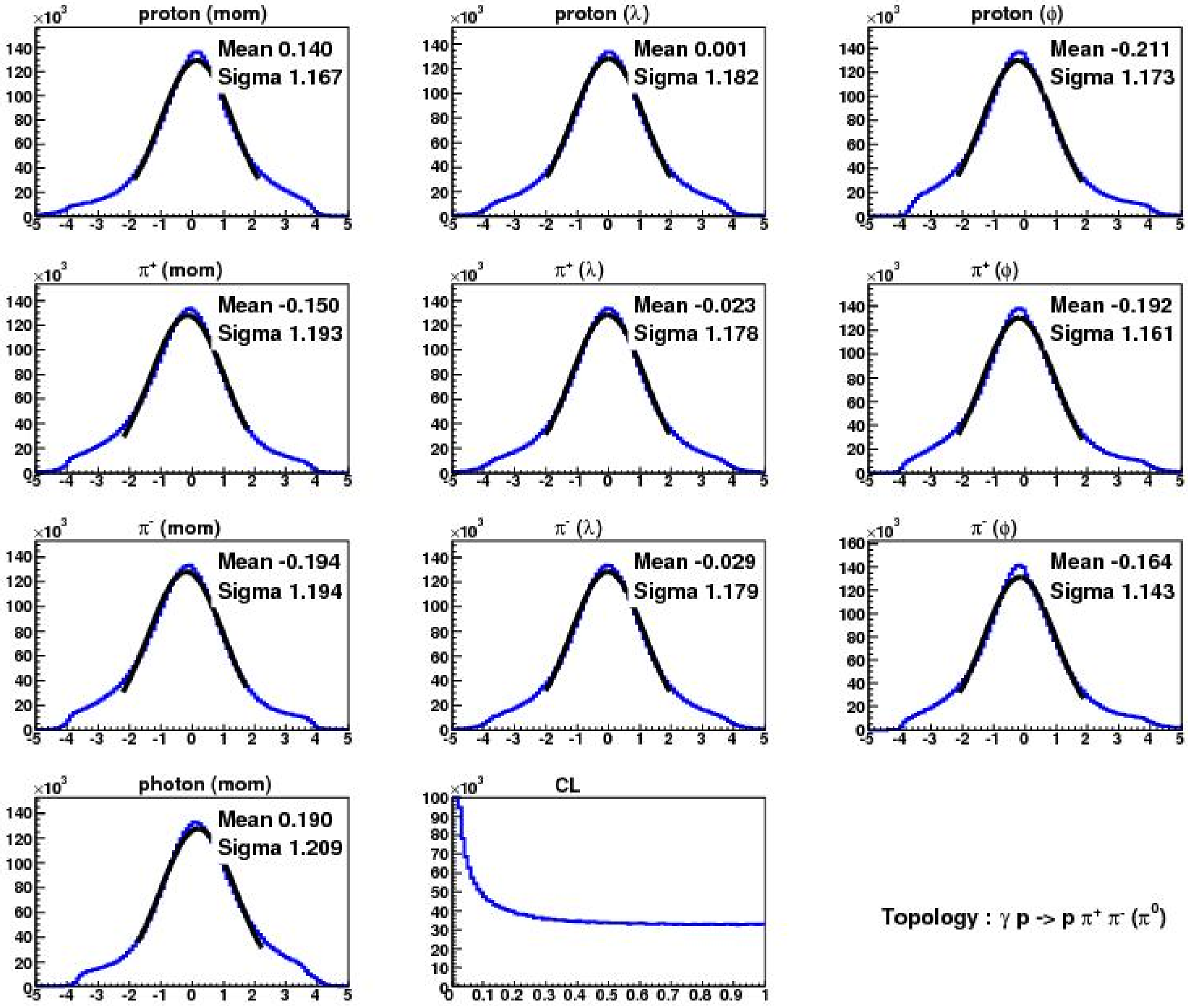

Figure 3.8: The g12 pull and CL distributions for the reaction $\gamma p \to p\,\pi^+\pi^-\,(\pi^0)$ (full statistics of Period 2). Note that the pull distributions are not Gaussian over the full range owing to the missing-particle hypothesis. The confidence-level distribution looks nicely flat, though.

E-counter scintillator bars could be attributed to gravitational forces [56]. The consequence of this time-dependent sagging was a misalignment of the scintillator bars which led to a small shift of the scattered electron's energy [57]. In the *g*9*a* and *g*12 experiment, the tagger sag was taken into account and corrected in the offline reconstruction code. No further photon energy correction was applied.

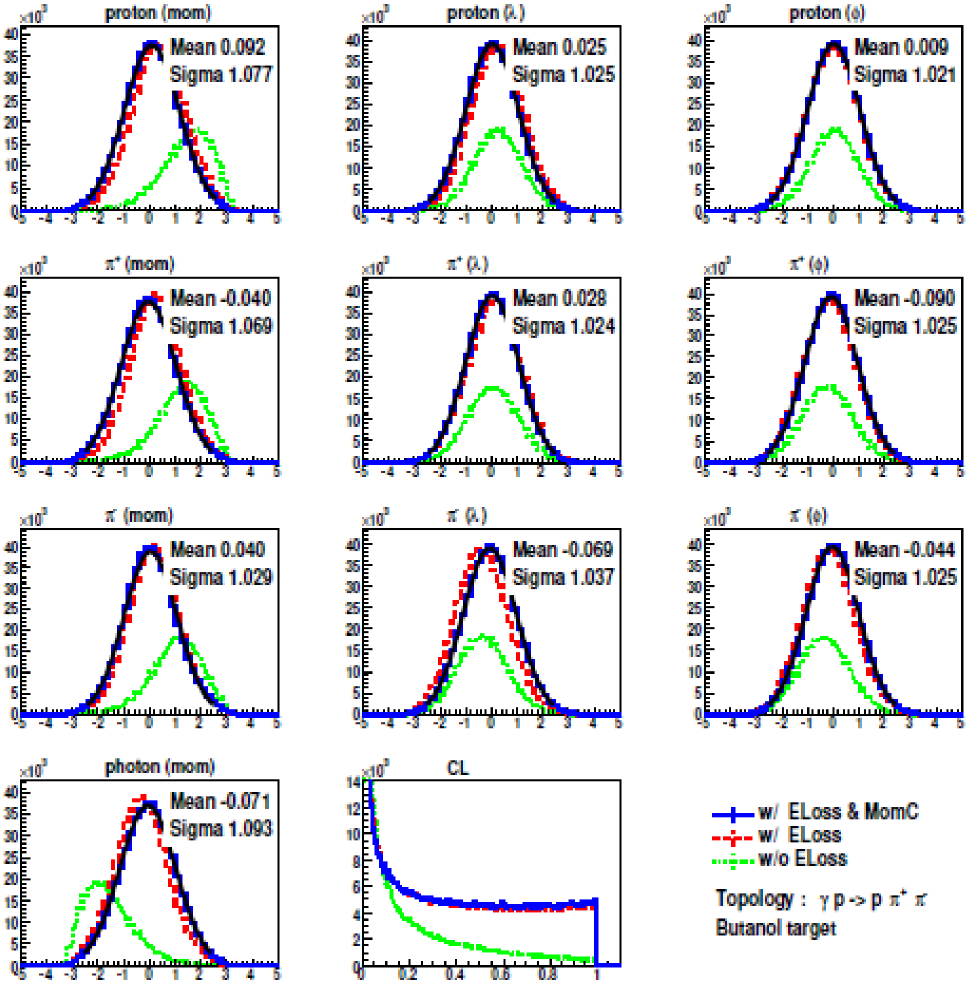

Figure 3.9: Example of $g9a$ pull and confidence level distributions from runs 55630-55678 of the butanol target [36]. The green line was made from the raw data without applying any corrections. The red lines was obtained after the Eloss package was applied. Finally, the red lines were obtained by applying the momentum correction. The black lines represent Gaussian fit to the data.

3.6.2 Enery-Loss (ELoss) Correction

As charged particles traveled from the production vertex to the active components of the CLAS spectrometer, they lost energy through inelastic scattering, atomic excitation or ionization when interacting with the target, target walls, support structures, beam pipe, Start Counter, and the air gap between the Start Counter and the Region 1 Drift Chambers. Therefore, the momentum reconstructed from the drift chambers was smaller than the momentum of the particle at the production vertex. To account and correct for this, the 4-vectors of the final-state particles were modified event-by-event using the "ELoss" package, which was developed for charged particles moving through CLAS [51]. This ELoss package determined the lost momentum of each particle in the materials it had interacted with. In this procedure, the particle's 4-momentum – as measured by the Region 1 Drift Chambers – was used to track the particle back to the reaction vertex in the target cell. The energy loss was then calculated based on the distance and the materials it traversed. The corresponding 4-vector was corrected by multiplying an ELoss correction factor to the magnitude of the momentum:

$$P_{\text{particle (ELoss)}} = \eta_{\text{particle}} \cdot P_{\text{particle (CLAS)}} \tag{3.11}$$

where $P_{x\,\text{(ELoss)}}$ is the momentum of the particle x after applying the energy-loss correction, $P_{x\,\text{(CLAS)}}$ is the raw momentum measured in CLAS and x is either the proton, π^+, or π^-. The parameters η_p, η_{π^+}, and η_{π^-} are the ELoss correction factors which modified the momentum by a few MeV, on average.

3.6.3 Momentum Corrections

The CLAS-g12 experimental setup was not absolutely perfect. For this reason, corrections of a few MeV had to be determined and applied to the final-state particles' momenta to account for unknown variations in the CLAS magnetic field (Torus Magnet) as well as inefficiencies and misalignments of the drift chambers. As a matter of fact, the momenta of the tracks as measured by the drift chambers exhibited a systematic shift within each sector as a function of the azimuthal angle ϕ of one of the tracks [46]. In our analyses, we have followed the CLAS-approved procedure outlined in Ref. [46].

The initial momentum corrections for the proton and the π^+ were determined by the group at Arizona State University (ASU) based on the single-track reactions $\gamma p \to pX$ and $\gamma p \to \pi^+ X$, respectively. The proton and π^+ momenta were then corrected such that the X-peak position did not show any ϕ-angle dependence. These corrections were then verified with the kinematic fitter by observing the quality of the pull distributions before and after applying the momentum corrections. All data sets were then fine-tuned and momentum corrections were also determined for the π^-. In a first step, we studied the momentum distributions of each final state particle and binned the data in five momentum ranges. In a second step, the kinematic fitting for the reaction $\gamma p \to p\,\pi^+\pi^-$ was performed and the pull distributions for different momentum bins were evaluated. The fine-tuning goal was to obtain pull fistributions which were Gaussiang in shape with a mean value = 0.

Some example distributions showing the effect of the momentum corrections on removing the ϕ-angle dependence are shown in Figure 3.10 and 3.11. Figure 3.10 shows the missing-mass (the π^- in the reaction $\gamma p \rightarrow p\pi^+X$) dependence on the ϕ angle for FROST data before and after the corrections.

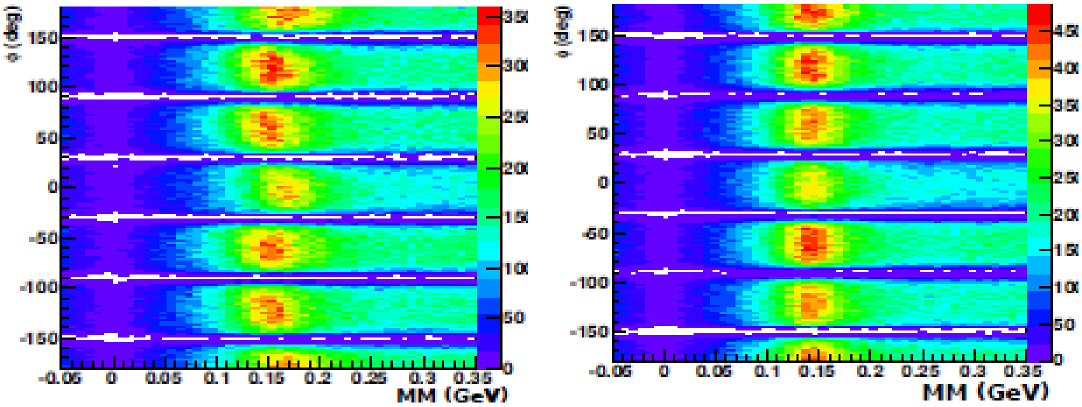

Figure 3.10: Azimuthal dependence of the missing mass X in the reaction $\gamma p \rightarrow p\pi^+X$ before (left) and after (right) the momentum corrections. The data shown are from the $g9b$ data set for $1.3 < E_\gamma < 1.4$ GeV [35].

The ”transverse momentum balance” plots shown in figure 3.11 describe an example of the effect of momentum corrections for π^+ from the $g12$ data. The transfer momentum balance for a given particle is defined as the sum of the momentum of other particles projected onto the line that is perpendicular to the beam having the same ϕ angle as the given particle minus its momentum transverse to the beam.

3.6.4 Bad or Malfunctioning Time-of-Flight Paddles

Some TOF paddles of the CLAS spectrometer were dead or malfunctioning during the $g9a$ and $g12$ experiments. The timing resolution of each paddle was investigated on a run-by-run basis to determine the stability throughout the experiment. Reference [46] contains the results of an extensive study on bad TOF paddles in CLAS-g12. The list of identified bad paddles recommended

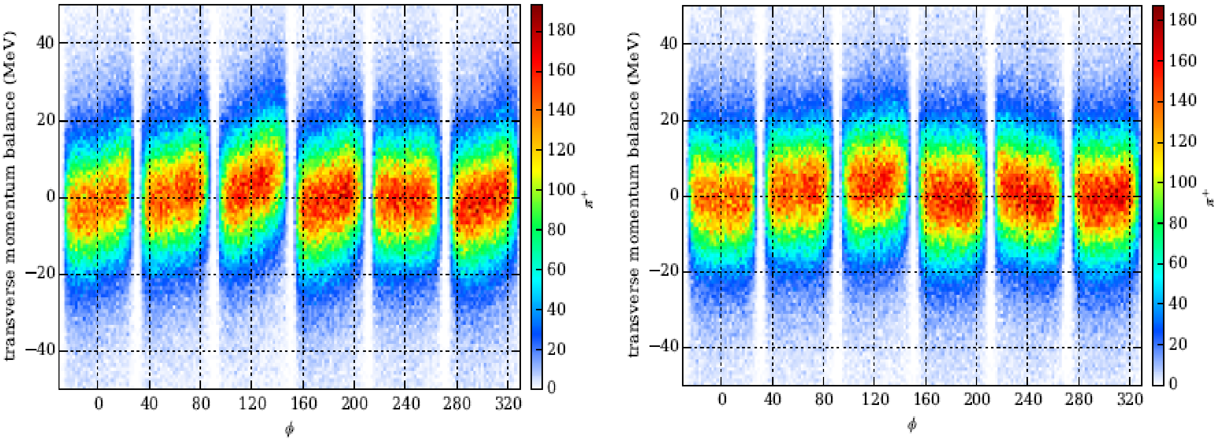

Figure 3.11: The transverse momentum balance of exclusive $p\pi^+\pi^-$ $g12$ events as a function of azimuthal angle ϕ before (left) and after (right) momentum corrections for π^+ track [46].

to knock out was taken directly from Table 19 of Ref. [46] and is also given in Table 3.3 for convenience.

Table 3.3: The list of bad time-of-flight paddles recommended to knock out [46].

Sector Number	Bad TOF Paddles in CLAS-g12
1	6, 25, 26, 35, 40, 41, 50, 56
2	2, 8, 18, 25, 27, 34, 35, 41, 44, 50, 54, 56
3	1, 11, 18, 32, 35, 40, 41, 56
4	8, 19, 41, 48
5	48
6	1, 5, 24, 33, 56

However, in this analysis we did not remove the bad paddles for the $g9a$ data because the final observables were extracted from the $g9a$ data by performing asymmetries in which the effect of the bad paddles canceled out in the ratios.

3.7 Monte Carlo Simulations for the $g12$ Experiment

To extract the differential cross sections for the reactions (1) $\gamma p \to p\,\omega$, and (2) $\gamma p \to K^0\,\Sigma^+$ from the $g12$ data, we needed to apply detector-acceptance corrections, where the latter accounted for the probability that an event of certain kinematics would be detected and recorded (also called efficiency corrections). This efficiency corrections were not required in the extraction of polarization observables from $g9a$ data since the detector acceptance effects canceled out in the ratios when the asymmetries were performed.

The performance of the detector was simulated in GEANT3 - based Monte-Carlo studies. We followed the steps outlined in Ref. [46] for generating events, digitization and smearing, as well as reconstruction.

The generated raw events were processed by GSIM to simulate the detector acceptance for each propagated track from the event vertex through the GEANT3-modeled CLAS detector. The CLAS smearing package known as GPP then processed the output to reflect the resolution of the detector. Finally, the A1C package was used to perform the *cooking*. We generated a total of 175 million $\gamma p \to p\,\omega \to p\,\pi^+\pi^-\pi^0$ phase-space events for the whole range of incident-photon energies, i.e. $1.1 < E_\gamma < 5.4$ GeV. We have also generated 11 million $\gamma p \to p\,\eta \to p\,\pi^+\pi^-\pi^0$ and 40 million $\gamma p \to K^0\,\Sigma^+ \to p\,\pi^+\pi^-\pi^0$ Monte Carlo events. To guarantee phase-space (generated) events which are flat in $\cos\theta^{\text{meson}}_{\text{c.m.}}$, we chose a t-slope of *zero.*

In this section, we show the quality of the simulated events by comparing various data distributions with Monte Carlo events:

1. In the CLAS-g12 experiment, the 40-cm-long liquid-hydrogen target was pulled upstream by 90 cm from the center of the CLAS detector. Figure 3.12 compares the z-vertex distribution for data and Monte Carlo events after applying our cut of $-110 < z$ vertex < -70 cm: $\gamma p \to p\,\omega$ (left) and $\gamma p \to K_S\,\Sigma^+$ (right). This figure shows that the vertex distribution is very well modeled.

2. Figure 3.13 and 3.14 shows the distributions of ϕ (azimuthal angle) and θ (polar angle) for the proton (top) and for the π^+ (bottom). The data and Monte Carlo distributions match well for the azimuthal angles of the proton and the π^+ as well as for the polar angle of the pion. However, the MC polar angle of the proton, θ_p, does not agree very well with the data. This is reasonable because our Monte Carlo events do not contain any reaction dynamics (simple generation of phase space events), but the distribution covers the same polar-angle range.

3. We also checked all the signal distributions (peaks for ω, η, and K_S) to see if our Monte Carlo mass resolution matches the real detector resolution. Figure 3.15 shows invariant-mass distributions for both data (black line) and Monte Carlo (red line) events. Since the mass resolution is slightly energy dependent, we compare data and Monte Carlo for $E_\gamma < 3$ GeV (left) and $E_\gamma > 3$ GeV (right). It is observed in this figure that the MC resolution is in reasonable agreement with the actual detector resolution.

Table 3.4: The detector resolutions for various channels for both data and Monte Carlo simulations.

Reaction	Resolution (Gaussian σ in [MeV])			
	Low Energy		High Energy	
	Data	MC	Data	MC
$\gamma p \to p\,\omega$	7.68	7.98	12.0	12.0
$\gamma p \to p\,\eta$	6.5	6.9	7.2	7.1
$\gamma p \to K_S\,\Sigma^+$	K_S Peak		Σ Peak	
	5.4	4.4	6.5	6.2

4. Figure 3.16 shows the distributions for the $\cos\theta^{\pi^-}_{\mathrm{c.m.}}$ versus z vertex for $\gamma p \to p\,\omega$ data and

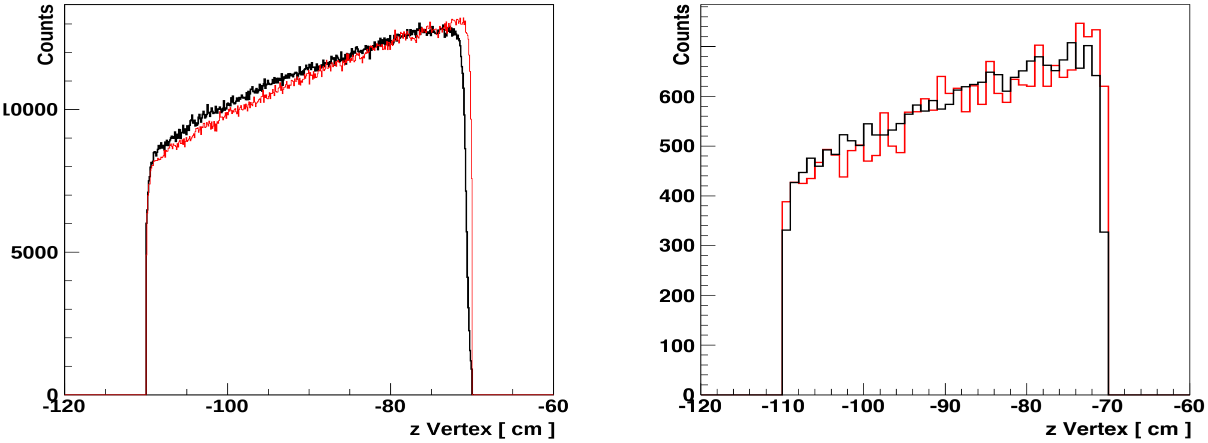

Figure 3.12: Left: The z-vertex distribution of $\gamma p \to p\,\omega$ events. The black line denotes the data, the read line denotes the Monte Carlo distribution; good agreement is observed. These figures were made using the full data statistics of 4.4 million events and an equal amount of Monte Carlo events after applying our z-vertex cut of $-110 < z < -70$ cm. Right: The z-vertex distribution of $\gamma p \to K_S\,\Sigma^+$ events.

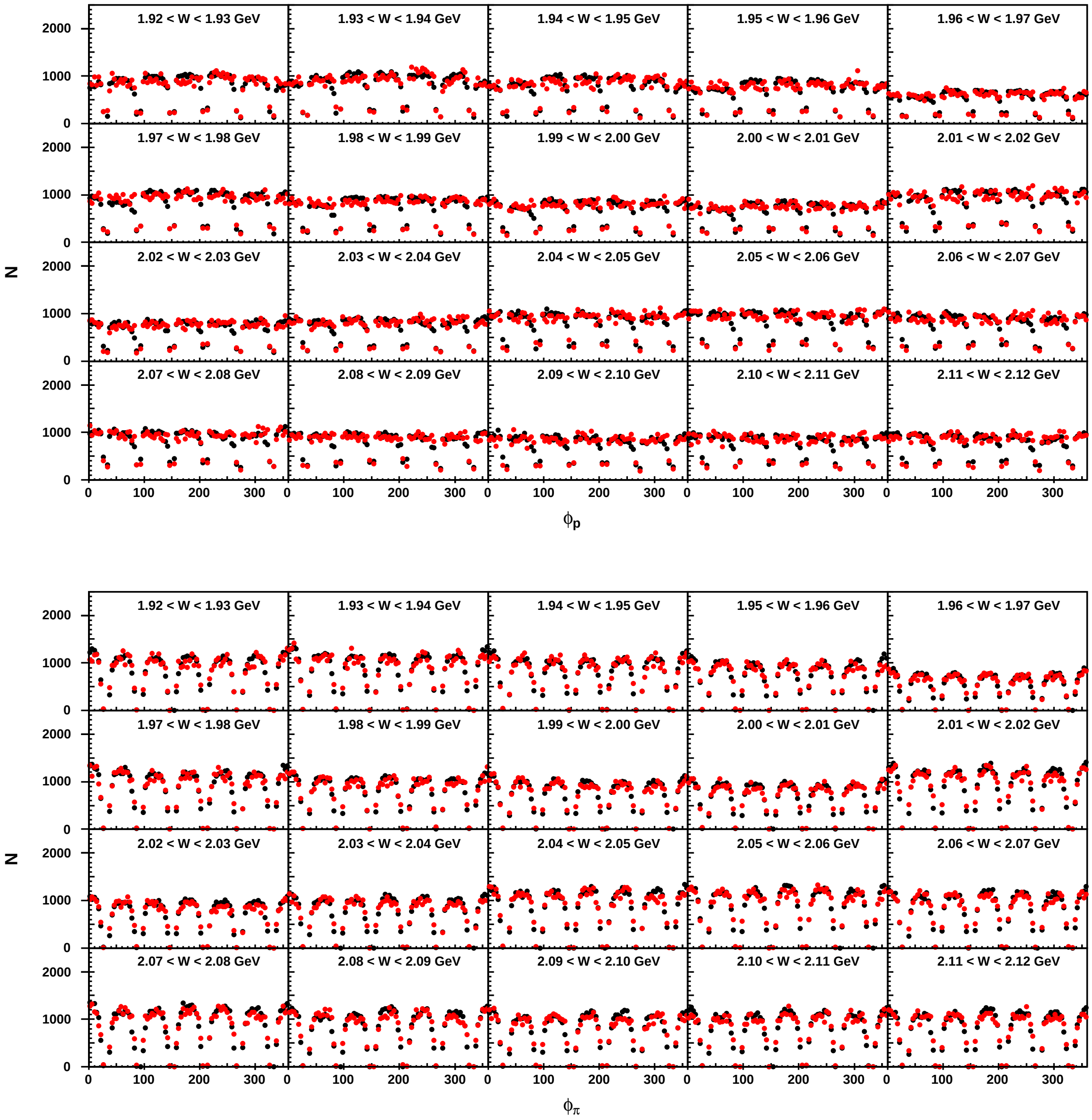

Figure 3.13: The azimuthal (ϕ) angle distributions of the proton (top row) and of the π^+ (bottom row) in the reaction $\gamma p \to p\,\omega$ for data (black line) and Monte Carlo events (red line). These figures were made using the full data statistics of 4.4 million events and the same number of Monte Carlo events. The ϕ_{π^+} and ϕ_p distributions are in very good agreement.

Monte Carlo events; the distributions are almost identical. In the very backward region of the target, an angle range of only about $-0.6 < cos\,\theta^{\pi^-}_{c.m.} < 0.8$ is covered, whereas $-0.8 < cos\,\theta^{\pi^-}_{c.m.} < 0.8$ is covered in the very forward region.

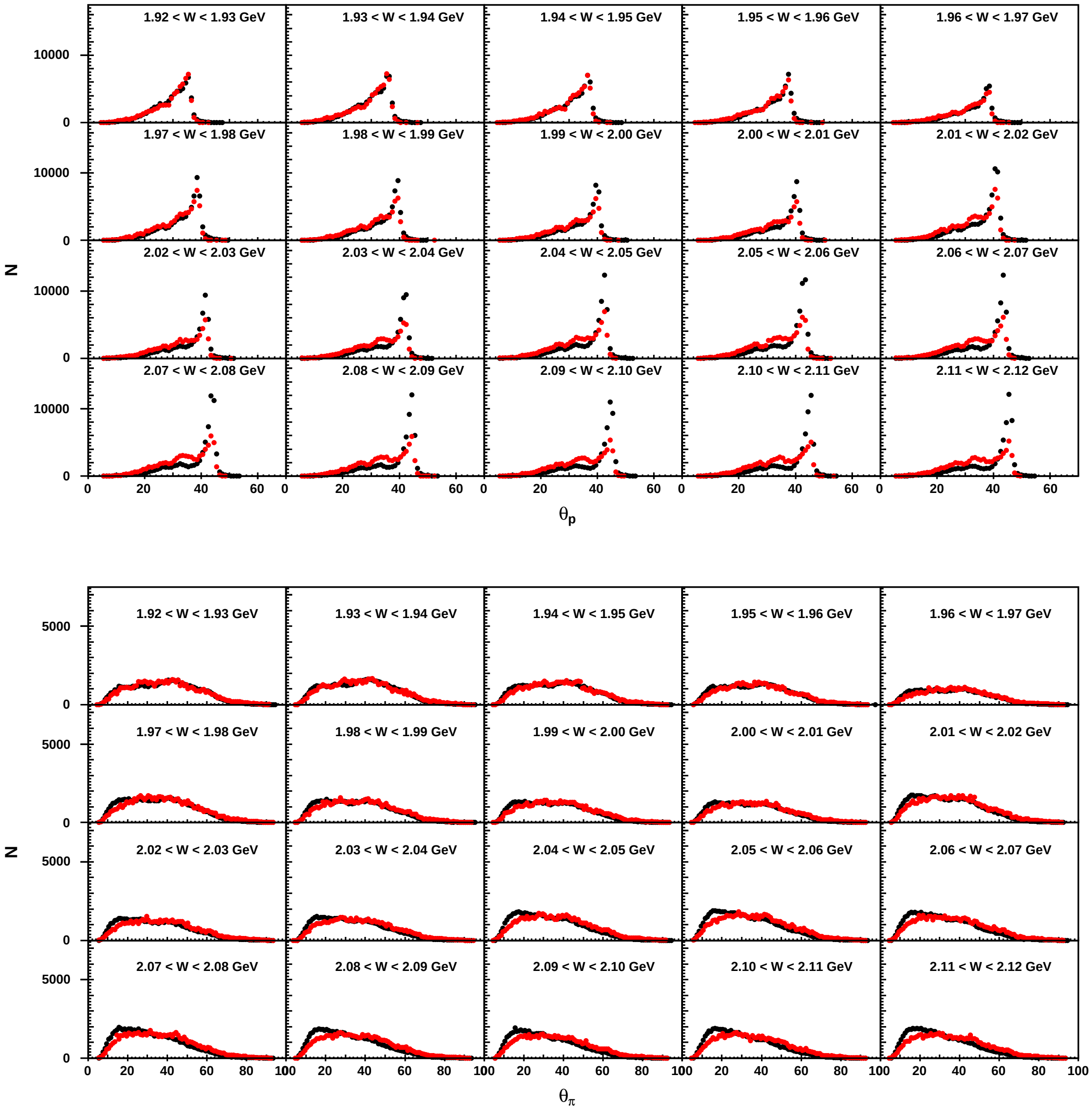

Figure 3.14: The polar (θ) angle distributions of the proton (top row) and of the π^+ (bottom row) in the reaction $\gamma p \to p\,\omega$ for data (black line) and Monte Carlo events (red line). These figures were made using the full data statistics of 4.4 million events and the same number of Monte Carlo events. The θ_{π^+} distributions are in very good agreement.

5. The quality of the kinematic fitting for the Monte Carlo events is shown in the pull and confidence-level (CL) distributions for the reaction $\gamma p \to p\pi^+\pi^-$ (Fig. 3.18) and for the reaction $\gamma p \to p\,\omega \to p\pi^+\pi^-\pi^0$ (Fig. 3.19). A summary of the mean and σ values is given

Table 3.5: Final mean ($\bar{x}$) and σ values of Gaussian fits to our g12 pull distributions after applying all corrections. Note that the values for $p\,\pi^+\pi^-\,(\pi^0)$ are based on distributions which cannot be perfect Gaussians owing to the missing-particle hypothesis.

	proton			π^+			π^-			γ
	mom.	λ	ϕ	mom.	λ	ϕ	mom.	λ	ϕ	E

Monte Carlo: $\gamma p \to p\,\pi^+\pi^-$

$\bar{x}$	0.023	0.003	0.042	0.053	−0.002	0.041	0.053	0.004	0.040	−0.056
σ	1.117	1.045	1.010	1.017	1.028	0.997	1.018	1.048	0.994	1.102

Monte Carlo: $\gamma p \to p\,\pi^+\pi^-\,(\pi^0)$

$\bar{x}$	0.040	0.018	0.024	0.027	0.000	0.024	0.022	0.004	0.030	−0.052
σ	1.078	1.054	1.081	1.045	1.056	1.015	1.055	1.056	1.004	1.086

in Table 3.5. Recall that each of these distributions should have a mean of *zero* and width of *one.* The agreement of the extracted values with these ideal values is very good. The CL distributions are flat toward *one.*

To further check the quality of the confidence levels in all kinematic regions, we considered the normalized slope of the distribution:

$$\bar{a} = \frac{a}{a/2 + b}, \tag{3.12}$$

where a is the slope and b is the intercept obtained by fitting the confidence-level distribution to a linear function. Figure 3.17 shows examples of confidence-level distributions and their respective normalized slopes. If the errors are overestimated (underestimated), then the confidence-level distribution will have a positive (negative) slope. In line with the procedure outlined in Ref. [54], we would consider the covariance matrix to be acceptable if all kinematic regions yielded normalized slopes in the range $[-0.5, 0.5]$. Figure 3.20 shows the normalized slopes extracted in $(p, \cos\theta)$ bins for the proton and the π^-. Notice that all kinematic regions (excluding edge bins with low statistics) have $|\bar{a}| < 0.5$. Thus, we conclude that the covariance matrix is acceptable.

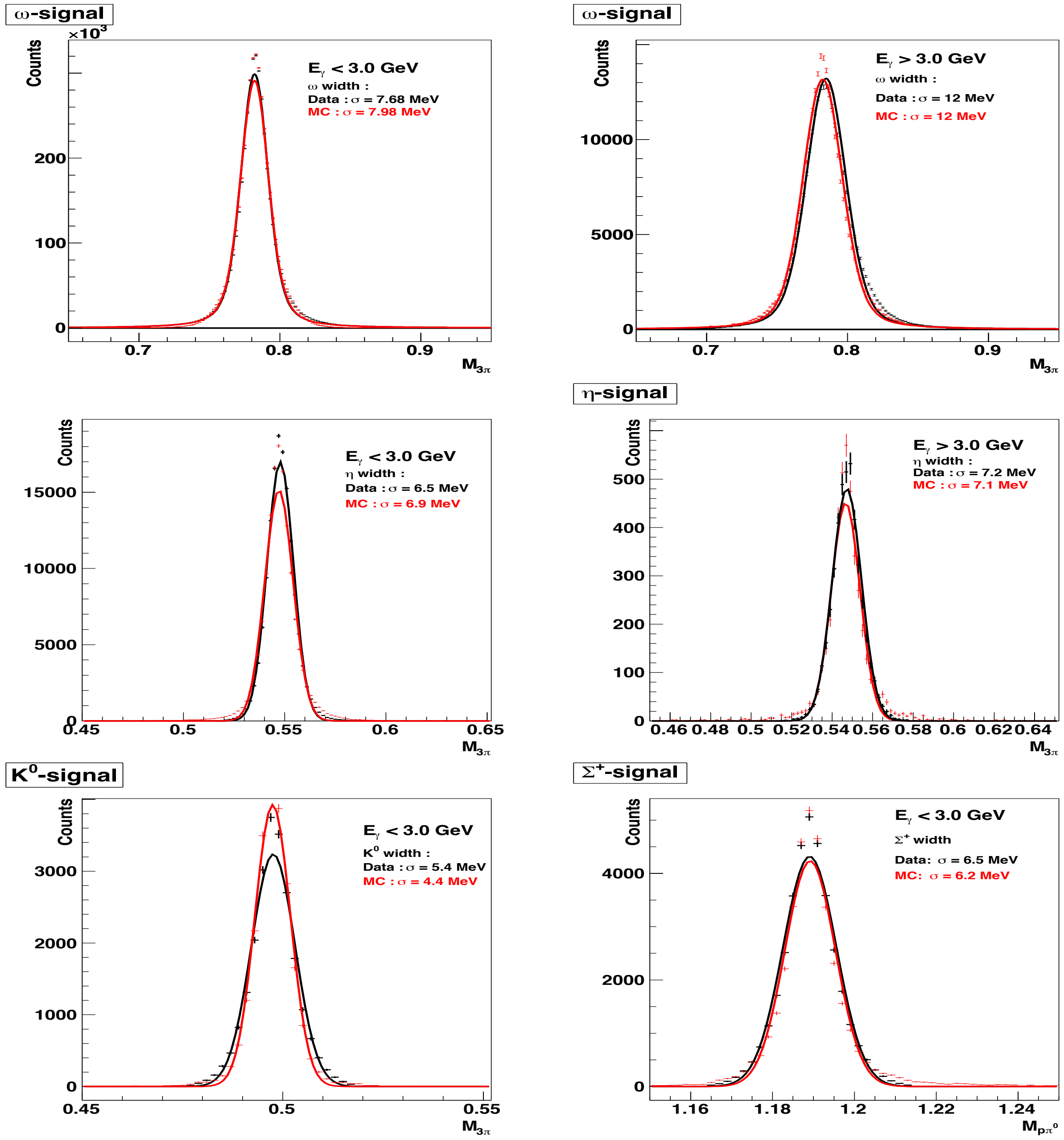

Figure 3.15: Invariant mass (signal) distributions for data (black line) and Monte Carlo (red line). The left distributions are for $E_\gamma < 3.0$ GeV, the right distibutions are for $E_\gamma > 3.0$ GeV. Top row: The $M_{\pi^+\pi^-\pi^0}$ distribution showing the ω meson. Middle row: The $M_{\pi^+\pi^-\pi^0}$ distribution showing the η meson. Bottom row: The $M_{\pi^+\pi^-}$ distribution showing the K_S signal (left) and the $M_{p\pi^0}$ distribution showing the Σ signal (right). The overall agreement between the data and Monte Carlo distributions indicates that the GEANT simulations model the resolution of the actual detector reasonably well.

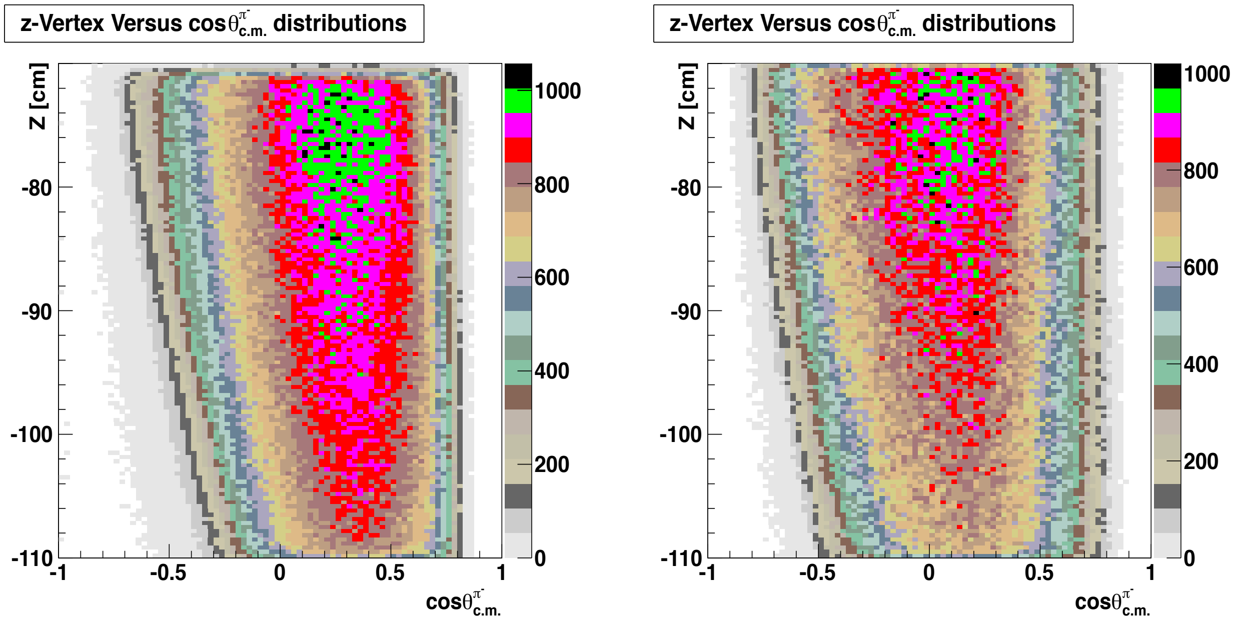

Figure 3.16: The z-vertex vs. $\cos\theta^{\pi^-}_{c.m.}$ distributions using a logarithmic color scale for data (left) and Monte Carlo events (right); the distributions are very similar. In the very backward region of the target, an angle range of only about $-0.6 < cos\,\theta^{\pi^-}_{c.m.} < 0.8$ is covered, whereas $-0.8 < cos\,\theta^{\pi^-}_{c.m.} < 0.8$ is covered in the very forward region.

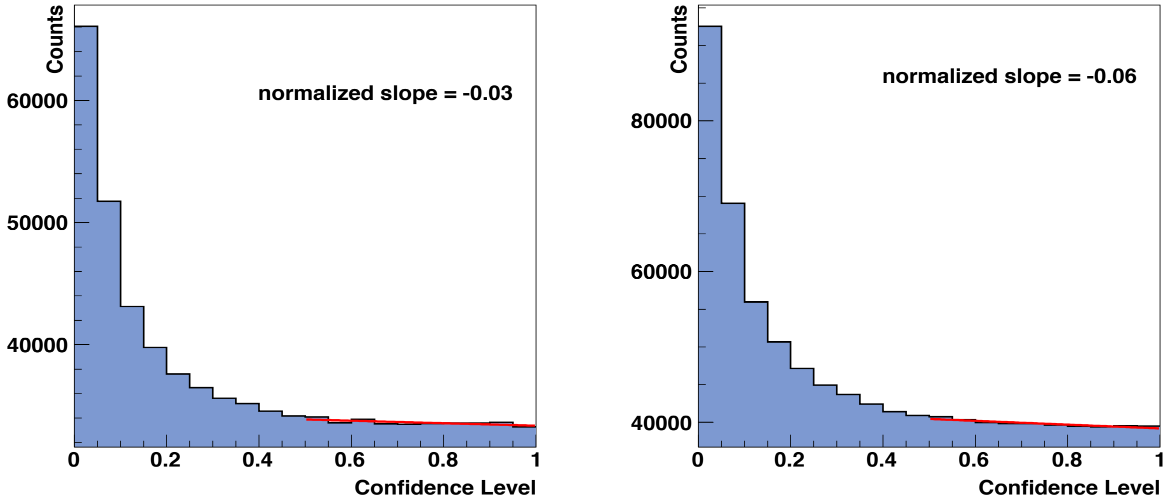

Figure 3.17: Examples of normalized slopes from confidence-level distributions for the proton (left) and for the π^- (right): Normalized slopes have been extracted by fitting the distributions in the range (0.5, 1) to a linear function.

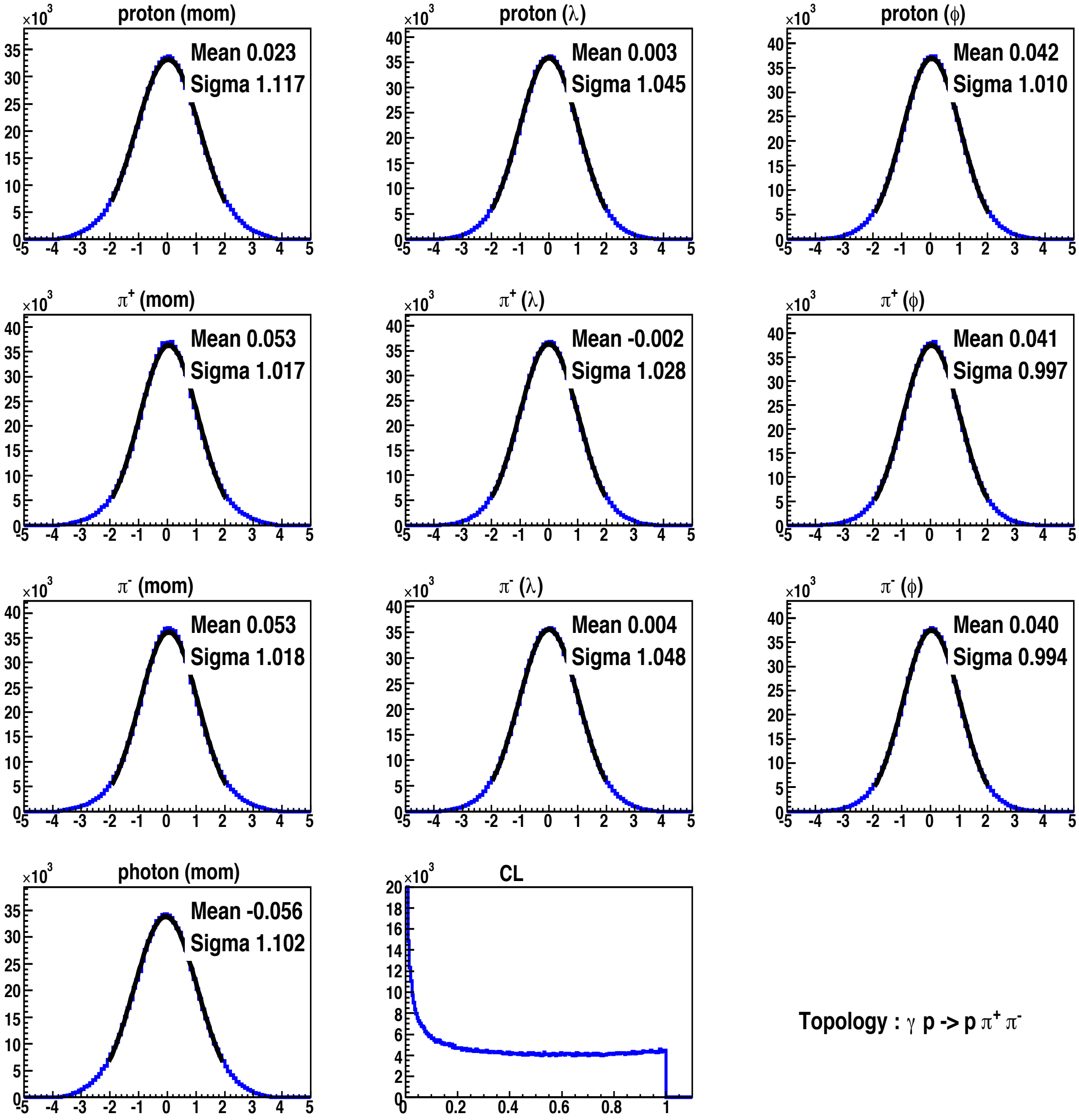

Figure 3.18: Monte Carlo (reaction: $\gamma p \to p\,\pi^+\pi^-$) pull and confidence-level distributions for the four-constraint fit to $p\,\pi^+\pi^-$ (check for energy and momentum conservation, no mass constraint) along with the mean and σ values of the fits. A summary of the mean and σ values of these fits (for data and Monte Carlo) can also be found in Table 3.5.

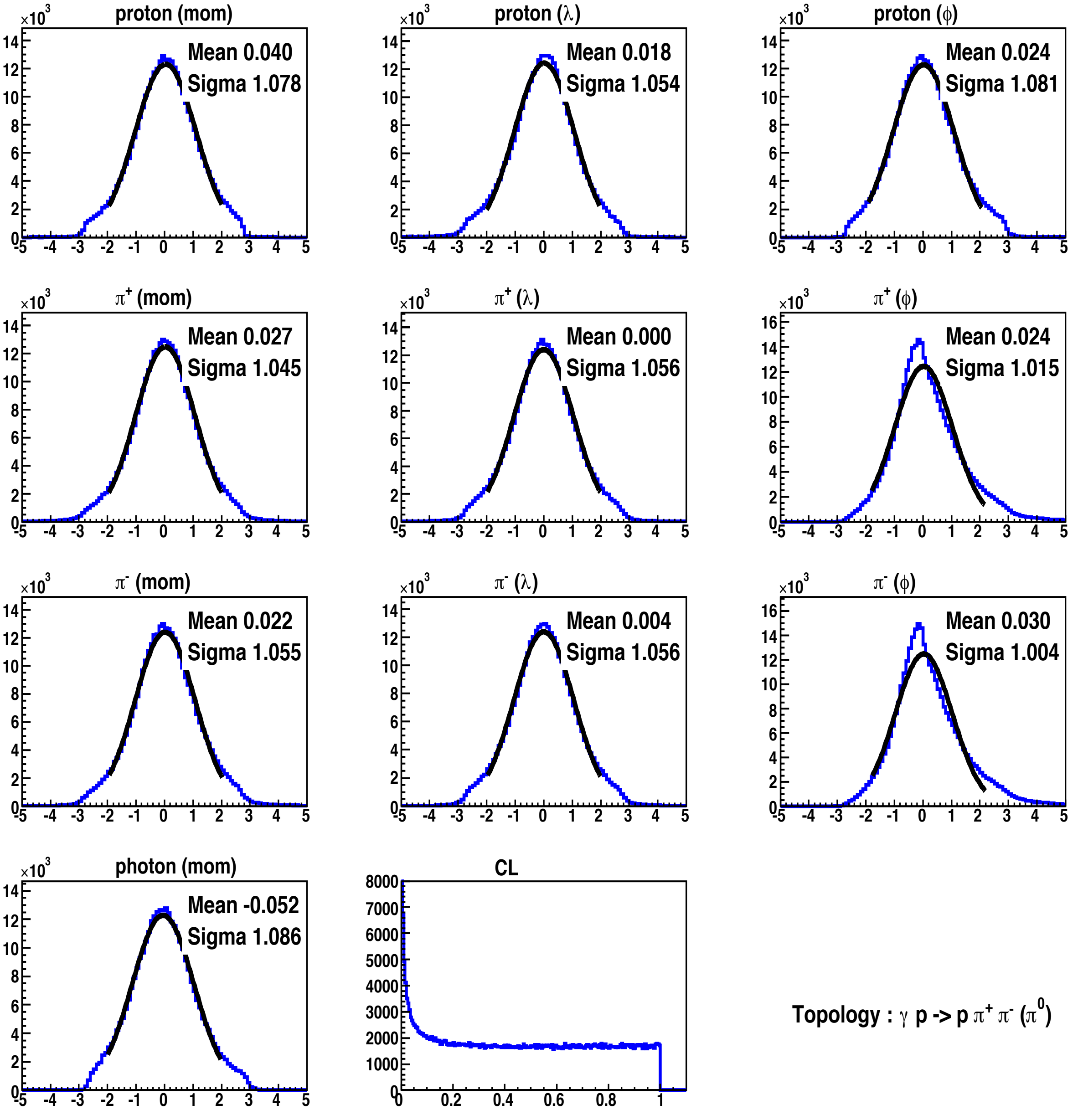

Figure 3.19: Monte Carlo (reaction: $\gamma p \to p\,\omega \to p\,\pi^+\pi^-\pi^0$) pull and confidence-level distributions for the one-constraint fit to $p\,\pi^+\pi^-$ (π^0) (no ω-mass constraint) along with the mean and σ values of the fits. Note that the pull distributions are not Gaussian over the full range owing to the missing-particle hypothesis. A summary of the mean and values of these fits (for data and Monte Carlo) can also be found in Table 3.5.

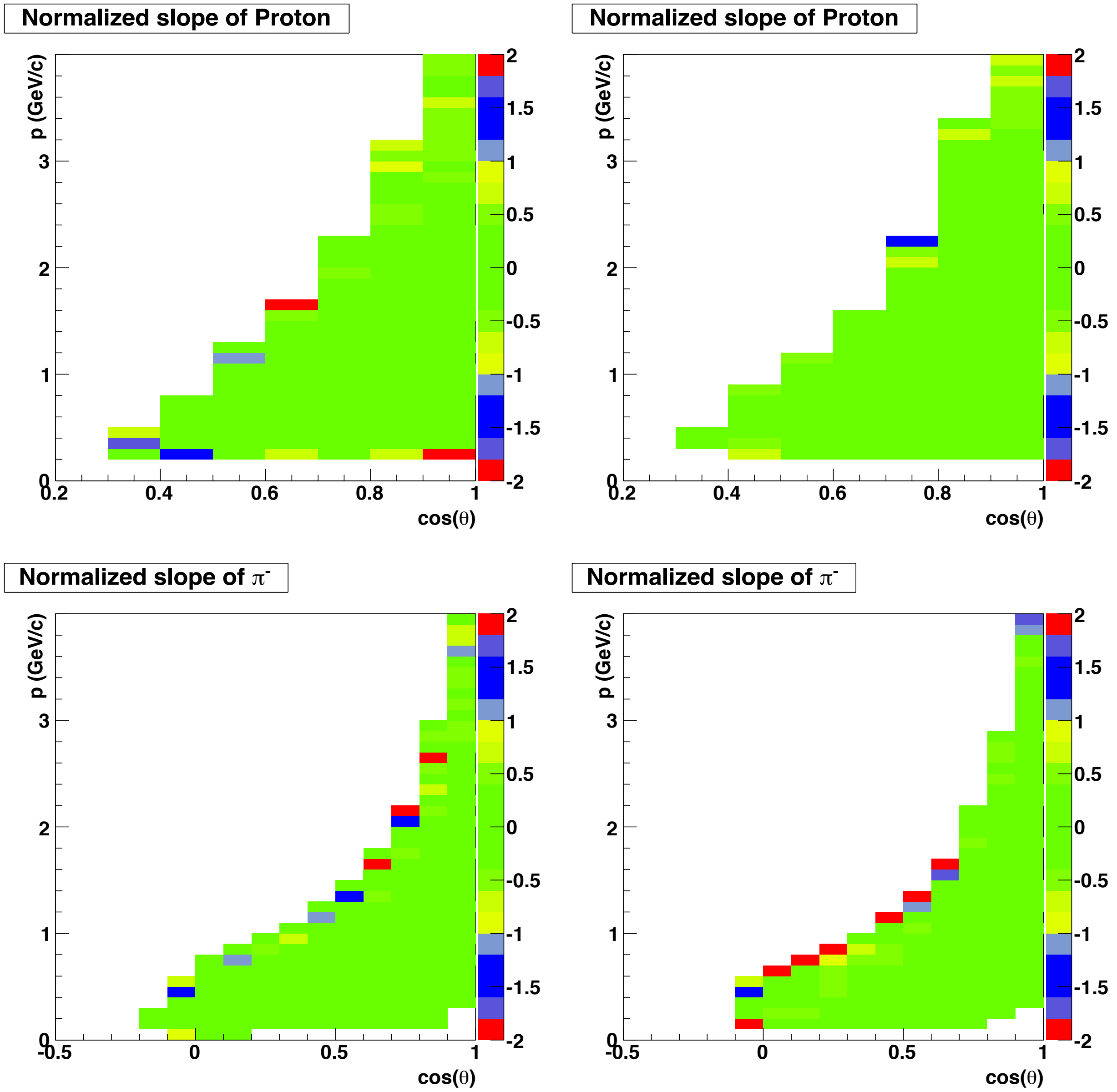

Figure 3.20: Confidence-level checks. Normalized confidence-level slopes presented in $\cos\theta$ versus p [GeV/c] distributions for the proton (top row) and for the π^- (bottom row). The results for the g12-data are shown on the left and for Monte Carlo on the right. Notice that - excluding edge bins with low statistics - all kinematic regions have $|\bar{a}| < 0.5$.

3.7.1 Trigger Simulation

To simulate the trigger conditions for our $g12$ data, we used the same technique that was developed for the measurement of the ω and η cross sections in the CLAS-$g11a$ experiment [25, 53]. The procedure is outlined in Ref. [58]. This technique used the *trigger word* or *trigger bit*, which was written into the BOS data during the cooking. The trigger conditions for the data that we used are described in section 2.1. In summary, the recorded events had:

1. Either three charged time-of-flight hits in three different sectors (three-sector events),
2. Or two hits in different sectors (two-sector events), in combination with at least one photon in the beam bucket whose energy was above 3.6 GeV. The term "beam bucket" refers to all photons that were detected during the life time of the trigger (detector).

Therefore, to simulate the trigger conditions in the Monte Carlo events, two pieces of information were needed:

1. The efficiency of the trigger as a function of particle type, momentum, and detector position (trigger efficiency map).
2. The probability for having at least one photon with $E_\gamma > 3.6$ GeV (two-sector events).

(1) The trigger efficiency map was derived using $\gamma p \to p\,\pi^+\pi^-$ events and required all three tracks to be detected in three different sectors. If the trigger were 100 % efficient, then all three detected particles would also be recorded in the trigger word, i.e. contributed to the trigger decision. However, if the trigger were not 100 %, an event with three charged tracks would still be reconstructed, although one of the tracks would not fire the trigger (and be recorded in the trigger word). Therefore, it was possible to build a map of the trigger efficiency for each particle type as a function of sector, time-of-flight paddle, and azimuthal angle. The trigger efficiency map for the π^-, π^+, and the proton are shown in Fig. 3.23, 3.24, and 3.25.

(2) The probability for two-sector events of having at least one photon with $E_\gamma > 3.6$ GeV in the beam bucket could be determined by comparing energy-dependent intensity distributions of two-sector and three-sector events. These distributions are shown in Fig. 3.21. A discontinuity at about 3.6 GeV is clearly observed in the left distribution (two-sector events) due to the additional photon-energy requirement. Further structures can be seen around 3 GeV and 4.4 GeV owing to

broken tagger scintillators. On the other hand, the right figure shows a smooth distribution for three-sector events because events were recorded independent of their photon energy.

Figure 3.22 shows the ratio of two-sector events and three-sector events. Since the physics for using an unpolarized beam is independent of the azimuthal angle, we expect the ratio to be flat. And we clearly see two flat distributions that disconnect at about 3.6 GeV. By fitting the two plateaus using a zeroth-order polynomial below and above 3.6 GeV, we concluded that the probability for two-sector events of having at least one photon with an energy above 3.6 GeV is about 0.51.

After building the efficiency map and determining the probability for having at least one photon with an energy above 3.6 GeV for two-sector events, we simulated the Monte Carlo events using the following steps:

1. The efficiency map was based on events that had all three particles in different sectors. Therefore, we cut out events if two particles ended up in the same sector (for both data and MC events).
2. For each event, we generated three random numbers between 0 and 1 for the three final-state particles, denoted by R_p, R_{π^+}, and R_{π^-}.

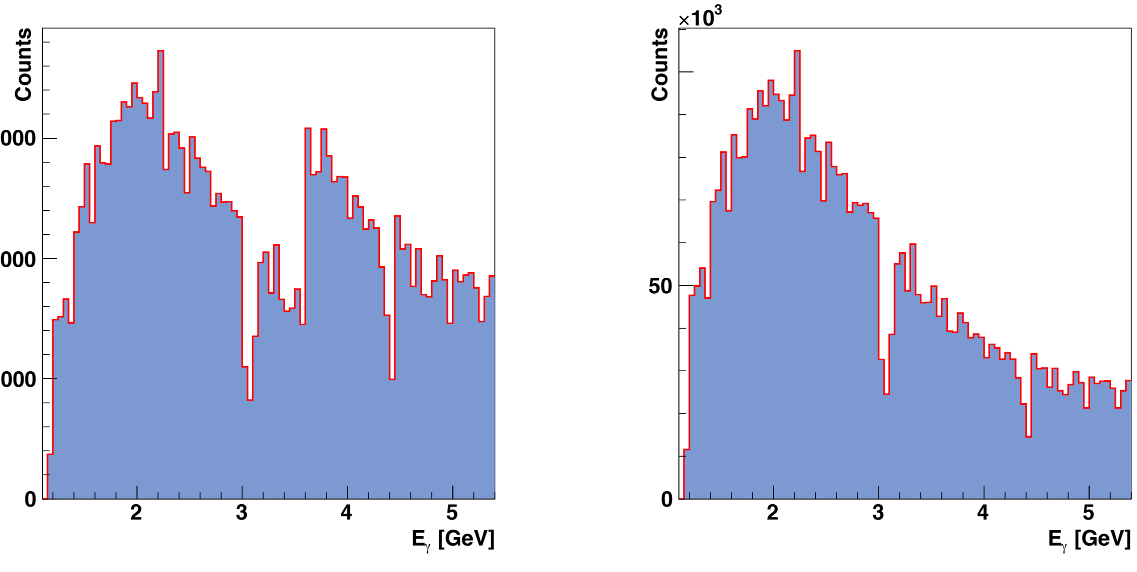

Figure 3.21: The distribution of events as a function of beam energy. The left figure shows the distribution for two-sector events. It clearly shows a discontinuity at 3.6 GeV. The right figure shows the distribution for three-sector events. The distribution is smooth since there is no additional photon-energy requirement.

(a) Denoting the trigger efficiency for each particle P_p, P_{π^+}, and P_{π^-}, then the particles were considered to fire the trigger if the generated random number were smaller than the efficiencies. For example, we considered the proton to fire the trigger if $R_p < P_p$.

(b) If all particles fired the trigger, we kept the Monte Carlo event no matter what the photon energy was.

(c) If only two particles fired the trigger and the photon energy was above 3.6 GeV, we kept the event.

(d) If only two particles fired the trigger and the photon energy was below 3.6 GeV, then we generated another random number, R_{tagger} . If $R_{\text{tagger}} < 0.51$, then we kept the event. Otherwise, if If $R_{\text{tagger}} > 0.51$, the Monte Carlo event was discarded.

3. If no particle or only one particle fired the trigger, then the Monte Carlo event was discarded.

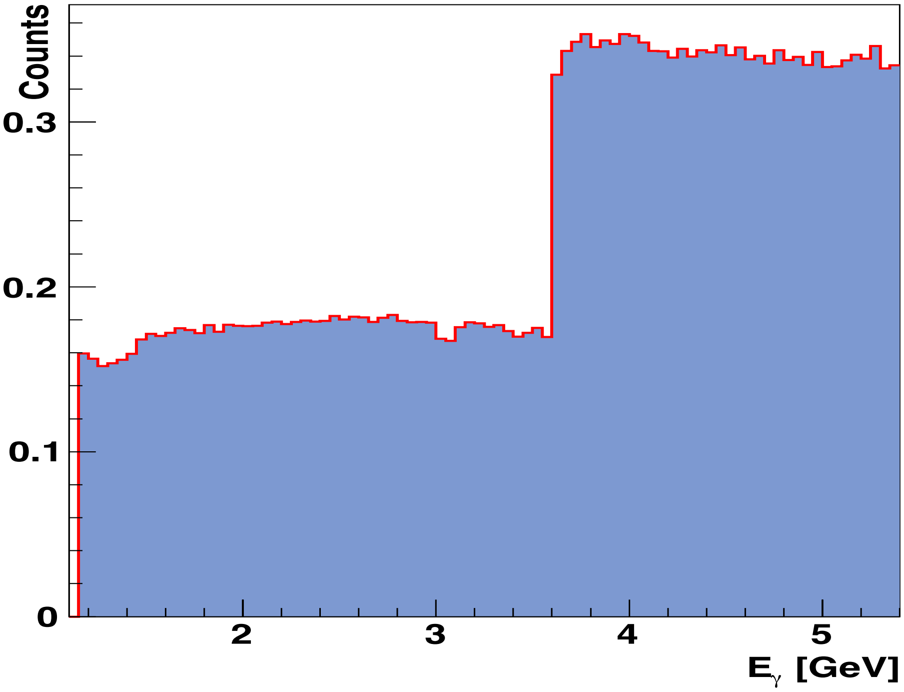

Figure 3.22: The ratio of two-sector and three-sector events. The discontinuity at 3.6 GeV is an effect of the trigger condition. The ratios are flat as expected because the physics of using an unpolarized beam must be independent of the azimuthal angle. By fitting these ratio distributions below and above 3.6 GeV, we studied the probability for tow-sector events of having at least one photon in the beam bucket with $E_\gamma > 3.6$ GeV. This probability was determined to be 0.51.

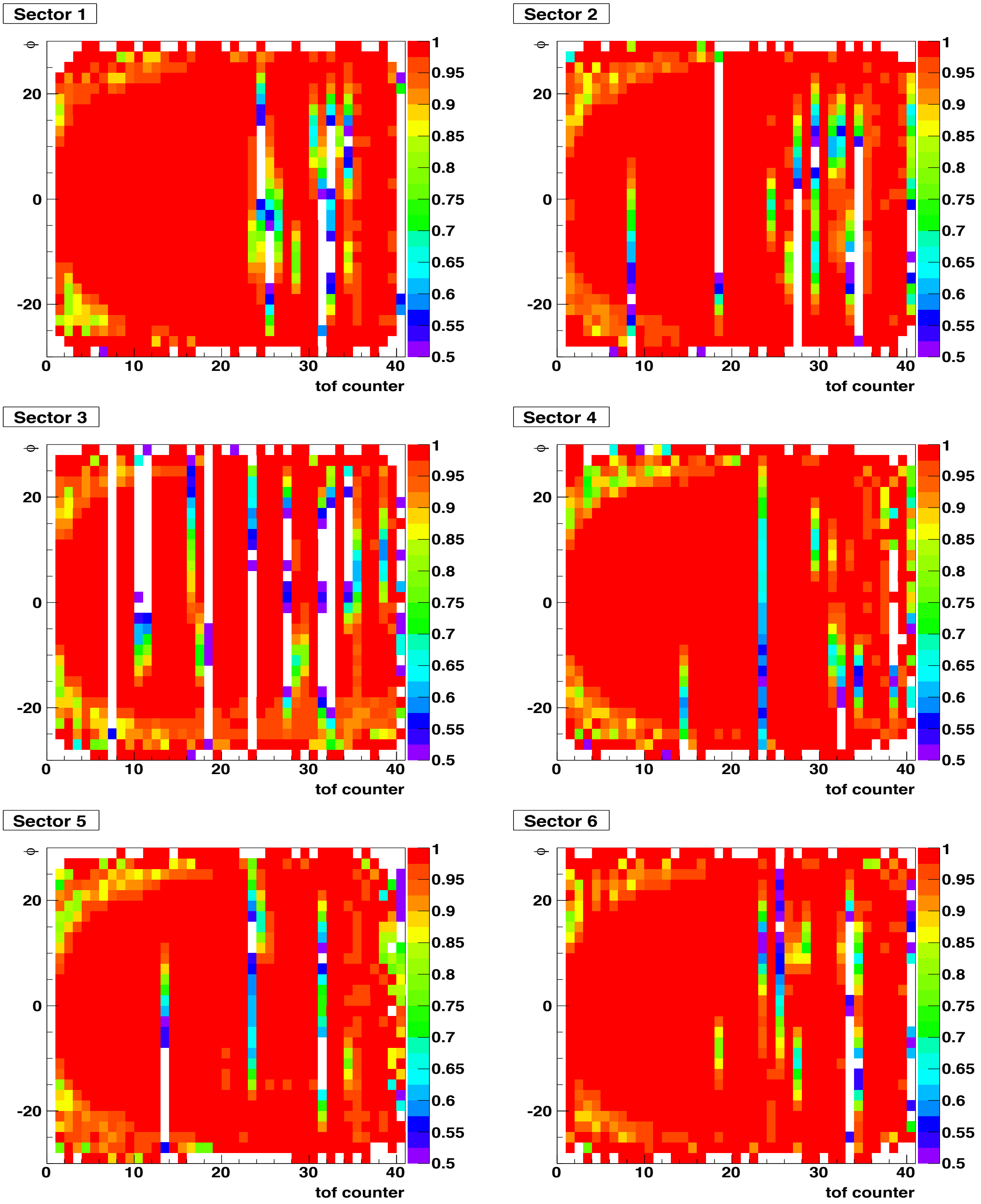

Figure 3.23: Trigger efficiency map for the π^- as a function of sector, tof-paddle number, and azimuthal angle.

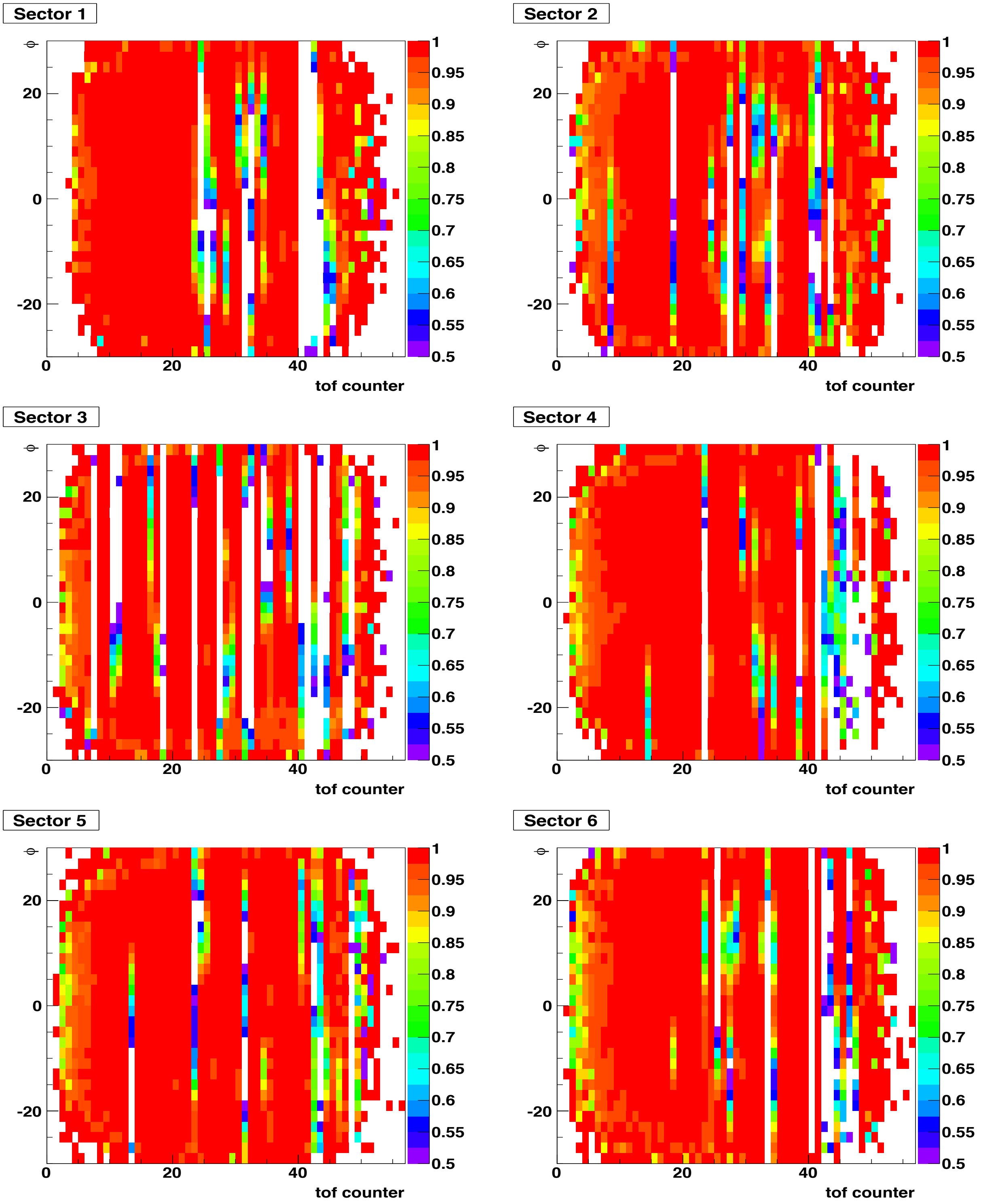

Figure 3.24: Trigger efficiency map for the π^+ as a function of sector, tof-paddle number, and azimuthal angle.

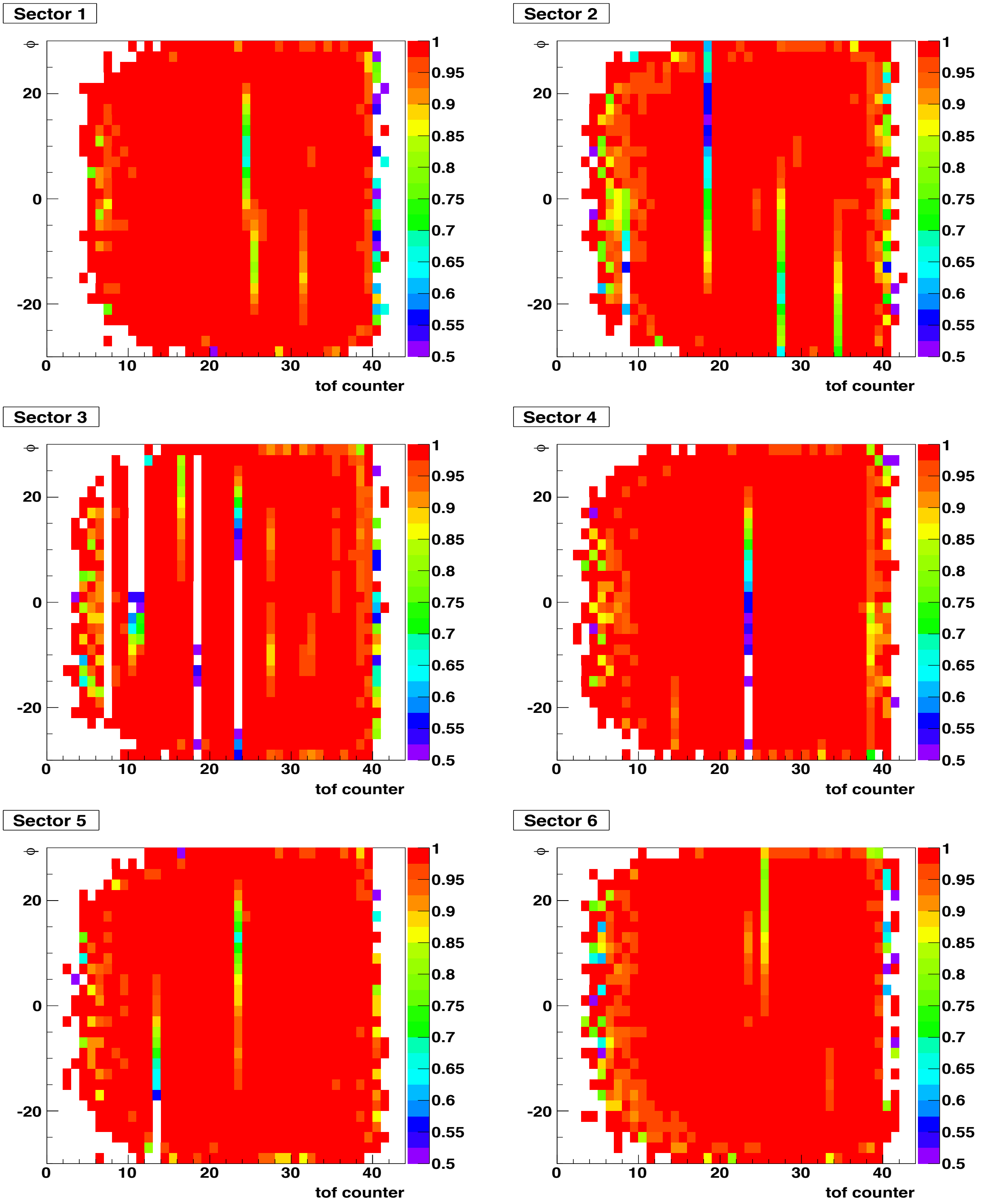

Figure 3.25: Trigger efficiency map for the proton as a function of sector, tof-paddle number, and azimuthal angle.

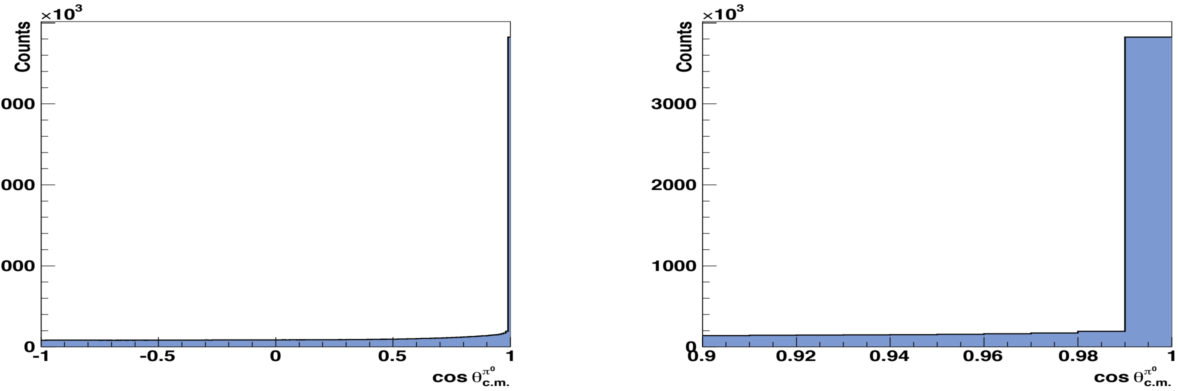

Figure 3.26: Left: The $\cos\theta^{\pi^0}_{\text{c.m.}}$ distribution of all 18 million $\gamma p \to p\,\pi^+\pi^-\,(\pi^0)$ events from the $g12$ data which passed a $p > 0.001$ CL cut. This figure shows an excess of events in the very forward region. Right: The same figure zoomed in on the forward region.

3.8 The Angular Distribution of the Undetected π^0

The channel $\gamma p \to p\,\pi^+\pi^-$ has a significantly larger cross section than $\gamma p \to p\,\pi^+\pi^-\,(\pi^0)$. This fact, coupled with the relatively small difference in the missing masses of the two channels, makes $p\,\pi^+\pi^-$ leakage into the $p\,\pi^+\pi^-\,(\pi^0)$ sample a cause for concern. In this section, we consider the possibility of $p\,\pi^+\pi^-$ leakage resulting from selecting the wrong photon.

If the incorrect photon has a higher energy than the correct one, the extra energy will create a fake π^0 that will move along the beam direction. Consider a $\gamma p \to p\,\pi^+\pi^-$ event that was produced in the detector. Our analysis procedure will attempt to reconstruct a π^0 from the missing momentum, $\vec{p}_{\text{miss}}$. Since the event produced was actually a $p\,\pi^+\pi^-$ event, the missing transverse momentum measured should be approximately zero, regardless of whether the correct photon has been found. Thus, the momentum vector of the reconstructed π^0 must point (approximately) along the beam direction: $\vec{p}_{\text{miss}} \approx \pm|\vec{p}_{\text{miss}}|\,\hat{z}$.

Therefore, we expect any leakage from the $\gamma p \to p\,\pi^+\pi^-$ channel, due to an incorrect photon selection, to result in an excess of events in the very forward direction with $\cos\theta^{\pi^0}_{\text{c.m.}} \approx +1$. Figure 3.26 clearly shows a pronounced excess of events in the very forward direction. Therefore, we cut out all events with $\cos\theta^{\pi^0}_{\text{c.m.}} > 0.99$.

3.9 Fiducial Volume Cuts

Geometric fiducial volume cuts have been applied according to the *nominal* scenario outlined in Section 5.3 of the analysis note [46]. These volumes were regions of the detector that were not well modeled and needed to be removed from the analysis. For example, the magnetic field varied rapidly close to the torus coils making these regions difficult to simulate. Thus, any particle whose trajectory was near a torus coil was identified and subsequently, the event was excluded from our analysis. The effect of this particular cut was most dramatic in the forward region, where the coils occupied a larger amount of the solid angle.

In a brief summary, such regions for all the g12 data, where the detector acceptance was well behaved and reliably reproduced in simulations, were expressed as an upper and lower limit of the difference in azimuthal angle between the center of a given sector and a particle track. Because of the hyperbolic geometry of CLAS and the presence of the toroidal magnetic field, the fiducial boundaries on ϕ were functions of momentum p, charge, and polar angle θ of each track. The boundaries were evaluated separately in each sector, nominally defined as the ϕ values in which occupancy drops below 50 % of that in the respective sector's flat region. The flat regions were defined as $-10^\circ < \phi < 10^\circ$. The nominal upper and lower ϕ limits depended strongly on particle charge, p and θ, hence the need for functional characterization and extrapolation.

In order to determine the fiducial limits for charged hadrons, a sample of exclusive $p\,\pi^+\pi^-$ events was sliced into $5 \times 15 \times 6$ bins in p, θ, and sector, respectively. The ϕ distributions for π^+ and π^- were then plotted separately in each bin. The upper and lower ϕ limits of these first-generation plots were found according to the *nominal* fiducial definition of 50 % occupancy. The results from the first-generation fits were represented in second-generation plots of ϕ_{min} and ϕ_{max} vs. θ and fit with hyperbolas, chosen since they replicate the projection of the detector. In a last step, the second-generation fitting parameters were plotted vs. p in third-generation plots. These third-generation plots were fit to power functions and the fit results defined the sought-after functional form $\phi_{\text{min}}(\theta, p)$ and $\phi_{\text{max}}(\theta, p)$ for each sector. The sector-integrated results for positive and negative hadron tracks compose the nominal fiducial region.

The fiducial volume cuts were not applied in the $g9a$ data since the effect canceled out in the ratios of the asymmetries.

3.10 Event Statistics after Applying all Cuts and Corrections

The process of developing and applying energy, momentum and other necessary corrections during the course of this analysis served the purpose of correcting for the effects of the experimental setup, therefore resulting in a data set that was as nature intended it. Additionally, determining and enforcing cuts used in the analysis served not only to remove the remaining instrumental effects of the experimental setup but also to remove the contributions from physics events not of interest to the analysis (the hadronic or electromagnetic background). Through the application of the proper vertex position, photon and particle identification variables, this background could be reduced considerably. Table 3.6 shows how many events survived after applying various cuts.

Table 3.6: The table shows the remaining statistics after various cuts. Note that Topology 4 implies kinematic fitting imposing no missing particle as well as energy and momentum conservation.

$Final\#$ of events			
$g9a$		$g12$	
$\gamma p \to p\,\omega$	$\gamma p \to K^0\,\Sigma$	$\gamma p \to p\,\omega$	$\gamma p \to K^0\,\Sigma$
62300	873	4.2 M	22890

3.11 Beam and Target Polarization

3.11.1 Circularly-Polarized Photon Beam - Degree of Polarization

The $g9a$ and $g12$ experiments used circularly-polarized photons that were produced via bremsstrahlung of longitudinally-polarized electrons from an amorphous radiator. The degree of circular polarization of these bremsstrahlung photons, $\delta_{\odot}$, could be calculated from the longitudinal polarization of the electron beam, δ_{e^-}, multiplied by a numerical factor. Using $x = E_\gamma / E_{\mathrm{e}^-}$, the degree of polarization was given by the Maximon-Olson formula [59]:

$$\delta_{\odot}(x) = \delta_{\mathrm{e}^-} \cdot \frac{4x - x^2}{4 - 4x + 3x^2}\,. \tag{3.13}$$

Figure 3.27 shows that the degree of circular polarization is roughly proportional to the photon-beam energy. In the $g12$ experiment, the electron beam (CEBAF) energy was 5.715 GeV for all the runs that we used in this analysis, while the CEBAF-energies of 1.645 GeV and 2.478 GeV were used in the *g*9*a* experiment.

The polarization of the electron beam was measured regularly using the Møller polarimeter, which makes use of the helicity-dependent nature of Møller scattering. Table 3.7 summarizes the Møller measurements of the electron-beam polarization in the *g*12 experiment, δ_{e^-}. Note that only the measurement for the second run range (56476 - 56643) was used here. During the g12 experiment, Hall B did not have priority and as a result, the polarization of the beam was delivered as a byproduct (based on the requirements of the other halls). Although the polarization fluctuated, the majority of the g12 runs had a beam polarization close to 70 % with a total uncertainty estimated to be 5 %.

For the *g*9*a* experiment, average values of 84.80 % and 83.02 % were used for the electron-beam polarization as shown in table **??**.

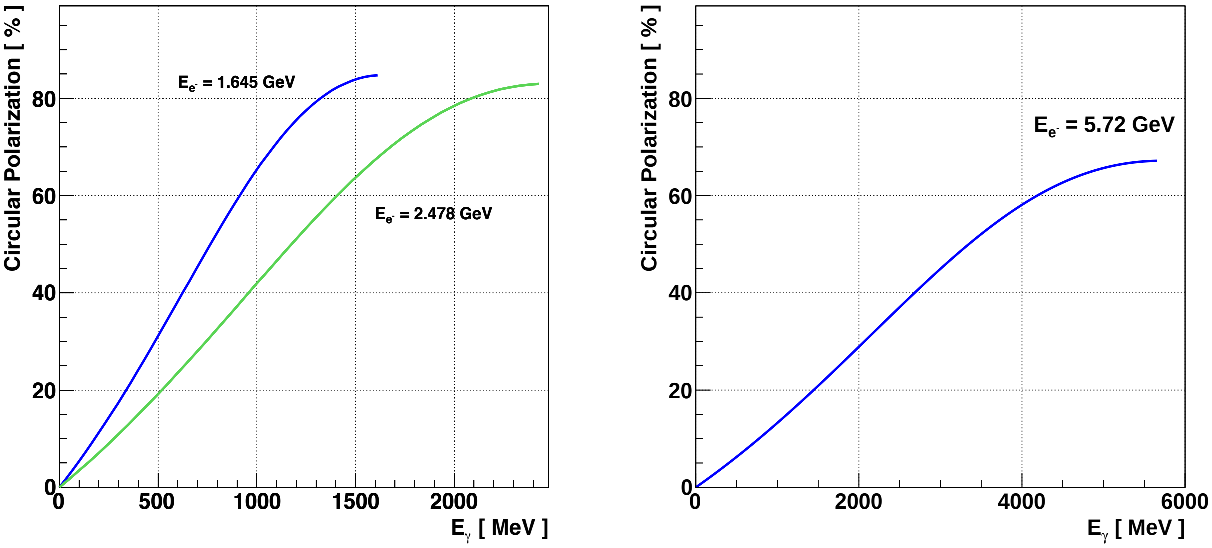

Figure 3.27: Left: Degree of circular-photon polarization as a function of incident-photon energy for the *g*9*a* experiment with the CEBAF-energies of 1.645 GeV and 2.478 GeV [33]; the electron-beam polarization for each period is listed in table **??**. Right: Degree of circular-photon polarization as a function of incident-photon energy for the g12 CEBAF-energy of 5.715 GeV; the electron-beam polarization was 67.17 %.

Table 3.7: Møller measurements of the electron-beam polarization for the $g12$ experiment. Only the measurement for the run range 56476 - 56643 was used in our analysis.

Run Range	Electron-Beam Polarization δ_{e^-} (Møller Readout)
56355 - 56475	$(81.221 \pm 1.48)\,\%$
56476 - 56643	$(67.166 \pm 1.21)\,\%$
56644 - 56732	$(59.294 \pm 1.47)\,\%$
56733 - 56743	$(62.071 \pm 1.46)\,\%$
56744 - 56849	$(62.780 \pm 1.25)\,\%$
56850 - 56929	$(46.490 \pm 1.47)\,\%$
56930 - 57028	$(45.450 \pm 1.45)\,\%$
57029 - 57177	$(68.741 \pm 1.38)\,\%$
57178 - 57249	$(70.504 \pm 1.46)\,\%$
57250 - 57282	$(75.691 \pm 1.46)\,\%$
57283 - 57316	$(68.535 \pm 1.44)\,\%$

The degree of circular polarization was not a continuous function of the center-of-mass energy. Therefore, we used the following equation to determine the polarization for center-of-mass bins:

$$\bar{\delta}_{\odot} \,=\, \frac{1}{N^{+}+N^{-}} \sum_{i\,\in\,\Delta\tau} \delta_{\odot}\,(W)\,, \tag{3.14}$$

where $N^{\pm}$ was the total number of $\gamma p \to p\,\omega$ and $\gamma p \to K^0\Sigma^+$ events (used for the observable $\mathbf{E}$) for the two helicity states and W was the center-of-mass energy; $\delta_{\odot}\,(W)$ was calculated from Equation 3.13. Average values were derived for each center-of-mass bin and are shown in table 3.9 for the $g9a$ experiment and table 3.10 for the $g12$ experiment.

3.11.2 Circularly-Polarized Photon Beam - Orientation of the Helicity States

The direction of the beam polarization depended on the condition of the half-wave plate (HWP) which was either IN or OUT. In CLAS-g12, the longitudinal polarization of the electron beam was flipped pseudo-randomly at a high rate with many sequences of helicity $(+\,,-)$ or $(-\,,+)$ signal per second. Occasionally, the HWP was inserted in the circularly-polarized laser beam of the electron gun to reverse helicities and thus, the beam polarization phase was changed by 180°. The HWP was inserted and removed at semi-regular intervals throughout the experimental run to ensure that no polarity-dependent bias was manifested in the measured asymmetries.

For the $g9a$ and most of the g12 runs, the information could be retrieved from the "level1-trigger latch word" of the TGBI bank. Bit 16 in this word described the photon helicity-state corresponding to the sign of the electron-beam polarization as shown in Table 3.11. Alternatively, the g12 run-group provided the following method:

```
int GetHelicity(clasHEVT_t *HEVT)
{
   int helicity = 0;
   int readout = HEVT->hevt[0].trgprs;
   if(readout > 0) helicity = 1;
   if(readout < 0) helicity = -1;
   return helicity;
}
```

When the HWP was OUT, a bit-16 value of "one" meant that the beam polarization was parallel to the beam direction and a value of "zero" that the beam polarization was antiparallel to the beam. When the HWP was IN, the directions of the beam polarization were switched. Table 3.12 and table 3.13 show the HWP settings in the $g9a$ and $g12$ data sets. The information shown in these table were experimentally confirmed by studying the beam asymmetries $I^{\odot}$ in the two-pion channel.

Table 3.8: Møller measurement of the electron-beam polarization for the $g9a$ experiment.

Electron-beam energy E_e	Date	Run number	Electron-beam polarization δ_e	
				Average
1.645 GeV	Nov. 12, 2007	55544	$+85.228 \pm 1.420$	84.789 ± 0.470
			-78.523 ± 1.350	
			-79.150 ± 1.26	
			$+88.700 \pm 1.480$	
	Nov. 13, 2007	55552	$+84.167 \pm 1.330$	
			-84.725 ± 1.530	
	Nov. 19, 2007	55588	-86.531 ± 1.380	
			$+88.409 \pm 1.440$	
			$+87.753 \pm 1.480$	
2.478 GeV	Nov. 28, 2007	55608	-82.534 ± 1.400	83.016 ± 0.789
	Nov. 28, 2007	55608	-79.450 ± 1.410	
			$+80.060 \pm 1.400$	
	Jan. 07, 2008	56194	-83.267 ± 1.380	
	Feb. 08, 2008	56202	-83.248 ± 1.320	

Table 3.9: The average degrees of circular polarization for $g9a$ W bins

Center-of-Mass Energy [GeV]	Average Degree of Circular Polarization, $\bar{\delta}_\odot$	
	$E_{e^-} = 1.645$ GeV	$E_{e^-} = 2.478$ GeV
1.25	0.22172 ± 0.00007	
1.30	0.26349 ± 0.00006	
1.35	0.31319 ± 0.00007	0.20442 ± 0.00019
1.40	0.36416 ± 0.00008	0.22325 ± 0.00007
1.45	0.41810 ± 0.00008	0.25841 ± 0.00008
1.50	0.47551 ± 0.00009	0.29194 ± 0.00010
1.55	0.53077 ± 0.00010	0.32929 ± 0.00010
1.60	0.58695 ± 0.00013	0.36861 ± 0.00012
1.65	0.64083 ± 0.00015	0.40909 ± 0.00014
1.70	0.69159 ± 0.00017	0.44555 ± 0.00021
1.75	0.73866 ± 0.00019	0.49416 ± 0.00020
1.80	0.77739 ± 0.00022	0.53564 ± 0.00022
1.85	0.80903 ± 0.00024	0.57837 ± 0.00031
1.90	0.83162 ± 0.00025	0.61849 ± 0.00029
1.95	0.84239 ± 0.00034	0.65746 ± 0.00031
2.00		0.69530 ± 0.00035
2.05		0.72835 ± 0.00037
2.10		0.75822 ± 0.00040
2.15		0.78291 ± 0.00045
2.20		0.80441 ± 0.00051
2.25		0.81792 ± 0.00059
2.30		0.82581 ± 0.00065

3.11.3 Beam-Charge Asymmetry in Data Sets with Circularly-Polarized Photons

The electron-beam polarization was toggled between the helicity-plus (h^+) and the helicity-minus (h^-) state at a rate of about 30 Hz. At this large rate, the photon-beam flux for both helicity states should be the same, on average. However, small beam-charge asymmetries of the electron beam could cause instrumental asymmetries in the observed *hadronic* asymmetries and had to be considered. The beam-charge asymmetry could be calculated from the luminosities of h^+ and h^- events:

$$\Gamma^{\pm} = \alpha^{\pm}\,\Gamma = \frac{1}{2}\,(1 \pm \bar{a}_c)\,\Gamma\,, \tag{3.15}$$

Table 3.10: The average degrees of circular polarization for $g12$ W bins

Center-of-Mass Energy [GeV]	Average Degree of Circular Polarization, $\bar{\delta}_{\odot}$ $E_{e^-} = 5.715$ GeV
1.70 - 1.75	0.150
1.75 - 1.80	0.164
1.80 - 1.85	0.179
1.85 - 1.90	0.194
1.90 - 1.95	0.210
1.95 - 2.00	0.226
2.00 - 2.05	0.243
2.05 - 2.10	0.261
2.10 - 2.15	0.279
2.15 - 2.20	0.298
2.20 - 2.25	0.317
2.25 - 2.30	0.336
2.30 - 2.35	0.356
2.35 - 2.40	0.377
2.40 - 2.45	0.397
2.45 - 2.50	0.418
2.50 - 2.55	0.438
2.55 - 2.60	0.459
2.60 - 2.65	0.479
2.65 - 2.70	0.500
2.70 - 2.75	0.519
2.75 - 2.80	0.538
2.80 - 2.85	0.556
2.85 - 2.90	0.574
2.90 - 2.95	0.590
2.95 - 3.00	0.605
3.00 - 3.05	0.619
3.05 - 3.10	0.631
3.10 - 3.15	0.642
3.15 - 3.20	0.651
3.20 - 3.25	0.658

where Γ was the total luminosity and the parameters $\alpha^{\pm}$ denoted the fraction of h^+ and h^- events. The parameters $\alpha^{\pm}$ depended on the mean value of the electron-beam charge asymmetry, $\bar{a}_c$, which was studied in other CLAS experiments and typically less than 0.2 %, e.g. Ref. [60, 61]. Since the beam-charge asymmetry was very small, it could be considered negligible.

Table 3.11: Helicity signal from the TGBI bank for the two half-wave-plate positions. In the table, the sign $+(-)$ denotes the beam polarization was parallel (anti-parallel) to the beam direction. However, this information is not crucial for our analysis since we also double-checked the polarization in different ways.

TGBI latch1	Beam Helicity	
Bit 16	$\lambda/2$ (OUT)	$\lambda/2$ (IN)
1	$+$	$-$
0	$-$	$+$

Table 3.12: The HWP condition in each period of the *g9a* data sets

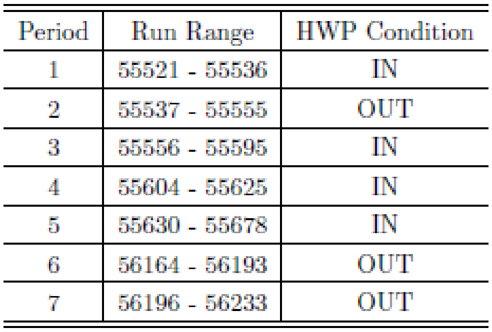

Period	Run Range	HWP Condition
1	55521 - 55536	IN
2	55537 - 55555	OUT
3	55556 - 55595	IN
4	55604 - 55625	IN
5	55630 - 55678	IN
6	56164 - 56193	OUT
7	56196 - 56233	OUT

Table 3.13: The half-wave plate (HWP) condition in the g12 data sets. In our analysis, only Period 2 was used.

Period	Run Range	HWP Condition
1	56519 and earlier	
2	56520 - 56594, 56608 - 56646	IN
3	56601 - 56604, 56648 - 56660	
4	56665 - 56667	
5	56605, 56607, 56647	
6	56668 - 56670	
7	56897 and later	
8	57094 and later	

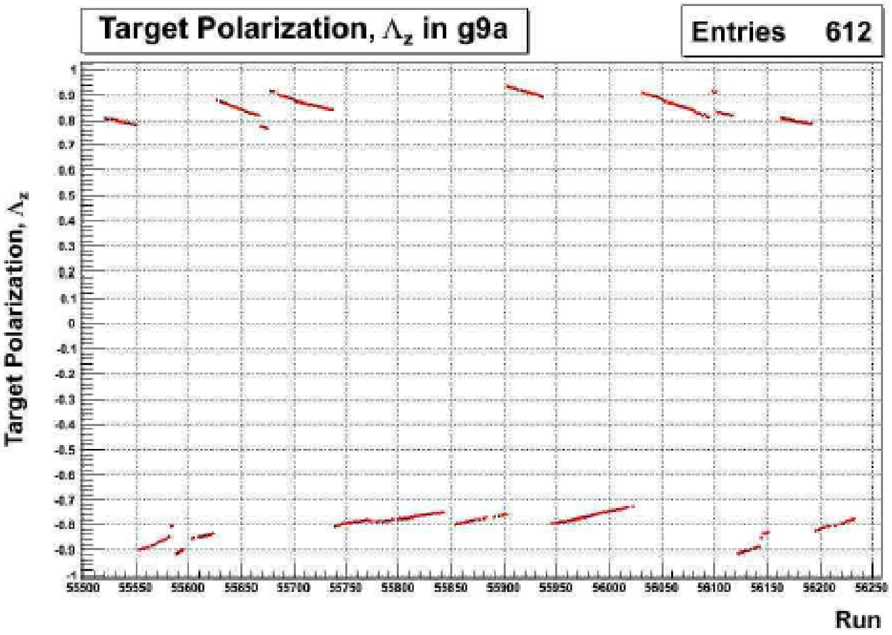

Figure 3.28: Target polarization versus run number measured in the *g*9*a* experiment [36].

Table 3.14: Definition of the target polarization settings in *g*9*a*. The first sign denotes the direction of the proton polarization relative to the magnetic field and the second sign denotes the direction of the holding magnet relative to the beam.

L++ : Positive target polarization	L+− : Negative target polarization
L−− : Positive target polarization	L−+ : Negative target polarization

3.11.4 Target Polarization in the *g*9*a* experiment

The FROST-*g*9*a* experiment utilized a longitudinally-polarized frozen-spin butanol target. The target was polarized a total of 21 times during *g*9*a* runs, with an average starting polarization of 84 % in the positive spin state and −86 % in the negative. Typical relaxation times for the target were about 2800 hours to 3600 hours for positive polarization and about 1400 hours to 1900 hours for negative polarization. The target was re-polarized and the polarizarion also reversed about once per week.

The direction of the target polarization was defined by two quantities: the direction of the proton polarization with respect to the holding field and the direction of the magnetic field with respect to the beam. The target settings in $g9a$ are summarized in table 3.14. In our $g9a$ analysis, the final directions of the target polarization were determined from the target asymmetry or P_z in the reaction $\gamma p \to p\pi^+\pi^-$. Table 3.15 shows the results after our consistency studies using the target asymmetry, P_z.

Table 3.15: The condition of the beam and target polarization for each $g9a$ period used in our analysis.The arrows ⇒ (⇐) denote a target polarization parallel (anti-parallel) to the beam direction.

Period	Run range	Beam polarization The condition of the half-wave plate	Target polarization
1	55521 - 55536	IN	⇐
2	55537 - 55555	OUT	⇐
3	55556 - 55595	IN	⇒
4	55604 - 55625	IN	⇒
5	55630 - 55678	IN	⇐
6	56164 - 56193	OUT	⇒
7	56196 - 56233	OUT	⇐

3.12 Signal-Background Separation: Q-Factor Method

The remaining step in preparing a clean event sample of the reaction in question is the removal of background underneath the signal peak. The (event-based) Q-factor method used for the background separation in the $p\,\pi^+\pi^-\,\pi^0$ final states (including $\gamma p \to p\,\omega \to p\,\pi^+\pi^-\pi^0$ as well as $\gamma p \to K^0\,\Sigma^+ \to p\,\pi^+\pi^-\pi^0$) is described in the following sections.

3.12.1 General Description of the Method

In this event-based method, the set of coordinates that described the multi-dimensional phase space of the reaction was categorized into two types: *reference* and *non-reference* coordinates [76]. The signal and background shapes had to be known *a priori* in the reference coordinate but this knowledge was not required in the non-reference coordinates. Mass was typically chosen as the reference coordinate. For each event, we then set out to find the N_c nearest neighbors in the phase space of the non-reference coordinates. This was similar to binning the data using a dynamical bin width in the non-reference coordinates and making sure that we had N_c events per fit.

The mass distribution of the N_c events (including the candidate event) in the reference coordinate was then fitted with a total function defined as:

$$f(x) \,=\, N\,\cdot\left[f_s\,\cdot\,S(x)\,+\,(1\,-\,f_s)\,\cdot\,B(x)\right], \tag{3.16}$$

where $S(x)$ denoted the signal and $B(x)$ the background probability density function. N was a normalization constant and f_s was the signal fraction with a value between 0 and 1. The RooFit package of the CERN ROOT software [62] was used for the fit procedure. Since N_c was usually a small number (of the order of a few hundred events), an unbinned maximum likelihood method was used for the fitting. The Q factor itself was given by:

$$Q \,=\, \frac{s(x)}{s(x)\,+\,b(x)}\,, \tag{3.17}$$

where x was the value of the reference coordinate for the candidate event, $s(x) = f_s \cdot S(x)$ and $b(x) = (1 - f_s) \cdot B(x)$. The Q factor could then be used as an event weight to determine the signal contribution to any physical distribution.

Table 3.16: The non-reference coordinates Γ_i and their ranges Δ_i.

Γ_i	Non-Reference Coordinate	Maximum Range Δ_i
Γ_0	$\cos\Theta^{\omega}_{\text{c. m.}}$	2
Γ_1 & Γ_2	$\cos\theta_{\text{HEL}}$ and ϕ_{HEL}	2 & 2π [radians]
Γ_3	$\phi^{\omega}_{\text{lab}}$	2π [radians]
Γ_4	λ	1
Γ_5	incident photon energy E_γ (or W)	20 MeV (10 MeV below 2.1 GeV)

3.12.2 The Q-Factor Method for the Reaction $\gamma p \to p\,\omega \to p\,\pi^+\pi^-\pi^0$ from the $g12$ Data Sets

The kinematic variables that described the reaction $\gamma p \to p\,\omega$ were chosen to be the incident-photon energy, E_γ, and the center-of-mass angle of the outgoing ω, $\cos\theta^{\omega}_{\text{c. m.}}$. Since we reconstructed the ω from its decay into $\pi^+\pi^-$ (π^0), we also considered the relevant kinematic variables which described the five-dimensional phase space of the 3π system. The ω decay was thus entirely defined by five independent kinematic variables (including the invariant $\pi^+\pi^-\pi^0$ mass we used as *reference* variable). In total, we chose six *non-reference* variables:

- The incident photon energy E_γ (or alternatively, the total center-of-mass energy W),
- The two angles of the ω meson in the helicity frame, $\cos\theta_{\text{HEL}}$ and ϕ_{HEL},
- The center-of-mass azimuthal and polar angles of the ω, and
- The decay parameter $\lambda \propto |\,\vec{p}_{\pi^+} \times \vec{p}_{\pi^-}|^2$ [54].

The six non-reference coordinates and their maximum ranges used in the Q-factor method applied to the $g12$ data sets are summarized in table 3.16.

For the signal-background separation in the $\omega \to \pi^+\pi^-\pi^0$ analysis, we initially applied a small $CL > 0.001$ cut (from kinematic fitting) on the $\gamma p \to p\,\pi^+\pi^-$ (π^0) final state. This loose CL cut significantly reduced the background, in particular from $\gamma p \to p\,\pi^+\pi^-$ events. We then used the event-based technique to select ω events.

The data were divided into data subsets based on the photon energy (20-MeV wide bins). We chose the number of 1000 nearest-neighbor events for each candidate event in the phase space spanned by the non-reference coordinates. The $\pi^+\pi^-\pi^0$ invariant mass distribution of these 1000 events was then fitted over the mass range 650 - 900 MeV using the unbinned maximum-likelihood technique. Since the natural width of the ω meson is 8.49 MeV and thus, at the level of the detector resolution, we chose a Voigtian function for the signal pdf. The Voigtian function is a convolution of a Gaussian, which was used to describe the resolution, and a Breit-Wigner, which described the natural line shape of the resonance. The background shape was modeled with a second-order Chebychev polynomial for incident photon energies above 1400 MeV. Close to the reaction threshold of $E_\gamma \approx 1109$ MeV, the ω signal peak is located very close to the upper 3π phase space boundary. For this reason, we chose an Argus function instead of a Chebychev polynomial to describe the background shape.

Table 3.17 shows the parameters of the signal and background pdfs and the constraints imposed on them. The two pdfs were used to construct a total pdf (see Equation 3.16) and the Q factor of the candidate event was extracted using Equation 3.17.

Table 3.17: Parameters of the signal and background probability-density functions. A Voigtian was used to describe the ω signal and a second-order Chebychev polynomial (an Argus function for $E_\gamma < 1.4$ GeV) was used to describe the background over the $\pi^+\pi^-\pi^0$ mass range 650 - 900 MeV.

Probability Density Function	Parameters	Initial Value	Fit Range
Voigtian	mean, μ	782.65 MeV [52]	fixed
	width, σ	8.0 MeV	0 - 30 MeV
	natural width, Γ	8.49 MeV [52]	fixed
Chebychev ($E_\gamma > 1.4$ GeV)	c_0	0.5	0.0 - 1.8
	c_1	0.1	-1.2 - 1.2
Argus ($E_\gamma < 1.4$ GeV)	endpoint, m_0	820 MeV	790.0 - 950.0 MeV
	slope, c	-1.0	-10.0 - 0.2

There were some analyses step that we performed to check the quality of the signal-background separation:

1. Once the fit parameters were determined in an individual likelihood fit, we performed a least-square "fit" of the same mass distribution from the 1000 events. Among other things, this allowed us to plot the distribution of reduced-χ^2 values as a goodness-of-fit measure. The

left column of Figure 3.29 shows several such reduced-χ^2 distributions for a few randomly-selected example E_γ bins: (top to bottom row) $E_\gamma \in [1.64,\ 1.66]$ GeV, $E_\gamma \in [2.10,\ 2.12]$ GeV, $E_\gamma \in [4.00,\ 4.02]$ GeV, $E_\gamma \in [5.00,\ 5.02]$ GeV. These reduced-χ^2 distributions peak fairly close to the ideal value of *one*. Given the fairly small number of events in these distributions, we also concluded that the fitter picks up statistical fluctuations. This resulted in overconstrained fits and slightly smaller reduced-χ^2 values, about 0.7 - 0.8 on average.

2. Defined in terms of the pion momenta in the rest frame of the ω meson, the quantity $\lambda = |\,\vec{p}_{\pi^+} \times \vec{p}_{\pi^-}|^2 \,/\, \lambda_{\,\mathrm{max}}$ is proportional to the $\omega \to \pi^+\pi^-\pi^0$ decay amplitude as a consequence of isospin conservation [25] with $\lambda_{\,\mathrm{max}}$ defined as [63]:

$$\lambda_{\,\mathrm{max}} \,=\, T^2 \left(\frac{T^2}{108} + \frac{mT}{9} + \frac{m^2}{3} \right) \tag{3.18}$$

   for a totally symmetric decay, where $T = T_1 + T_2 + T_3$ is the sum of the $\pi^{\pm,\,0}$ kinetic energies and m is the $\pi^\pm$ mass. The parameter λ varies between 0 and 1 and shows a linearly-increasing distribution as expected for a vector meson.

   Figure 3.29 (center column) shows the λ distributions for the same energy bins as for the corresponding reduced-χ^2 distributions in the left column. The (red) signal was generated by weighting event-by-event the (black) full distribution with the Q values; the (blue) background distribution was generated by weighting the full distribution with $1 - Q$. The linear behavior of the ω signal events is clearly visible.

Finally, $\omega \to \pi^+\pi^-\pi^0$-mass distributions showing the full statistics in a given energy bin are presented in Figure 3.29 (right column) for the selected E_γ bins discussed above and in 20-MeV-wide bin for the entire CLAS-g12 energy range in Figures 3.30 - 3.33. Since we analyzed a total of 215 energy bins, we show the mass distribution for every sixth energy bin in these figures.

3.12.3 The Q-Factor Method for the Reaction $\gamma p \to p\,\omega \to p\,\pi^+\pi^-\pi^0$ from the $g9a$ Data Sets

Frozen beads of butanol (C_4H_9OH) were used for the target material. When the butanol was polarized, only the 10 *free* hydrogen nucleons of the butanol could be polarized. Thus, contributions from the free-proton events had to be separated from contributions of events off bound nucleons in ^{12}C and ^{16}O. The latter were subject to Fermi motion and the signals from them showed no particular structures since the particle peaks were broadened and mostly washed out. A *dilution factor* describes the signal fraction and is generally defined as the ratio of the free-proton contribution to the full butanol cross section. A simple calculation based on the chemical formula of butanol yields $10/74 = 0.135$ as the ideal dilution factor. However, we also applied the Q-factor method for the $g9a$ data sets to remove the background contributions from the bound nucleons. We used the same coordinates as in the $g12$ data sets shown in table 3.18 below. However, a number of nearest neighbors, $N_c = 300$ was chosen instead of $N_c = 1000$ due to the statistics limitation in the $g9a$ data sets. The example of resulting invariant mass distributions are shown in figure 3.34.

Table 3.18: The non-reference coordinates Γ_i and their ranges Δ_i for the $g9a$ data sets.

Γ_i	Non-Reference Coordinate	Maximum Range Δ_i
Γ_0	$\cos\Theta^{\omega}_{\text{c. m.}}$	2
Γ_1 & Γ_2	$\cos\theta_{\text{HEL}}$ and ϕ_{HEL}	2 & 2π [radians]
Γ_3	$\phi^{\omega}_{\text{lab}}$	2π [radians]
Γ_4	λ	1
Γ_5	incident photon energy E_γ-lab	100 MeV

3.12.4 The Q-Factor Method for the Reaction $\gamma p \to K^0_S\,\Sigma^+$ from the $g12$ Data Sets

The reconstruction of the $K^0_S\,\Sigma^+$ final state differs from the ω. While the latter is based directly on the $\pi^+\pi^-\pi^0$ system, the strange K_S is reconstructed from the $\pi^+\pi^-$ system and the remaining π^0 originates from the baryon decay. Since the $K_S \to \pi^+\pi^-$ and the $\Sigma^+ \to p\pi^0$ are highly correlated (associated strangeness production), the reference quantity can either be the invariant $\pi^+\pi^-$ mass or the invariant $p\pi^0$ mass. We determined Q values independently applying both approaches, which serves as a cross check when comparing the cross sections. Table 3.19 shows the non-reference variables used for the background subtraction in this reaction. The quantities in parentheses are the non-reference coordinates used for the Q values based on the invariant $p\pi^0$ mass.

Since the cross section for the reaction $\gamma p \to K^0\,\Sigma^+$ is relatively small, the observed statistics is low and the invariant $\pi^+\pi^-$ mass is dominated by background in the mass region of the K_S (see Fig. 3.35, top left). Therefore, we considered two mass cuts before we applied the Q-factor method:

1. Strangeness is conserved in electromagnetic and strong interactions. For this reason, the K_S meson is produced together with a Σ^+ baryon (in our analysis). The life time of the Σ^+ ($\tau = (0.8018 \pm 0.0026) \times 10^{-10}$ s) is fairly long since it can only decay weakly. We thus

applied a narrow cut of 20 MeV around the Σ^+ mass of 1189.37 MeV [52]. The effect can be seen in Figure 3.35 (top row). The left side shows the *raw* $\pi^+\pi^-$ distribution of all g12 $\pi^+\pi^-\pi^0$ events in Period 2 (see Table 3.2), whereas the right side shows the same distribution after the Σ^+ cut. The background is significantly reduced and the K_S peak is clearly visible; the $K_S\,\Sigma^+$ statistics is only marginally affected.

2. The dominant reaction contributing to the $p\,\pi^+\pi^-\pi^0$ final state is ω production. The bottom row of Figure 3.35 shows the invariant $\pi^+\pi^-\pi^0$ mass vs. the corresponding $\pi^+\pi^-$ mass (left side). The vertical band for the ω is clearly visible and moreover, it exhibits a maximum intensity in the vicinity of the K_S in the projection onto the $\pi^+\pi^-$ axis. Therefore, we applied a mass cut to remove contributions from ω production: $m_{\pi^+\pi^-\pi^0} < 752$ MeV and $m_{\pi^+\pi^-\pi^0} > 812$ MeV. The resulting (final) $\pi^+\pi^-$ mass distribution showing the K_S peak is given on the right side. A comparison of Figure 3.35 (top right) and Figure 3.35 (bottom right) indicates that only little $K_S\,\Sigma^+$ statistics is lost due to the ω cut.

The two-dimensional distribution also explains the two structures which can be observed in the projection onto the $\pi^+\pi^-$ axis (right side of Figure 3.35): (1) The peak around 400 MeV is the reflection of the $\eta \to \pi^+\pi^-\pi^0$ which is cut off at the phase-space boundary, and (2) the enhancement around 550 MeV is most likely based on the η decaying into $\pi^+\pi^-\gamma$.

To subtract the background for the $K_S\,\Sigma^+$ final state, the selected g12 data were divided into 50-MeV-wide incident-photon energy bins for the cross-section measurement and 100-MeV-wide energy bins for the measurement of the induced polarization. We then chose a 1000 nearest-neighbor events for each signal candidate in the phase space spanned by the non-reference coordinates. The

Table 3.19: The non-reference coordinates Γ_i and their ranges Δ_i. Note that we used 100-MeV-wide incident-photon bins for the induced polarization.

Γ_i	Non-Reference Coordinate	Maximum Range Δ_i
Γ_0	incident-photon energy E_γ	50 MeV
Γ_1 & Γ_2	$\cos\theta_{\pi^+}$ ($\cos\theta_p$) & ϕ_{π^+} (ϕ_{π^0}) in the $\pi^+\pi^-$ ($p\pi^0$) rest frame	2 & 2π
Γ_3	$\cos\Theta^{K_S}_{\mathrm{c.m.}}$ in the center-of-mass frame	2
Γ_4	$\phi^{K_S}_{\mathrm{lab}}$	2π
Γ_5	$\cos$ (opening angle $\angle(p,\,\pi^0)$)	2

Table 3.20: Parameters of the signal & background probability-density functions. A Gaussian was used to describe the signal and a second-order Chebychev polynomial to describe the background.

		Ref. Coordinate: $\pi^+\pi^-$ Mass		Ref. Coordinate: $p\pi^0$ Mass	
		Initial Value	Fit Range	Initial Value	Fit Range
Gaussian pdf	Mean, μ	497.61 MeV [52]	fixed	1189.37 MeV [52]	fixed
	Width, σ	4.5 MeV	2.0 - 8.0 MeV	4.5 MeV	0.0 - 9.0 MeV
Chebychev pdf	c_0	0.1	-1.5 - 1.5	0.1	-1.5 - 1.5
	c_1	0.1	-1.5 - 1.5	0.1	-1.5 - 1.5

invariant $\pi^+\pi^-$ mass distribution of these 1000 events was fitted over the mass range 473 - 523 MeV for the K_S and independently, the $p\pi^0$ distribution was fitted over the mass range 1149 - 1229 MeV for the Σ^+ using the unbinned maximum-likelihood technique. Since the K_S decays weakly into $\pi^+\pi^-$ with a mean life τ of about $(8.954 \pm 0.004) \times 10^{-11}$ s [52] (and has thus a narrow natural width), we chose a Gaussian function for the signal pdf and a second-order Chebychev polynomial for the background. Table 3.20 shows the parameters of the signal and background pdfs and the constraints imposed on them.

Figures 3.37 - 3.41 show the complete set of invariant $\pi^+\pi^-$ mass distributions (left) and the corresponding $p\pi^0$ mass distributions (right) for 100-MeV-wide incident-photon energy bins in the range $E_\gamma \in [\,1100,\ 3000\,]$ MeV (full statistics used in this analysis). Finally, Fig. 3.36 presents example distributions of $E_\gamma \in [1400,\ 1500]$ MeV and $E_\gamma \in [1600,\ 1700]$ MeV.

Note that a full set of Q values for all events is not necessarily unique. If the Q values are determined for the K_S, then the weighted $\pi^+\pi^-$ mass distribution will show a clear separation of K_S signal and background. However, the $p\pi^0$ mass distribution weighted with the same Q values will still exhibit some background under the Σ^+ signal. The same is true if the Q values are determined for the Σ^+, in which case some background under the K_S will be observed. For a counting experiment like a cross-section measurement, either approach can be used. For an analysis however which requires the full event information, a more sophisticated method would be needed, e.g. a simultaneous fit of both mass distributions.

The measurement of the Σ^+ recoil polarization was based on the asymmetry between the proton count rate above and below the reaction plane, taken in the Σ^+ rest frame (for more details, see

Section 4.4). For this reason, we used the invariant $p\pi^0$ mass as the reference coordinate in the determination of Q values for both the final cross sections and the polarization observable. The (kinematic) decay information – the crucial opening angle between the proton and the π^0 – was added to the distance metric (Table 3.19). The K_S-peak-beased Q values were used to cross-check our final cross-section results.

3.12.5 The Q-Factor Method for the Reaction $\gamma p \to K_S^0\,\Sigma^+$ from the $g9a$ Data Sets

For the $K_S\Sigma^+$ channel from the $g9a$ data sets, we have concentrated on using the invariant $\pi^+\pi^-$ as a reference variable since the Σ^+ peak is hardly visible in the $p\pi^0$ invariant mass distributions as shown in figure 3.42. The suboptimal quality of the Σ^+ peak originates from the fairly poor resolution of the $p\pi^0$ system, which make the background subtraction challenging.

Table 3.21 shows the non-reference coordinates Γ_i and their ranges used in the Q-factor method. We use the same signal and background probability-density functions as in $g12$ and described in table 3.20. We have also applied the same ω and Σ^+ mass cut as shown in figure 3.43. Finally, Fig. 3.44 presents example distributions of the resulting $\pi^+\pi^-$ invariant mass.

Table 3.21: The non-reference coordinates Γ_i and their ranges Δ_i for the Q-factor method applied to the $K_S\Sigma^+$ channel from the $g9a$ data sets.

Γ_i	Non-Reference Coordinate	Maximum Range Δ_i
Γ_0	incident-photon energy E_γ	200 MeV
Γ_1 & Γ_2	$\cos\theta_{\pi^+}$ & ϕ_{π^+} in the $\pi^+\pi^-$ rest frame	2 & 2π
Γ_3	$\cos\Theta^{K_S}_{\mathrm{c.\,m.}}$ in the center-of-mass frame	2
Γ_4	$\phi^{K_S}_{\mathrm{lab}}$	2π
Γ_5	$\cos\left(\text{opening angle } \angle\,(p,\,\pi^0)\right)$	2

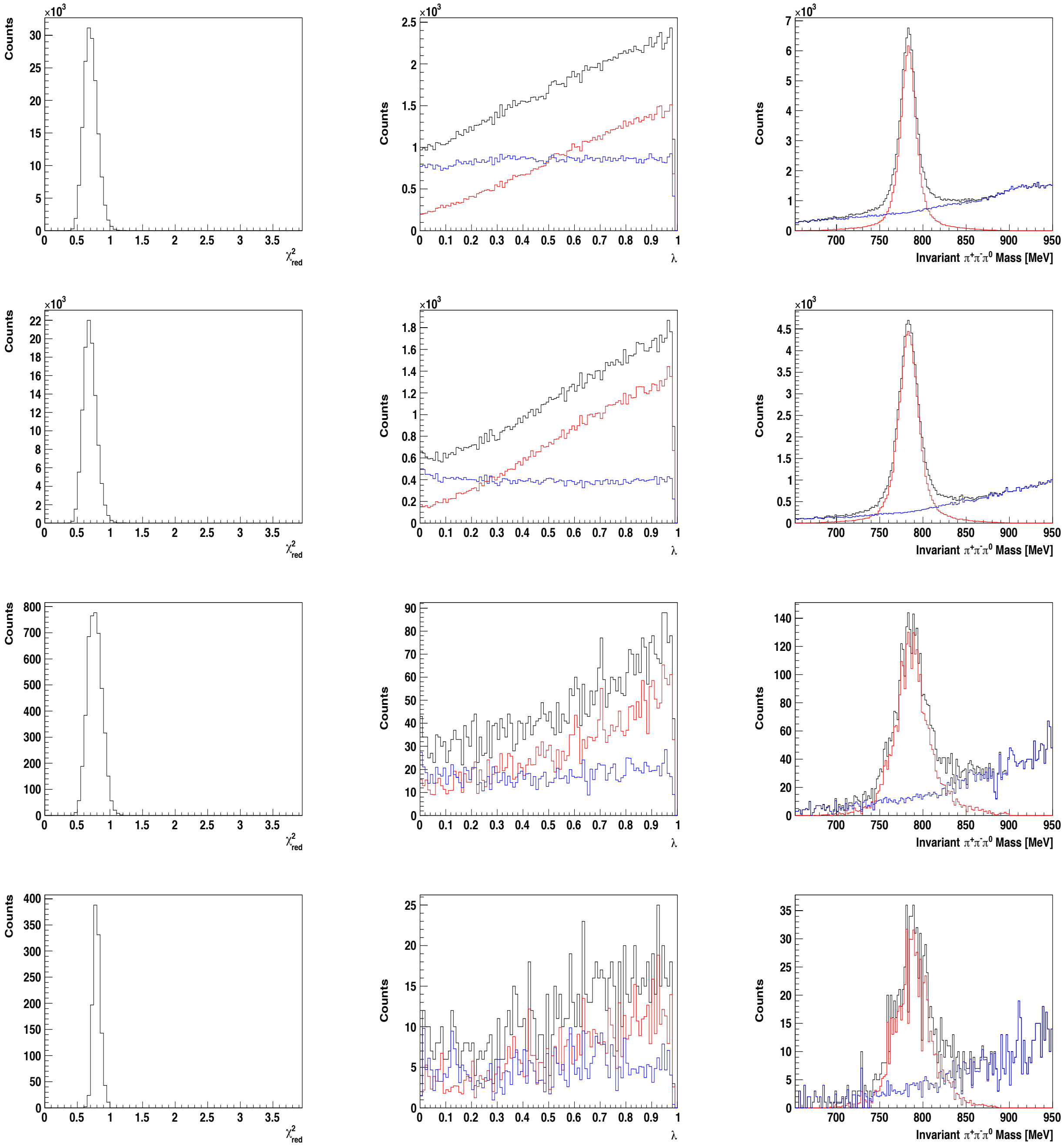

Figure 3.29: Quality checks - shown are randomly selected E_γ bins across a wide range in the incident photon energy: (top to bottom row) $E_\gamma \in [1.64,\, 1.66]$ GeV, $E_\gamma \in [2.10,\, 2.12]$ GeV, $E_\gamma \in [4.00,\, 4.02]$ GeV, $E_\gamma \in [5.00,\, 5.02]$ GeV. (Left column) Examples of reduced-χ^2 distributions. (Center) Examples of λ distributions. (Right) The full mass distribution for the energy bin. The black line denotes the full distribution, the red line the signal, and the blue solid line the background distribution.

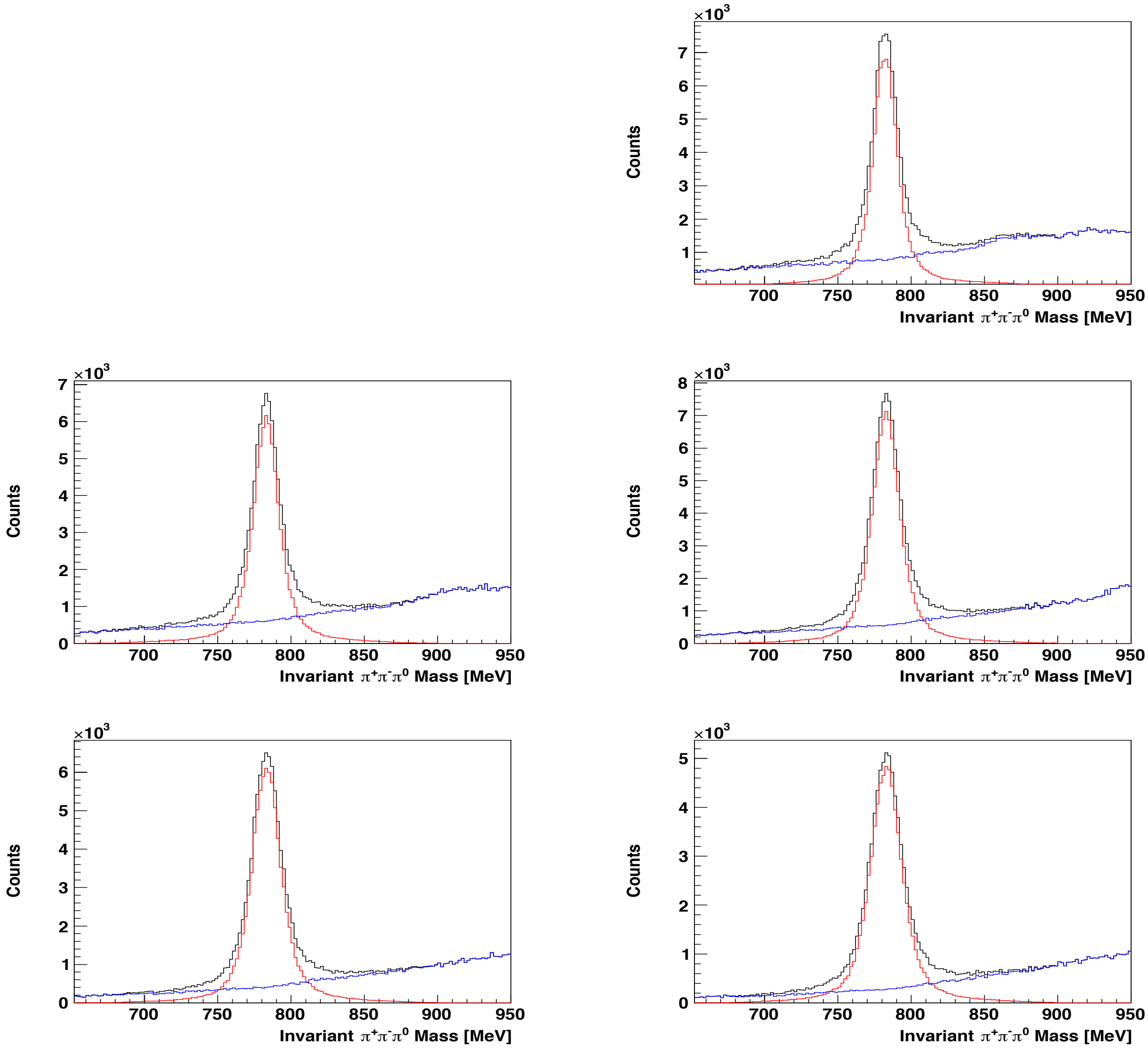

Figure 3.30: Invariant $\pi^+\pi^-\pi^0$ mass distributions for the reaction $\gamma p \to p\,\omega$. Shown is every sixth 20-MeV-wide E_γ bin starting at $E_\gamma \in [1200, 1220]$ MeV (top left), $E_\gamma \in [1220, 1240]$ MeV (top right), etc.

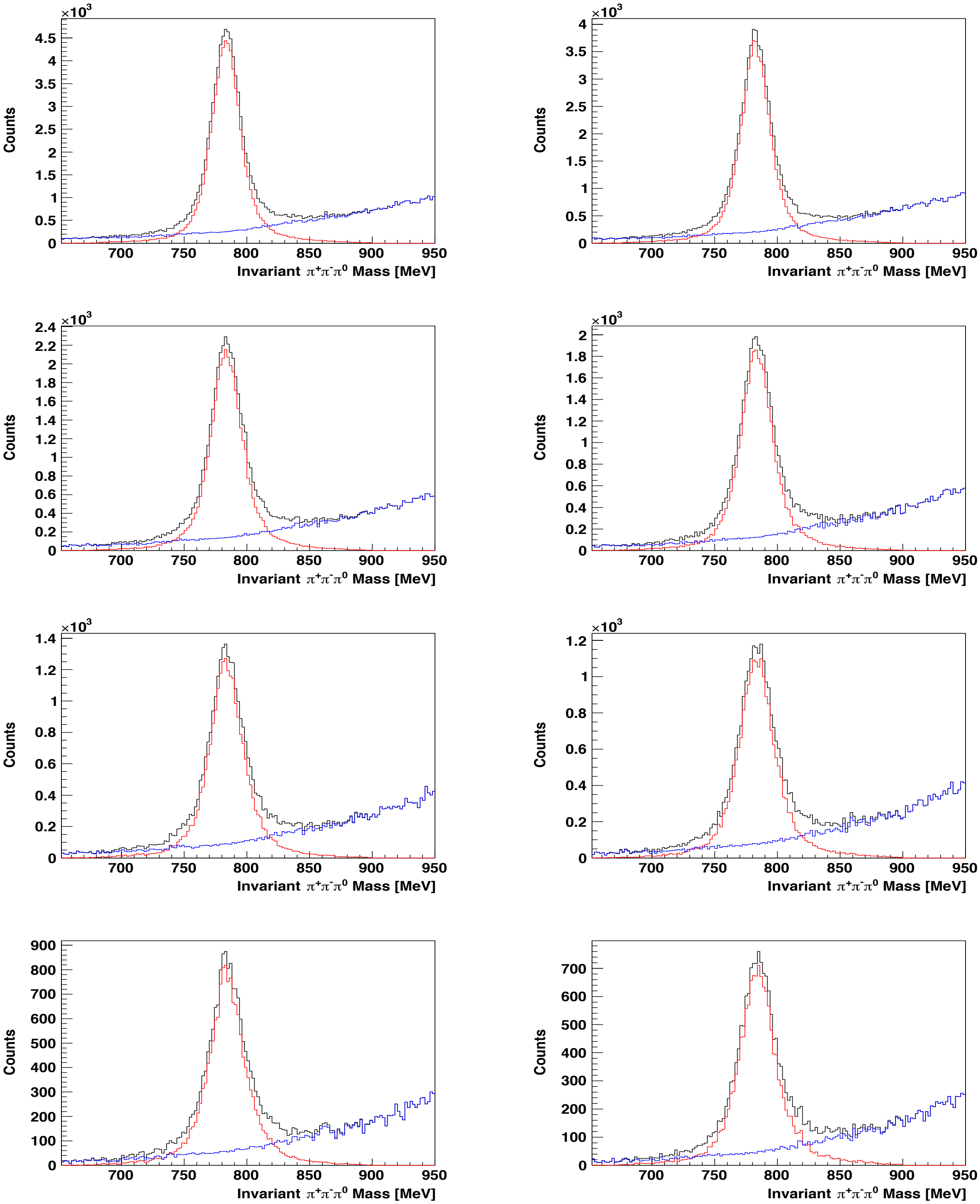

Figure 3.31: Invariant $\pi^+\pi^-\pi^0$ mass distributions for the reaction $\gamma p \to p\,\omega$. Shown is every sixth 20-MeV-wide E_γ bin starting at $E_\gamma \in [2120,\, 2140]$ MeV (top left), $E_\gamma \in [2140,\, 2160]$ MeV (top right), etc.

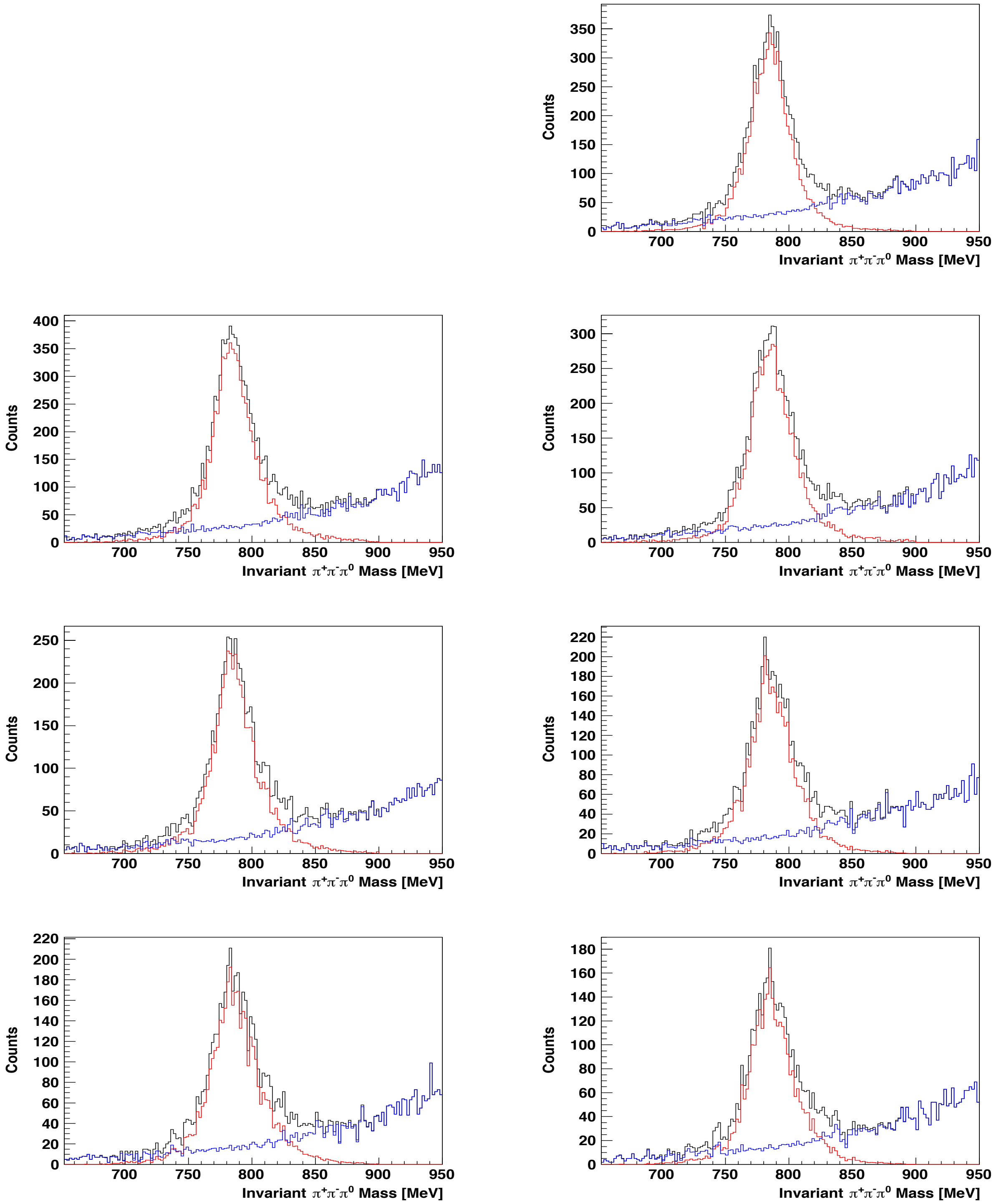

Figure 3.32: Invariant $\pi^+\pi^-\pi^0$ mass distributions for the reaction $\gamma p \to p\,\omega$. Shown is every sixth 20-MeV-wide E_γ bin starting at $E_\gamma \in [3200,\ 3220]$ MeV (top right). The [3080, 3100] MeV bin is missing owing to tagger inefficiencies.

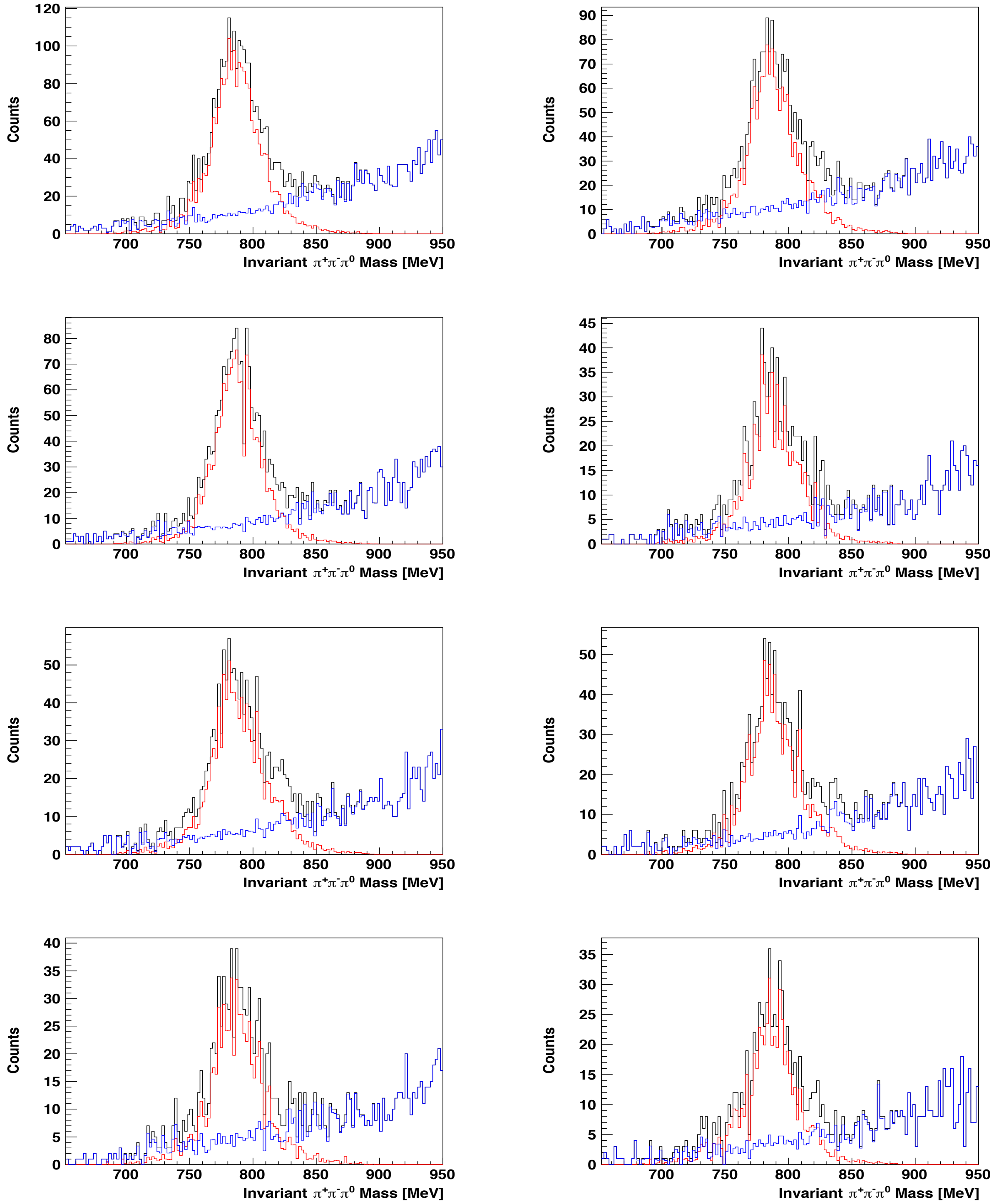

Figure 3.33: Invariant $\pi^+\pi^-\pi^0$ mass distributions for the reaction $\gamma p \to p\,\omega$. Shown is every sixth 20-MeV-wide E_γ bin starting at $E_\gamma \in [4080, 4100]$ MeV (top left), $E_\gamma \in [4200, 4220]$ MeV (top right), etc.

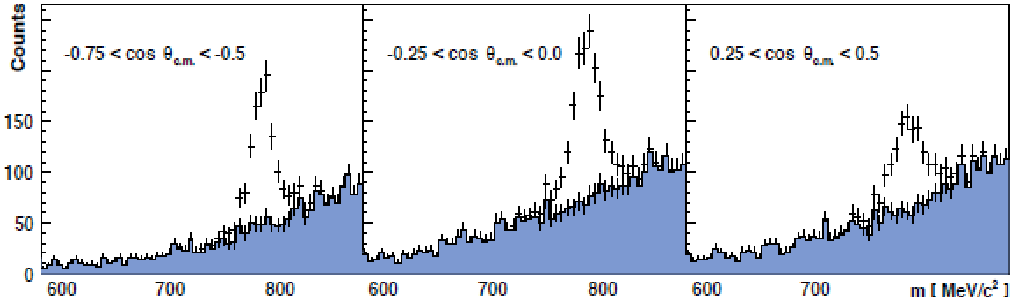

Figure 3.34: Examples of invariant $\pi^+\pi^-\pi^0$ mass distributions for the reaction $\gamma p \to p\omega$ from the $g9a$ data sets in the photon energy range $E_\gamma \in [1.5; 1.6]$ GeV [33]. The solid blue area indicates the background.

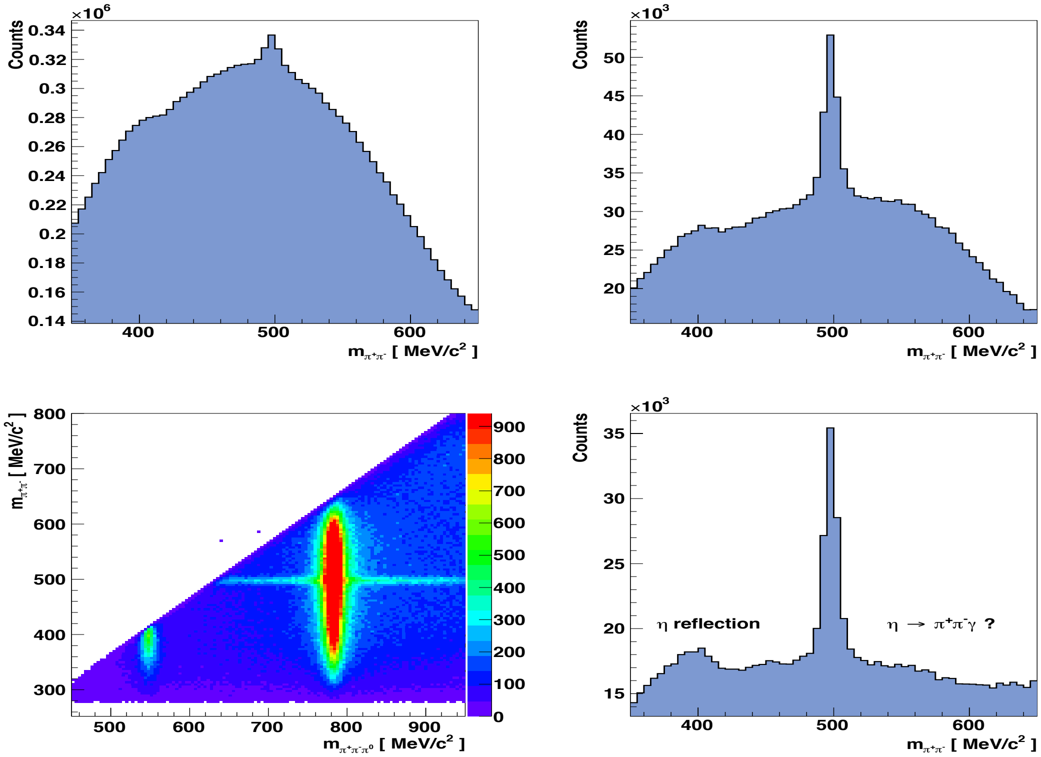

Figure 3.35: Top row: Invariant $\pi^+\pi^-$ mass distribution of all g12 $\pi^+\pi^-\pi^0$ events in Period 2 (left) and the same invariant $\pi^+\pi^-$ mass distribution after the Σ^+ cut (right). Bottom row: Invariant $\pi^+\pi^-\pi^0$ mass vs. the corresponding $\pi^+\pi^-$ mass of all g12 $\pi^+\pi^-\pi^0$ events in Period 2 (left) and the same invariant $\pi^+\pi^-$ mass distribution shown in the top row after the ω and the Σ^+ cuts (right).

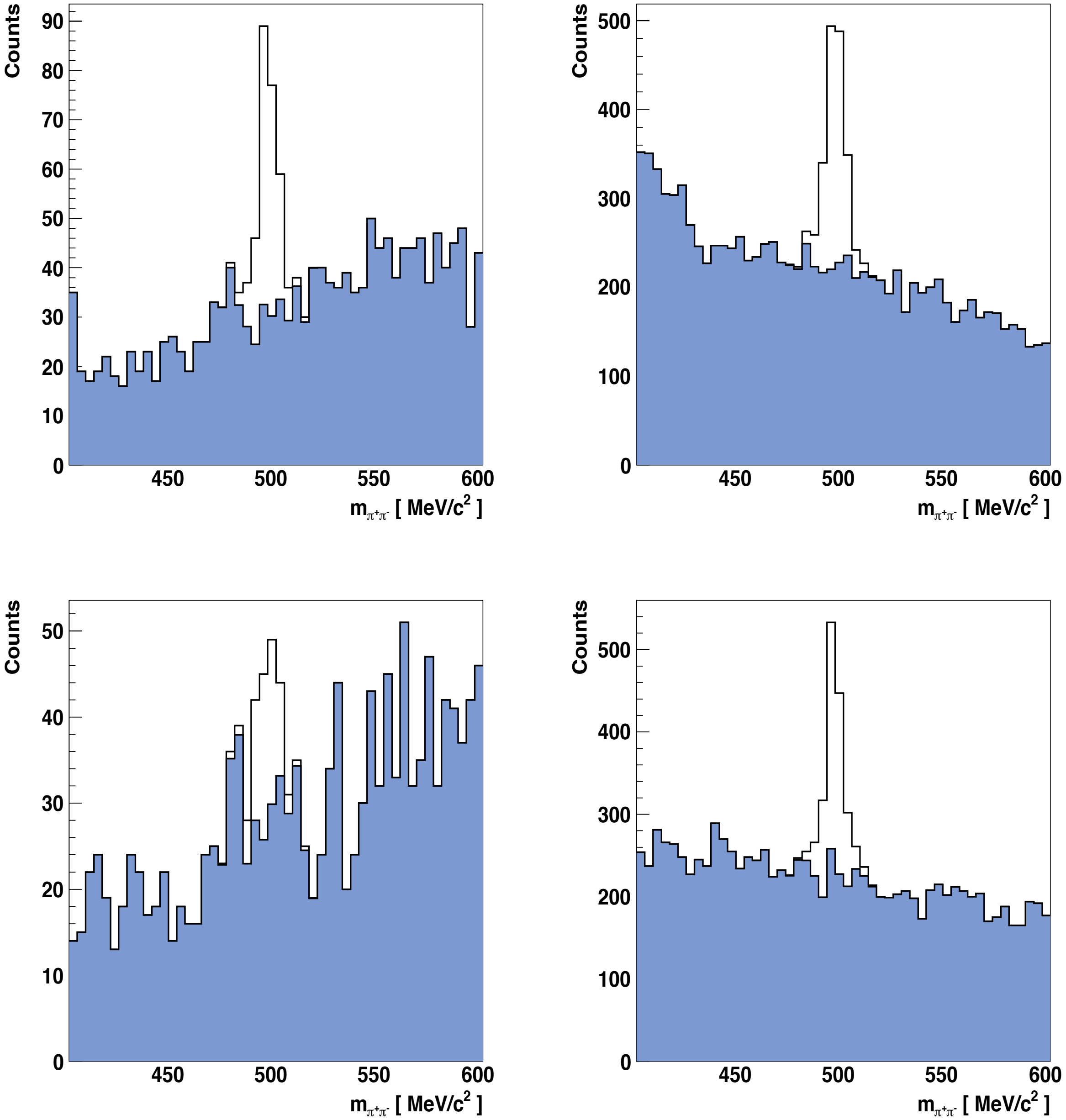

Figure 3.36: Examples of $\pi^+\pi^-$ distributions for $\gamma p \to K_S\,\Sigma^+$. Top row: $E_\gamma \in [1400, 1500]$ MeV. Bottom row: $E_\gamma \in [1600, 1700]$ MeV. The left side is for $-0.6 < \cos\theta^{K_S}_{\text{c.m.}} < -0.4$, the right side is for $0.0 < \cos\theta^{K_S}_{\text{c.m.}} < 0.2$.

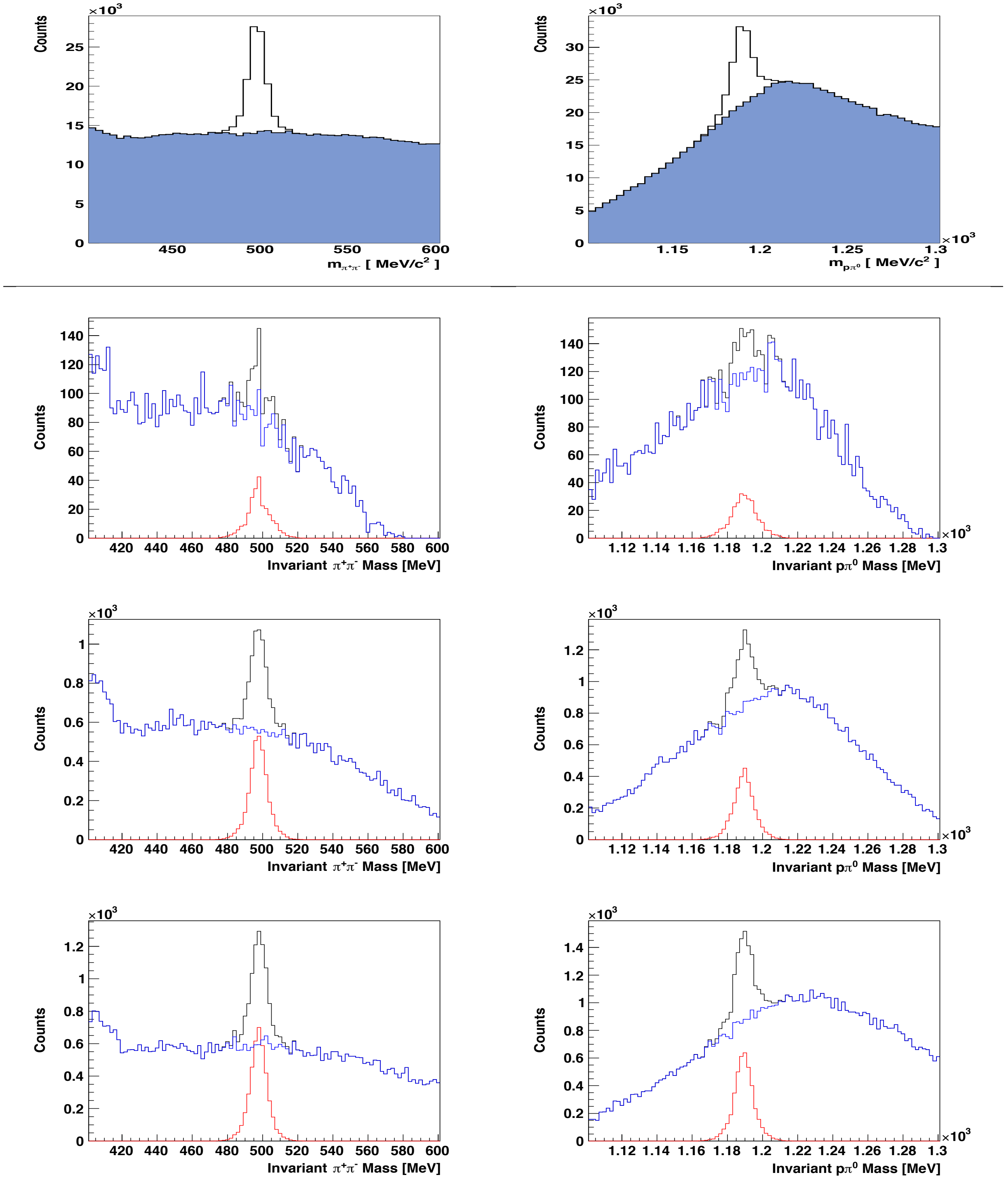

Figure 3.37: Invariant $\pi^+\pi^-$ distributions (left column) and the corresponding $p\pi^0$ distributions (right column) for the reaction $\gamma p \to K_S\,\Sigma^+$. Shown are the full statistics (top row) and 100-MeV-wide energy bins starting at $E_\gamma \in [1.1, 1.2]$ GeV (second row), $E_\gamma \in [1.2, 1.3]$ GeV (third row), etc.

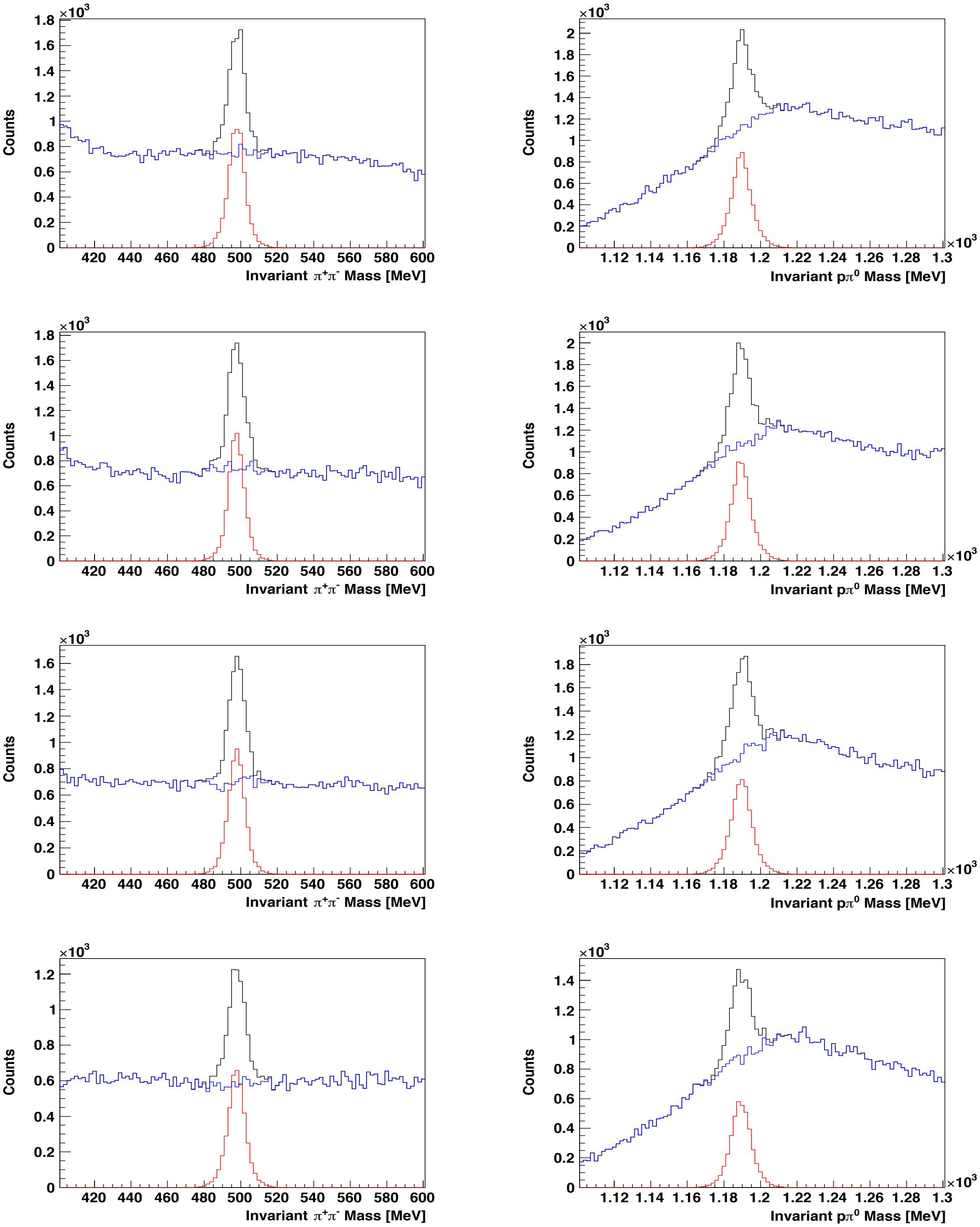

Figure 3.38: Invariant $\pi^+\pi^-$ distributions (left column) and the corresponding $p\pi^0$ distributions (right column) for the reaction $\gamma p \to K_S\,\Sigma^+$. Shown are 100-MeV-wide energy bins starting at $E_\gamma \in [1400, 1500]$ MeV (top row), $E_\gamma \in [1500, 1600]$ MeV (second row), etc.

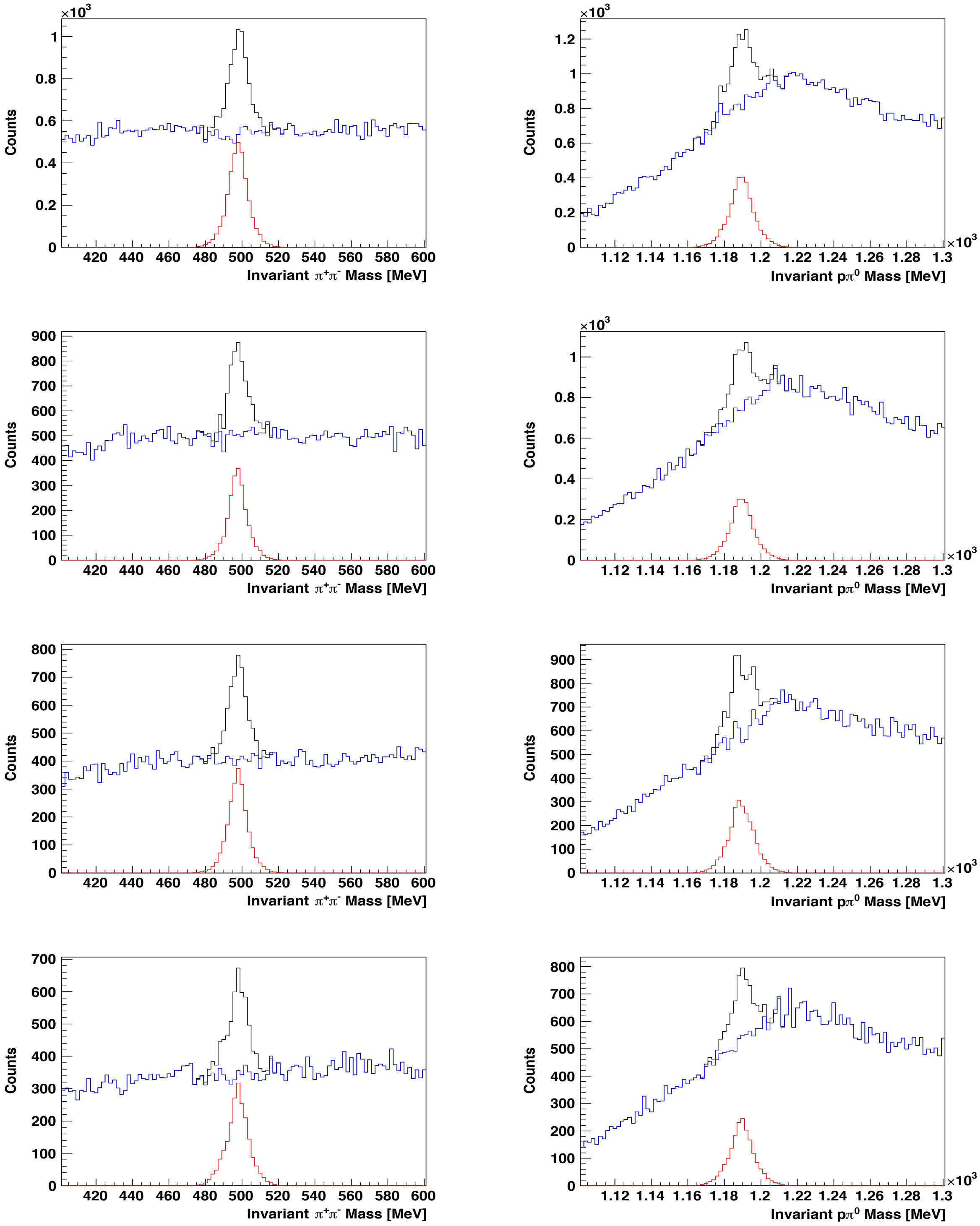

Figure 3.39: Invariant $\pi^+\pi^-$ distributions (left column) and the corresponding $p\pi^0$ distributions (right column) for the reaction $\gamma p \rightarrow K_S\,\Sigma^+$. Shown are 100-MeV-wide energy bins starting at $E_\gamma \in [1800,\,1900]$ MeV (top row), $E_\gamma \in [1900,\,2000]$ MeV (second row), etc.

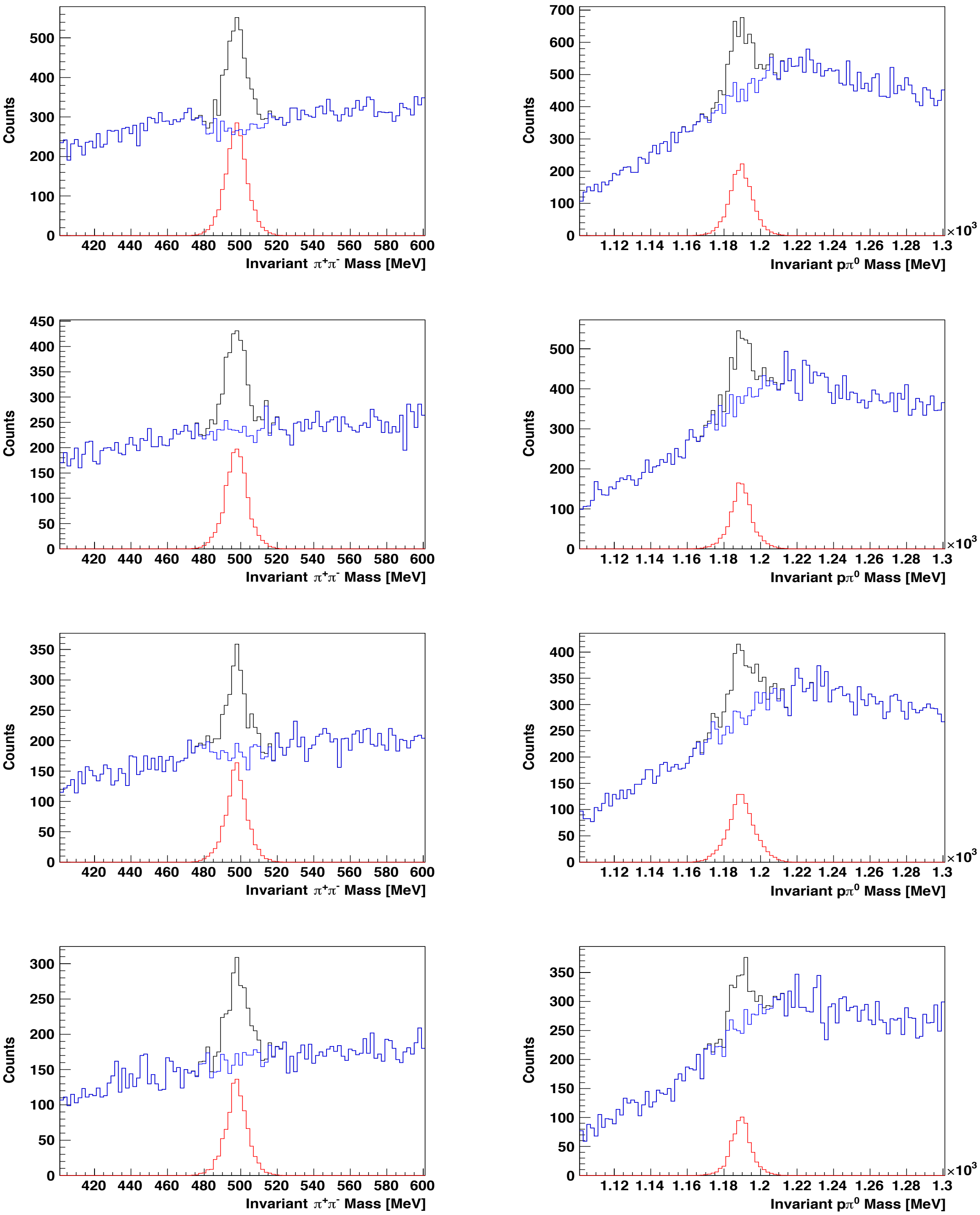

Figure 3.40: Invariant $\pi^+\pi^-$ distributions (left column) and the corresponding $p\pi^0$ distributions (right column) for the reaction $\gamma p \to K_S\,\Sigma^+$. Shown are 100-MeV-wide energy bins starting at $E_\gamma \in [2200,\ 2300]$ MeV (top row), $E_\gamma \in [2300,\ 2400]$ MeV (second row), etc.

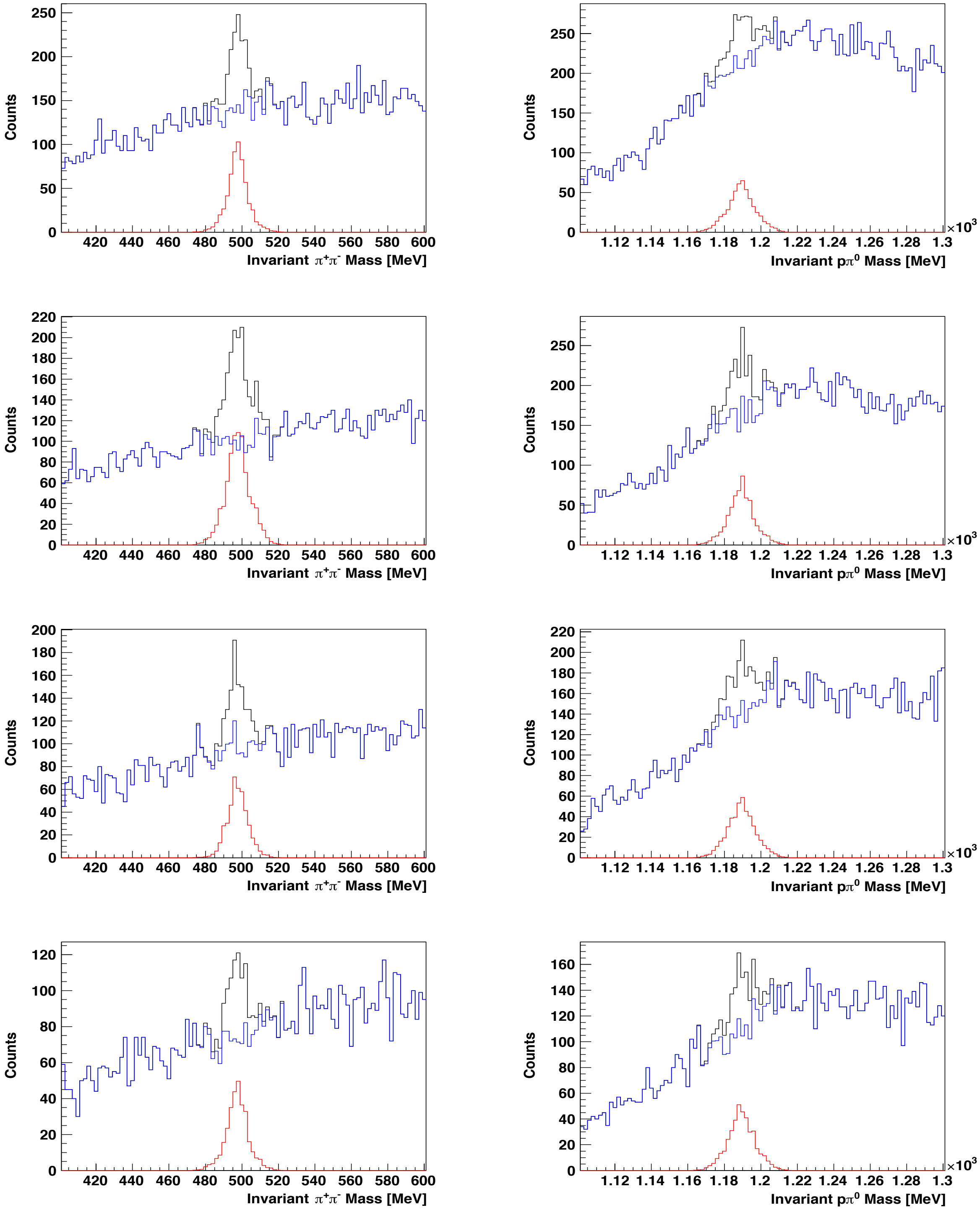

Figure 3.41: Invariant $\pi^+\pi^-$ distributions (left column) and the corresponding $p\pi^0$ distributions (right column) for the reaction $\gamma p \to K_S\,\Sigma^+$. Shown are 100-MeV-wide energy bins starting at $E_\gamma \in [2600, 2700]$ MeV (top row), $E_\gamma \in [2700, 2800]$ MeV (second row), etc.

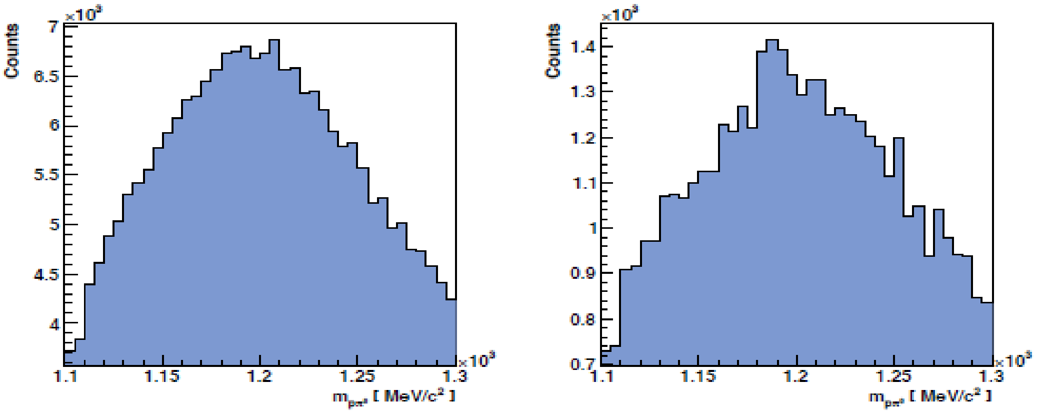

Figure 3.42: Invariant $p\pi^0$ mass distribution of all $g9a$ $\pi^+\pi^-\pi^0$ events (left) and the same mass distribution after 30 MeV cut around the K_S peak (right). The Σ^+ is hardly visible and only slightly improves after the K_S mass cut.

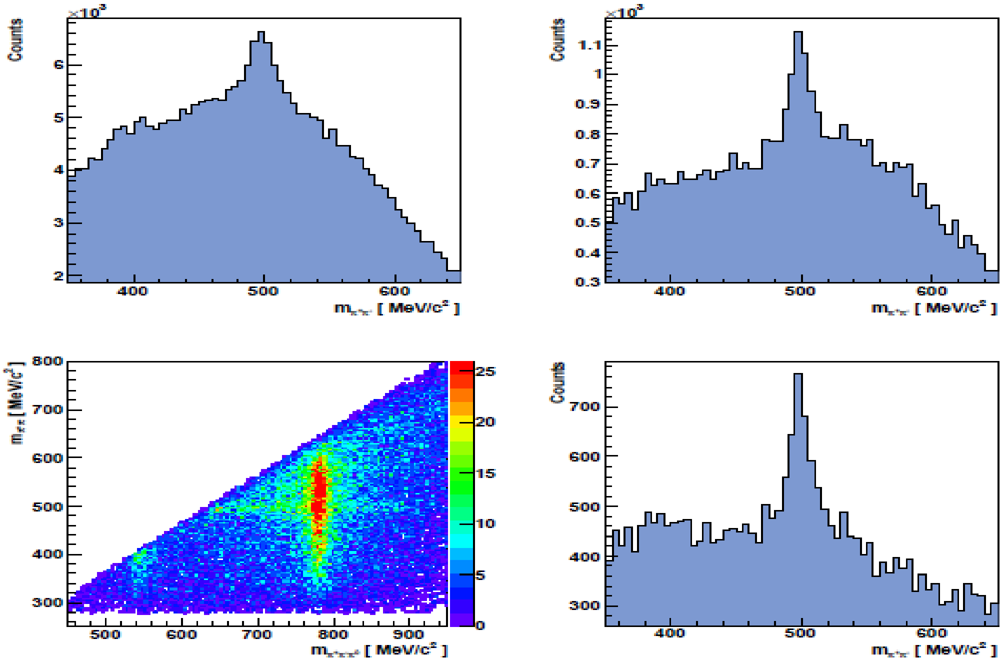

Figure 3.43: Top row: Invariant $\pi^+\pi^-$ mass distribution of all $g9a$ events (left) and the same mass distribution after a narrow cut of 20 MeV around the Σ^+ peak. Bottom row: Invariant $\pi^+\pi^-\pi^0$ mass vs. the corresponding $\pi^+\pi^-$ mass of all $g9a$ events (left) and the same invariant $\pi^+\pi^-$ mass distribution shown in the top row after the ω and the Σ^+ cuts (right).

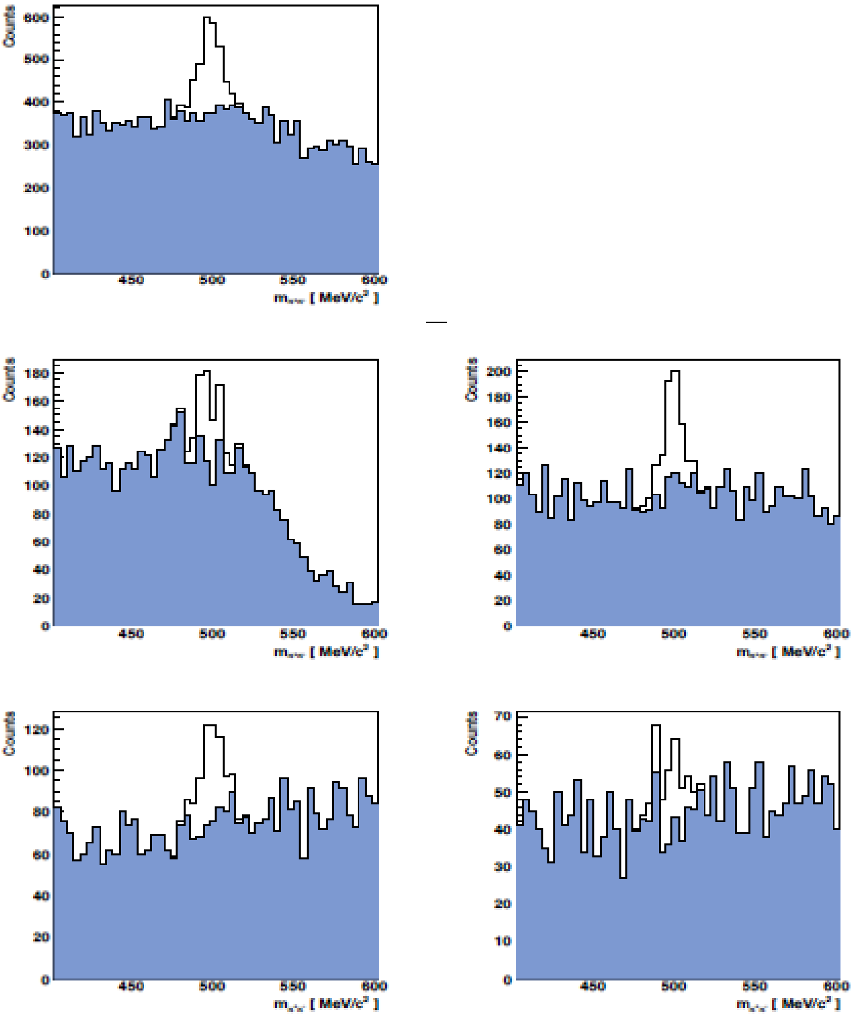

Figure 3.44: Invariant $\pi^+\pi^-$ distributions for the reaction $\gamma p \rightarrow K_S\Sigma^+$. Shown are the full statistics (top row) and 200-MeV-wode energy bins starting at $E_\gamma \in [1.1, 1.3]$ GeV (second row, left) up to $E_\gamma \in [1.7, 1.9]$ GeV (third row, right).

CHAPTER 4

GENERAL PHYSICS ANALYSIS

After all corrections and cuts were applied and signal-background separation was carried out, the extraction of cross sections (and some polarization observables) from the carefully selected events could commence. This chapter presents the methodology used in the extraction of these observables from the experimental data.

4.1 Kinematics and Observables

4.1.1 Binning and Angles in the $\gamma p \to p\,\omega$ Analysis

The kinematics of ω photoproduction off the proton can be completely described by two kinematic variables. We chose these variables to be the incident photon energy, E_γ (alternatively W), and the cosine of the polar angle of the ω meson in the center-of-mass frame, $\cos\Theta^{\omega}_{\mathrm{c.m.}}$, where the z-axis was defined along the incoming photon beam (see Figure 4.1). Alternatively, we also used the Mandelstam variable t and a representation of the differential cross sections in $\mathrm{d}\sigma/\mathrm{d}t$.

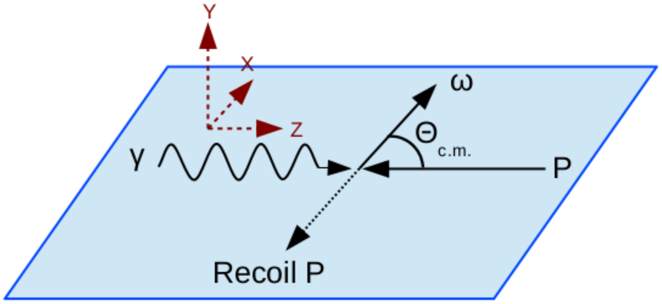

Figure 4.1: A diagram describing the kinematics of the reaction $\gamma p \to p\,\omega$. The blue plane represents the center-of-mass production plane composed of the initial photon and the recoiling proton. The angle $\Theta_{c.m.}$ denotes the angle between the initial proton and the ω meson in the center-of-mass system. The z-axis is chosen to be along the direction of the incoming photon beam. The y-axis is defined as $\hat{y} = \frac{\hat{p}_{rec} \times \hat{z}}{|\hat{p}_{rec} \times \hat{z}|}$, where $\hat{p}_{rec}$ is a unit vector along the momentum of the recoil proton. The x-axis then lies in the production plane. Image source [34].

We have extracted differential cross sections, $\mathrm{d}\sigma/\mathrm{d}\Omega$ and $\mathrm{d}\sigma/\mathrm{d}t$, as well as spin-density matrix elements (SDMEs) from the $g12$ data sets, for the incident-photon energy range $1.5 < E_\gamma < 5.4$ GeV or $1.92 < W < 3.3$ GeV. The data were binned in 20-MeV-wide W bins for the differential cross sections, and in 20-MeV-wide W bins for the SDMEs, and both covered an energy range from $1.92 < W < 3.3$ GeV. Note that CLAS had poor acceptance for three-track events in the very forward and backward directions in the center-of-mass frame.

We have also extracted one double polarization observable, which is the helicity asymmetry, E, from the $g9a$ data sets, for the incident-photon energy range $1.1 < E_\gamma < 2.3$ GeV. The data were binned in 100-MeV-wide E_γ bins 6.2.1.

4.1.2 Binning and Angles in the $\gamma p \to K^0\,\Sigma^+$ Analysis

The $K^0\,\Sigma^+$ final state is a two-body final state consisting of a meson (M) and a baryon (B), very similar to the previous reaction (M $= \omega$; B $= p$). For this reason, the kinematics is again represented by the diagram in Figure 4.1 when the recoil p is replaced with the Σ^+ and the ω is replaced with the K^0.

We have extracted the differential cross sections $\mathrm{d}\sigma/\mathrm{d}\Omega$ for the incident-photon energy range $1.15 < E_\gamma < 3.0$ GeV and the induced polarization, P, of the Σ^+ hyperon from the $g12$ data sets. For the cross sections, we have used 50-MeV-wide E_γ bins in the incident-photon energy and 0.1-wide angle bins in $\cos\Theta^{K_S}_{\mathrm{c.m.}}$.

The angular distribution of the decay nucleon is given by [64, 65]:

$$W\,(\Theta_N)\;=\;\frac{1}{2}\,(1\,+\,\alpha\,P\cos\,(\Theta_N))\,, \tag{4.1}$$

where the parameter P denotes the hyperon polarization and Θ_N is the decay angle of the nucleon measured with respect to the normal of the production plane of K^0_S and Σ^+ in the Σ^+ rest frame. For the recoil polarization, we have used 100-MeV-wide E_γ bins in the incident-photon energy and 0.1-wide angle bins in $\cos\Theta_{\,\mathrm{c.m.}}$ of the K_S.

We have also extracted the helicity asymmetry, E, for the reaction $\gamma p \to K^0\,\Sigma^+$ from the $g9a$ data sets, for the incident-photon energy range $1.1 < E_\gamma < 2.1$ GeV. The data were binned in 200-MeV-wide E_γ bins and and 0.4-wide angle bins in $\cos\Theta^{K_S}_{\mathrm{c.m.}}$.

4.2 Extraction of Cross Sections in $\gamma p \to p\,\omega / K^0\,\Sigma^+$ from the $g12$ Data Sets

The differential cross sections for all reactions were determined according to

$$\frac{\mathrm{d}\sigma}{\mathrm{d}\Omega} \;=\; \frac{N_{\text{reaction}}}{A_{\text{reaction}}}\;\frac{1}{N_\gamma\,\rho_{\text{target}}}\;\frac{1}{\Delta\Omega}\;\frac{1}{BR}\,, \tag{4.2}$$

where

ρ_{target} : target area density
N_{reaction} : number of reconstructed data events in an (E_γ, $\cos\theta_{\text{c.m.}}$) or (W, $\cos\theta_{\text{c.m.}}$) bin
N_γ : number of photons in an E_γ bin (photon flux)
A_{reaction} : acceptance in an (E_γ, $\cos\theta_{\text{c.m.}}$) or (W, $\cos\theta_{\text{c.m.}}$) bin
$\Delta\Omega$: solid-angle interval $\Delta\Omega = 2\pi\,\Delta\cos(\theta_{\text{c.m.}})$
BR : decay branching fraction.

The target area density, i.e. the number of atoms in the target material per cross-sectional area (orthogonal to the photon beam), is given by

$$\rho_{\text{target}} \;=\; 2\,\frac{\rho(\mathrm{H_2})\,N_A\,L}{M_{\text{mol}}\,(\mathrm{H_2})}\,, \tag{4.3}$$

where $\rho(\mathrm{H_2}) = 0.0711 \pm 1.75\cdot 10^{-5}$ g/cm^3 [46] is the density of the liquid hydrogen target used in the $g12$ experiment, and $M_{\text{mol}} = 2.01588$ g/mol is the molar mass of liquid $\mathrm{H_2}$. $N_A = 6.022\cdot 10^{23}$ mol^{-1} is the Avogadro number and $L = 40.0$ cm the length of the $g12$-target cell. The factor of two accounts for the molecular composition of hydrogen ($\mathrm{H_2}$).

We have used a value of $\rho_{\text{target}} = 16.992\,\cdot\,10^{-7}\mu\mathrm{b}^{-1}$ for all cross sections.

An object's solid angle in steradians is equal to the area of the segment of a unit sphere, centered at the angle's vertex, that the object covers. A solid angle in steradians equals the area of a segment of a unit sphere in the same way a planar angle in radians equals the length of an arc of a unit circle. The solid angle of a sphere measured from any point in its interior is 4π sr. In spherical coordinates:

$$\Omega \;=\; \iint\limits_S \sin\theta\,\mathrm{d}\theta\,\mathrm{d}\phi \;=\; 2\cdot 2\pi \;=\; 4\pi\,, \tag{4.4}$$

where 2π originates from integrating over $\mathrm{d}\phi$ and the factor of 2 from integrating over $\sin\theta\,\mathrm{d}\theta$. Since the differential cross sections are integrated over ϕ_{lab}, but are binned in $\cos\theta_{\text{c.m.}}$, we used

$\Delta\Omega = 2\pi\, \Delta\cos(\theta_{\text{c.m.}})$ in Equation 4.2 and $\Delta\cos(\theta_{\text{c.m.}}) = 2\ /\ (\#\text{ of angle bins})$:

$$\Delta\Omega \;=\; 2\pi \,\cdot\, 2\,/\,20 \;=\; 0.6283. \tag{4.5}$$

We have used the following values [52] for the branching fraction of our channels:

$p\,\omega$: Fraction $\Gamma_i\,/\,\Gamma = (89.2 \pm 0.7)\,\%$ ($\omega \,\rightarrow\, \pi^+\pi^-\pi^0$), i.e. $BR \,=\, 0.892$.

$K^0\,\Sigma^+$: Fraction $\Gamma_i\,/\,\Gamma = (69.20 \pm 0.05)\,\%$ ($K_S \,\rightarrow\, \pi^+\pi^-$) as well as
$\Gamma_i\,/\,\Gamma = (51.57 \pm 0.30)\,\%$ ($\Sigma^+ \,\rightarrow p\,\pi^0$), i.e. $BR \,=\, 0.5 \,\cdot\, 0.5157 \,\cdot\, 0.6920 \,=\, 0.1784$.

The factor of 0.5 for $K^0\,\Sigma^+$ accounts for the mixture of K^0 being 50 % K_S and 50 % K_L.

For the absolute normalization, we have used the standard CLAS GFLUX package which was originally developed by James Ball and Eugene Pasyuk [67]. A detailed description on how to use GFLUX for the CLAS-g12 experiment can be found in Ref. [46]. Table 4.1 gives the actual numbers we have used for all cross sections: $\gamma p \rightarrow p\,\omega$ and $\gamma p \rightarrow K_S\,\Sigma^+$.

CEBAF delivers electrons in bunches separated by 2 ns. Increasing the current in the accelerator increases the number of electrons in each bunch. Most of the g12 data were recorded at high curents of 60 - 65 nA, which corresponded to a photon flux of about $5 \times 10^8\,\gamma$ per second. The high current of the g12 experiment led to some ambiguity in selecting the correct photon for some events. About 14.26 % of all events had more than one incident photon that passed the *coincidence-time* cut or $|\Delta\, t_{\text{TGPB}}| \,<\, 1$ ns (Section 3.3.1).

In the determination of the cross sections, we had to correct for the 14.26 % of all events which had more than one photon candidate within the allowed coincidence-time window. Since the Monte Carlo did not simulate the incident photons and the corresponding timing, we corrected the photon flux by 85.74 % or simply multiplied the signal yield by $1\,/\,0.8574 \;=\; 1.166$.

4.3 Extraction of Spin-Density Matrix Elements in $\gamma p \rightarrow\, p\omega$ from the $g12$ Data Sets

The decay distribution of the ω meson yields information about its polarization. This polarization information can also be used to gain insight into the nature of the production amplitudes. The description of the angular distribution of the decay-plane normal relative to the production rest frame is often referred to as Schilling equation [68]. Since the ω is a spin-1 particle, its polarization information contained in the spin-density matrix has nine complex elements. For an unpolarized photon beam however, parity, hermiticity and normalization reduce the number of independent elements to four real quantities, three of which are measurable. These are typically chosen to be ρ^0_{00}, ρ^0_{1-1} and $\mathrm{Re}(\rho^0_{10})$.

The Schilling equation for the normalized angular distribution in vector-meson photoproduction using an unpolarized beam and an unpolarized target is given by:

$$\begin{aligned}\frac{dN}{d\cos\theta\, d\phi} &= W(\theta,\phi)\\ &= \frac{3}{4\pi}\left(\frac{1}{2}(1-\rho^0_{00}) + \frac{1}{2}(3\rho^0_{00}-1)\cos^2\theta - \rho^0_{1-1}\sin^2\theta\,\cos 2\phi - \sqrt{2}\,Re(\rho^0_{10})\sin 2\theta\cos\phi\right),\end{aligned} \tag{4.6}$$

where the (θ,ϕ) distribution is defined in the *Adair* frame. If the four-momentum of the incident photon and ω meson in the overall center-of-mass frame are denoted by k and q, respectively, the coordinate system in the Adair frame is defined as:

$$\hat{z} = \hat{k} \qquad \hat{y} = \frac{\vec{k}\times\vec{q}}{|\vec{k}\times\vec{q}|} \qquad \hat{x} = \hat{y}\times\hat{z}. \tag{4.7}$$

The decay angles are defined as:

$$\cos\theta = \hat{\pi}\cdot\hat{z} \tag{4.8}$$

$$\cos\phi = \frac{\hat{y}\cdot(\hat{z}\times\hat{\pi})}{|\hat{z}\times\hat{\pi}|} \qquad \sin\phi = -\frac{\hat{x}\cdot(\hat{z}\times\hat{\pi})}{|\hat{z}\times\hat{\pi}|}, \tag{4.9}$$

where $\hat{\pi}$ is equal to the normal to the decay plane in the ω rest frame.

The set of Spin-Density Matrix Elements (SDMEs) for each $(\cos^{\omega}_{\mathrm{c.m.}}, \sqrt{s})$ bin can be extracted using the event-based Extended Maximum Likelihood Method (EMLM). We begin by defining the likelihood function as:

$$\mathcal{L} = \left(\frac{\bar{n}^n}{n!}e^{-\bar{n}}\right)\prod_i^n \mathcal{P}(\vec{x}, X_i), \tag{4.10}$$

where the term in parentheses is the Poisson probability of obtaining n events with the expected value $\bar{n}$. $\mathcal{P}(\vec{x}, X_i)$ is the probability density function of event i with parameter set $\vec{x}$ and kinematic factors X_i.

The goal is to find the set of parameters $\vec{x} = \{\rho^0_{00}, \rho^0_{1-1}, Re(\rho^0_{10})\}$ that maximizes $\mathcal{L}$. The likelihood function in the form of Eqn. 4.10, when iterated over a large number of events, grows quickly to very large values. Since the natural logarithm is a monotonously-increasing function, it is computationally easier to work with $-\ln\mathcal{L}$ instead of $\mathcal{L}$. Thus, minimizing $-\ln\mathcal{L}$ is equivalent to maximizing $\mathcal{L}$. From Eqn. 4.10, we can write the *log likelihood* as:

$$-\ln\mathcal{L} \,=\, -n\ln\bar{n} \,+\, \ln n! \,+\, \bar{n} \,-\, \sum_i^n \ln\mathcal{P}(\vec{x},\, X_i)\,. \tag{4.11}$$

The probability density for each event is proportional to the production cross section $\sigma_{\gamma p \to p\,\omega}\,(X_i)$, the decay amplitude $A_{\omega \to \pi^+\pi^-\pi^0}\,(X_i)$, the normalized angular distribution $W(\vec{x},\, X_i)$, and the detector acceptance $\eta\,(X_i)$. Therefore, we can write the probability density as:

$$\mathcal{P}(\vec{x}, X_i) \,=\, \frac{\sigma_{\gamma p \to p\,\omega}\,(X_i)\,A_{\omega \to \pi^+\pi^-\pi^0}\,(X_i)\,W(\vec{x},\, X_i)\,\eta(X_i)}{\int \sigma_{\gamma p \to p\,\omega}\,(X_i)\,A_{\omega \to \pi^+\pi^-\pi^0}\,(X_i)\,W(\vec{x},\, X_i)\,\eta(X_i)\,d\Phi}\;. \tag{4.12}$$

The goal is to measure the set of $\vec{x} = \{\rho^0_{00},\, \rho^0_{1-1},\, Re\rho^0_{10}\}$ for each $(\cos^{\omega}_{\text{c.m.}},\, \sqrt{s})$ bin. Since the production cross section, $\sigma_{\gamma p \to p\,\omega}\,(\cos^{\omega}_{c.m},\, \sqrt{s})$, is just a number, it can be dropped from the probability density function:

$$\mathcal{P}(\vec{x}, X_i) \,=\, \frac{A_{\omega \to \pi^+\pi^-\pi^0}\,(X_i)\,W(\vec{x},\, X_i)\,\eta(X_i)}{\int A_{\omega \to \pi^+\pi^-\pi^0}\,(X_i)\,W(\vec{x},\, X_i)\,\eta(X_i)\,d\Phi}\;. \tag{4.13}$$

The cross section for ω photoproduction is defined as:

$$\sigma_{\gamma p \to p\,\omega} \,=\, \frac{N}{\mathcal{F}\,\rho_{\text{target}}\,l_{\text{target}}\,N_A\,/\,A_{\text{target}}}\,, \tag{4.14}$$

where N is the number of scattering events, $\mathcal{F}$ is the photon flux, ρ_{target}, l_{target}, A_{target} are the density, length, and atomic weight of the target, respectively; N_A is Avogadro's number. Therefore, the expected number of data events $\bar{n}$ is:

$$\bar{n} \,=\, \frac{\mathcal{F}\,\rho_{\text{target}}\,l_{\text{target}}\,N_A}{A_{\text{target}}}\,\sigma_{\gamma p \to p\,\omega}\int A_{\omega \to \pi^+\pi^-\pi^0}\,(X_i)\,W(\vec{x},\, X_i)\,\eta(X_i)\,d\Phi\,. \tag{4.15}$$

The log likelihood function now takes the form:

$$-\ln\mathcal{L} \,=\, T_F\,\sigma_{\gamma p \to p\,\omega}\int A_{\omega \to \pi^+\pi^-\pi^0}\,(X_i)\,W(\vec{x},\, X_i)\,\eta(X_i)\,d\Phi \,-\, \sum_i^n \ln W(\vec{x},\, X_i) \,+\, F(X_i) \,+\, C\,, \tag{4.16}$$

where

$$T_F \,=\, \frac{\mathcal{F}\,\rho_{\text{target}}\,l_{\text{target}}\,N_A}{A_{\text{target}}}\,, \tag{4.17}$$

C is a constant and $F(X_i)$ is a function that depends only on the kinematics. We can drop C and $F(X_i)$ from the Eqn. 4.16 since they do not depend on the parameters $\vec{x}$. The integration is done numerically using the *Monte Carlo* technique.

For this technique, N_{raw} events are randomly generated according to $\gamma p \to p\,\omega$, with $\omega \to \pi^+\pi^-\pi^0$ phase space. The integral can then be approximated by:

$$\int A_{\omega\to\pi^+\pi^-\pi^0}\,(X_i)\,W(\vec{x},\,X_i)\,\eta(X_i)\,d\Phi \;\approx\; \frac{\int d\Phi}{N_{\text{raw}}}\sum_i^{N_{\text{raw}}} A_{\omega\to\pi^+\pi^-\pi^0}\,(X_i)\,W(\vec{x},\,X_i)\,\eta(X_i)\,. \tag{4.18}$$

To obtain the values for $\eta(X_i)$, each event is run through a GEANT-based detector simulation package, discussed in detail in Section 3.7. This procedure simulates the acceptance of the CLAS detector by rejecting those events that do not survive the data analysis. Thus, for each event, the acceptance is $\eta(X_i) = 0$ or 1. We denote the number of accepted Monte Carlo events by N_{acc}. We can then rewrite the integral approximation as:

$$\int A_{\omega\to\pi^+\pi^-\pi^0}\,(X_i)\,W(\vec{x},\,X_i)\,\eta(X_i)\,d\Phi \;\approx\; \frac{\int d\Phi}{N_{\text{raw}}}\sum_i^{N_{\text{acc}}} A_{\omega\to\pi^+\pi^-\pi^0}\,(X_i)\,W(\vec{x},\,X_i)\,. \tag{4.19}$$

The decay amplitude $A_{\omega\to\pi^+\pi^-\pi^0}$ is proportional to the pion's momentum in the ω rest frame [63] and proportional to the λ quantity that we defined in Section 3.12.1:

$$A_{\omega\to\pi^+\pi^-\pi^0} \;\propto\; \lambda \;=\; \frac{|\vec{p}_{\pi^+}\;\times\;\vec{p}_{\pi^-}|^2}{T^2\left(\frac{T^2}{108}\;+\;\frac{mT}{9}\;+\;\frac{m^2}{3}\right)}\;, \tag{4.20}$$

where T is the sum of the $\pi^{\pm,0}$ and m is the $\pi^{\pm}$ mass.The value of λ varies between 0 and 1. Thus, the phase-space integral on the right side of Eqn. 4.19 is:

$$\int d\Phi \;=\; \int d\Omega\,d\lambda \;=\; 4\pi\,. \tag{4.21}$$

Finally, the log-likelihood function takes on the form:

$$-\ln\mathcal{L} \;=\; T_F\,\sigma_{\gamma p\to p\,\omega}\,\frac{4\pi}{N_{\text{raw}}}\sum_i^{N_{\text{acc}}}\lambda_i\,W(\vec{x},\,X_i) \;-\; \sum_i^{n}\ln W(\vec{x},\,X_i)\,. \tag{4.22}$$

After obtaining the Q value for each event, which provides the probability that the event is a $p\,\omega$ event, this Q value can be used to weight the event's contribution to the log likelihood:

$$-\ln\mathcal{L} \;=\; T_F\,\sigma_{\gamma p\to p\,\omega}\,\frac{4\pi}{N_{\text{raw}}}\sum_i^{N_{\text{acc}}}\lambda_i\,W(\vec{x},\,X_i) \;-\; \sum_i^{n} Q_i\,\ln W(\vec{x},\,X_i)\,, \tag{4.23}$$

where Q_i is the Q value for event i. The CERNLIB package MINUIT was used to minimize $-\ln\mathcal{L}$. The minimization algorithm that we used is called MIGRAD.

4.4 Extraction of the Hyperon Polarization in $\gamma p \to K^0\,\Sigma^+$ from the $g12$ Data Sets

The Σ^+ is produced via the electromagnetic (or strong) interaction but decays to a proton and a π^0 via the weak interaction. Since the weak decay violates parity, the polarization of the Σ^+ can be extracted from the angular distribution of one of the decay products in the Σ^+ rest frame. This observable is called recoil (or induced) polarization and is named P (Eqn. 4.1).

The kinematic situation is shown schematically in Fig. 4.2. The incident photon and the recoiling K^0 define the reaction plane. The angular distribution of the proton in the Σ^+ rest frame is then described by (see Eqn. 4.1):

$$W(\theta_p) \,=\, \frac{1}{2}\,(1 \,+\, \alpha P\,\cos{(\theta_p)})\,,$$

where θ_p is the angle between the proton momentum vector in the Σ^+ rest frame and the normal of the reaction plane. The parameter α is the degree of parity mixing and for $\Sigma^+ \to p\pi^0$, has a value of $\alpha \,=\, -0.98 \pm 0.016$ [52].

To determine the polarization observable, we integrate over all the events above the reaction plane (up) as well as below the reaction plane (down). The P observable can then be expressed as:

$$P \,=\, \frac{2}{\alpha}\,\frac{\sigma_{\rm up} \,-\, \sigma_{\rm down}}{\sigma_{\rm up} \,+\, \sigma_{\rm down}}\,. \tag{4.24}$$

Since the whole detector is ϕ symmetric, acceptance effects in the enumerator and the denominator cancel out. Therefore, we can also express the polarization observable P simply in terms of count rates:

$$P \,=\, \frac{2}{\alpha}\,\frac{N_{\rm up} \,-\, N_{\rm down}}{N_{\rm up} \,+\, N_{\rm down}}\,, \tag{4.25}$$

where $N_{\rm up}$ and $N_{\rm down}$ are the number of events with the proton in the direction above and below the reaction plane, respectively.

4.5 Extraction of the Helicity Asymmetry in $\gamma p \to p\,\omega/K^0\,\Sigma^+$ from the $g9a$ Data Sets

Data with an unpolarized- or a circularly-polarized beam in combination with an unpolarized- or a longitudinally-polarized target are isotropic in the lab azimuthal angle since the polarization(s)

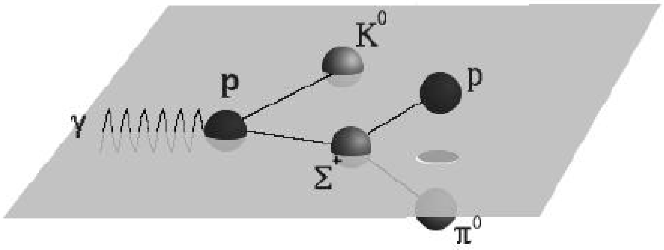

Figure 4.2: The recoil polarization of the Σ^+ shown schematically. The plane indicates the reaction plane defined by the incoming γ and the outgoing Σ^+ in the center-of-mass frame. Image source [37].

lie along the z-axis in the lab frame. Hence, the angular distribution in the lab frame of any final-state particle will be flat after an acceptance correction. In such cases, the asymmetry – in any kinematic bin – between the number of events with orthogonal polarization orientations is just a number (instead of a function of the lab azimuthal angle). The polarization observables are then easily extracted from these measured asymmetries. Thus, measuring E is a simple counting experiment.

In the case of the helicity asymmetry, E, the data were divided into two subsets based on the spin orientations of the beam and the target. Using *g9a* data, the observable could be determined seven times from the seven different *g9a* periods. Two data sets with $\rightarrow$ and $\leftarrow$ beam helicity were required and either $\Rightarrow$ or $\Leftarrow$ target polarization, wehere $\rightarrow$ ($\leftarrow$) and $\Rightarrow$ ($\Leftarrow$) indicate if the photon helicity and target polarization are parallel (antiparallel) to the beam axis.

Since the beam helicity flips at a large rate, the flux, Φ, and the acceptance, ϵ, are the same for both subsets. For the same reason, the degree of beam polarization for the two helicity states can be considered the same and is denoted by $\delta_\odot$. Then, in any kinematic bin, for the circularly-polarized beam and longitudinally-polarized target, the number of events for each helicity and spin orientation can be related to $\mathbf{E}$ using Equation 1.29. They are given by:

$$\begin{aligned} N^{\Rightarrow}_{\rightarrow} &= \Phi\,\epsilon\,\sigma_0\,(\,1\,-\Lambda_z\;\delta_\odot\,\mathbf{E}\,)\,,\\ N^{\Leftarrow}_{\rightarrow} &= \Phi\,\epsilon\,\sigma_0\,(\,1\,+\Lambda_z\;\delta_\odot\,\mathbf{E}\,)\,,\\ N^{\Rightarrow}_{\leftarrow} &= \Phi\,\epsilon\,\sigma_0\,(\,1\,+\Lambda_z\;\delta_\odot\,\mathbf{E}\,)\,,\\ N^{\Leftarrow}_{\leftarrow} &= \Phi\,\epsilon\,\sigma_0\,(\,1\,-\Lambda_z\;\delta_\odot\,\mathbf{E}\,)\,. \end{aligned} \tag{4.26}$$

where $\delta_\odot$ denotes the degree of circular-beam polarization and Λ_z indicates the degree of longitudinal-target polarization. Therefore, the helicity asymmetry, $\mathbf{E}$, in a kinematic bin is given by:

$$\begin{aligned} \mathbf{E} &= \frac{1}{\Lambda_z\,\delta_\odot}\,\frac{N^{\Rightarrow}_{\leftarrow} - N^{\Rightarrow}_{\rightarrow}}{N^{\Rightarrow}_{\leftarrow} + N^{\Rightarrow}_{\rightarrow}}\,, \\ &= \frac{1}{\Lambda_z\,\delta_\odot}\,\frac{N^{\Leftarrow}_{\rightarrow} - N^{\Leftarrow}_{\leftarrow}}{N^{\Leftarrow}_{\rightarrow} + N^{\Leftarrow}_{\leftarrow}}\,. \end{aligned} \tag{4.27}$$

If each event is assigned a weight, w_i (a Q value, for instance), then the effective number of signal events for the two beam-helicity states will be given by:

$$N' = \sum_{i=1}^{N} w_i\,. \tag{4.28}$$

The asymmetry is then formed from these effective counts.

Table 4.1: Total g12 photon flux for 50-MeV-wide incident photon-energy bins used in our analyses for the run range 56521 - 56646 (Period 2).

E_γ [GeV]	Photon Flux	E_γ [GeV]	Photon Flux	E_γ [GeV]	Photon Flux
		2.50 - 2.55	302735185984.0	4.00 - 4.05	140606283698.0
		2.55 - 2.60	259964248500.0	4.05 - 4.10	149223684420.0
1.10 - 1.15	4337260656.3	2.60 - 2.65	254886921499.0	4.10 - 4.15	140423638221.0
1.15 - 1.20	337833236168.0	2.65 - 2.70	259744931434.0	4.15 - 4.20	167418318127.0
1.20 - 1.25	574495330532.0	2.70 - 2.75	224963728409.0	4.20 - 4.25	152175155236.0
1.25 - 1.30	496274905472.0	2.75 - 2.80	203753682420.0	4.25 - 4.30	160068141472.0
1.30 - 1.35	485238697908.0	2.80 - 2.85	242060106771.0	4.30 - 4.35	128465044374.0
1.35 - 1.40	349080941294.0	2.85 - 2.90	238390370808.0	4.35 - 4.40	90453090800.2
1.40 - 1.45	508526554976.0	2.90 - 2.95	231067058790.0	4.40 - 4.45	64699027048.5
1.45 - 1.50	497502848514.0	2.95 - 3.00	201595160599.0	4.45 - 4.50	158368725065.0
1.50 - 1.55	460473338930.0	3.00 - 3.05	233214036559.0	4.50 - 4.55	158892370026.0
1.55 - 1.60	399150479194.0	3.05 - 3.10	184728636406.0	4.55 - 4.60	136955763789.0
1.60 - 1.65	446872653860.0	3.10 - 3.15	213765127885.0	4.60 - 4.65	137198213594.0
1.65 - 1.70	395792605738.0	3.15 - 3.20	164173778322.0	4.65 - 4.70	139594283568.0
1.70 - 1.75	415054272952.0	3.20 - 3.25	199344803385.0	4.70 - 4.75	142168709686.0
1.75 - 1.80	408411797706.0	3.25 - 3.30	207673397085.0	4.75 - 4.80	102093637851.0
1.80 - 1.85	397650894046.0	3.30 - 3.35	178704643413.0	4.80 - 4.85	123160541637.0
1.85 - 1.90	345708998882.0	3.35 - 3.40	196705358312.0	4.85 - 4.90	147419199730.0
1.90 - 1.95	365121651368.0	3.40 - 3.45	191004264574.0	4.90 - 4.95	155283230557.0
1.95 - 2.00	304992117538.0	3.45 - 3.50	179980234595.0	4.95 - 5.00	120930458861.0
2.00 - 2.05	336131767024.0	3.50 - 3.55	77594303520.0	5.00 - 5.05	116822823306.0
2.05 - 2.10	347415226190.0	3.55 - 3.60	284139117094.0	5.05 - 5.10	150662097632.0
2.10 - 2.15	291012042438.0	3.60 - 3.65	186509696181.0	5.10 - 5.15	139170116274.0
2.15 - 2.20	329423974509.0	3.65 - 3.70	155345103910.0	5.15 - 5.20	129656508095.0
2.20 - 2.25	349551671915.0	3.70 - 3.75	159517908396.0	5.20 - 5.25	137811011294.0
2.25 - 2.30	260462654486.0	3.75 - 3.80	160555585107.0	5.25 - 5.30	116376757558.0
2.30 - 2.35	306607804116.0	3.80 - 3.85	170460273002.0	5.30 - 5.35	135718523976.0
2.35 - 2.40	289476321935.0	3.85 - 3.90	162365775438.0	5.35 - 5.40	125968316090.0
2.40 - 2.45	256426694871.0	3.90 - 3.95	164569658388.0	5.40 - 5.45	134541705938.0
2.45 - 2.50	241361136501.0	3.95 - 4.00	173623146606.0	5.40 - 5.45	134541705938.0
				5.45 - 5.50	

CHAPTER 5

SYSTEMATIC UNCERTAINTIES

5.1 Systematic Uncertainties in the $g12$ Experiment

5.1.1 Contribution from the Q- Factor Method

Assigning a Q value to a particular event required to fit the mass distribution of the event and its neighbors using the likelihood technique. The covariance matrix, C_η, for the set of fit parameters, $\vec{\eta}$, could be used to determine the uncertainty of the Q value for the given event:

$$\sigma_Q^2 \,=\, \sum_{i,\,j} \frac{\partial Q}{\partial \eta_i} \left(C_\eta^{-1} \right) \frac{\partial Q}{\partial \eta_j} \,. \tag{5.1}$$

The Q factor method led to some correlations among events and their nearest neighbors because events could serve as neighbors for many *seed* events. The systematic "correlation" uncertainty of the ω yield due to this method in a particular kinematic bin was then given by:

$$\sigma_\omega^2 \,=\, \sum_{i,\,j} \sigma_Q^i \, \rho_{ij} \, \sigma_Q^j \,, \tag{5.2}$$

where the sum $i,\, j$ was taken over the events in the bin, σ_Q^i and σ_Q^j were the fit uncertainties for events i and j, and ρ_{ij} was the correlation factor between events i and j. The correlation factor simply represented the fraction of shared nearest-neighbor events.

If we assumed 100 % correlation between events in a kinematic bin, then the uncertainty of the ω yield could be written as:

$$\sigma_\omega^2 \,=\, \Big(\sum_i^N \sigma_Q^i \Big)^2 \,. \tag{5.3}$$

This assumption could significantly overestimate the uncertainty. In this analysis, we did not use the assumption of 100 %- correlated events but properly determined the uncertainties according to Eqn. 5.2. The uncertainty contribution from the Q-factor method could then be added to the statistical uncertainty to obtain the total "statistics-based" uncertainty:

$$\sigma^2 \,=\, \sigma_\omega^2 \,+\, \sigma_{\text{statistical}}^2 \,. \tag{5.4}$$

We also implemented this procedure for all other channels.

Propagation of the Uncertainty from the Q- Factor Method. Consider a *simple* counting experiment, for example the determination of the induced polarization in the decay of the Σ^+ hyperon (Eqn. 4.25):

$$P = \frac{2}{\alpha}\,\frac{N_{\rm up} - N_{\rm down}}{N_{\rm up} + N_{\rm down}} = \frac{2\,A}{\alpha}\,,$$

where $N_{\rm up}$ and $N_{\rm down}$ were the total number of events with the proton in the direction above and below the reaction plane, respectively. The uncertainty in the Q value of each event only affected the counts, and not the parameter α. Equation 5.2 showed that the uncertainty of the count in a particular bin due to the Q-factor method was:

$$\sigma_N^2 = \sum_{i,\,j} \sigma_Q^i\,\rho_{ij}\,\sigma_Q^j\,,$$

where σ_Q^i is the fit uncertainty in the Q value of the $i^{\rm th}$ event, N is the total number of events and ρ_{ij} is the correlation between the $i^{\rm th}$ and the $j^{\rm th}$ event (which is equal to the fraction of the number of common nearest neighbors. Depending on the available statistics in an analysis, it is often more convenient to assume that all events are 100 % correlated and to overestimate the uncertainties than to calculate the actual correlations, ρ_{ij}. This can be very time consuming and computationally demanding. In our g12 analysis, we chose to find the actual correlations because we found that σ_N was significantly over (under)estimated when 100 % (0 %) correlation between events was assumed.

From standard error propagation, and writing P as a function of the counts, $P = f(N_{\rm up}, N_{\rm down})$:

$$\begin{aligned} \sigma_P &= \sqrt{\left(\frac{\partial f}{\partial N_{\rm up}}\right)^2 \sigma_{N_{\rm up}}^2 + \left(\frac{\partial f}{\partial N_{\rm down}}\right)^2 \sigma_{N_{\rm down}}^2} \\ &= \frac{4}{\alpha\,(N_{\rm up} + N_{\rm down})^2}\,\sqrt{N_{\rm down}^2\,\sigma_{N_{\rm up}}^2 + N_{\rm up}^2\,\sigma_{N_{\rm down}}^2}\,. \end{aligned} \tag{5.5}$$

If $\sigma_{N_{\rm up}} = \sigma_{N_{\rm down}} = \sigma_N$, the above equation simplified to:

$$\sigma_P = \frac{4\,\sigma_N}{\alpha\,(N_{\rm up} + N_{\rm down})}\,\sqrt{\frac{N_{\rm up}^2 + N_{\rm down}^2}{(N_{\rm down} + N_{\rm up})^2}}\,. \tag{5.6}$$

Therefore, $\sigma_{N_{\rm up}}$ and $\sigma_{N_{\rm down}}$ could be found by using Eqn. 5.2, and substituting them into Eqn. 5.5 then yielded σ_P. Similarly, one could follow the method outlined above to analytically find the contribution of the Q-factor method to the total systematic uncertainty in any other observable associated with a simple counting experiment (cross section measurements, for instance).

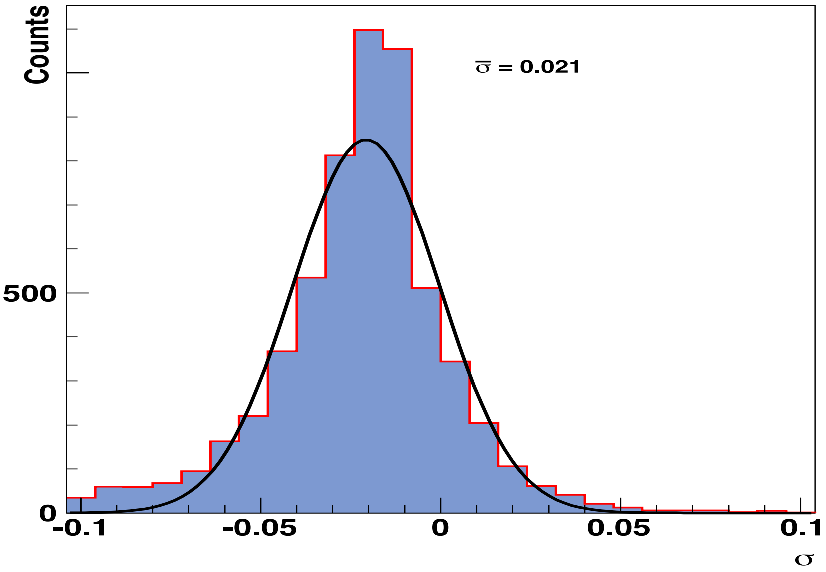

Figure 5.1: The distribution of contributions to the total systematic uncertainty from the CL cut, integrated over all energy and angle bin.

5.1.2 Contribution from the Confidence-Level Cut

Another source of the total systematic uncertainty that we considered was the confidence-level (CL) cut. The procedure to determine the uncertainty of this cut was to re-calculate the cross sections based on various CL-cut values. We have studied various CL cuts from 0.1 % to 5 %.

Denoting the originally-measured value of the differential cross section for a kinematic bin A_0, and the newly-measured value based on the new CL cut A_n, then the absolute uncertainty will be:

$$\sigma_{\text{CL}} = \frac{|A_n - A_o|}{A_o} . \tag{5.7}$$

The corresponding distribution of Eqn. 5.7 for all energy and angle bins is shown in Fig. 5.1. We fitted this distribution with a Gaussian and used the width, $\bar{\sigma} = 2.1\,\%$, as the contribution to the systematic uncertainty from the CL cut.

5.1.3 Further Contributions from the g12 Systematics

The general study of the g12 systematics has been discussed in the g12 analysis note [46] and is summarized in Table 5.1 below.

Table 5.1: Summary of contributions to the total systematic uncertainty [46].

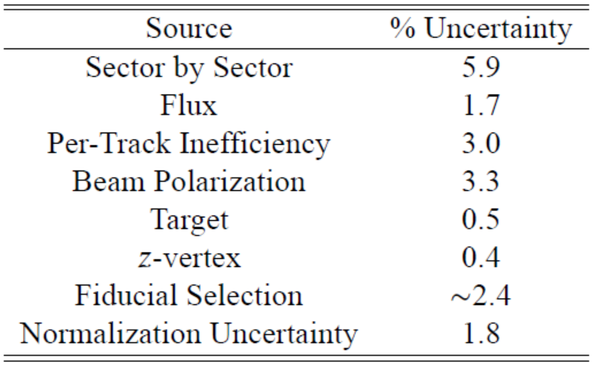

Source	% Uncertainty
Sector by Sector	5.9
Flux	1.7
Per-Track Inefficiency	3.0
Beam Polarization	3.3
Target	0.5
z-vertex	0.4
Fiducial Selection	~2.4
Normalization Uncertainty	1.8

As an example, the sector-by-sector normalization was derived using the acceptance-corrected yields for different sectors as shown in Figure 5.2. The uncertainty was calculated using the deviation of the yield in each sector from the average acceptance-corrected yield of all six sectors.

5.1.4 Contribution from the Beam Polarization

The beam-helicity asymmetry (in a simple counting experiment) is inversely proportional to the average degree of the beam polarization. This relation has been shown for the hyperon recoil-polarization P in the reaction $\gamma p \to K_S\,\Sigma^+$ (see Eqn. 4.25), where the asymmetry is inversely proportional to the parameter α. Hence, from error propagation, it is clear that any uncertainty in the determination of the average beam polarization led to the same percentage uncertainty in the polarization observable.

5.1.5 Contribution from the Beam-Charge Asymmetry

Section 3.11.3 discussed the beam-charge asymmetry in detail. Since these contributions were very small, effects on the observables were considered negligible.

5.1.6 Contribution from the Accidental Photons

In Section 3.3.1, we discussed how initial photons were selected. Even after following the full selection procedure, some accidental photons remained. The fraction could be estimated from a comparison in the yields between the central peak with the neighboring beam buckets in the coincidence-time distribution. For example, the fraction was at most 2.5 % in g12 (see Figure 5.3).

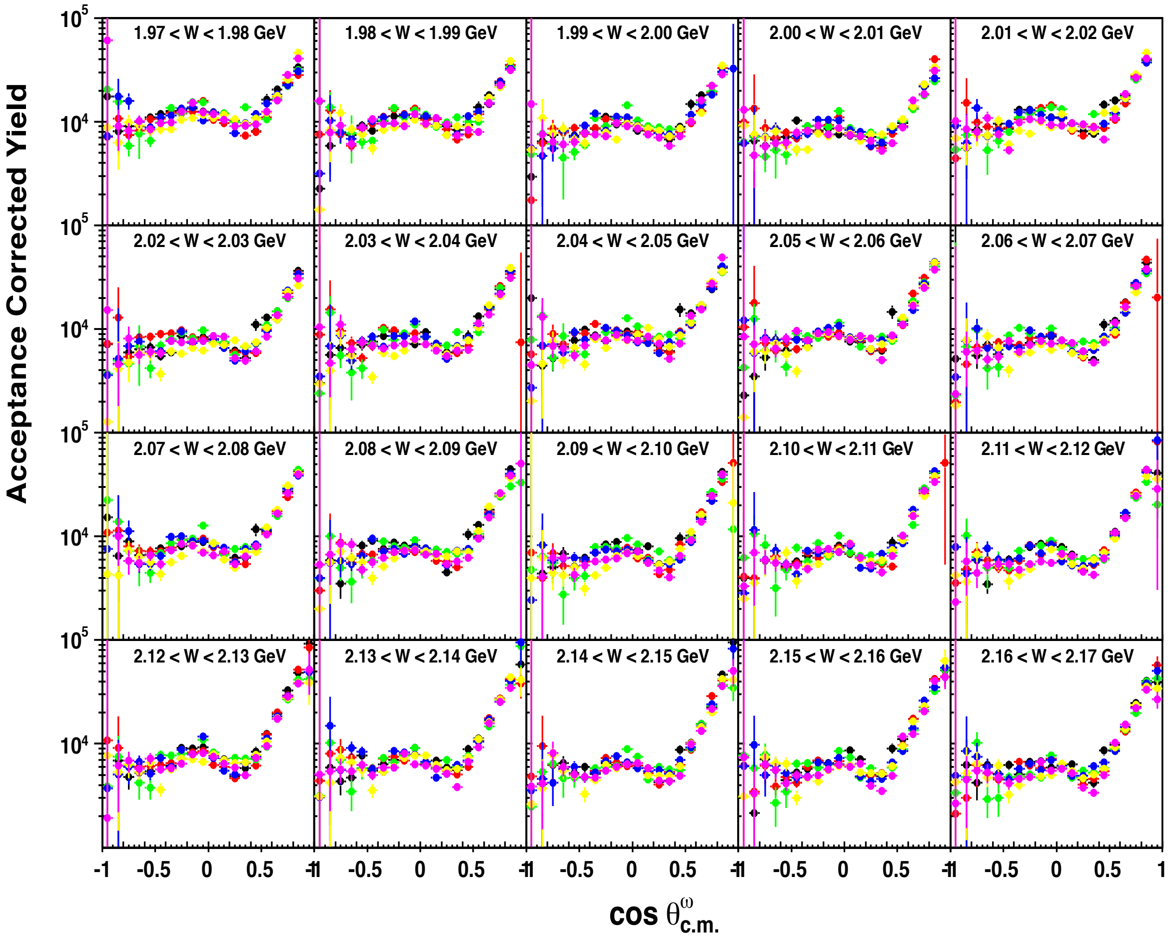

Figure 5.2: The acceptance-corrected ω yields for different sectors. The six different colors represent the six different CLAS sectors.

These accidentals led to a small overestimation in the photon flux by the same factor in all data sets. Therefore, in counting experiments, the accidentals did not affect the polarization observables since the factor canceled out in the asymmetry.

5.1.7 Systematic Uncertainties in the Determination of SDMEs

If we Taylor-expand $-\ln\mathcal{L}(\alpha)$ around $\alpha = \alpha^*$ where α^* is the correct parameter that minimizes $-\ln\mathcal{L}$:

$$-\ln\mathcal{L}(\alpha) \;=\; -\ln\mathcal{L}(\alpha^*) \;-\; (\alpha \;-\; \alpha^*)^2 \;\frac{1}{2}\,\frac{\mathrm{d}^2\ln\mathcal{L}}{\mathrm{d}\alpha^2}\bigg|_{\alpha\,=\,\alpha^*}\,, \tag{5.8}$$

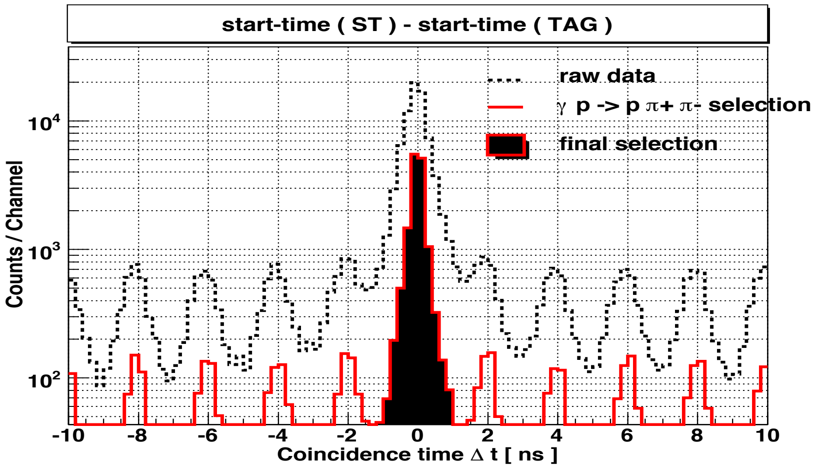

Figure 5.3: Coincidence-time distributions of tagged photons for the raw data (dotted histogram) and after applying all $\gamma p \to p\,\pi^+\pi^-$ selection cuts (solid histogram). Events of the center bins filled in black indicate the candidates of the final selection. The fraction of remaining accidental photons in the central bucket was at most 2.5 %.

then we can write $-\ln\mathcal{L}$ as:

$$-\ln\mathcal{L}(\alpha) \;=\; C\,e^{\frac{(\alpha\,-\,\alpha^*)^2}{2\sigma^2}}\,, \tag{5.9}$$

where C is a constant and $\sigma^2 = \left(\frac{d^2\ln\mathcal{L}}{d\alpha^2}\bigg|_{\alpha=\,\alpha^*}\right)^{-1}$.

Therefore, $-\ln\mathcal{L}$ shows a Gaussian distribution with σ as the statistical uncertainty that is returned by MINUIT. However, we then multiply $\ln\mathcal{L}$ by a factor of two so that it takes the approximate form of a χ-square distribution and the interpretation of the deviation is similar to the interpretation of the sum of squares in least-square regression. Therefore, the final function that needs to be minimized is $-2\ln\mathcal{L}$ which gives us:

$$\sigma^2 \;=\; \frac{1}{2}\left(\frac{d^2\ln\mathcal{L}}{d\alpha^2}\bigg|_{\alpha\,=\,\alpha^*}\right)^{-1} \tag{5.10}$$

as the statistical uncertainty.

We considered the propagated Q-value uncertainties as the systematic uncertainties for the SDMEs. The procedure was based on the variation of the Q value according to:

$$Q\,-\,\sigma_Q \,<\, Q \,<\, Q\,+\,\sigma_Q\,,$$

where σ_Q was the uncertainty of Q.

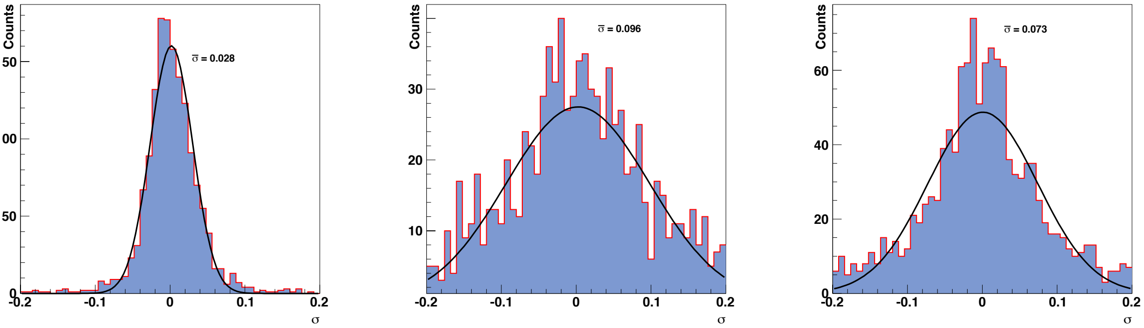

Figure 5.4: Distributions of the systematic uncertainties for the spin-density matrix elements ρ^0_{00} (top left), ρ^0_{1-1} (top right), and Reρ^0_{10} (bottom row), integrated over all energies and angles.

If we denote the originally-measured value of the SDME by A_o and the newly-determined value (based on the new Q) as A_n, then the uncertainty was calculated as

$$\sigma_\rho = \frac{|A_n - A_o|}{A_o} \,. \tag{5.11}$$

The SDMEs' uncertainty distributions – integrated over all energies and angles – are shown in Figure 5.4. We considered $\bar{\sigma} = 2.1\,\%$, $9.6\,\%$ and $7.3\,\%$ the values of the systematic uncertainties for the elements ρ^0_{00}, ρ^0_{1-1} and Re(ρ^0_{10}), respectively.

5.1.8 Total Systematic Uncertainty

The error bars shown in all preliminary results include the Q-factor uncertainties that have been combined with the statistical uncertainties in quadrature. The uncertainties stem from the relevant sources that have been described in previous sections and also include some channel-specific uncertainties, i.e. branching fractions of the decay mode. The total systematic uncertainty for each observable is listed in the table below.

5.2 Systematic Uncertainties in the $g9a$ Experiment

The overall systematic uncertainty includes uncertainties in the background-subtraction method, the degree of photon-beam and target-proton polarization, and the contributions from the electron-beam charge asymmetry. The systematic uncertainty in the ω and $K\Sigma$ yields in a kinematic bin due to the Qfactor method was obtained and propagated using the same method described in section 5.1.1. The electron-beam polarization that was toggled between h^+ and h^- helicity states at

Table 5.2: Total systematic uncertainty for each observable from the $g12$ data sets.

Source	$\gamma p \to p\,\omega$	$\gamma p \to K^0\,\Sigma^+$	P_{Σ^+}
Sector by Sector	5.9 %	5.9 %	5.9 %
Flux	1.7 %	1.7 %	1.7 %
Target	0.5 %	0.5 %	0.5 %
z-vertex	0.4 %	0.4 %	0.4 %
Fiducial Selection	2.4 %	2.4 %	2.4 %
Normalization	1.8 %	1.8 %	1.8 %
Branching Fraction	0.7 %	0.05 % and 0.3 %	-
Parity Mixing, α	-	-	0.02 %

a rate of 29.560 Hz in the $g9a$ experiment had beam-charge asymmetries, which is described in section 3.11.3. However, the contributions from this source of the systematic uncertainty were less that 0.4 % and considered negligible.

The systematic uncertainties in the degree of photon-beam and target-proton polarization are applied as global factors of 2 % and 3 %, respectively. An additional possible source of systematic uncertainty is the presence of accidental photons. The fraction of accidental photons was at most 2.5 %. It ws estimated from comparing the central peak with the neighboring electron beam buckets in the *coincidence-time* spectrum, which is defined per photon as the difference between the Tagger time and the Start Counter time at the interaction point. Accidental photons lead to an overestimation of the event numbers but drop out in the asymmetry of event counts.

CHAPTER 6

FINAL RESULTS

6.1 Results from the $g12$ Experiment

6.1.1 Results for the $\gamma p \to p\,\omega$ Reaction

The following section presents and discusses our final results in ω photoproduction. We compare with previous CLAS results whenever these are available.

Differential Cross Sections in $\gamma p \to p\,\omega$. Figures 6.2-6.7 show the differential cross sections of the reaction $\gamma p \to p\,\omega$, covering the center-of-mass energy range $1.92 < W < 3.30$ GeV. The CLAS-g12 results are shown in black. Also shown in the figures (if available) are the previous results from the CLAS-g11a experiment (red points) [25]. The uncertainties for both data sets (CLAS g11a and g12) include the Q-factor uncertainties and the statistical uncertainties added in quadrature. We simply followed the example of g11a to properly compare our results.

The results are presented in 10-MeV-wide center-of-mass energy bins, which yields a total of 130 energy bins. Please note that some g12 bins are missing due to some tagger inefficiencies: (1) $2.73 < W < 2.75$ GeV and (2) $2.55 < W < 2.61$ GeV. In general, the agreement with the previous CLAS-g11a measurements is very good. Some discrepancies at low energies are observed but toward higher energies, the agreement becomes better. In fact, the agreement can be considered excellent at center-of-mass energies above 2.18 GeV (with the exception of some bins above $W \approx 2.77$ GeV). The g12/g11a ratio distribution is shown in Figure 6.1. Note that this distribution is not necessarily expected to be Gaussian but we used a Gaussian fit to determine a mean value.

The data at $E_\gamma > 4.0$ GeV are first-time measurements with unprecendented statistical quality and will bridge the gap between these lower-energy CLAS data and data from the 12-GeV era.

Spin-Density Matrix Elements in $\gamma p \to p\,\omega$. Figure 6.9-6.23 show the spin-density matrix elements (SDMEs) – ρ^0_{00}, $\mathrm{Re}(\rho^0_{10})$, and ρ^0_{1-1} – for the reaction $\gamma p \to p\,\omega$, covering the center-of-mass energy range $1.92 < W < 3.12$ GeV. The CLAS g12 results are shown as black data points. Also

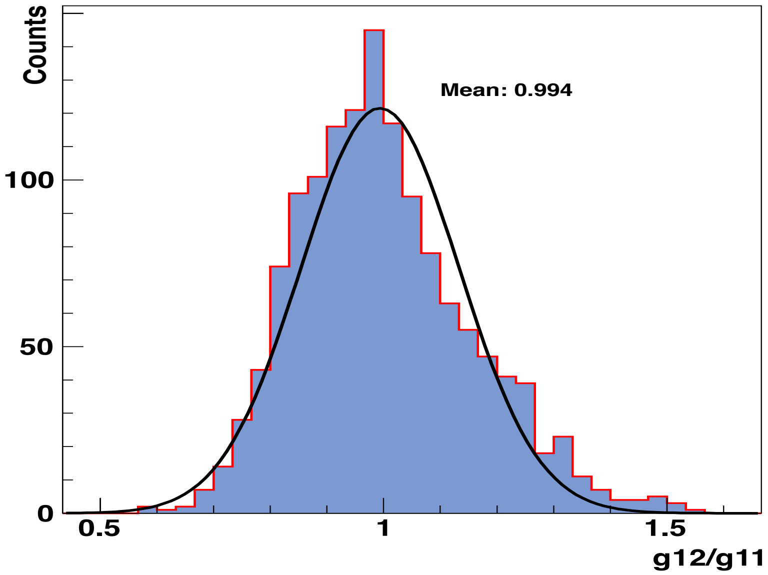

Figure 6.1: The g12/g11a ratio distribution of the $\gamma p \to p\,\omega$ cross sections results.

shown in the figure are the previous results from the CLAS-g11a experiment (red data points) [25]. The shown uncertainties for both data sets are only statistical.

The results are presented in 10-MeV-wide W bins for $1.92 < W < 2.72$ GeV, and in 20-MeV-wide energy bins for $2.72 < W < 3.12$ GeV. Please note the broken tagger modules in the g12 data at $2.73 < W < 2.75$ GeV and $2.55 < W < 2.61$ GeV. Our data are in good agreement with the previous CLAS g11a results for the element $Re(\rho^0_{10})$ results, while the agreement for the elements ρ^0_{00} and ρ^0_{1-1} is acceptable. Some discrepancies are observed in the forward direction at low energies. The high-energy results ($E_\gamma > 4.0$) GeV are first-time measurements.

6.1.2 Results for the $\gamma p \to K^0\,\Sigma^+$ Reaction

Charged K photoproduction, e.g. in $\gamma p \to K^+\,\Lambda$ and $\gamma p \to K^+\Sigma^0$, has been extensively studied in recent years at CLAS and elsewhere. However, the K^0 channel has tended to be sidelined. This appears entirely unjustified, though. To study s-channel resonance excitations, the photoproduction of neutral kaons offers some distinctive advantages over charged ones, because the photons cannot directly couple to the (vanishing) charge of the meson. Data on the isospin-related $K^0\,\Sigma^+$ and $K^+\,\Sigma^0$ channels are also important to disentangle contributions from N^* and Δ^* resonances.

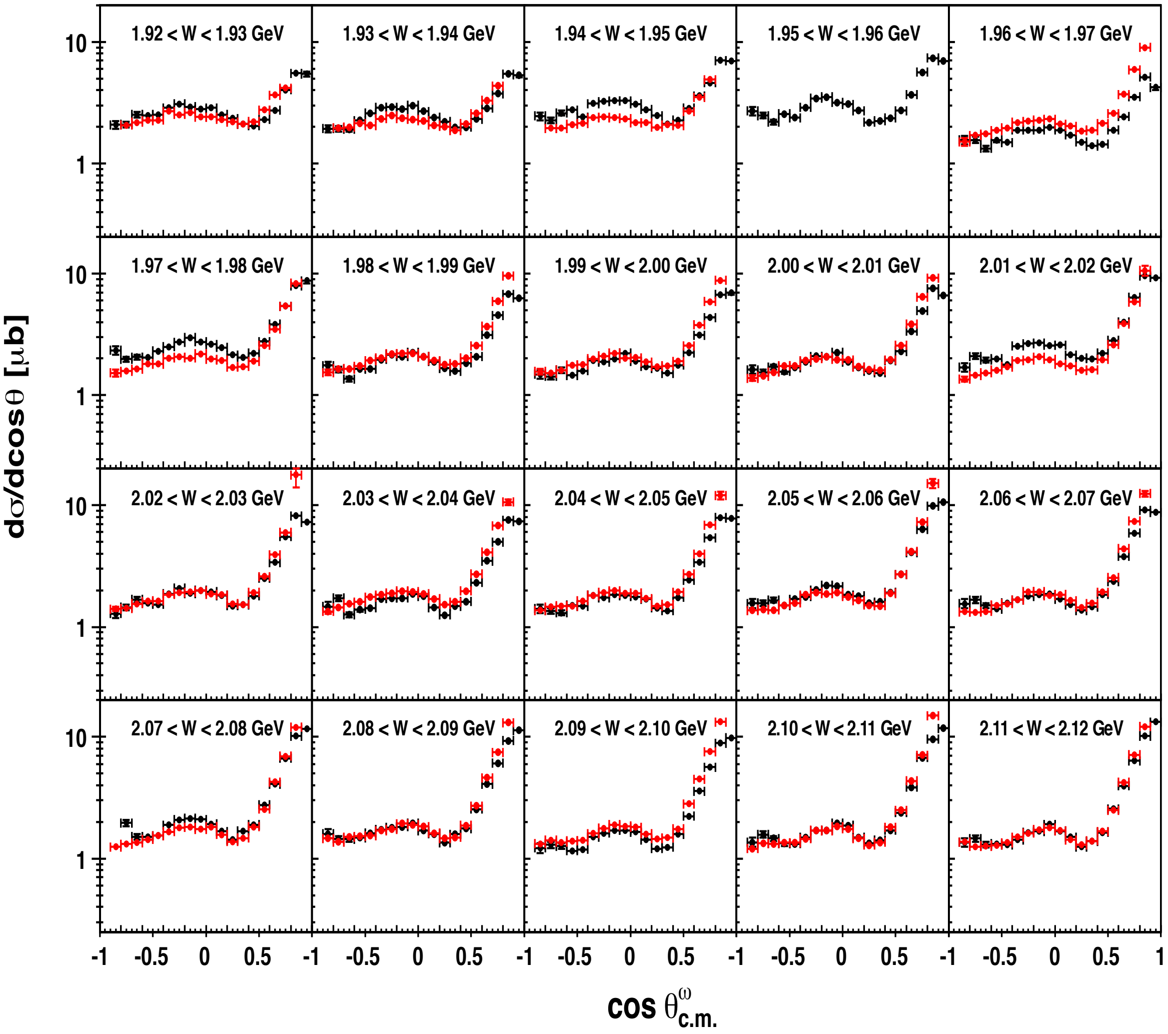

Figure 6.2: The differential cross sections in the reaction $\gamma p \to p\,\omega$ for the center-of-mass energy range $1.92 < W < 2.12$ GeV from g12 (black data points) in comparison with the previous CLAS measurements from g11a [25] (red points). The given uncertainties for both data sets comprise the statistical uncertainties and the Q-factor uncertainties added in quadrature.

At CLAS, the differential cross sections for the reaction $\gamma p \to K^0\,\Sigma^+$ have been studied using g1c data [69] and g11a data [70, 71] but results have never been published. The additional extraction of the Σ^+ hyperon transverse polarization was also part of the research of Ref. [71] and was published as a standalone analysis in Physical Review C [75].

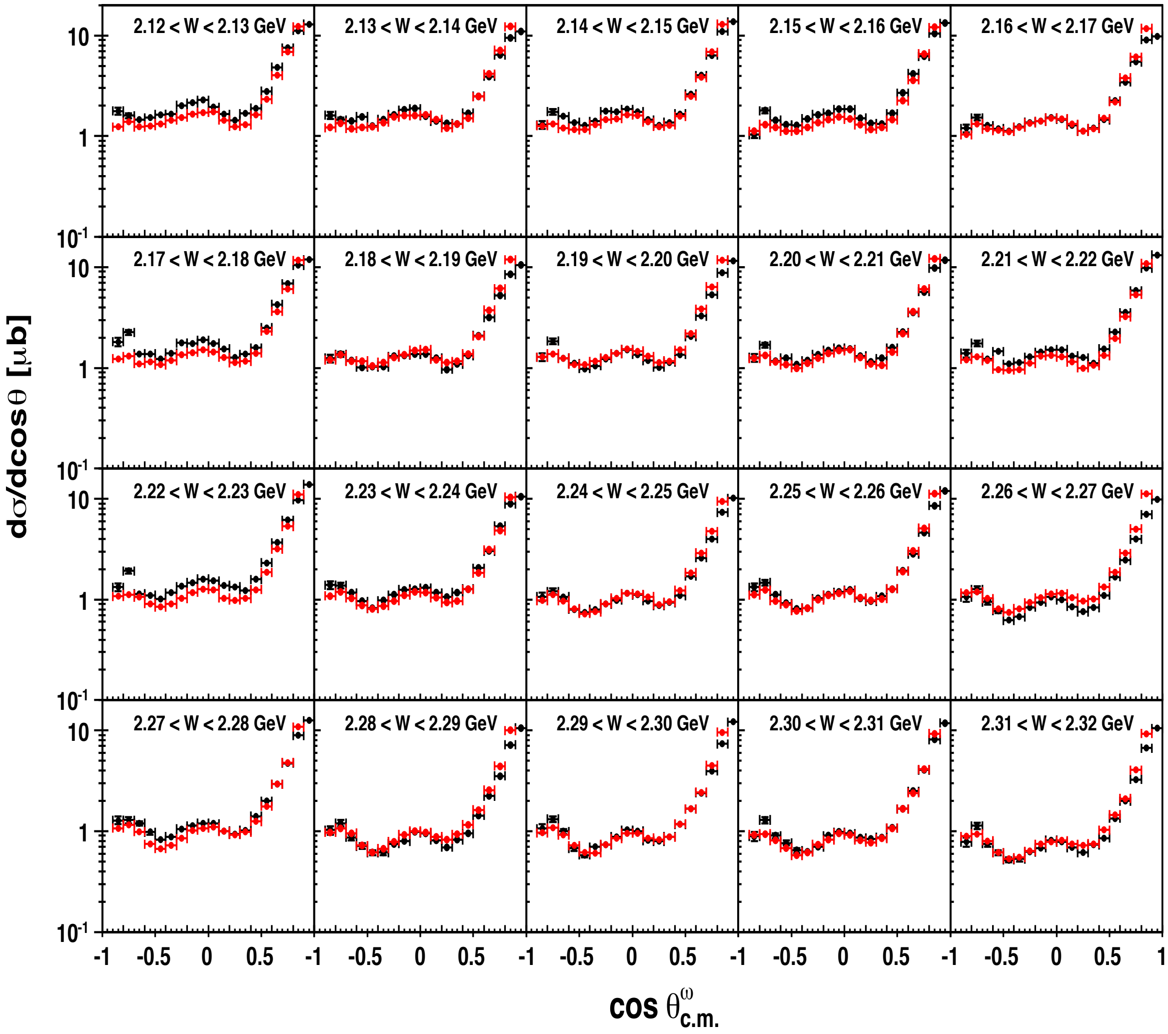

Figure 6.3: The differential cross sections in the reaction $\gamma p \to p\,\omega$ for the center-of-mass energy range $2.12 < W < 2.32$ GeV from g12 (black data points) in comparison with the previous CLAS measurements from g11a [25] (red points). The given uncertainties for both data sets comprise the statistical uncertainties and the Q-factor uncertainties added in quadrature.

Differential Cross Sections in $\gamma p \to K^0\,\Sigma^+$. Figure 6.24 and 6.25 show the g12 differential cross sections of the reaction $\gamma p \to K^0\,\Sigma^+$ in 50-MeV-wide incident-photon energy bins, covering the energy range $1.15 < E_\gamma < 2.90$ GeV. The uncertainties include the Q-factor uncertainties and the statistical uncertainties added in quadrature.

Figure 6.26 shows again our CLAS-g12 differential cross sections for the reaction $\gamma p \to K^0\,\Sigma^+$

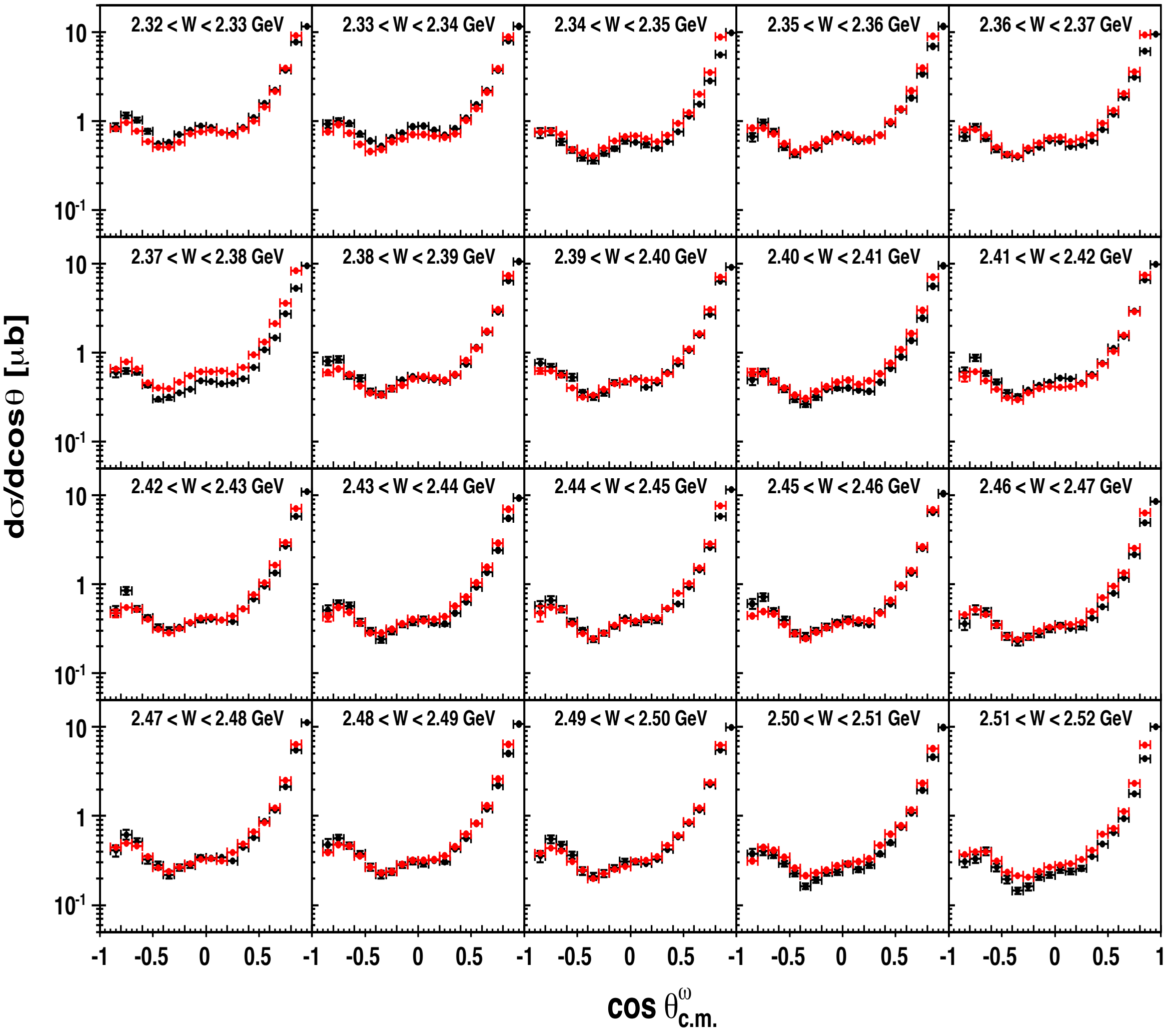

Figure 6.4: The differential cross sections in the reaction $\gamma p \to p\,\omega$ for the center-of-mass energy range $2.32 < W < 2.52$ GeV from g12 (black data points) in comparison with the previous CLAS measurements from g11a [25] (red points). The given uncertainties for both data sets comprise the statistical uncertainties and the Q-factor uncertainties added in quadrature.

(black data points), now presented in 100-MeV-wide incident-photon energy bins and covering the energy range $1.15 < E_\gamma < 2.25$ GeV. Also shown in the figure are the previous results from the CB-ELSA Collaboration (red data points) [72] and from the CBELSA/TAPS Collaboration (blue data points) [73]. We have adjusted our energy binning to these published results to facilitate the comparison. The shown uncertainties are statistical only for all data points. We consider the

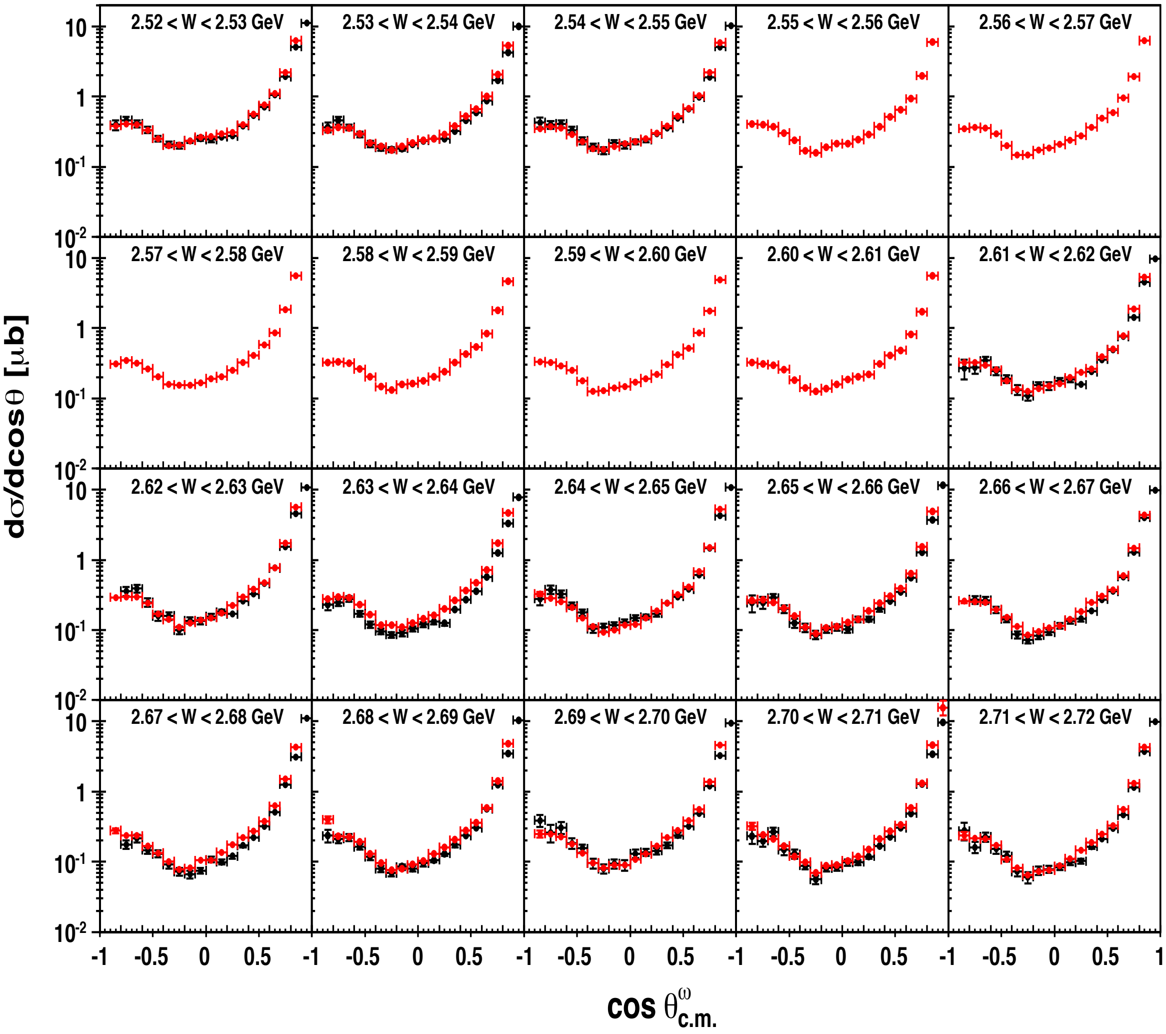

Figure 6.5: The differential cross sections in the reaction $\gamma p \to p\,\omega$ for the center-of-mass energy range $2.52 < W < 2.72$ GeV from g12 (black data points) in comparison with the previous CLAS measurements from g11a [25] (red points). The given uncertainties for both data sets comprise the statistical uncertainties and the Q-factor uncertainties added in quadrature. Please note that the g12 data suffer from broken tagger paddles in the energy range $2.55 < W < 2.61$ GeV (around $E_\gamma \approx 3.0$ GeV).

agreement among the data sets reasonably good.

In general, all data sets show a similar trend. The cross sections exhibit a flat distribution close to the reaction threshold, which indicates baryon resonance contributions, and then develop an almost linear forward-angle peaking behavior toward higher energies. The slope of these distribu-

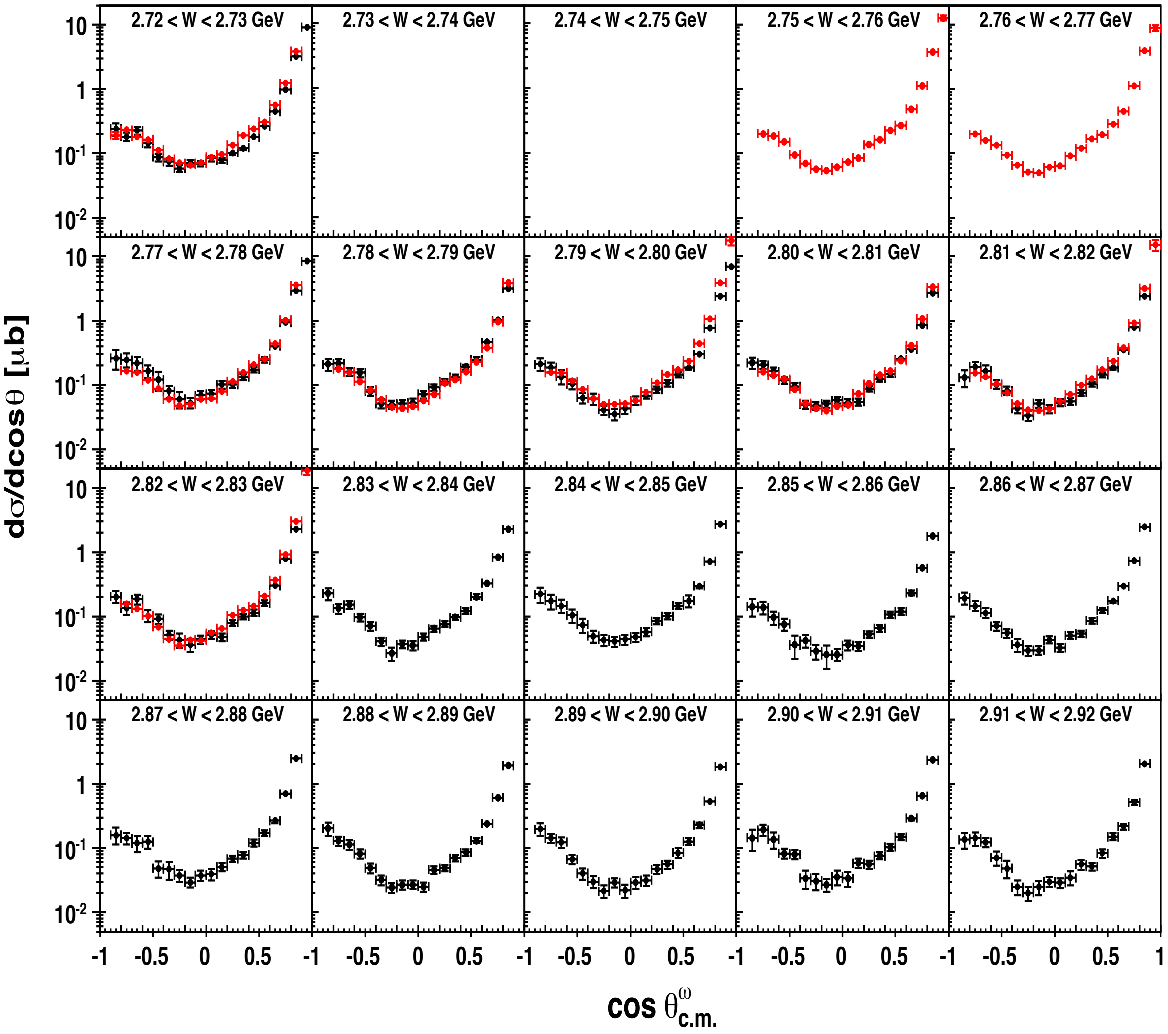

Figure 6.6: The differential cross sections in the reaction $\gamma p \to p\,\omega$ for the center-of-mass energy range $2.72 < W < 2.92$ GeV from g12 (black data points) in comparison with the previous CLAS measurements from g11a [25] (red points). The given uncertainties for both data sets comprise the statistical uncertainties and the Q-factor uncertainties added in quadrature. Please note again that the g12 data suffer from broken tagger paddles in the energy range $2.73 < W < 2.77$ GeV (around $E_\gamma \approx 3.6$ GeV).

tions starts to decrease again above $E_\gamma \approx 1.7$ GeV. Figure 6.27 shows the energy dependence of all cross section results (CLAS g12, CB-ELSA, CBELSA/TAPS) in 0.1-wide $\cos_{\text{c.m.}}$ bins for the K^0.

The CBELSA/TAPS Collaboration previously reported on an anomaly [73] which was considered visible in the CBELSA/TAPS data as a sudden drop of the cross section at forward angles

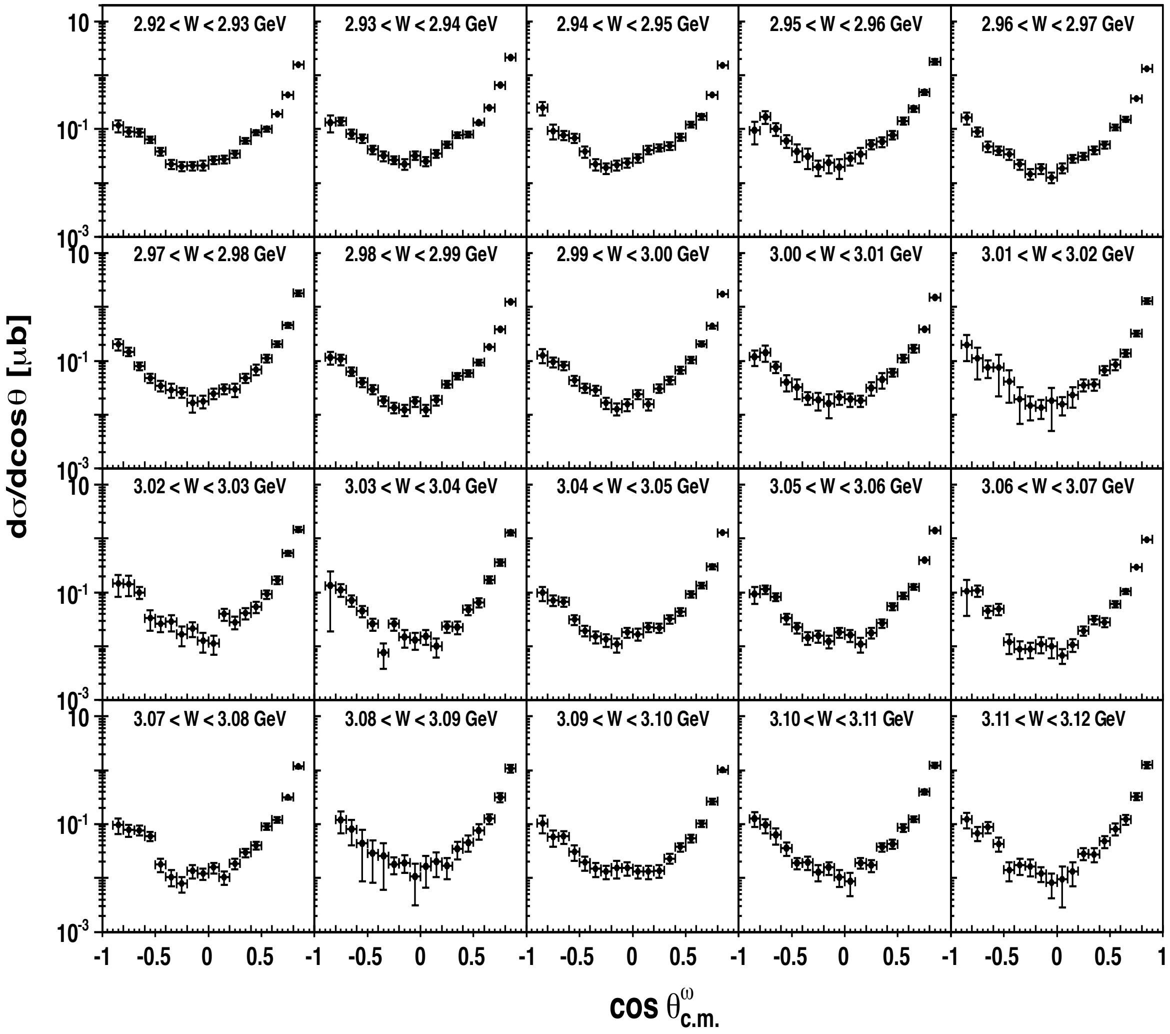

Figure 6.7: The differential cross sections in the reaction $\gamma p \to p\,\omega$ for the center-of-mass energy range $2.92 < W < 3.12$ GeV from g12 (black data points). The given uncertainties comprise the statistical uncertainties and the Q-factor uncertainties added in quadrature. These data represent first-time measurements.

around $E_\gamma \approx 1.7$ GeV. Taken directly from Ref. [73], the authors claim that *the differential cross section exhibits increasing forward-peaking with energy, but only up to the* K^* *threshold. Beyond, it suddenly returns to a flat distribution with the forward cross section dropping by a factor of four. In the total cross section, a pronounced structure is observed between the* $K^*\,\Lambda$ *and* $K^*\,\Sigma$ *thresholds.* In fact, the incident-photon energy bin $1.65 < E_\gamma < 1.75$ GeV (see Fig. 6.26) shows a fairly large

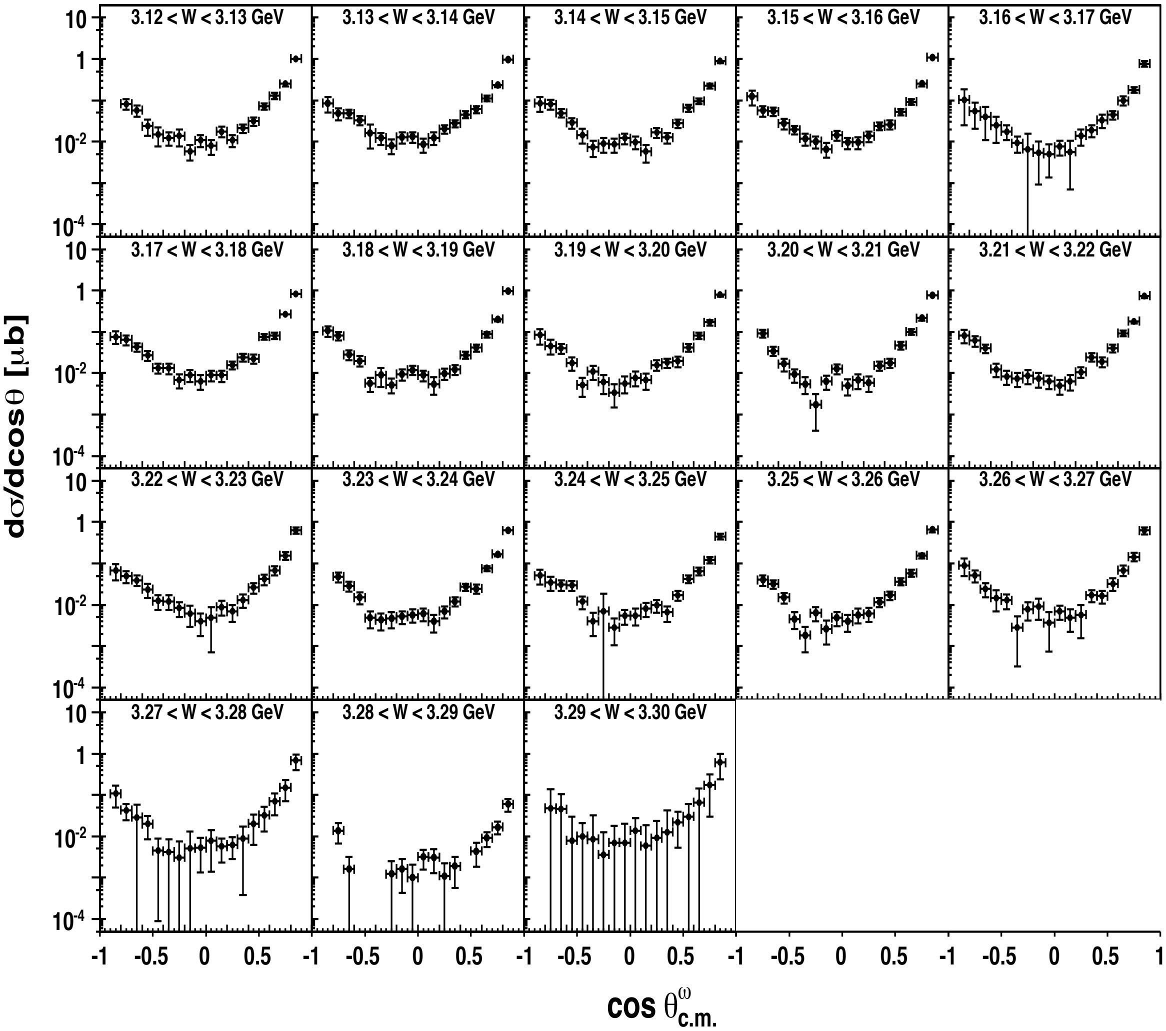

Figure 6.8: The differential cross sections in the reaction $\gamma p \to p\,\omega$ for the center-of-mass energy range $3.12 < W < 3.30$ GeV from g12 (black data points). The given uncertainties comprise the statistical uncertainties and the Q-factor uncertainties added in quadrature. These data represent first-time measurements.

discrepancy between our results and the CBELSA/TAPS results and the sudden intensity drop of the CBELSA/TAPS data is clearly seen. However, Fig. 6.26 also shows that our data do not exhibit this anomaly. On the contrary, the g12 cross sections show a smooth transition across all energy bins. We believe that an instrumental effect in the CBELSA/TAPS data (e.g. affecting the photon flux determination) is likely the origin for the observed sudden drop.

Induced Hyperon Polarization in $\gamma p \to K^0\,\Sigma^+$. Figure 6.28, 6.29, and 6.30 show the hyperon polarization in the reaction $\gamma p \to K^0\,\Sigma^+$ from CLAS g12 in comparison with the results from three previous measurements.

(1) Figure 6.28 shows the hyperon polarization from CLAS g12 (red points), presented in 100-MeV-wide energy bins and covering the energy range $1.15 < E_\gamma < 3.05$ GeV. Also shown in the figure are the previous results from CBELSA/TAPS (blue points) [74]. The given uncertainties for the g12 data are the statistical uncertainties and the Q-factor uncertainties added in quadrature. The agreement is good within the statistical uncertainties.

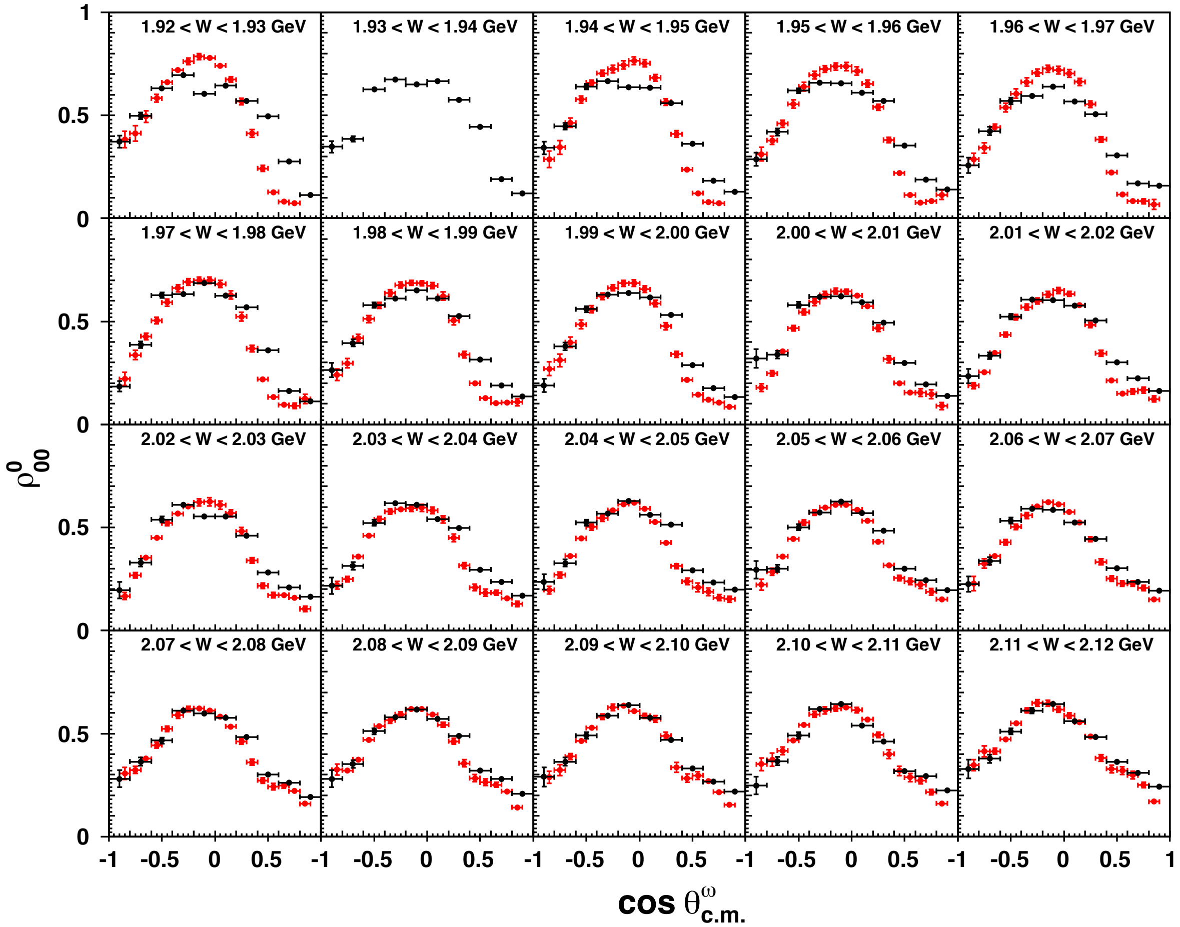

Figure 6.9: The spin-density matrix element ρ^0_{00} in the reaction $\gamma p \to p\,\omega$ for $1.92 < W < 2.12$ GeV from g12 (black data points) in comparison with the previous CLAS measurements from g11a (red data points). The shown uncertainties for both data sets are statistical only.

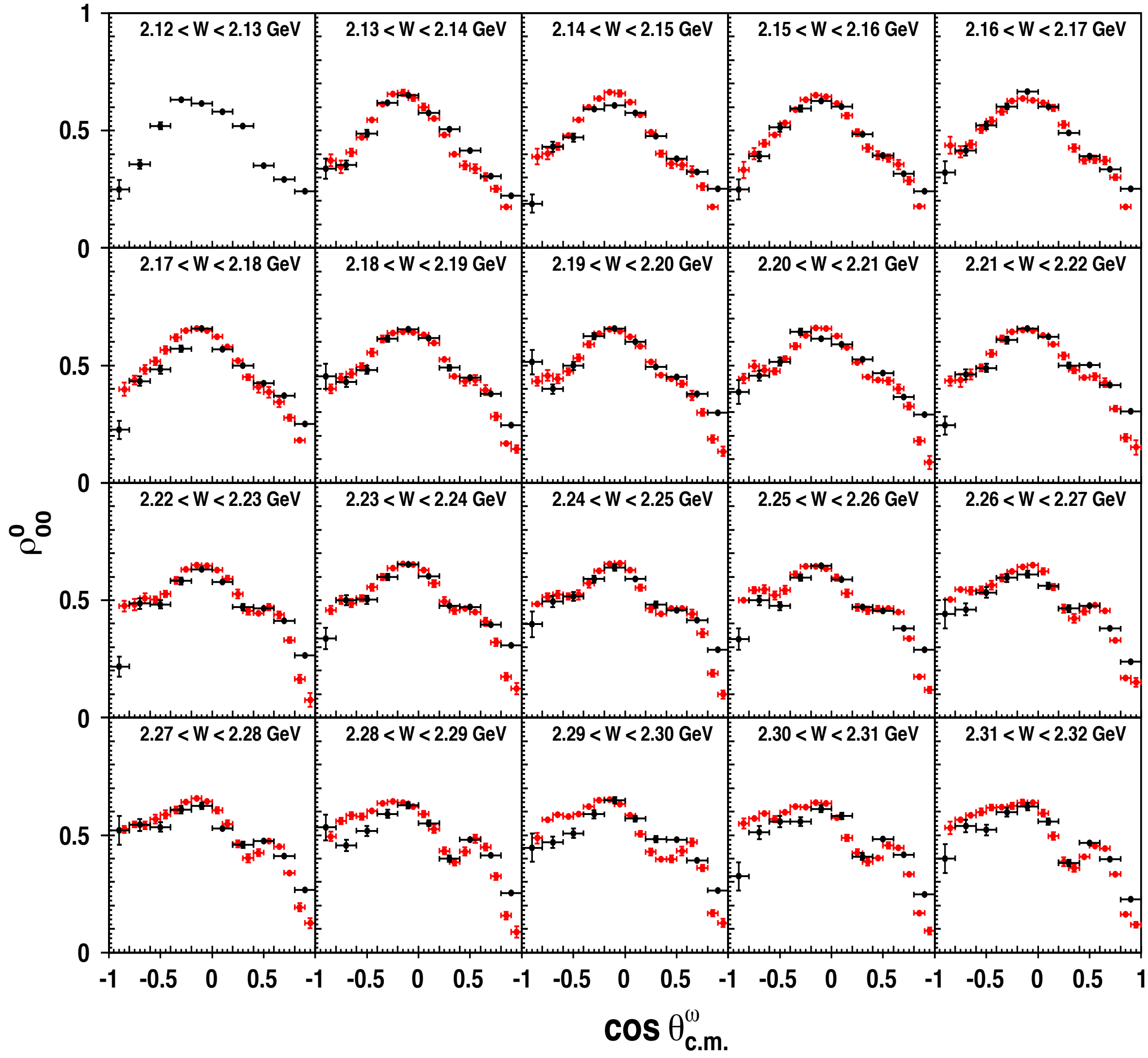

Figure 6.10: The spin-density matrix element ρ^0_{00} in the reaction $\gamma p \to p\,\omega$ for $2.12 < W < 2.32$ GeV from g12 (black data points) in comparison with the previous CLAS measurements from g11a (red data points). The shown uncertainties for both data sets are statistical only.

(2) Figure 6.29 shows the hyperon polarization from CLAS g12 (red points), presented in 300-MeV-wide energy bins and covering the energy range $1.15 < E_\gamma < 2.25$ GeV. Also shown in the figure are the previous results from CB-ELSA (blue points) [72]. The given uncertainties for the g12 data are statistical only. The agreement is again good within the statistical uncertainties.

(3) Figure 6.30 shows the hyperon transverse polarization from CLAS g12 (red points), presented

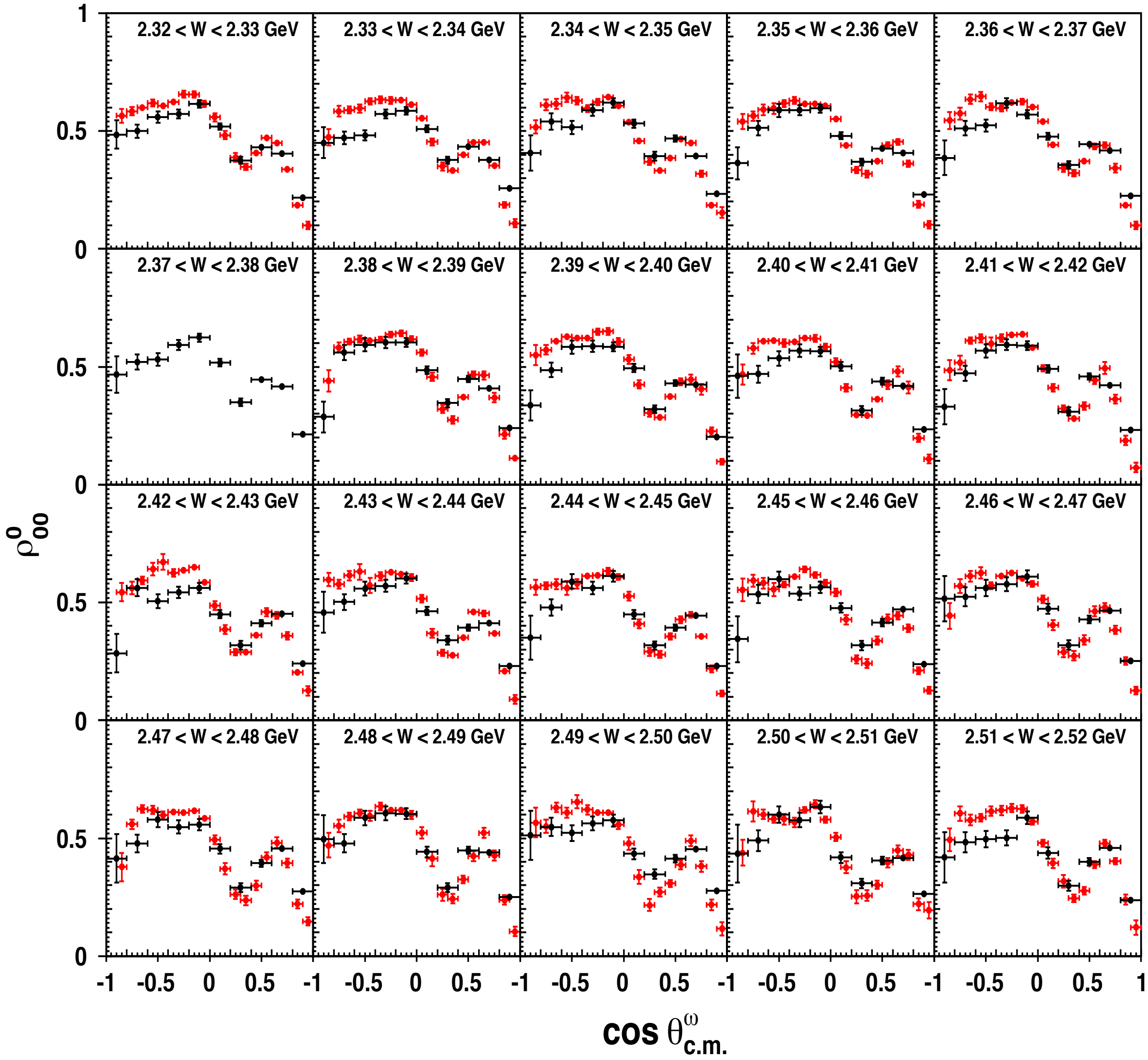

Figure 6.11: The spin-density matrix element ρ^0_{00} in the reaction $\gamma p \to p\,\omega$ for $2.32 < W < 2.52$ GeV from g12 (black data points) in comparison with the previous CLAS measurements from g11a (red data points). The shown uncertainties for both data sets are statistical only.

in 170-MeV-wide energy bins and covering the energy range $1.16 < E_\gamma < 3.03$ GeV. Also shown in the figure are the previous results from CLAS-g11a (blue points) [75]. Please note that in this comparison, we used the incident photon and the recoiling Σ^+ to define the reaction plane, which resulted in a sign flip. The given uncertainties for the g12 data are statistical only. Major discrepancies are clearly observed, in particular at lower energies.

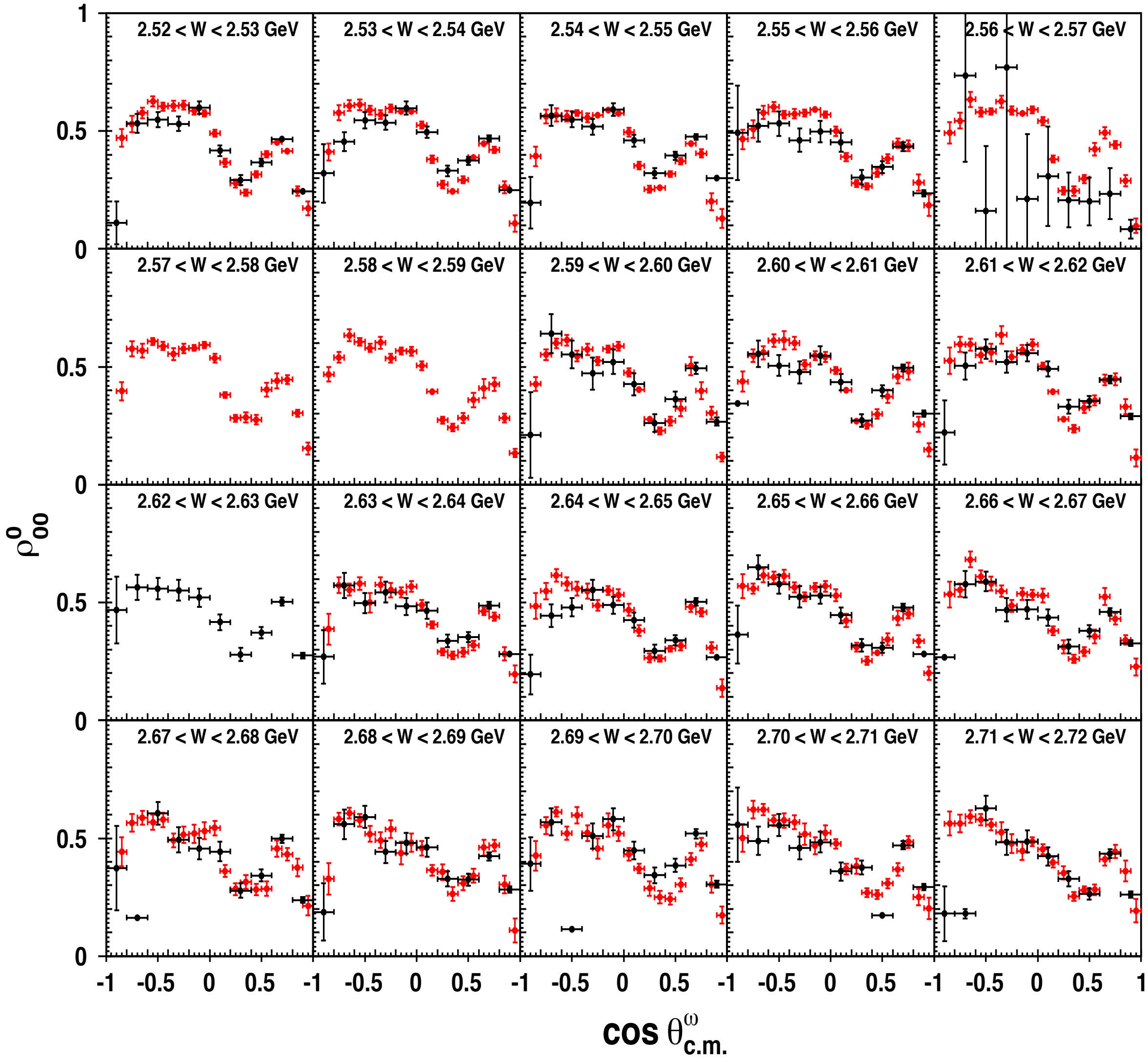

Figure 6.12: The spin-density matrix element ρ^0_{00} in the reaction $\gamma p \to p\,\omega$ for $2.52 < W < 2.72$ GeV from g12 (black data points) in comparison with the previous CLAS measurements from g11a (red data points). Please note that the g12 data suffer from broken tagger paddles that affected the energy range $2.56 < W < 2.59$ GeV (around $E_\gamma \approx 3.0$ GeV). The shown uncertainties for both data sets are statistical only.

We have compared the unpublished cross section results of Ref. [71], which were based on the same data used for the polarization observable of Ref. [75], with our cross section results (not shown here) and also found major discrepancies. However, our angular distributions are in reasonable agreement with the unpublished cross section results of Ref. [70] (also not shown here). We do

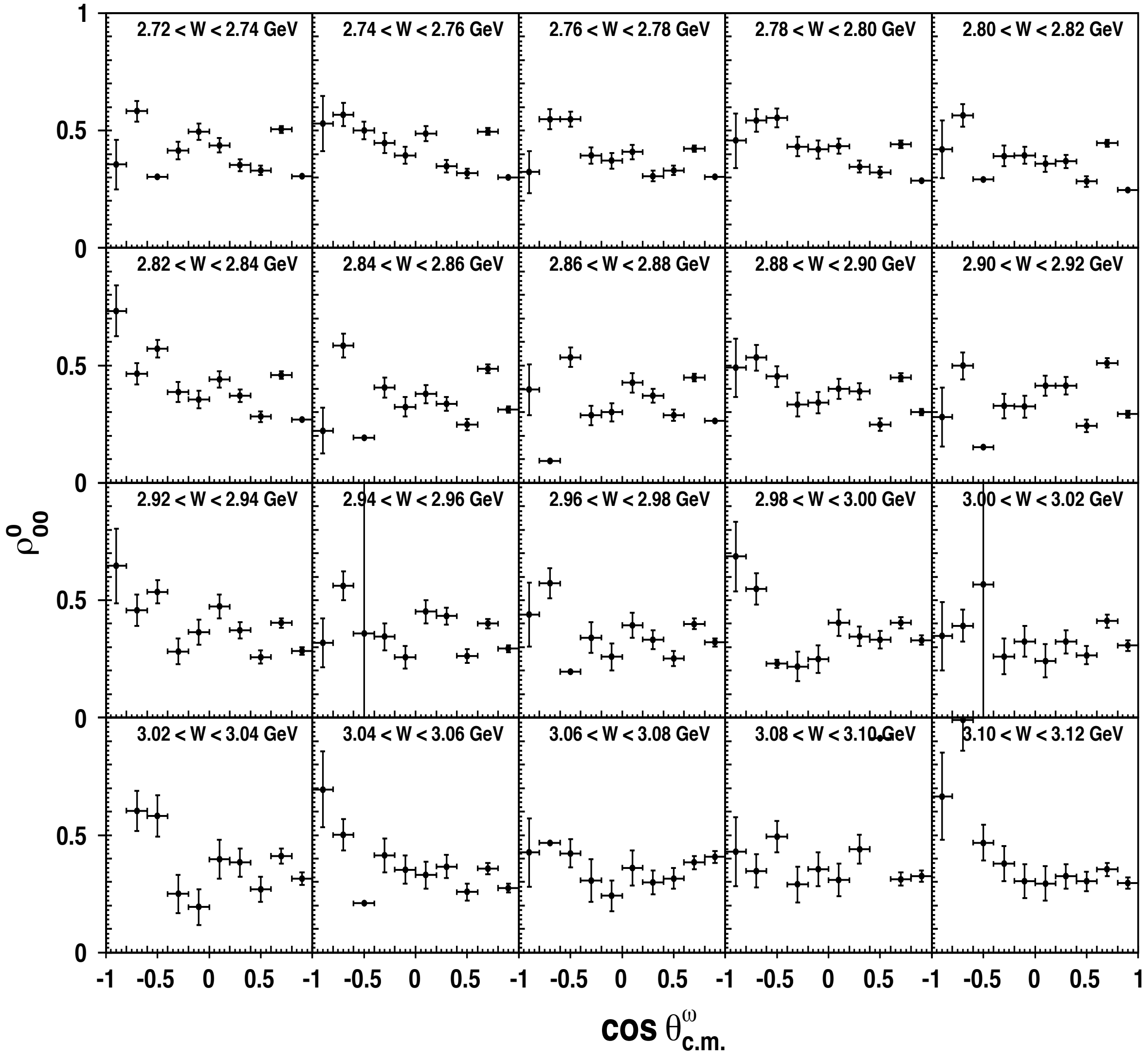

Figure 6.13: The spin-density matrix element ρ^0_{00} in the reaction $\gamma p \to p\,\omega$ for $2.72 < W < 3.12$ GeV from g12 (black data points) in comparison with the previous CLAS measurements from g11a (red data points). The shown uncertainties for both data sets are statistical only.

not believe that the blue data points are correct in Fig. 6.30, particularly for the two energy bins $1.50 < E_\gamma < 1.67$ and $1.67 < E_\gamma < 1.84$.

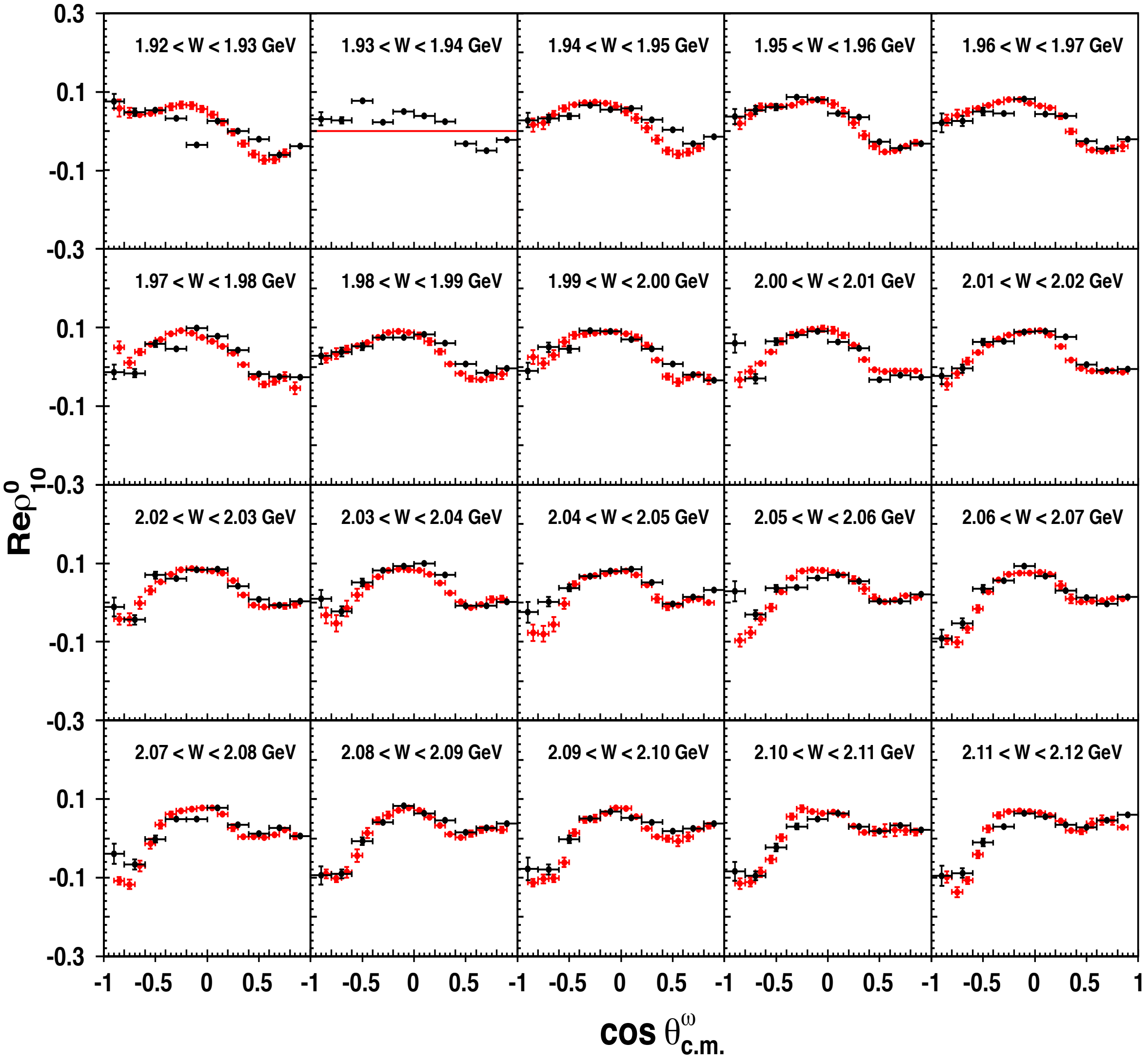

Figure 6.14: The spin-density matrix element $Re(\rho^0_{10})$ in $\gamma p \to p\,\omega$ for $1.92 < W < 2.12$ GeV from g12 (black data points) in comparison with the previous CLAS measurements from g11a (red data points). The shown uncertainties for both data sets are statistical only.

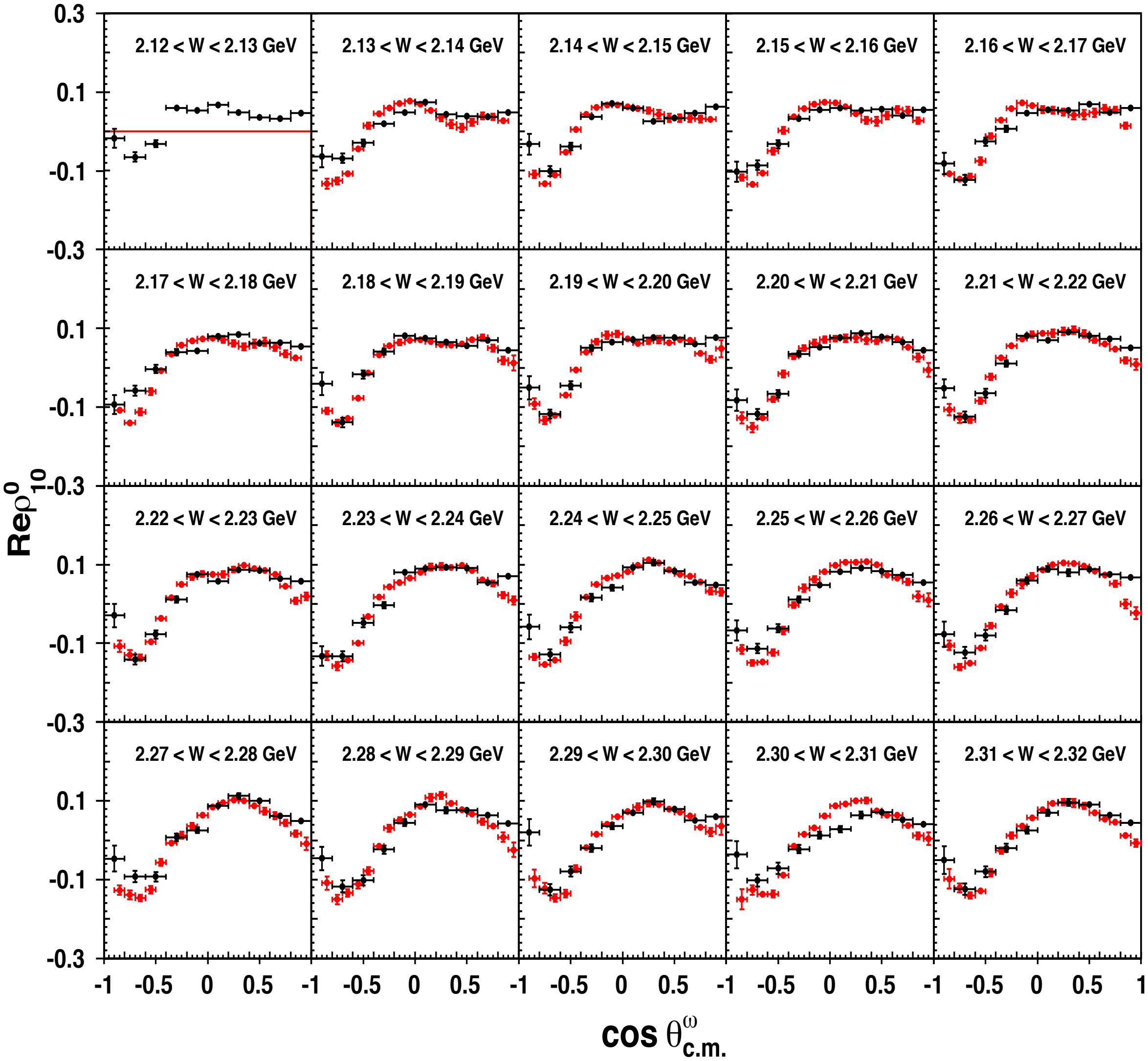

Figure 6.15: The spin-density matrix element $Re(\rho^0_{10})$ in $\gamma p \to p\,\omega$ for $2.12 < W < 2.32$ GeV from g12 (black data points) in comparison with the previous CLAS measurements from g11a (red data points). The shown uncertainties for both data sets are statistical only.

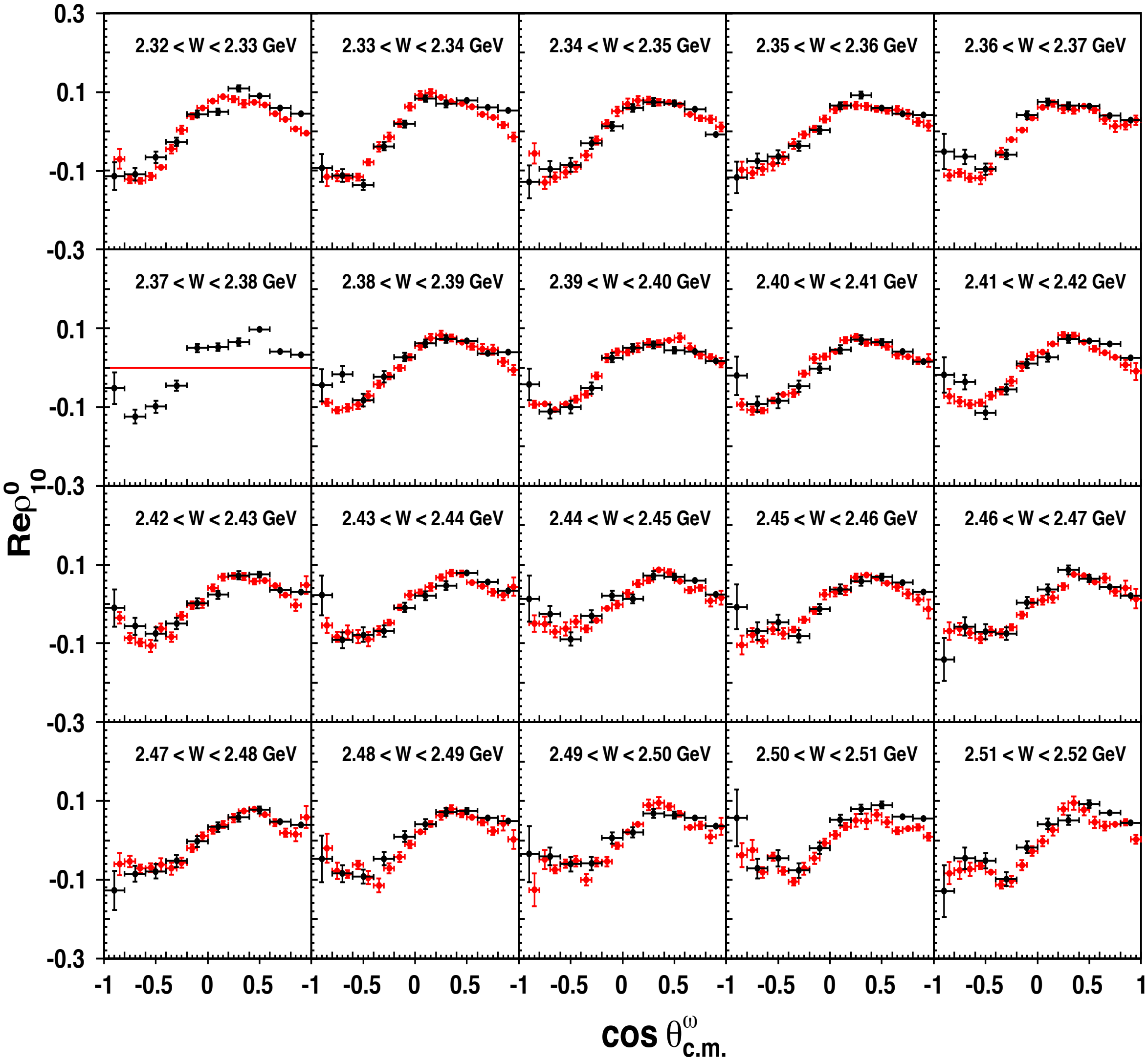

Figure 6.16: The spin-density matrix element $Re(\rho^0_{10})$ in $\gamma p \to p\,\omega$ for $2.32 < W < 2.52$ GeV from g12 (black data points) in comparison with the previous CLAS measurements from g11a (red data points). The shown uncertainties for both data sets are statistical only.

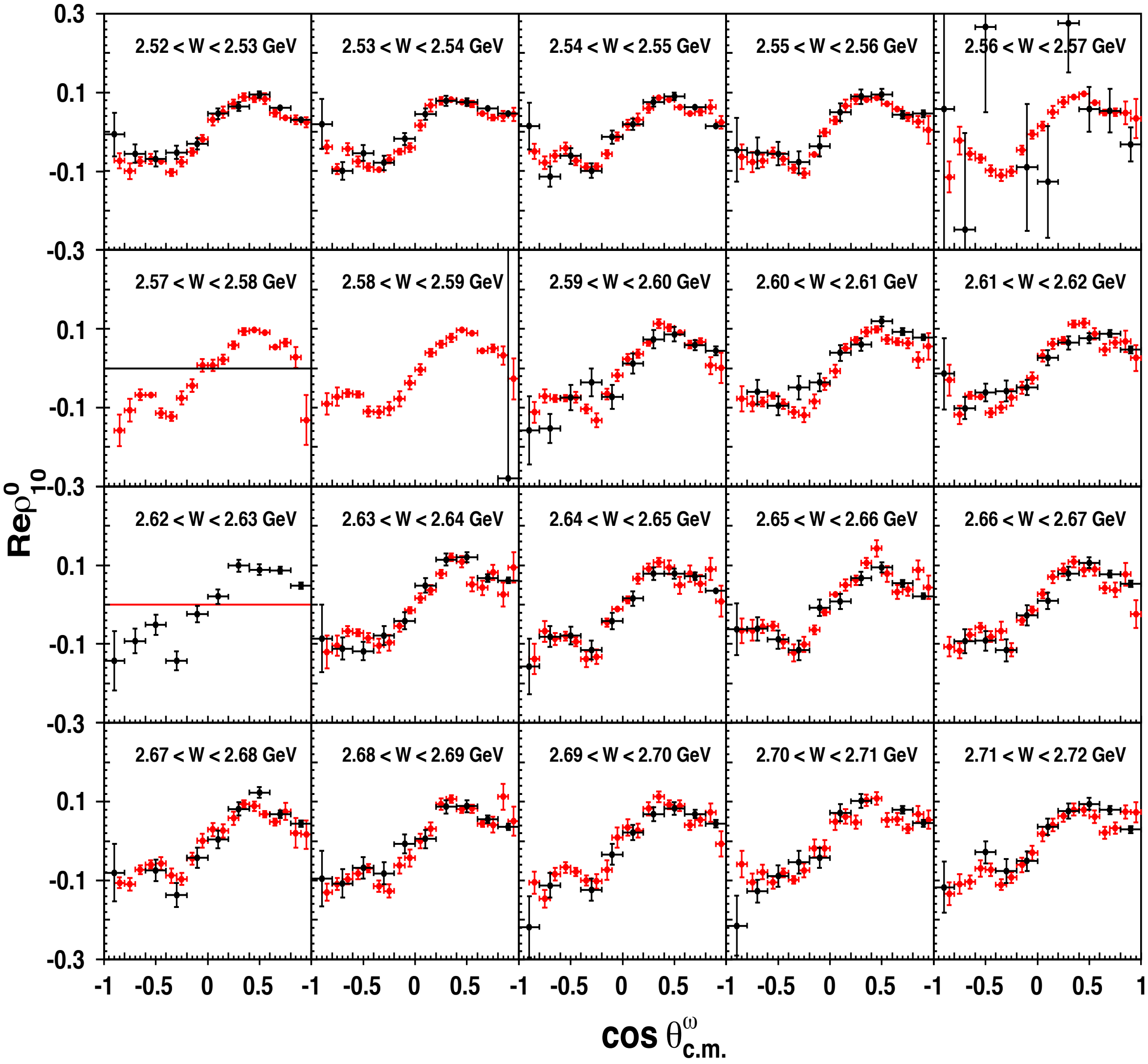

Figure 6.17: The spin-density matrix element $Re(\rho^0_{10})$ in $\gamma p \to p\,\omega$ for $2.52 < W < 2.72$ GeV from g12 (black data points) in comparison with the previous CLAS measurements from g11a (red data points). Please note that the g12 data suffer from broken tagger paddles that affected the energy range $2.56 < W < 2.59$ GeV (around $E_\gamma \approx 3.0$ GeV). The shown uncertainties for both data sets are statistical only.

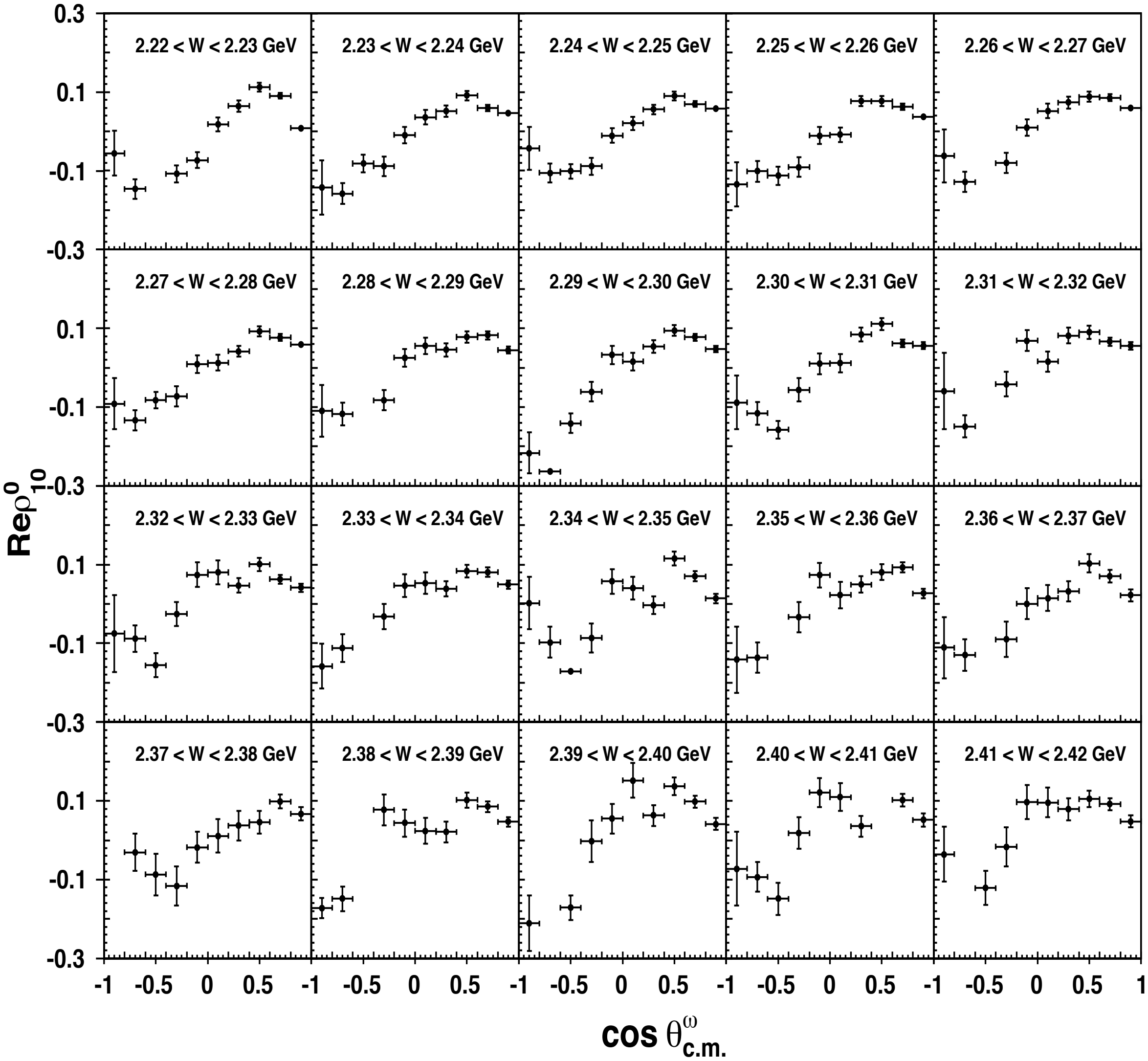

Figure 6.18: The spin-density matrix element $Re(\rho^0_{10})$ in $\gamma p \to p\,\omega$ for $2.72 < W < 3.12$ GeV from g12 (black data points) in comparison with the previous CLAS measurements from g11a (red data points). The shown uncertainties for both data sets are statistical only.

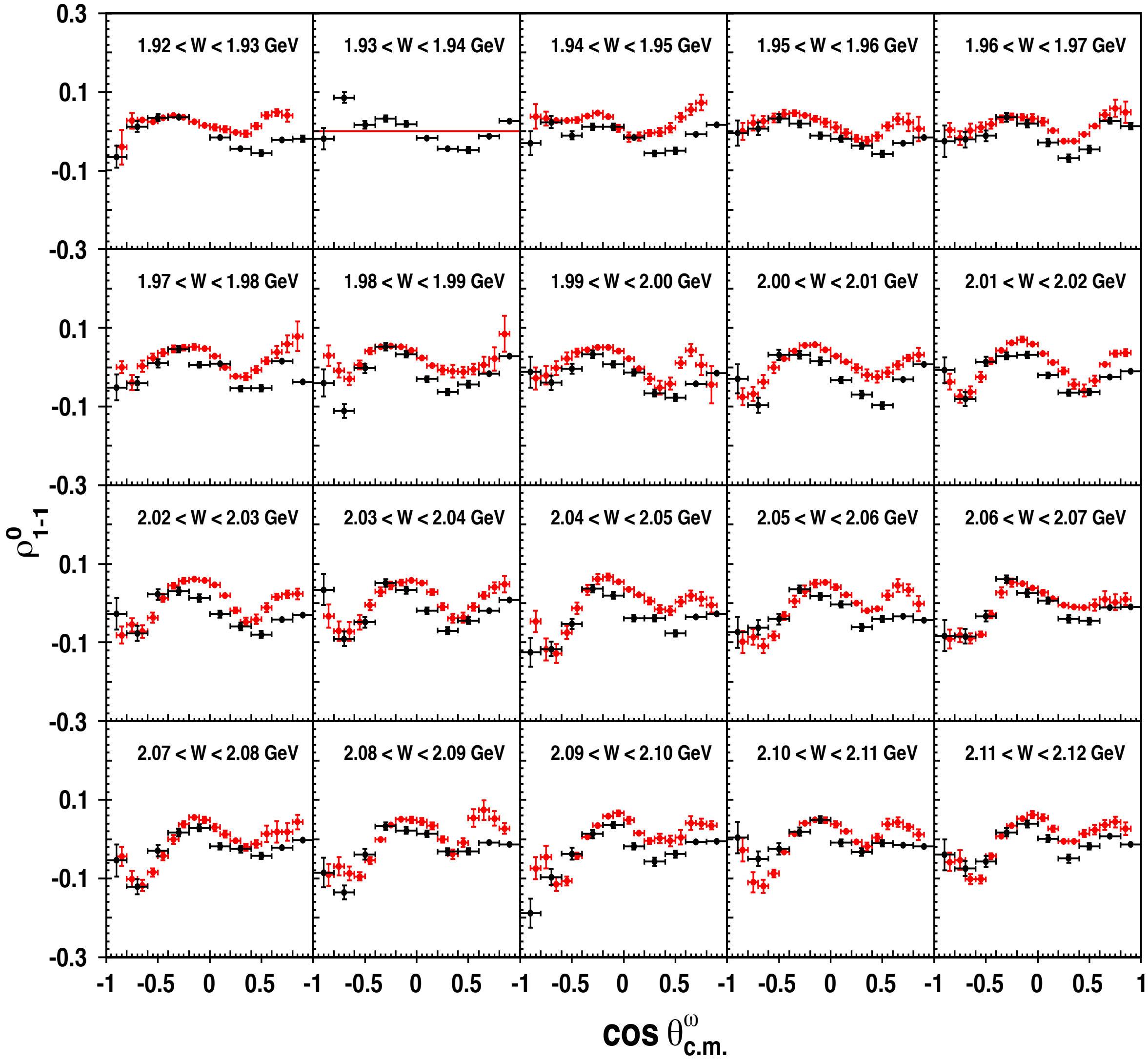

Figure 6.19: The spin-density matrix element ρ^0_{1-1} in the reaction $\gamma p \to p\omega$ for $1.92 < W < 2.12$ GeV from g12 (black data points) in comparison with the previous CLAS measurements from g11a (red data points). The shown uncertainties for both data sets are statistical only.

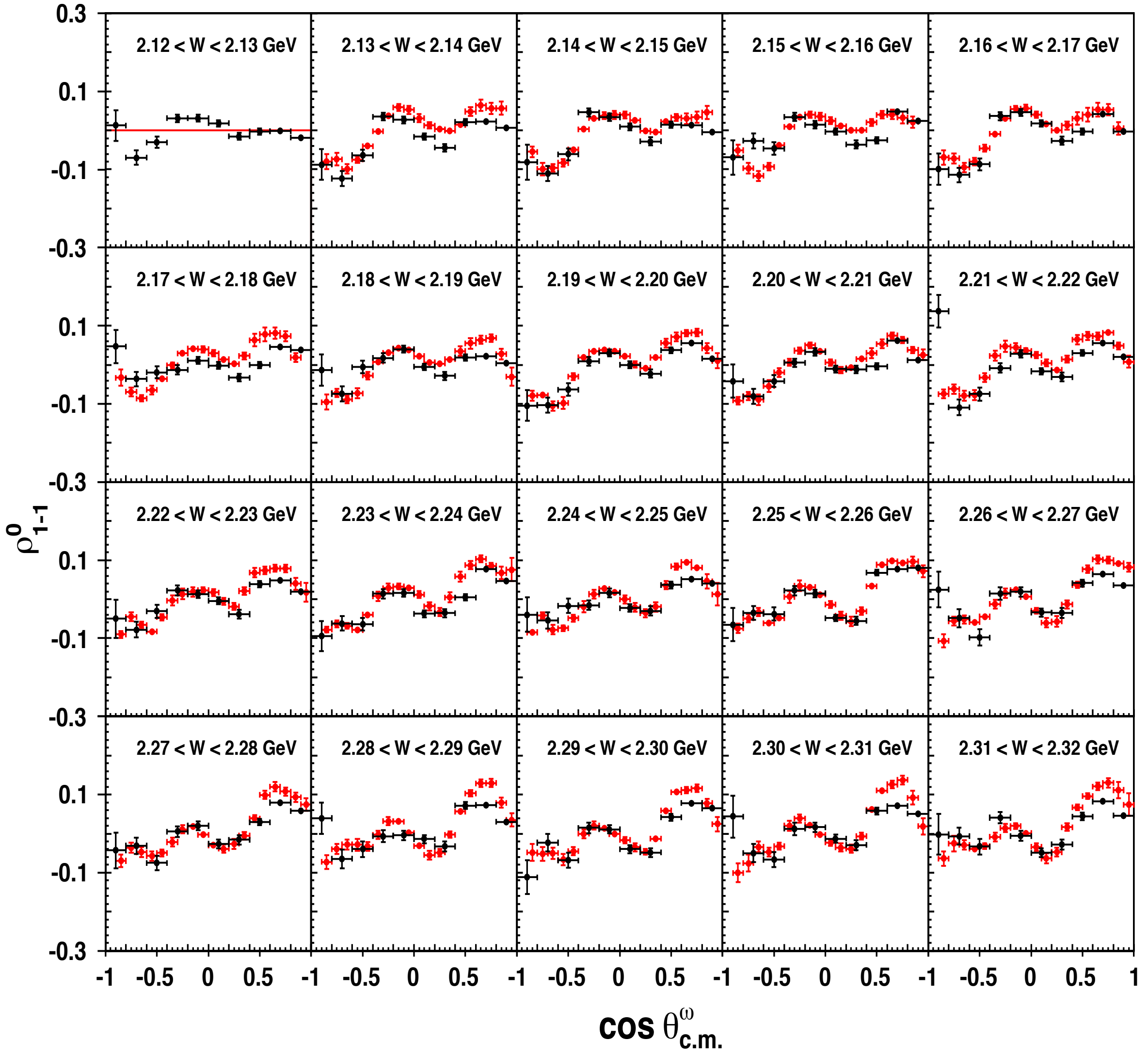

Figure 6.20: The spin-density matrix element ρ^0_{1-1} in the reaction $\gamma p \to p\omega$ for $2.12 < W < 2.32$ GeV from g12 (black data points) in comparison with the previous CLAS measurements from g11a (red data points). The shown uncertainties for both data sets are statistical only.

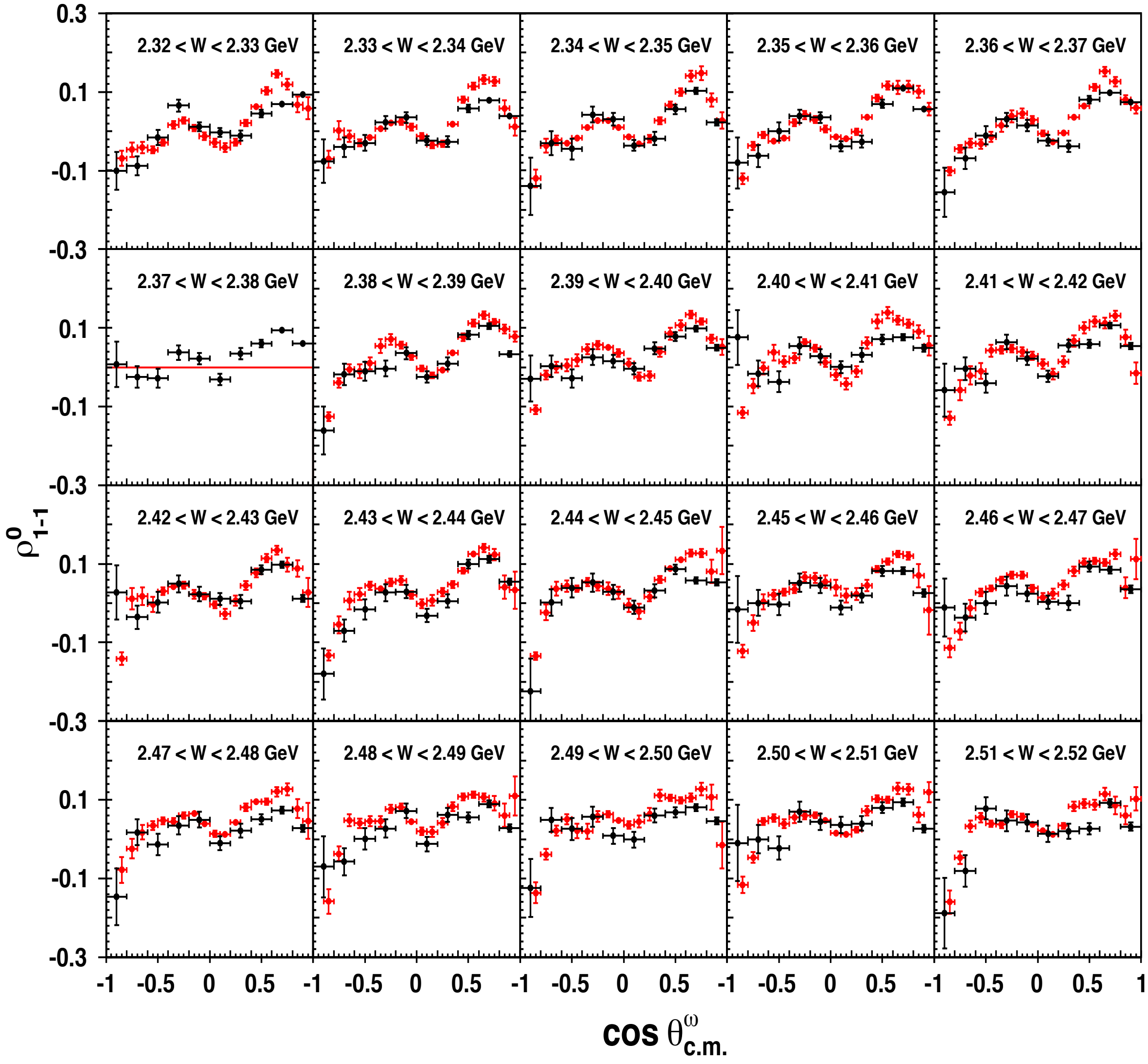

Figure 6.21: The spin-density matrix element ρ^0_{1-1} in the reaction $\gamma p \to p\omega$ for $2.32 < W < 2.52$ GeV from g12 (black data points) in comparison with the previous CLAS measurements from g11a (red data points). The shown uncertainties for both data sets are statistical only.

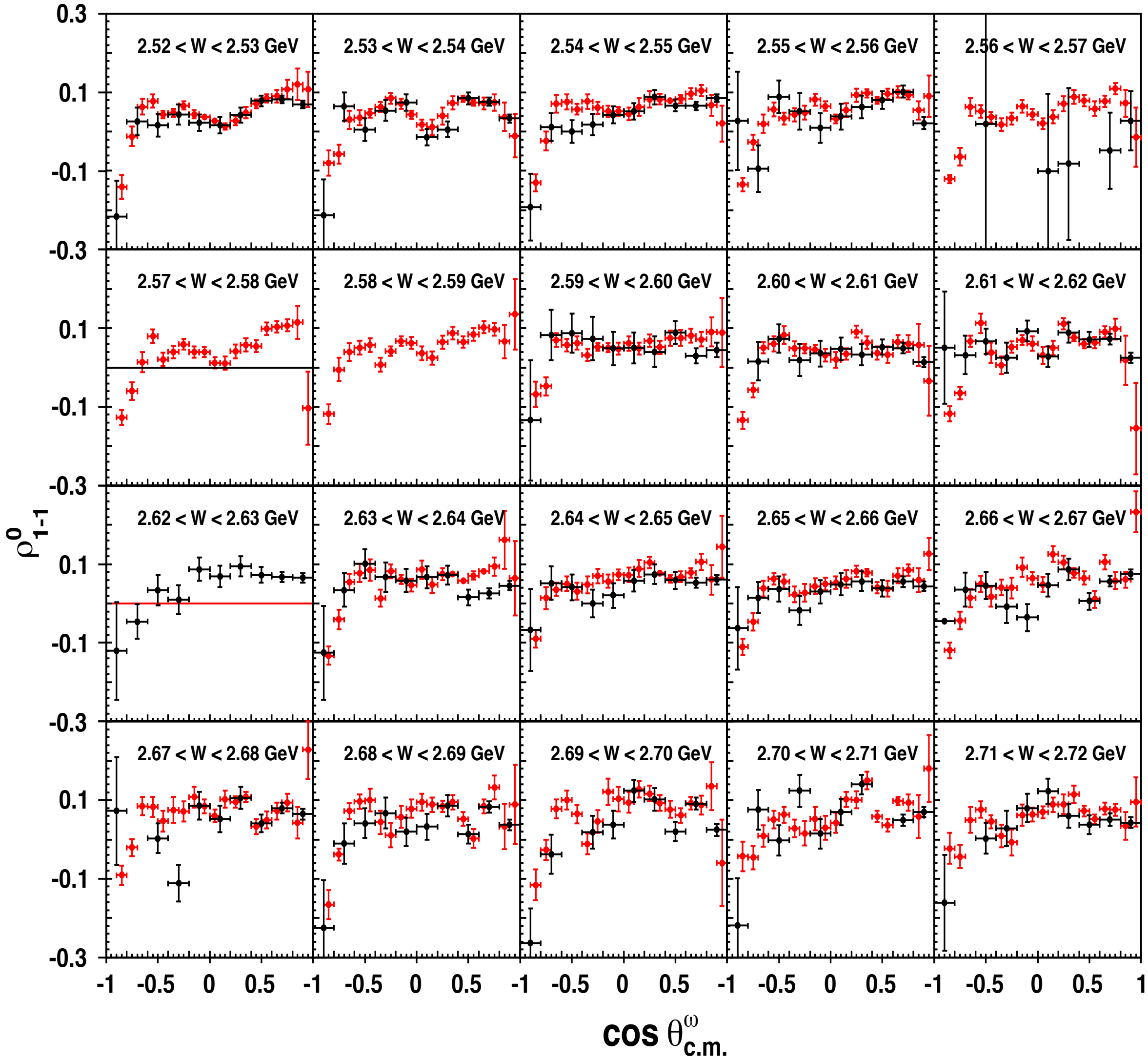

Figure 6.22: The spin-density matrix element ρ^0_{1-1} in the reaction $\gamma p \to p\omega$ for $2.52 < W < 2.72$ GeV from g12 (black data points) in comparison with the previous CLAS measurements from g11a (red data points). Please note that the g12 data suffer from broken tagger paddles that affected the energy range $2.56 < W < 2.59$ GeV (around $E_\gamma \approx 3.0$ GeV). The shown uncertainties for both data sets are statistical only.

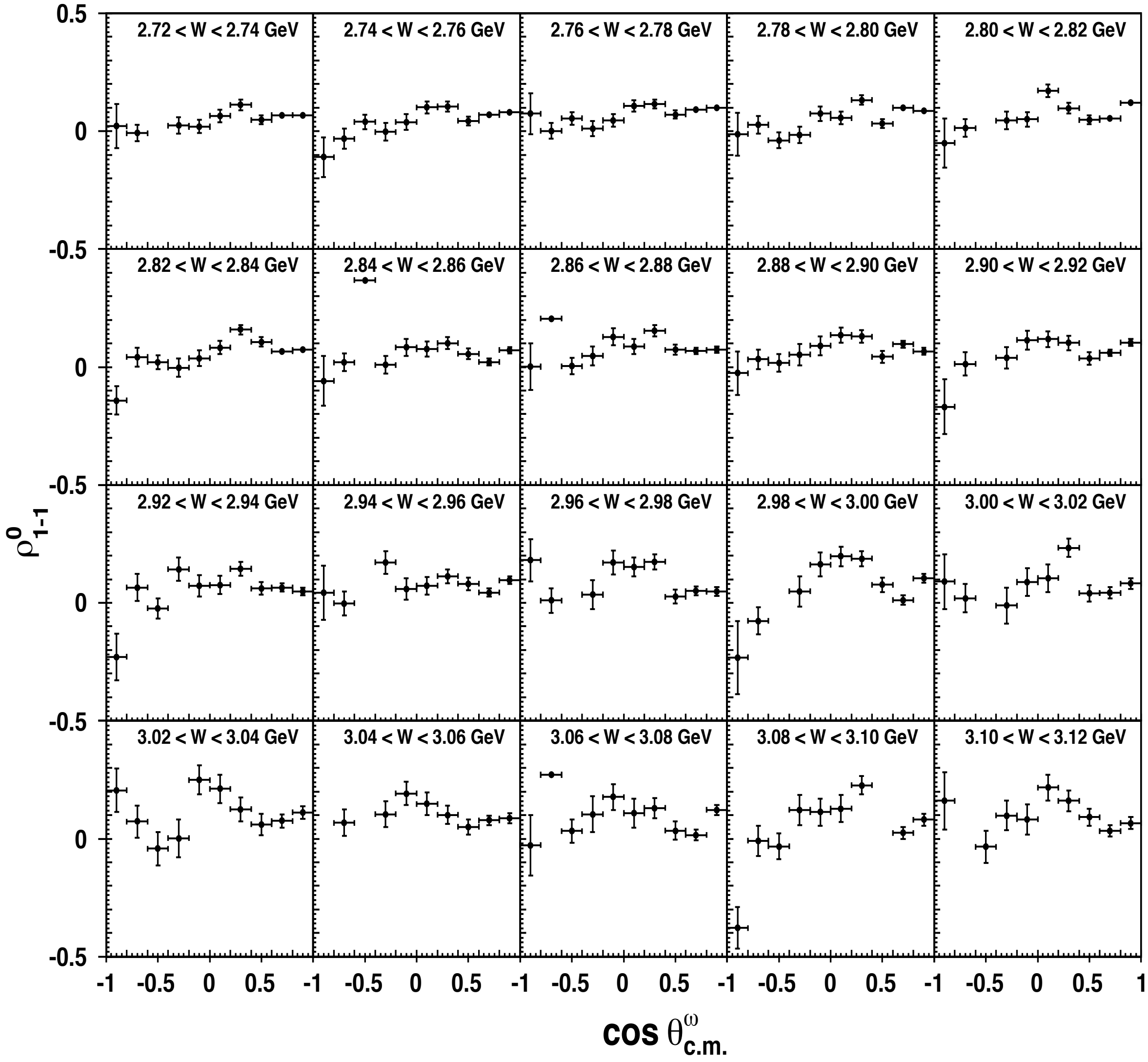

Figure 6.23: The spin-density matrix element ρ^0_{1-1} in the reaction $\gamma p \to p\omega$ for $2.72 < W < 3.12$ GeV from g12 (black data points) in comparison with the previous CLAS measurements from g11a (red data points). The shown uncertainties for both data sets are statistical only.

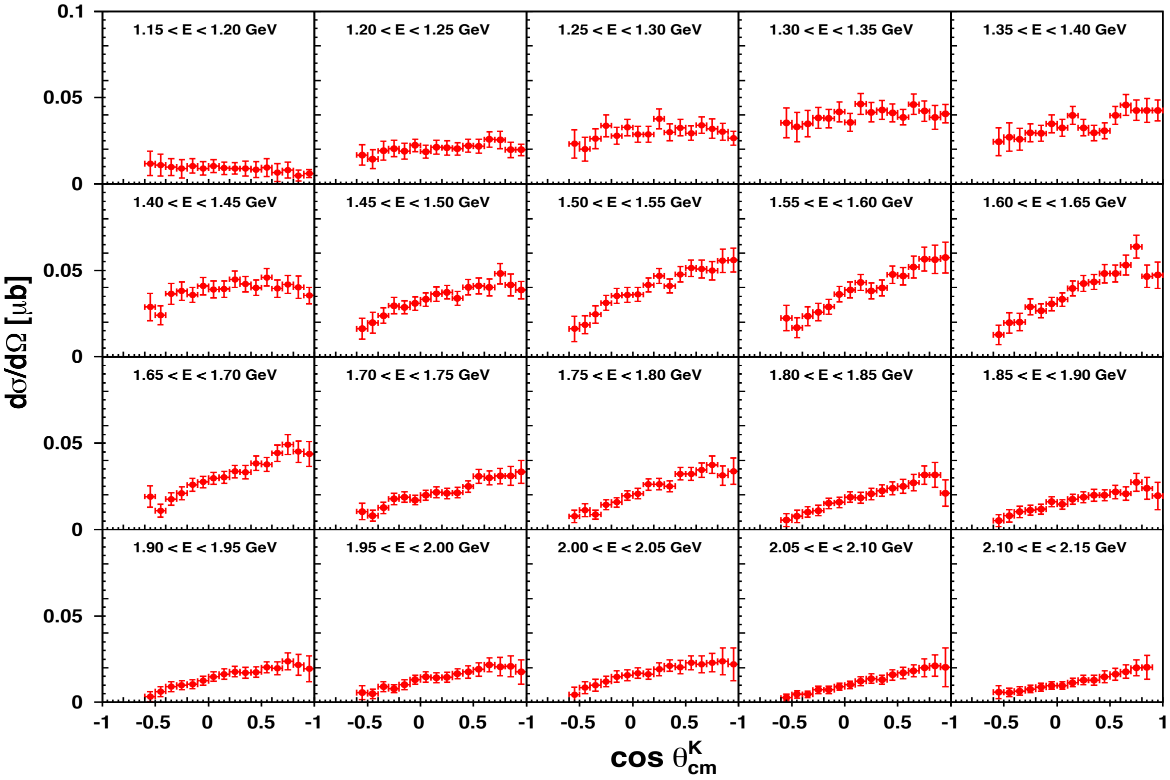

Figure 6.24: The differential cross sections in the reaction $\gamma p \to K^0\,\Sigma^+$ for the incident-photon energy range $1.15 < E_\gamma < 2.15$ GeV from CLAS g12. The given uncertainties comprise the statistical uncertainties and the Q-factor uncertainties added in quadrature.

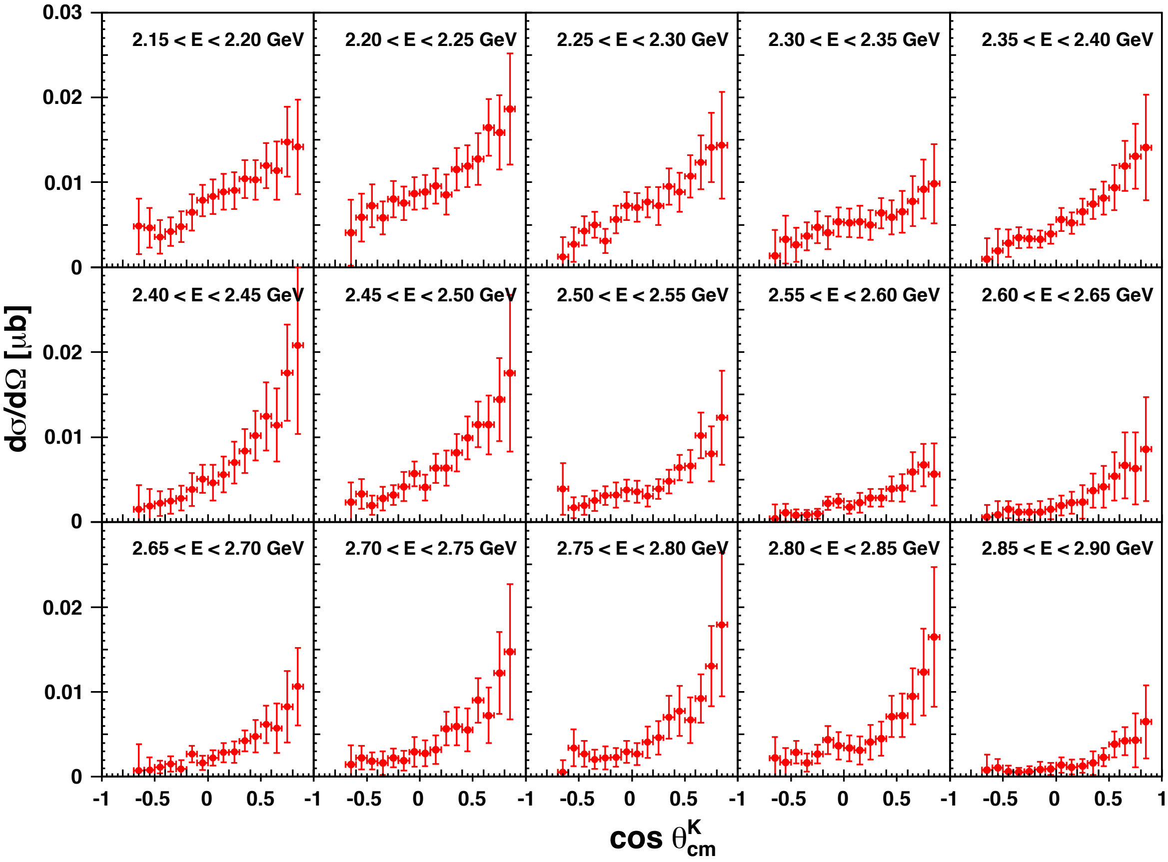

Figure 6.25: The differential cross sections in the reaction $\gamma p \to K^0\,\Sigma^+$ for the incident-photon energy range $2.15 < E_\gamma < 2.90$ GeV from CLAS g12. The given uncertainties comprise the statistical uncertainties and the Q-factor uncertainties added in quadrature.

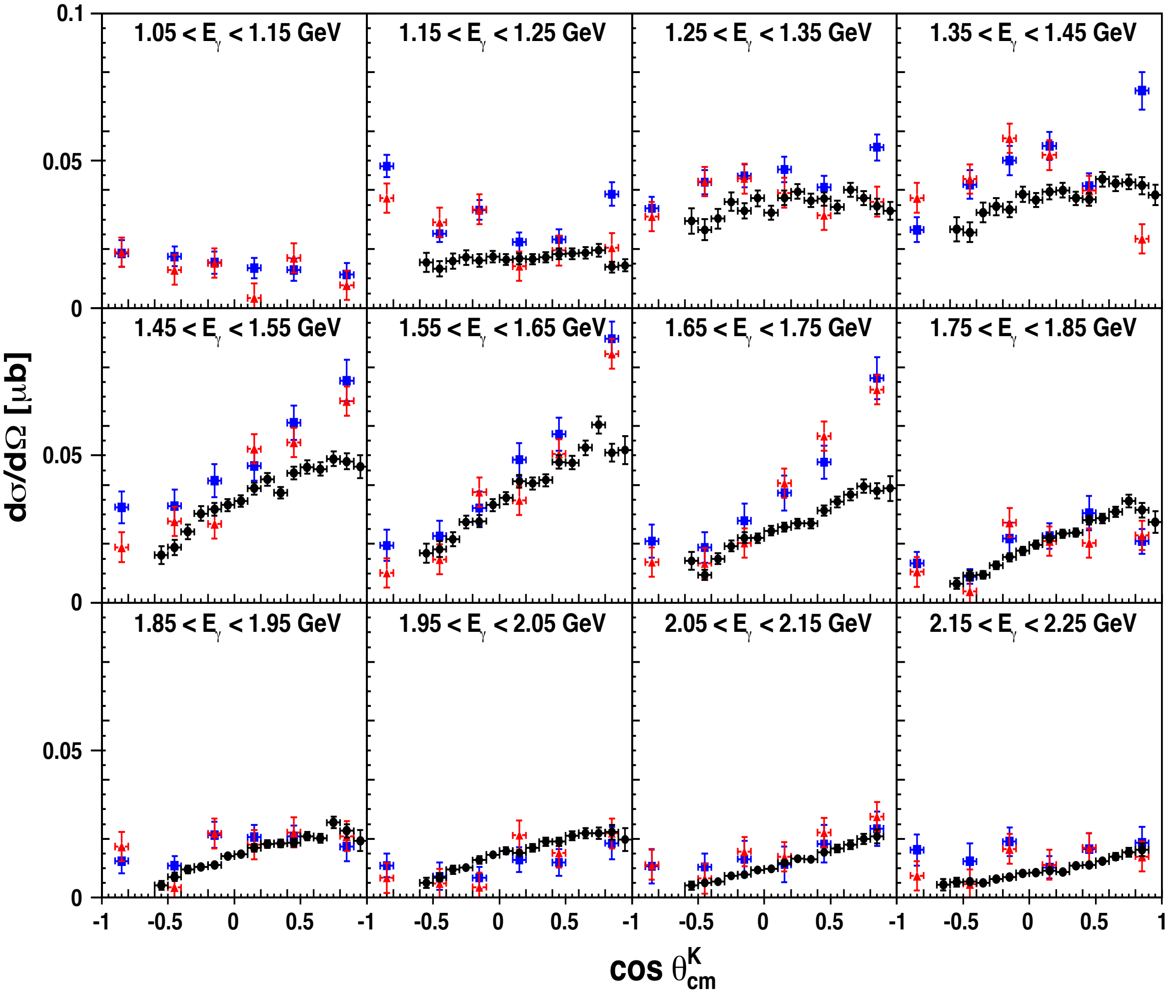

Figure 6.26: The differential cross sections in the reaction $\gamma p \to K^0\,\Sigma^+$ for the incident-photon energy range $1.15 < E_\gamma < 2.25$ GeV in 100-MeV-wide energy bins from g12 (black data points) in comparison with the previous measurements from CBELSA/TAPS [73] (blue data points) and CB-ELSA [72] (red data points). The given uncertainties for the g12 data are statistical only to facilitate the comparison.

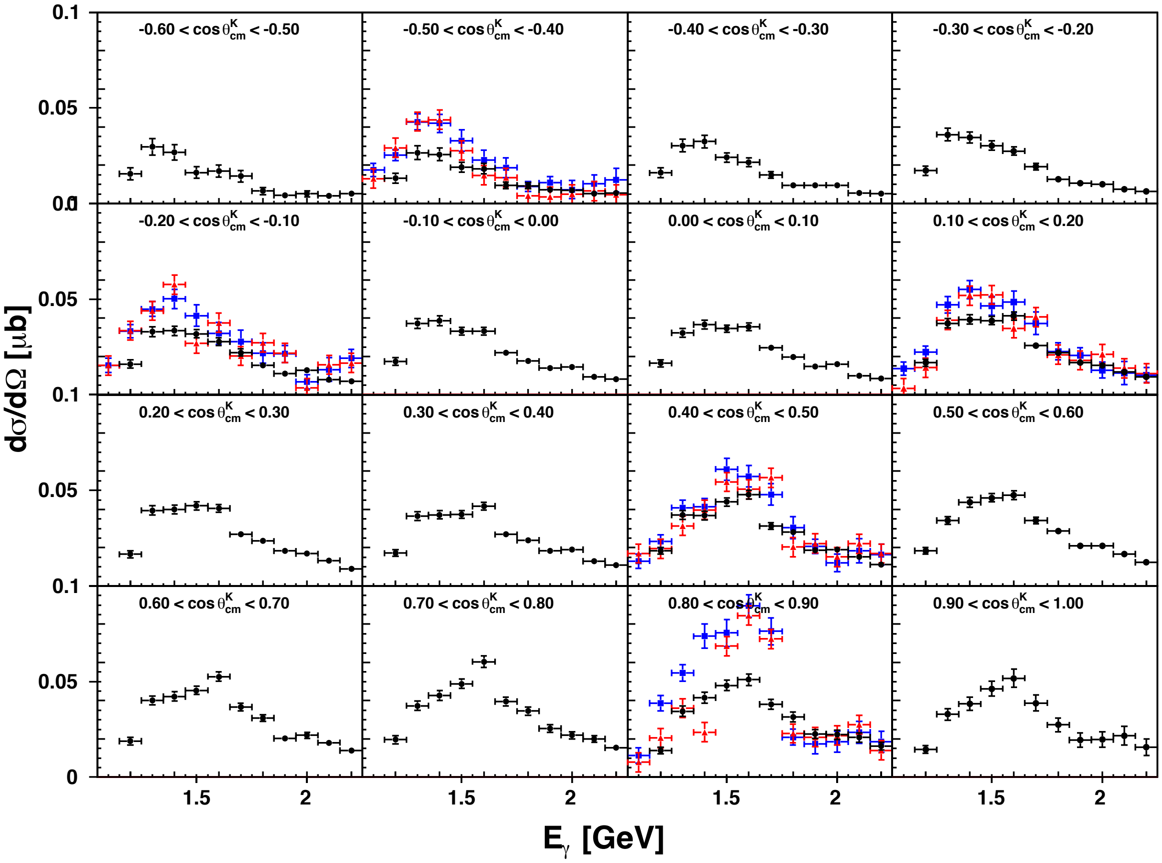

Figure 6.27: The differential cross sections in the reaction $\gamma p \to K^0\,\Sigma^+$ for the incident-photon energy range $1.15 < E_\gamma < 2.25$ GeV in 0.1-wide $\cos\theta_{\text{c.m.}}$ bins from g12 (black data points) in comparison with the previous measurements from CBELSA/TAPS [73] (blue data points) and Crystal Barrel [72] (red data points). The given uncertainties for the g12 data are statistical only to facilitate the comparison.

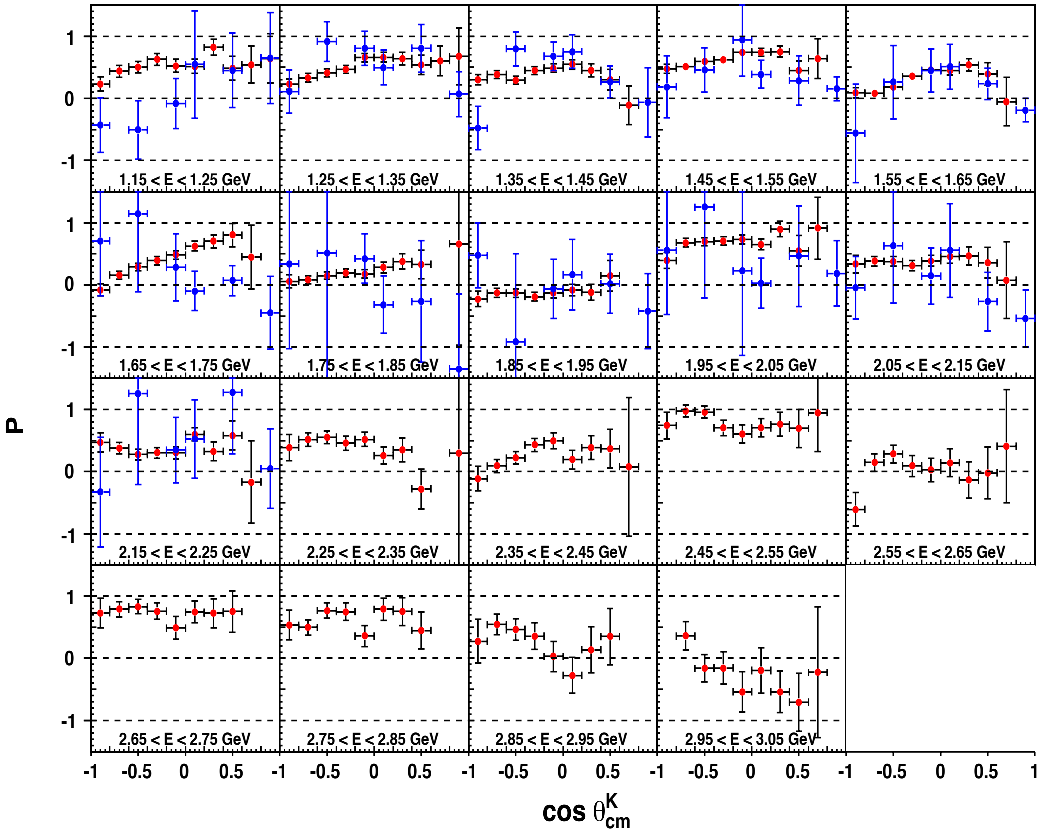

Figure 6.28: The hyperon polarization in the reaction $\gamma p \to K^0\,\Sigma^+$ for the incident-photon energy range $1.15 < E_\gamma < 3.05$ GeV from CLAS g12 (red points) in comparison with the previous measurements from CBELSA/TAPS [74] (blue points). The given uncertainties for the g12 data are the statistical uncertainties and the Q-factor uncertainties added in quadrature.

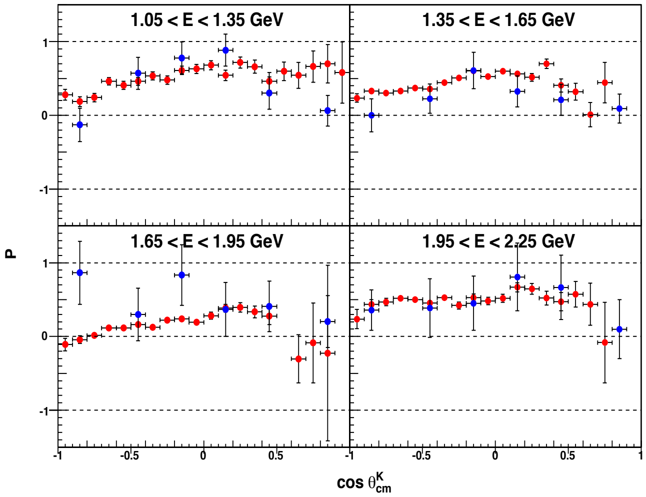

Figure 6.29: The hyperon polarization for $\gamma p \rightarrow K^0\,\Sigma^+$ in the energy range $1.15 < E_\gamma < 2.25$ GeV from CLAS g12 (red points) in comparison with previous measurements from CB-ELSA [72] (blue points). The given uncertainties for the g12 data are statistical only.

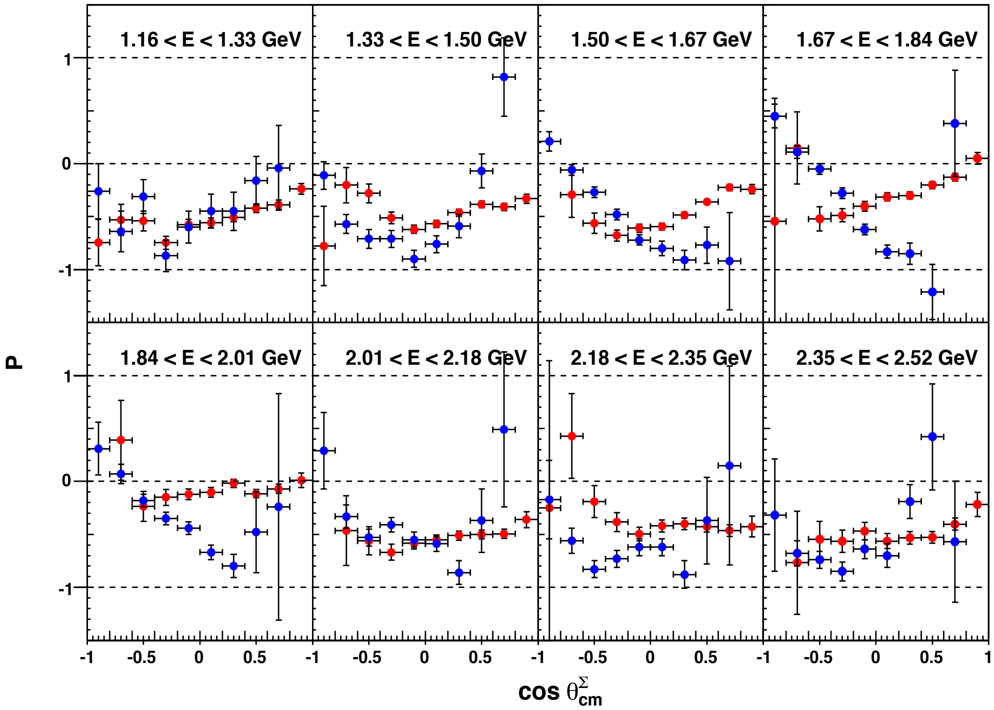

Figure 6.30: The hyperon polarization for $\gamma p \rightarrow K^0\,\Sigma^+$ in the energy range $1.16 < E_\gamma < 2.52$ GeV from CLAS g12 (red points) in comparison with the previous measurements from CLAS g11a (blue points). The given uncertainties for the g12 data are statistical only.

6.2 Results from the $g9a$ Experiment

6.2.1 Results for the $\gamma p \to p\,\omega$ Reaction

The Helicity Asymmetry E in $\gamma p \to p\,\omega$. This section presents and discusses our final results for the first CLAS measurement of the helicity asymmetry **E** in the reaction $\gamma p \to p\omega \to p\pi^+\pi^-\pi^0$.

Figure 6.31 shows our measurement of the helicity asymmetry - polarization observable - **E** - associated with a longitudinally-polarized target and a circularly-polarized beam for the whole available energy range $E_\gamma \in [1.1, 2.3]$ GeV (red circle). The data are given in 100 MeV-wide energy bins. The available statistics was sufficient for eight data points in cos $\theta^{\omega}_{c.m.}$. The systematic uncertainties are given as bands at the bottom of each distribution.

Also shown in the figure are the published results from the CBELSA/TAPS collaboration [27] (blue). Both data sets are consistent in their asymmetry behavior (same sign for almost every data point). However, large discrepancies in the magnitude are visible, in particular at low energies, $E_\gamma <$ 1.5 GeV. The CBELSA/TAPS results suffer from huge statistical fluctuations, which can partially explain the observed discrepancies. Moreover, significant contributions from the double-pion reaction $\gamma p \to \pi^0\pi^0$ made the background subtraction in that analysis challenging.

The BnGa group has recently reported on a PWA [32] that, at the time, was resticted to ω data from the CBELSA/TAPS experiment alone. The new BnGa-PWA solution, which is based on the CLAS data, is shown in Figure 6.31 as a solution. In the BnGa analysis, close to the reaction threshold, $J^P = 3/2^+$ remains the leading resonant partial wave and shows a strong peak with a maximum around $W =$ 1.8 GeV. This wave is identified with the $N(1720)3/2^+$ state. The $J^P = 1/2^-$ wave has a maximum close to the reaction threshold, which can be identified with the $N(1895)1/2^-$ resonance. The $N(1680)5/2^+$, $N(2000)5/2^+$ and $N(2100)3/2^-$ resonances are also identified. The non-resonant contributions, π exchange in the t-channel was found to remain small across the analyzed energy range, while pomeron t-channel exchange gradually grew from the reaction threshold to dominate all other contributions above $W =$ 2 GeV.

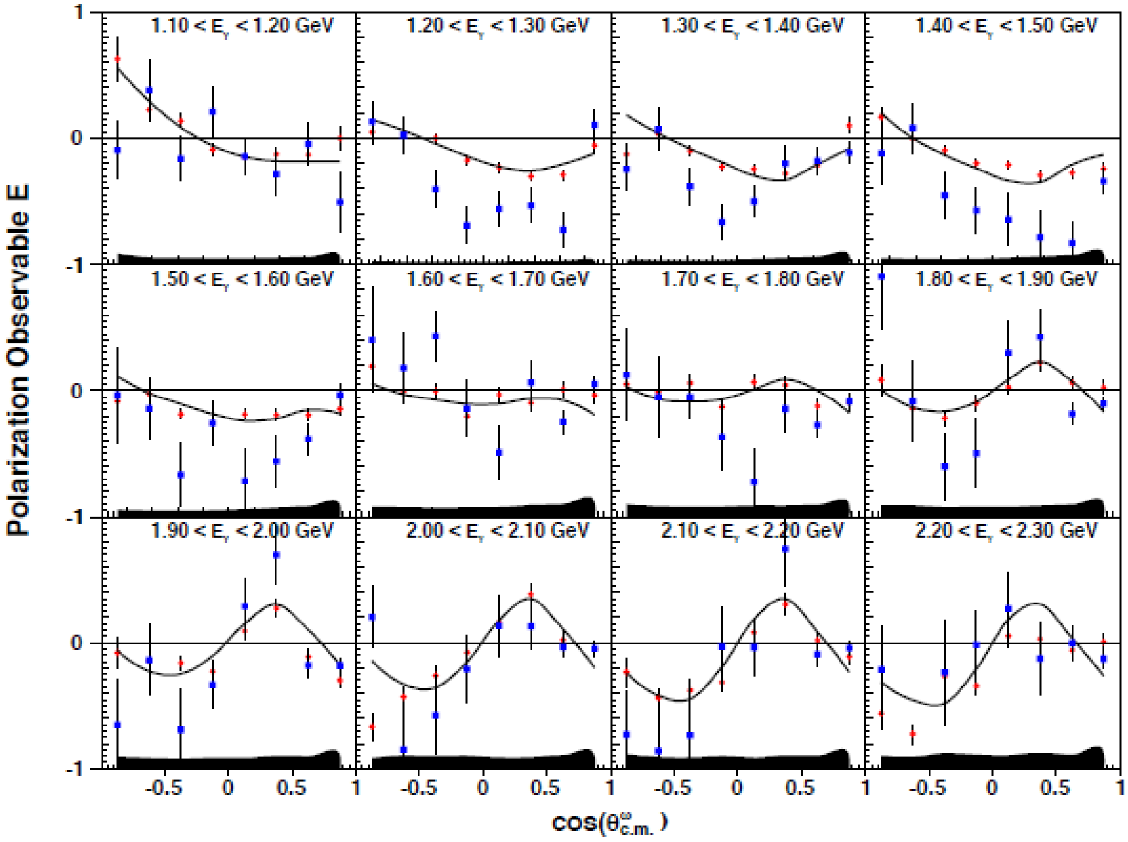

Figure 6.31: Measurement of the helicity asymmetry **E** in the reaction $\gamma p \to p\omega$ using a circulary-polarized photon beam and a longitudinally-polarized target. The data are shown in 100-MeV-wide bins for the photon energy range $E_\gamma \in$ [1.1, 2.3] GeV. The CLAS-FROST results in red circle are compared with results from the CBELSA/TAPS collaboration [27] in blue box, which used the radiative decay mode, $\omega \to \pi^0\gamma$. The black solid line represents the BnGa PWA solution. The data points include statistical uncertainties only; the total systematic uncertainty is given as bands at the bottom of each distribution.

6.2.2 Results for the $\gamma p \to K^0\,\Sigma^+$ Reaction

The Helicity Asymmetry E in $\gamma p \to K^0\,\Sigma^+$. This section presents and discusses our final results for the first-time measurement of the helicity asymmetry **E** in the reaction $\gamma p \to K^0\,\Sigma^+ \to p\pi^+\pi^-\pi^0$.

Figure 6.32 shows the observable in 200-MeV-wide energy bins using five 0.4-wide angle bins in cos $\theta^K_{c.m.}$. The blue bar for each data point denotes the uncertainty comprising the statistical and Q-value total uncertainty added in quadrature. A large fraction of this overall uncertainty accounts for the scaling of the asymmetry with theproduct of beam and target polarization, which has a similar effect on the uncertainty. To demonstrate this scaling effect, we show superimposed (in black) in Figure 6.32 the uncertainty without considering the beam and target polarization.

Despite the fairly large uncertainties, a certain trend can be observed in the distributions. The negative slope at very low energies close to the reaction threshold appears to switch to a flatter distribution in the second energy bin, and finally turn into a positive slope in the third energy bin. All data points appear to be positive above 1.3 GeV.

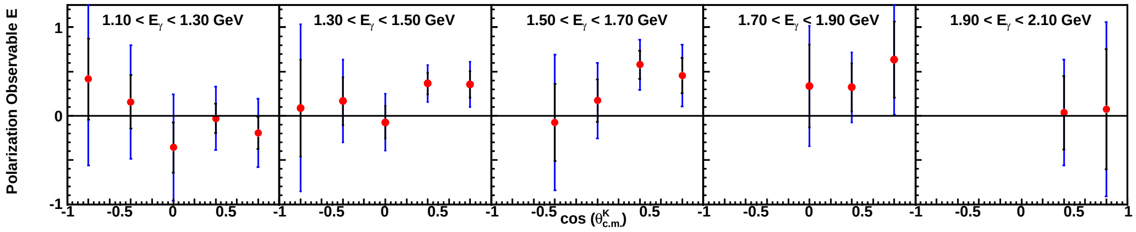

Figure 6.32: Measurement of the helicity asymmetry in the reaction $\gamma p \to K^0\,\Sigma^+$ utilizing a circularly-polarized photon beam and a longitudinally-polarized target. The results are shown in 200-MeV-wide bins for the photon energy range $E_\gamma \in$ [1.1, 2.3]; see text for more details.

CHAPTER 7

SUMMARY AND OUTLOOK

Spectroscopy is a tool, utilized by physicists to understand how quark and gluon dynamics give rise to the spectrum of hadrons. Studying the spectra of composite systems has yielded a number of great scientific discoveries. The spectrum of chemical elements inspired the concept of the atom, and atomic spectroscopy led to the development of quantum mechanics. The "Eighfold Way" classification for hadrons then established the existence of three valence quarks. Currently, at the forefront of fundamental research is the mapping of the whole spectrum of excited baryons in order to establish the dynamics of quarks and gluons in making these hadrons.

However, the spectrum of baryons is very complicated due to the broad and overlapping nature of the baryon resonances. It is also not well understood since many predicted excited states have not been experimentally observed. These *missing* resonances are predicted to couple strongly to photon beams and decay to final states involving a heavier meson, such as the vector mesons ω, ρ and ϕ. These factors motivated the measurement of differential cross sections, the spin density matrix elements and the helicity asymmetry $\mathbf{E}$ for $\gamma p \to p\omega$ using CLAS at Jefferson Laboratory. Another channel of interest is the strangeness production in $\gamma p \to K^0\Sigma^+$. The strange quark generates another degree of freedom and gives additional information not available from the nucleon-nucleon scattering. We have measured the differential cross sections, helicity asymmetry $\mathbf{E}$ and recoil hyperon polarization $\mathbf{P}$ from this channel. These measurements were performed using circularly-polarized photons in two different experiments, utilized Frozen Spin Target (FROST) in the $g9a$ experiment, and unpolarized liquid hydrogen in the $g12$ experiment.

The results from our measurements will significantly augment the world database of differential cross sections and polarization observables. The differential cross sections and the spin density matrix elements result in $\gamma p \to p\omega$ from the $g12$ experiment have large statistics that extend beyond the resonances region, and are expected to play a crucial role in probing the Regge theory. The extracted $\mathbf{E}$ observable for $\gamma p \to K^0\Sigma^+$ is a first-time measurement at all energies. The high statistics differential cross sections and $\mathbf{P}$ data have been partial-wave analized by the BnGa group and are expected to identify some new resonances. The **E** data for the reaction $\gamma p \rightarrow p\omega$ have been partial-wave analyzed within the BnGa coupled-channels framework and contributions from five poorly-established nucleon resonances have been identified.

Table 7.1 shows the star-ratings of nucleon resonances according to PDG 2004 (black) [77] and the ratings in PDG 2018 (red) [78]. This shows the remarkable efforts of the hadronic physics community in understanding QCD. 6 new resonances have been found since the last 15 years of the photoproduction experiments and 2 of them were seen in our $\gamma p \rightarrow p\omega$ channel.

The CLAS collaboration members have contributed to the field by publishing around 200 papers from 2004 to 2018, but they have only published one observable for the $K^0\Sigma^+$ channel. Thus, the results from our measurements will significantly enrich the world database. These results are in preparation for publication and several more observables for this channel are being analyzed at Florida State University.

The $N^\star$ spectroscopy only covered 2 members of the ground-state baryons. Thus, we need to complete the spectroscopy program by mapping the excited baryons with strangeness content. These experiments are now performed at JLab using GlueX detector in Hall-D as well as CLAS12 detector in Hall-B.

Table 7.1: The star-ratings of nucleon resonances according to PDG 2004 (black) and PDG 2018 (red). Table source [78].

The impact of photoproduction on baryon resonaces	black: PDG 2004	****	Existence is certain.
	red: PDG 2018	***	Existence is very likely.
	green: Removal	**	Evidence of existence is fair.
	blue: BESIII resonances	*	Evidence of existence is poor.

			– Status as seen in –									
Particle	J^P	Overall	$N\gamma$	$N\pi$	$\Delta\pi$	$N\sigma$	$N\eta$	ΛK	ΣK	$N\rho$	$N\omega$	$N\eta'$
N	$1/2^+$	****										
N(1440)	$1/2^+$	****	****	****	****	***	*			*		
N(1520)	$3/2^-$	****	****	****	****	**	****			****		
N(1535)	$1/2^-$	****	****	****	***	*	****			**		
N(1650)	$1/2^-$	****	****	****	***	*	****	***	**	**		
N(1675)	$5/2^-$	****	****	****	****	***	*	*	*	*		
N(1680)	$5/2^+$	****	****	****	****	***	*	*	*	****		
N(1700)	$3/2^-$	***	**	***	***	*	*	**	*	*		
N(1710)	$1/2^+$	****	****	****	**		***	**	*	*	*	
N(1720)	$3/2^+$	****	****	****	***	*	*	****	*	**	*	
N(1860)	$5/2^+$	**	*	**		*	*					
N(1875)	$3/2^-$	***	**	**	*	**	*	*	*	*	*	
N(1880)	$1/2^+$	***	**	*	**	*	*	**	**		**	
N(1895)	$1/2^-$	****	****	*	*	*	****	**	**	*	*	****
N(1900)	$3/2^+$	****	****	**	**	*	*	**	**		*	**
N(1990)	$7/2^+$	**	**	**			*	*	*			
N(2000)	$5/2^+$	**	**	**	**	*	*	*	*	**	*	
N(2040)	$3/2^+$	*		*								
N(2060)	$5/2^-$	***	***	**	*	*	*	*	*	*	*	
N(2100)	$1/2^+$	***	**	***	**	**	*	*		*	*	**
N(2120)	$3/2^-$	***	***	**	**	**		**	*		*	*
N(2190)	$7/2^-$	****	****	****	****	**	*	**	*	*	*	
N(2220)	$9/2^+$	****	**	****			*	*	*			
N(2250)	$9/2^-$	****	**	****			*	*	*			
N(2300)	$1/2^+$	**		**								
N(2570)	$5/2^-$	**		**								
N(2600)	$11/2^-$	***		***								
N(2700)	$13/2^+$	**		**								

BIBLIOGRAPHY

[1] M. Thomson, "Modern Particle Physics," ISBN 978-1-107-03426-6, Cambridge University Press (2013).

[2] X. J. Wen, E. J. Ferrer and V. de la Incera, "Anisotropic structure of the running coupling constant in a strong magnetic field," Extreme QCD Conference (2015).

[3] M. Poghosyan, "An introduction to Regge Field Theory," Wilhelm und Else Heraeus Physics Summer School (2013).

[4] S. Capstick and N. Isgur, "Baryons in a Relativized Quark Model with Chromodynamics," Phys. Rev. D **34**, 2809 (1986).

[5] S. Capstick and W. Roberts, "Quark Models of Baryon Masses and Decays," Prog. Part. Nucl. Phys. **45**, S241-S331 (2000).

[6] K. Peters, "A Primer on Partial Wave Analysis," Int. Journal of Modern Physics A **21**, No. 24, (2006).

[7] C. Hanretty, "Measurement of The Polarization Observables I^S and I^C for $\gamma p \to p\pi^+\pi^-$ Using The CLAS Spectrometer," PhD thesis, Florida State University (2011).

[8] V. Crede and W. Roberts, "Progress Towards Understanding Baryon Resonances," Rept. Prog. Phys. **76**, 076301 (2013).

[9] K. A. Olive *et al.*, "Particle Data Group," Chin. Phys. C **38**, 090001 (2014).

[10] R. G. Edwards *et al.*, "Excited State Baryon Spectroscopy from Lattice QCD," Phys. Rev. D **84**, 074508 (2011).

[11] R. Hofstadter and R. McAllister, "Electron Scattering from the Proton," Phys. Rev. **98**, 217 (1955).

[12] J. I. Friedmann and H. W. Kendall, "Deep Inelastic Electron Scattering," Ann. Rev. Nucl. Sci. **22**, 203-254 (1972).

[13] D. Schildknecht, "Vector Meson Dominance," Acta. Phys. Polon. **B37**, 595-608 (2006).

[14] A. Bodek *et al.*, "Experimental Studies of the Neutron and Proton Electromagnetic Structure Functions," Phys. Rev. D **20**, 1471-1552 (1979).

[15] J. Ashman *et al.* [EMC Collaboration], "A measurement of the spin asymmetry and determination of the structure function $g1$ in deep inelastic muon-proton scattering," Phys. Lett. B **206**, 364-370 (1988).

[16] W. -M. Yao *et al.* [Particle Data Group], "Review of Particle Physics," J. Phys. G **33**, 1 (2006).

[17] K. Nakamura *et al.* [Particle Data Group], "Review of Particle Physics," J. Phys. G **37**, 075021 (2010).

[18] M. Pichowsky, C. Savkli and F. Tabakin *et al.* "Polarization Observables in Vector Meson Photoproduction," Phys. Rev. C **53**, 593 (1996).

[19] V. A. Nikonov *et al.*"Further evidence for $N(1900)P_{13}$ from photoproduction of hyperons," Phys. Lett. B **662**, 245-251 (2008).

[20] J. Ballam *et al.* [SLAC Collaboration], "Vector-Meson Production by Polarized Photons at 2.8, 4.7, and 9.3 GeV ," Phys. Rev. D **7**, 3150 (1973).

[21] R. W. Clift *et al.* [Daresbury Collaboration], "Observation of a baryon exchange dip and parton effects in backward photoprodcution of ω ," Phys. Lett. B **72**, 144 (1977).

[22] M. Battaglieri *et al.* [CLAS Collaboration], "Photoproduction of ω Meson on the Proton at Large Momentum Transfer," Phys. Rev. Lett **90**, 022002 (2003).

[23] J. Barth *et al.* [SAPHIR Collaboration], "Low-energy photoproduction of ω-mesons," Eur. Phys. J. A **18**, 117 (2003).

[24] F. Klein *et al.* [CBELSA/TAPS Collaboration], "Beam asymmetries in near-treshold ω photoproduction off the proton," Phys. Rev. D **78**, 117101 (2008).

[25] M. Williams *et al.* [CLAS Collaboration], "Differential cross sections and spin density matrix elements for the reaction $\gamma p \to p\omega$," Phys. Rev. C **80**, 065208 (2009).

[26] I. I. Strakovsky *et al.* [A2 Collaboration], "Photoproduction of the ω Meson on the Proton Near Threshold," Phys. Rev. C **91**, 045207 (2015).

[27] H. Eberhardt *et al.* [CBELSA/TAPS Collaboration], "Measurement of double polarisation asymmetries in ω-photoproduction," Phys. Lett. B **750**, 453-458 (2015).

[28] A. Wilson *et al.* [CBELSA/TAPS Collaboration], "Photoproduction of ω mesons off the proton," Phys. Lett. B **749**, 407-413 (2015).

[29] M. Williams *et al.* [CLAS Collaboration], "Partial Wave Analysis of the reaction $\gamma p \to p\omega$ and the Search for Nucleon Resonances," Phys. Rev. C **80**, 065209 (2009).

[30] R. Erbe *et al.* [ABBHHM Collaboration], "Multipion and Strange-Particle Photoproduction on Protons at Energies up to 5.8 GeV," Phys. Rev. **188**, 2060 (1969).

[31] R. Lawall *et al.* [SAPHIR Collaboration], "Measurement of the reaction $\gamma p \to K^0\Sigma$ at photon energies up to 2.6 GeV," Eur. Phys. J. A **24**, 275 (2005).

[32] I. Denisenko *et al.*, "$N^\star$ decays to $N\omega$ from new data on $\gamma p \to p\omega$," Phys. Lett. B **755**, 97-101 (2016).

[33] Z. Akbar *et al.* [CLAS Collaboration], "Measurement of the helicity asymmetry E in $\omega \to \pi^+\pi^-\pi^0$ photoproduction," Phys. Rev. C **96**, 065209 (2017).

[34] P. Roy *et al.* [CLAS Collaboration], "Measurement of the beam asymmetry Σ and the target asymmetry T in the photoproduction of ω mesons off the proton using CLAS at Jefferson Laboratory," Phys. Rev. C **97**, 055202 (2018).

[35] P. Roy, "Measurement of Polarization Observables in Vector Meson Photoproduction Using a Transversely-Polarized Frozen-Spin Target and Polarized Photons at CLAS, Jefferson Lab," PhD thesis, Florida State University (2016).

[36] S. Park, "Measurement of Polarization Observables in $\gamma p \to p\pi^+\pi^-$ Using Circular Beam and Longitudinal Target Polarization and The CLAS Spectrometer at Jefferson Laboratory," PhD thesis, Florida State University (2013).

[37] R. J. J. Castelijn, "Photoproduction of strange mesons and hyperons on the proton," PhD thesis, University of Groningen (2006).

[38] N. K. Walfrod, "The Search for Missing Resonances in $\gamma p \to K^+ + \Lambda$ and $K^+ + \Sigma^0$ Using Circularly Polarized Photons on a Transversely Polarized Frozen Spin Target," PhD thesis, The Catholic University of America (2014).

[39] M. Saini, "Search for New and Unusual Strangeonia in Photoproduction using CLAS," PhD thesis, Florida State University (2013).

[40] B. A. Mecking *et al.*, "The CEBAF Large Acceptance Spectrometer (CLAS)," Nucl. Instrum. Meth. A **503**, 513 (2003).

[41] https://www.flickr.com/photos/jeffersonlab/

[42] D. I. Sober *et al.*, "The bremsstrahlung tagged photon beam in Hall B at JLab," Nucl. Instrum. Meth. A **440**, 263 (2000).

[43] https://userweb.jlab.org/ ckeith/Frozen/Frozen.html

[44] http://www.jlab.org/ christo/g11a target.html

[45] http://www.jlab.org/Hall-B/

[46] Z. Akbar *et al.*, “g12 Analysis Procedures, Statistics and Systematics,” CLAS Note 2017-002 (2017).

[47] M. Kunkel, “Photoproduction of π^0 on Hydrogen with CLAS from 1.1 GeV - 5.45 GeV using $e^+ \, e^- \, \gamma$ Decay,” PhD thesis, Old Dominion University (2014).

[48] M. D. Mestayer *et al.*, “The CLAS drift chamber system,” Nucl. Instrum. Meth. A **449**, 81 (2000).

[49] E. S. Smith *et al.*, “The Time-of-Flight System for CLAS,” Nucl. Instrum. Meth. A **432**, 265 (1999).

[50] https://logbooks.jlab.org/book/hblog

[51] E. Pasyuk, “Energy-loss corrections for charged particles in CLAS,” CLAS Note 2007-016 (2007).

[52] C. Patrignani *et al.* [Particle Data Group], “Review of Particle Physics,” Chin. Phys. C **40**, no. 10, 100001 (2016).

[53] M. Williams *et al.* [CLAS Collaboration], “Differential cross sections for the reactions $\gamma p \to p\eta$ and $\gamma p \to p\eta'$,” Phys. Rev. C **80**, 045213 (2009).

[54] M. Williams, “Measurement of Differential Cross Sections and Spin Density Matrix Elements along with a Partial Wave Analysis for $\gamma p \to p\omega$ using CLAS at Jefferson Lab,” PhD thesis, Carnegie Mellon University (2007).

[55] M. Williams, C. A. Meyer, “Kinematic Fitting in CLAS,” CLAS Note 2003-017 (2003).

[56] S. Stepanyan *et al.*, “Energy Calibration of the JLab Bremsstrahlung Tagging System,” Nucl. Instrum. Meth. A **572**, 654 (2007)

[57] M. Dugger, C. Hanretty, “Correction to the incident-photon energy for g8b data,” CLAS Note 2009-030 (2009).

[58] D. Applegate *et al.*, “A Detailed Study of The Sources of Systematic Errors in the CLAS g11 Data,” CLAS Note 2006-017 (2006).

[59] H. Olsen and L. C. Maximon, “Photon and Electron Polarization in High-Energy Bremsstrahlung and Pair Production with Screening,” Phys. Rev. **114**, 887 (1959).

[60] S. Strauch *et al.* [CLAS Collaboration], “Beam-helicity asymmetries in double-charged-pion photoproduction on the proton,” Phys. Rev. Lett. **95**, 162003 (2005).

[61] Polarization of circularly polarized photon beam in g9b, `https://clasweb.jlab.org/rungroups/g9/wiki/index.php/Circular_Beam_Polarization`.

[62] W. Verkerke, D. Kirkby, "RooFit Users Manual v2.91," Document version 2.91-33, October 14th (2008).

[63] P. Weidenauer *et al.* [ASTERIX Collaboration], Z. Phys. C **59**, 387 (1993).

[64] T. D. Lee *et al.*, "Possible Detection of Parity Nonconservation in Hyperon Decay," Phys. Rev. **106**, 1367 (1957).

[65] R. Gatto, "Relations between the Hyperon Polarizations in Associated Production," Phys. Rev. **109**, no. 2, 610 (1958).

[66] W. Roberts and T. Oed, "Polarization observables for two-pion production off the nucleon," Phys. Rev. C **71**, 055201 (2005).

[67] J. Ball, E. Pasyuk, "Photon Flux Determination Through Sampling of "out-of-time" Hits with the Hall B Photon Tagger," CLAS Note 2005-002 (2005).

[68] K. Schilling, P. Seyboth and G. E. Wolf, Nucl. Phys. B **15**, 397 (1970) Erratum: [Nucl. Phys. B **18**, 332 (1970)].

[69] B. Carnahan, "Strangeness Photoproduction in the $\gamma p \to K^{)}\Sigma^{+}$ Reaction," Doctoral Dissertation (2003), The Catholic University of America.

[70] W. Tang, "Photoproduction of $K^{*+}\Lambda/\Sigma^{0}$ and $K^{0}\Sigma^{+}$ from proton using CLAS at Jefferson Lab," Doctoral Dissertation (2012), Ohio University.

[71] C. S. Nepali, Old Dominion University.

[72] R. Castelijns *et al.* [CBELSA/TAPS Collaboration], "Nucleon resonance decay by the $K^{0}\Sigma^{+}$ channel," Eur. Phys. J. A **35**, 39 (2008).

[73] R. Ewald *et al.* [CBELSA/TAPS Collaboration], "Anomaly in the $K_{S}^{0}\Sigma^{+}$ photoproduction cross section off the proton at the K^{*} threshold," Phys. Lett. B **713**, 180 (2012).

[74] R. Ewald *et al.* [CBELSA/TAPS Collaboration], "Measurement of polarisation observables in $K_{s}^{0}\Sigma^{+}$ photoproduction off the proton," Phys. Lett. B **738**, 268 (2014).

[75] C. S. Nepali *et al.* [CLAS Collaboration], "Transverse polarization of $\Sigma^{+}(1189)$ in photoproduction on a hydrogen target in CLAS," Phys. Rev. C **87**, no. 4, 045206 (2013).

[76] M. Williams, M. Bellis and C. A. Meyer, "Multivariate side-band subtraction using probabilistic event weight," J. Instrum. **4**, P10003 (2009).

[77] S. Eidelman *et al.* [Particle Data Group], "Review of Particle Physics," Phys. Lett. B **592**, 1 (2004).

[78] A. Ernst, Private communication.

BIOGRAPHICAL SKETCH

I was born in Purwokerto, a small city in Java Island, Indonesia. My entire childhood was spent in Purwokerto until I graduated from high school in 2003. During my school time, I was highly interested in physics. Thus, I joined a national physics competition and secured 11th rank in the national team, a team that will compete in the International Physics Olympiad (IPhO). After graduated from high school, I went to the most prestigious Indonesian university, Institut Teknologi Bandung (ITB), to pursue a Bachelor of Science degree in Physics. In completing my B.Sc. program, I studied Supersymmetric black holes in cosmological Einstein-Maxwell theory as the topic of my undergraduate thesis. I completed my bachelor degree from ITB by 2009. In 2011, I joined Sekolah Tinggi Keguruan dan Ilmu Pendidikan Surya (STKIP Surya), a college of education where its mission was to educate students from remote and underdeveloped areas in Indonesia, as Teaching Assistant. Simultaneously, I began to apply for doctoral programs in United States of America. I was offered an admission for the doctoral program at Department of Physics, Florida State University (FSU) in the Fall 2013. After I successfully passed the qualifying exam on August 2013, I joined the hadronic physics group with Professor Volker Crede as my advisor. Over the course of this work, I gave several talks in International conferences, CLAS collaboration meetings, and FSU nuclear seminars. In April 2018, I was awarded the John. D. Fox. Award in nuclear physics by the Department of Physics at Florida State University. In 2017, I published a paper in "Phys. Rev. C **96**, 065209 (2017)" as the first authors and in 2018, I published a paper in " Phys. Rev. C **97**, 055202 (2018)" as the second authors. Several more papers as a result of this analysis are currently in preparation.